INAUGURAL-DISSERTATION

zur
Erlangung der Doktorwürde
der
Naturwissenschaftlich-Mathematischen
Gesamtfakultät
der Ruprecht-Karls-Universität
Heidelberg

vorgelegt von
Dipl.-Phys. Achim Besser
aus Heidelberg

Tag der mündlichen Prüfung: 29.04.2009

Modeling the Coupling
of Mechanics and Biochemistry
in Cell Adhesion

Gutachter: Prof. Dr. Ulrich S. Schwarz
                Prof. Dr. Heinz Horner

Zusammenfassung:
Das Aktin-Zytoskelett, ein aus dem Biopolymer Aktin aufgebautes Filamentsystem, bestimmt maßgeblich die mechanischen Eigenschaften von biologischen Zellen. Andererseits wird das Aktin-Zytoskelett selbst durch mehrere biochemische Signaltransduktionspfade reguliert. Um das theoretische Verständnis dieser Kopplung von Mechanik und Biochemie voranzutreiben, wird hier ein Modell für Stressfasern entwickelt, die die typische Morphologie des Aktin-Zytoskeletts bei starker Zelladhäsion darstellen. Die Mechanik einer Stressfaser wird durch eine Kette von viskoelastischen Elementen beschrieben, die zudem lokal kontrahieren können. Das zunächst diskrete Modell wird durch einen Kontinuumslimes in eine partielle Differentialgleichung überführt. Die biochemische Regulation wird durch ein System von Reaktions-Diffusions-Gleichungen beschrieben die über die Kontraktionsaktivität an die Mechanik koppeln.

Zunächst wird die mechanische Stressfaser-Gleichung analytisch gelöst und insbesondere der komplexe Modulus exakt berechnet. Das Modell wird dann zur Auswertung experimenteller Daten verwendet, die von Kooperationspartnern beim Laserschneiden von Stressfasern gewonnen wurden. Dabei zeigt sich, dass Stressfasern in ihrer Umgebung verankert sind und dass die Lokalisierung bestimmter mechanosensitiver Proteine genau der theoretisch vorhergesagten Kraftverteilung folgt. Schließlich wird das Gesamtmodell angewandt, um Zellverhalten auf elastischen Substraten zu modellieren. Mittels einer Bifurkationsanalyse werden experimentell überprüfbare Vorhersagen abgeleitet, insbesondere sagt das Model Bistabilität und Hysterese in der Zelladhäsion voraus.

Abstract:
The actin cytoskeleton, which is a filament system made of actin biopolymers, mainly determines the mechanical properties of biological cells. In turn, the actin cytoskeleton is itself regulated by various biochemical signaling pathways. To advance the theoretical understanding of this coupling between mechanics and biochemistry, we developed a model for stress fibers which constitute the typical morphology of the actin cytoskeleton in mature cell adhesion. The mechanics of a stress fiber is described by a chain of viscoelastic elements that in addition may locally contract. The initial discrete model is transformed to a partial differential equation by performing a continuum limit. The biochemical regulation is modeled by a system of reaction diffusion equations that couple to the mechanics via the contractile activity along the fiber.

In the first part of this thesis, the mechanical stress fiber equation is solved analytically and in particular the complex modulus is exactly calculated. The model is then used for the analysis of experimental data, measured by collaborators in experiments on stress fiber laser nanosurgery. It turns out that stress fibers are considerably crosslinked to their environment and that the localization of certain mechanosensitive proteins correlates with the theoretically predicted stress distribution within the actin cytoskeleton. Finally, the complete model is used to describe cellular behavior on elastic substrates. By performing a bifurcation analysis theoretical predictions are derived that can be tested in future experiments, in particular, the model predicts bistability and hysteresis in cell adhesion.

Contents

List of Figures

List of Tables

List of Symbols

k_b	boundary stiffness	page 104
k_{int}	internal stress fiber stiffness	page 16
k_{ext}	external stiffness	page 16
$k_{N,int}$	internal stress fiber stiffness in N-th iteration step	page 21
K	Michaelis constant	page 89
L	stress fiber length	page 16
$\triangle L$	total contraction length	page 63
$\mathbf{M}_{elas}$	matrix containing elastic constants	page 25
$\mathbf{M}_{visc}$	matrix containing viscous constants	page 25
r	rate constant	page 89
S_m	amplitude of the m-th retardation time	page 34
T	period time	page 110
u	displacement	page 16
u_n	displacement of the n-th node	page 16
u_{ss}	displacement in the steady state	page 23
u_{ij}	strain tensor	page 18
$\mathbf{U}$	matrix of eigenvectors	page 27
v	contraction velocity	page 17
v_0	zero force velocity	page 17
v_n	contraction velocity of n-th element	page 17
$\vec{v}_l$	l-th eigenvector	page 26
V	maximum velocity	page 89
w	sarcomere length	page 96
$\vec{y}$	relative coordinates	page 26
γ_{int}	internal stress fiber viscosity	page 16
$\tilde{\gamma}_{int}$	effective internal viscosity	page 17
γ_{ext}	external viscosity	page 16
Γ	ratio of external over internal viscosity	page 23
δ	free contraction length	page 22
κ	ratio of external over internal stiffness	page 22
λ_l	l-th eigenvalue	page 26
ν	Poisson's ratio	page 18

ρ	correlation coefficient	page 61
σ	rope tension or stress within fiber	page 37
σ_0	stress within fiber before cut	page 38
σ_{ij}	stress tensor	page 19
τ	time scale associated with effective internal viscosity	page 22
τ_ϵ	time scale associated with external viscosity	page 22
τ_m	m-th retardation time	page 30
$\tau_{m,N}$	m-th retardation time in the N-th iteration step	page 29
ϕ_N	scaling factor in N-th iteration step	page 21
ω	angular frequency	page 43
$\tilde{}$	denotes non-dimensional quantities scaled with a or τ	page 23
$\bar{}$	denotes Laplace-transformed quantities	page 33

Chapter 1

Introduction

Any living organism is exposed to a diverse set of physical factors like temperature, light or mechanical cues as well as to many chemical factors like nutrients or odors. The efficient perception of this information and its subsequent processing and conversion into an accurate response are critical for the survival of each individual creature. The traditional five senses in higher organisms to perceive these environmental cues are taste, smell, vision, touch and hearing. Taste and smell are examples for chemoreception, vision is an example for photoreception and touch and hearing are examples for mechanoreception. The sensation is realized by specialized organs in higher organisms, like the nose, the tongue, the eye or the ear.

As physical factors, especially mechanical ones, play such a significant role for higher organisms, evolution has brought up a diverse set of other mechanisms for mechanosensation. For example, the gravitational force guides plant shoots towards the sky and their roots deeper into the soil. Bats have developed a sonar organ based on ultra sonic waves to actively sense their environment. Most types of fish are equipped with the so called lateral line organ which spans along their length. It allows them to sense subtle changes in the pressure field to coordinate swarming or chase after prey. In general these mechanical cues are transduced into a chemical or electrical signal. This process is termed *mechanotransduction* and is realized molecularly in many different ways [1]. Among the well characterized mechanisms is for example the tension-induced opening of ion channels which transduce external mechanical forces into influx of ions [2, 3].

From our every day notion we know that the behavior of higher multicellular organisms is influenced by environmental cues. However, it is equally important to understand how single cells respond to extracellular stimuli. Thereby, the signal processing and the response of a single cell has to be fundamentally different and much simpler than in higher organisms but still reliable and robust. For example, cellular motion can be directed by external stimuli. Unicellular green algae swim towards or away from light (phototaxis) [4]. Tissue cells can sense electric fields and crawl towards the cathodal end of the field (galvanotaxis) [5]. Another very well studied example is chemotaxis. Motile bacteria like Escherichia coli have developed sophisticated strategies to follow shallow gradients of nutrients or to escape from noxious chemicals. This chemically guided movement can be found also in multicellular organisms. The most prominent examples are the chase of neutrophils after pathogens, the search of sperm cells after

the egg and, subsequent to fertilization, directed cell migration during development.

Beside chemical stimuli, also many mechanical cues, like the rigidity of the cellular surrounding or mechanical stress, determine the behavior of certain tissue cells [6–9]. In principle, to sense mechanical cues in their environment, cells need to establish a physical connection to their surrounding as well as a force producing mechanism that allows active probing of the mechanical environment. The buildup of cellular connections, that is also necessary to form tissue, is in general called *cell adhesion* and is usually mediated by specialized transmembrane receptor proteins. These receptor proteins determine the architecture and the chemical compositions of the cellular "glue" in the contact area and mediate specific binding to other cells or macromolecules in their environment. Cellular contractile forces are established by molecular motor proteins that reside in muscle like structures that can contract upon consumption of chemical energy. The best studied example of such contractile structures are so called actin *stress fibers*. The cellular forces are transmitted through the cellular contacts to the extracellular environment. Interestingly, the chemical composition of these contacts, their growth and the biochemical signals that are initiated there, depend on the exerted mechanical stress. The resulting signals have an influence on many cellular processes but in particular also effect the contractile cellular forces. In this way a tight mechano-chemical feedback cycle is formed that is essential to perform the mechanotransduction for example of the rigidity of the cellular environment.

In cell adhesion, such mechano-chemical regulatory feedback mechanisms affect essential processes like tissue development and repair but also disease-related processes like growth and migration of cancer cells [10–12]. However, theoretical models describing the mechano-chemical feedback are still rare. This thesis aims at filling this gap and we want to show how models for the coupling of biochemistry and mechanics can be devised in a meaningful way and thereby provide further insight into such complex systems.

In the following, we will briefly discuss some recent experiments on single cells demonstrating that, in adhesion-related processes, cellular behavior is indeed not only controlled by biochemical cues, but also involves many physical determinants especially the geometry and the rigidity of the cellular environment as well as the mechanical stress in the tissue [1, 13–15]. The sensation of these mechanical cues depends on the capability of cells to actively probe their environment with cellular contractile forces and to convert this mechanical process into a biochemical signal. This is the onset of a complex mechano-chemical feedback mechanism that will be further elucidated below. Finally, we will specify some common experimental and modeling techniques used in this field and conclude the introduction with an outline of this thesis.

1.1 A sense of touch on the single cell level

Traditionally, the investigation of determining factors of single cell decision making or function in tissue, like cell differentiation or proliferation, has been strongly focused on chemical aspects, including detailed models for signal transduction [16, 17]. During recent years, however, it has become increasingly clear that there also exist a "sense of touch" on the single cell level which enables the cells to recognize the mechanical properties of their environment. By integrating this mechanical information they do adapt better to their environment. For example it has been shown that fibroblasts, these are cells derived from connective tissue, can sense a stiffness gradient in their environment and start to move towards the stiffer region, called durotaxis (Latin durus, hard). The experimental results by Lo et al. [6] are illustrated in Fig. 1.1. The stiffness gradient was produced by synthesizing two polyacrylamide gels of different stiffness. When cells reached the interfacial region coming from the softer side, they migrated over to the stiff substrate. In contrast, when cells approached the interface from the stiff side, they turned around to stay on the stiff substrate. It has also been shown that these cells better adhere on stiff substrates which is expressed by a decrease in motility, an increase in spread area and higher contractile forces exerted to stiffer environments [6–9].

The discrimination between soft or rigid substrates seems to be reduced on the single cell level as soon as cells form cell to cell contacts [6, 9]. Interestingly, Saez et al.[18] showed that monolayer tissue-patches formed by a few Madin-Darby canine kidney (MDCK) epithelial cells still orient along the axis of highest rigidity, see Fig. 1.1. In these experiments, substrates of anisotropic stiffness have been realized by micro arrays of elastic polymer pillars with elliptic cross section, see also Tan et al. [19]. The impact of stiffness on tissue organization was also shown by measuring the distribution of traction forces exerted on the micro pillars. Exerted traction forces were deduced from pillar deflection and were found to be maximal at the poles of the patch indicating that contraction mainly occurs along the axis of highest rigidity. Thus, the experiments by Saez et al. suggest that the rigidity of the cellular environment is indeed important also for tissue development.

Most strikingly, even fundamental cellular processes, like stem cell differentiation, are co-regulated by the stiffness of the environment. This has been shown by Engler et al. [20] plating naive mesenchymal stem cells (MSCs) derived from bone marrow on polyacrylamide substrates of different stiffness. On stiff substrates ($25 − 40$ kPa), that mimic the mechanical properties of crosslinked collagen of not yet calcified bone tissue, these cells differentiate to osteoblasts (bone cells). In contrast, on very soft substrates ($0.1 − 1$ kPa), that mimic the mechanical environment of brain tissue, cells transform to neurons (brain cells). Finally, within an intermediate stiffness range ($8 − 17$ kPa), that corresponds to the stiffness of striated muscle, MSCs adopt the morphology of myoblasts (muscle cells). These experiments demonstrate, that the tissue stiffness alone is sufficient to guide MSCs differentiation into a cell type that is appropriate for the given mechanical environment. These findings have obviously far reaching consequences for artificial tissue engineering and stem cell therapy. Moreover, it has been shown by shutting down motor activity by appropriate drugs that the elasticity dependent lineage
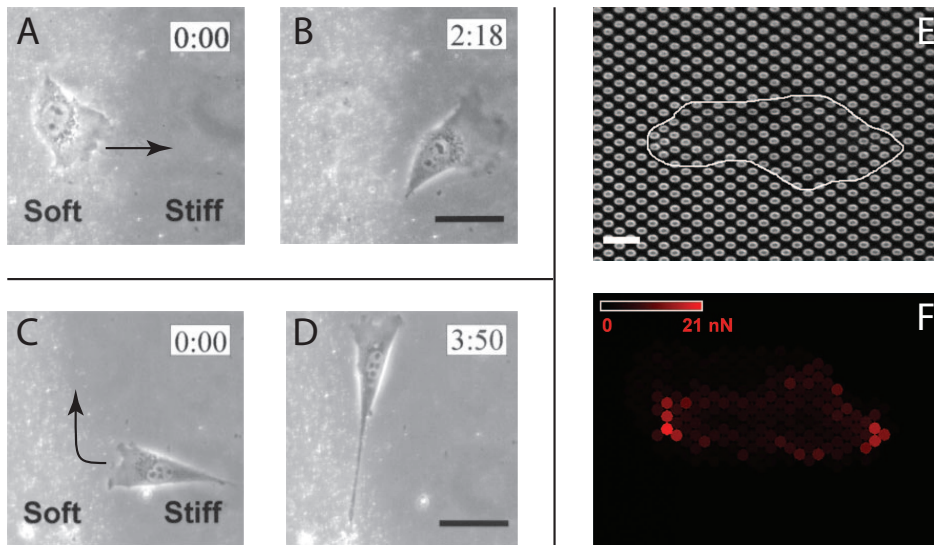
Figure 1.1: (A-B) Discovery of a "sense of touch" on the single cell level. Increase in substrate stiffness from left to right is visualized as a decease in density of embedded fluorescent beads (bright spots in (A-D)). (A,B) Cell migrates from the soft over to the stiff substrate and shows a subsequent increase in spread area. (C,D) When cells approach the interfacial region coming from the stiff side, they turn around in order to stay on the rigid substrate. The observed migration, directed by substrate rigidity, was termed durotaxis. Figures (A-D) were taken from [6]. (E-F) Saez et al. [18] employed micro arrays of elastic polymer pillars with elliptic cross section to investigate the impact of anisotropic elasticity on tissue organization. Patches of MDCK epithelial cells elongate preferentially along the axis of highest rigidity. (E) Shows the envelope of the patch (scale bar: $10\,\mu$m). (F) Color map of the traction force measured by pillar displacement. Highest values are reached at the two poles of the patch indicating an anisotropic stress distribution within the tissue. Figures (E,F) were taken from [18].

specification of MSCs necessitates cellular contractility. This is evidence for the fact, that cells need to have a force producing mechanism in order to actively sense their mechanical environment.

Beside the stiffness of the environment, also the application of mechanical stress to the cellular environment has an impact on cell behavior. In fact it can be argued that both high stiffness and increased prestress have the same effect on the energy investment required for cells to pull on their substrates [21]. By pulling or pushing the substrate in the proximity of a cell using a microneedle, Lo et al. [6] could provoke cell reorientation and migration into the direction where the strain in the substrate has been increased. Similarly, cells align parallel to the axis of applied strain when the substrate is statically or quasi statically stretched [22, 23]. In contrast, when cyclic strain of high frequency is applied, cells rather tend to orient away from the direction of strain [24, 25]. The cell reorientation can be partially explained either by assuming that cells tend to minimize the disruption of their intracellular scaffolds [26] or by assuming that cells reorient to actively maintain an optimal stress in their environment [27]. Since many tissue cells are subject to cyclic strain in their physiological environment, like in the heart, the vessel walls or in the gut, further understanding of the cellular

response to externally applied stress is essential in order to gain insight into the cellular self-assembly of these organs.

There is also increasing evidence that mechanotransduction plays an important role in many severe diseases, including asthma, osteoporosis, atherosclerosis and diabetes [28]. Increased rigidity might also constitute a barrier for regeneration in scar tissue, as it occurs in heart or brain strokes. Furthermore, cancer tissue is in most cases stiffer than normal tissue. This might correspond to an increase in cellular contractility and subsequent malfunction of mechanical induced signaling pathways [29]. At the same time, the increased rigidity of the environment was also shown to impact on cancer cell migration [12].

1.2 Cell adhesion: a mechano-chemically coupled system

In order to sense mechanical cues of their environment, cells need to establish a physical connection to the surrounding mechanical scaffold. In tissue, cells can either hook up among each other or reach out for the extracellular matrix (ECM). The latter mainly consists of collagen but in addition comprises a diverse set of other macromolecules that are all produced and secreted locally by specialized cells from the fibroblast family. This includes osteoblasts that form bone tissue by also calcifying the matrix [30]. Direct cell to cell connections are called adherens junctions and are based on the transmembrane receptor cadherin that mediates homophilic binding. The cell to ECM connections in culture are called *focal adhesions* and are based on the transmembrane receptor integrin that recognizes certain binding motives in the ECM, in particular the tripeptide Arg-Gly-Asp sequence or briefly RGD-sequence. Although these two connection types differ in molecular composition, they both form large protein plaques on the cytoplasmic side that connect them to actin filaments.

The actin filaments are part of the cytoskeleton which also comprises other biopolymers, namely, microtubules and intermediate filaments. These three types of biopolymers constitute the intracellular mechanical scaffold and play together in order to maintain the mechanical integrity of the cell. They are also involved in various mechanical processes, like intracellular transport or the positioning and separation of chromosomes during mitosis. Regarding mechanosensing, the actin cytoskeleton is of particular importance. Its network morphology is intimately regulated by various proteins which control nucleation, branching, capping, polymerization as well as crosslinking of the fibers. In addition, actin filaments are polar structures with the two ends exhibiting different polymerization kinetics. The so called plus end is growing quickly while the minus end is rather growing slowly. If the main crosslinker proteins are $\alpha-$actinin and the molecular motor protein myosin II, then the actin filaments bundle to so called actin *stress fibers* [33] that usually terminate in focal adhesions, see Fig. 1.2(A) or Fig. 1.3 for a schematic representation. It has been found that albeit being less ordered than striated muscle on the level of electron microscopy, stress fibers do exhibit a similar periodic organization. This can be shown experimentally by fluorescent labelling of α-actinin and myosin. These two proteins arrange sequentially along the
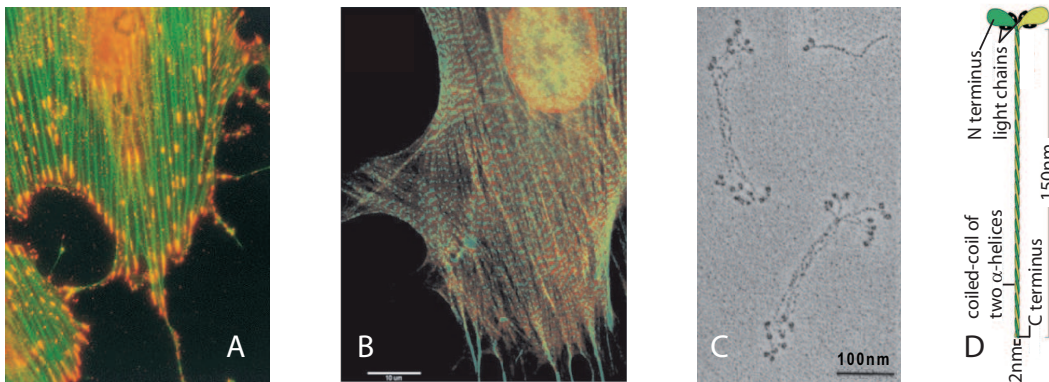
Figure 1.2: (A) Fluorescent micrograph of an adherent fibroblast. The green bundles are stress fibers that terminate at focal adhesions, shown in red. Figure was adopted from [30]. (B) Stress fibers in fibroblasts also have a sarcomeric like substructure similar to striated muscle. Fluorescently labelled proteins are α-actinin (in green) and myosin light chain (in red). These two components arrange sequentially along stress fibers and thereby form these regular striation patterns. Figure was taken from Peterson et al. [31]. (C) Electron micrograph of metal-shadowed myosins. Myosin is a dimer (upper right corner) and bundles to so called myosin minifilaments. Figure has been reproduced from data published by Trybus et al. [32]. (D) Myosin II is a dimer of two heavy chains, that form the tail and the two head domains. In addition, four light chains of two different kinds are present at the head domains while each head carries one chain of each kind. Myosin light chain regulates myosin binding to actin. Figure was adopted from [30].

fiber and thereby form a quite regular striation pattern, visualized in Fig. 1.2(B)[31]. The green regions correspond to the actin crosslinker α-actinin while the red regions correspond to myosin II molecular motors. Non-muscle myosin II is a dimer with two head domains and known to assemble into bipolar minifilaments consisting of 10-30 myosins. These minifilaments can be assembled in vitro and then visualized by electron microscopy, illustrated in Fig. 1.2(C)[32] and schematically shown in the cartoon of a stress fiber in Fig. 1.3. Each head domain of the myosin dimer also carries two different myosin light chains that regulate the binding of the head domain to actin filaments, see Fig. 1.2(D)[30]. If myosin light chain is phosphorylated, then the head domain is activated and can bind to the actin filaments. Under consumption of chemical energy, myosin goes through a force producing cycle and walks towards the plus end of the actin filament, hydrolyzing one ATP for each step. Since the actin filaments are arranged in antiparallel order, the bipolar myosin minifilaments thereby cause a contraction of the sarcomere like units, see Fig. 1.3.

This *actomyosin contractility* is the basic mechanism of force generation that enables cells to actively sense the mechanical properties of their environment and to convert this mechanical information into a biochemical signal. The mechanotransduction takes place preferentially at focal adhesions which are located at the mechanical interface between the extracellular and intracellular load-bearing scaffolds. Mechanotransduction might also occur all along stress fibers which is a quite new perspective and strongly supported through results presented within this thesis [34].

The mechanosensitivity of integrin mediated cell-matrix connections has been demon-
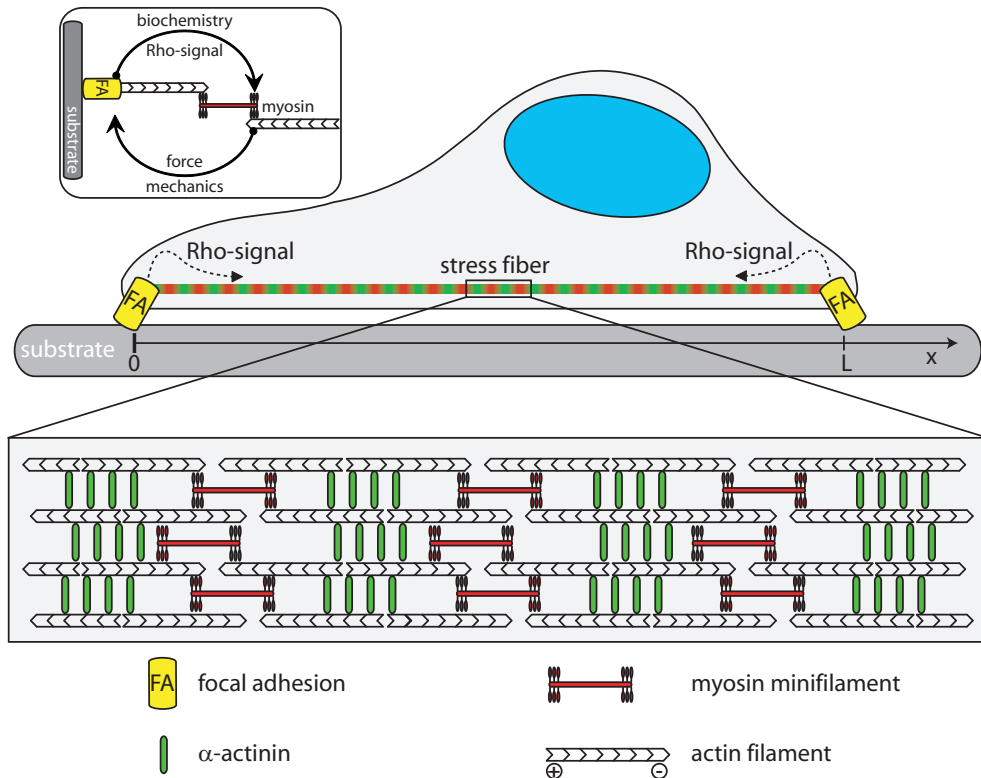
Figure 1.3: Cells adhere to the extracellular matrix by integrin-mediated contacts called focal adhesions. These contacts are the anchor points of stress fibers, which are actin filament bundles held together by the crosslinker molecule α-actinin and myosin II molecular motors. The myosins are assembled in myosin mini-filaments. Due to myosin motor activity stress fibers are under tension and exert forces to focal adhesions. This mechanical stimulus initiates biochemical signals (Rho-signal) that originate from focal adhesions and propagate into the cytoplasm, altering in turn myosin activity. Therefore the system of focal adhesions and stress fibers are connected by a biochemical and mechanical positive feedback loop (inset).

strated by varies types of experiments including biochemical stimulation with drugs or micro mechanical devices. By using optically trapped micro beads, it has been shown that nascent integrin connections mechanically fortify in dependence on the rigidity of the environment [35]. These initial connections that comprise only a few integrin molecules can develop to larger, dot like structures that are called *focal complexes*. As the size of focal complexes is about $1\,\mu$m they can be visualized by fluorescence microscopy and are usually found at the cell periphery [36]. Focal complexes can further mature to several microns large focal adhesions [36, 37] that on their cytoplasmic side recruit more than 90 components, mostly proteins, which physically reside in the adhesion structure [38], see also Fig. 4.1. However, the growth of the protein plaque requires actomyosin contractility. By applying shear stress to the cell with a microneedle, Riveline et al. [39] could show that the needed actomyosin contractility can be substituted by externally applied shear stress. Moreover, it has been shown that the

size of focal adhesions is proportional to the applied stress [40]. These experiments have demonstrated that focal adhesions are mechanosensitive protein aggregates and that their growth is strongly dependent on mechanical stress.

Molecularly, the precise mechanism of mechanotransduction at focal adhesions still has to be determined. However, some possibilities are lively discussed, for example, force induced conformational changes of single proteins or protein complexes into a high or low affinity state to possible binding partners. Recently, evidence along these lines has been reported for talin [41, 42] and integrin [43]. In a similar way forces could alter the enzymatic activity of kinases or phosphatases that are located in the adhesion contact [44].

In this way, focal adhesions have to be understood as localized spots where chemical as well as mechanical information is processed collectively. The outgoing signals then contribute to various signaling pathways. In particular, many up and down regulators of the two Rho-GTPases, Rac and Rho, have been found to be associated with focal adhesions. Rac and Rho are themselves the main regulators of the actin cytoskeleton. In many situations, Rac and Rho can be regarded as antagonists switching the actin cytoskeleton between different structural states [45]. Rac is known to stimulate the formation of focal complexes and lamellipodia which is a rather isotropic actin filament meshwork at the cell periphery [46], whereas Rho induces the formation of focal adhesions and stress fibers [47]. The Rho-pathway targets, among other things, the regulatory myosin light chain. By enhancing myosin light chain phosphorylation, more myosin heads along the myosin minifilaments can bind to actin fibers and perform their force producing cycle. Thus, activation of the Rho-pathway at focal adhesions leads to an increase in actomyosin contractility along stress fibers. The altered actomyosin forces are then transmitted back to the adhesion and change the biochemical signaling, presumably also the Rho signaling. In this way, a biochemical and mechanical feedback loop is formed that regulates the maturation of focal adhesions and the assembly of stress fibers. The investigation of this mechano-chemically coupled system of force induced biochemical signaling at focal adhesions on the one hand and the biochemical regulation of stress fiber contraction mechanics on the other hand is the focus of this thesis.

1.3   Experimental techniques

In order to investigate this mechano-chemically feedback in cell adhesion one can use experimental techniques that either interfere with the biochemical signaling pathway or with the mechanics of the actin cytoskeleton. The effect of the chemical or mechanical perturbation is then often visualized by fluorescence microscopy. Thereto, the proteins of interest are labelled with a fluorescent dye. This can be realized in several ways. If one is not interested in resolving the cellular response over time, then it is sufficient to fixate and thereby kill the cells after perturbation and stain the protein of interest with a fluorescently labelled antibody that is specific for this protein. However, if one is interested in live cell imaging during perturbation then it is necessary to transfect the cells with a DNA construct which codes for a fluorescently modified version of the
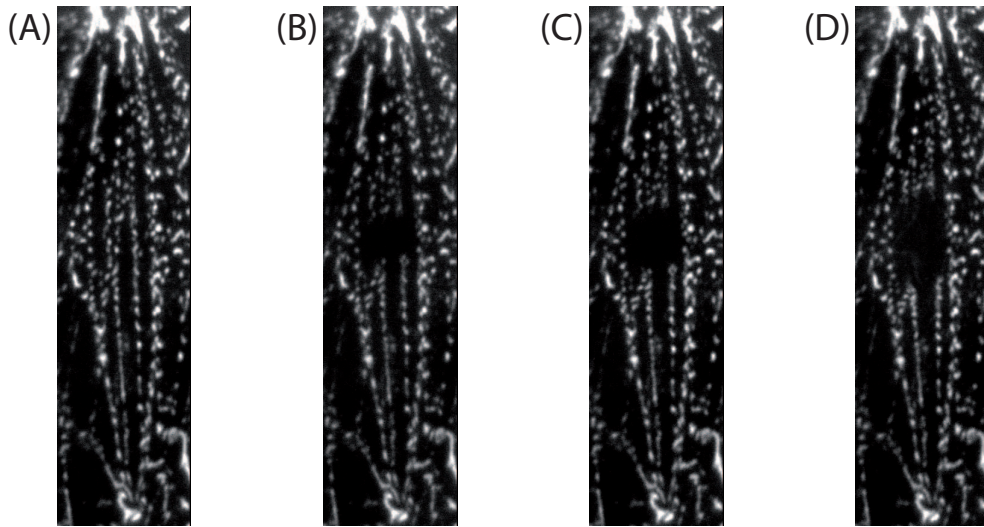
Figure 1.4: UV laser pulses can be used to dissect stress fibers. The mechanical perturbed cell was transfected to express fluorescently labelled α-actinin which forms a striation pattern. (A) Actin cytoskeleton before cut. (B) 1 s, shortly after cut. (C) During contraction phase, 4 s after cut. (D) After mechanical re-equilibration, 45 s after cut. Retraction is due to actomyosin contractility. α-actinin pattern can be used as an intrinsic ruler to analyze the retraction dynamics quantitatively. This is one subject of this thesis [34]. Courtesy of Julien Colombelli.

protein of interest. The transfection, that is the introduction of the genetic information into the cell, can be accomplished for example by electroporation [48], viral vectors [49] or liposomes [50]. The additional genetic information is then at least transiently expressed by the cell and the fluorescent copies of the protein can be visualized by fluorescence microscopy. Fluorescent proteins that are commonly used for transfections are green fluorescent protein (GFP), yellow fluoerescent protein (YFP), an engineered mutant of GFP, and more recently also the red dye called "cherry", originally derived from Discosoma sp. fluorescent protein "DsRed" that has been improved over many steps [51–53].

Perturbation of the biochemical signaling at focal adhesions can be performed by transfecting the cells with certain constantly active or inactive mutants of signaling proteins that usually reside in the adhesion plaque and various other techniques. Concerning the scope of this thesis, the most important possibilities are chemical drugs which alter directly or indirectly the activity of myosin II molecular motors. A chemical drug which is directly and specifically inhibiting myosin II activity is blebbistatin [54]. A more indirect way to affect myosin activity is by interfering with the Rho-signaling pathway. Here, common drugs are lysophosphatidic acid (LPA) [55] or calyculin A that both stimulate actomyosin contractility. Calyculin, for example, is an inhibitor of myosin light chain phosphatase and thereby enhances the phosphorylation of myosin light chain and subsequently myosin activity [56, 57]. The effect of this drug on stress fiber contraction dynamics will be studied *in silico* within this thesis [58].

Mechanical perturbations of cell adhesion can also be performed in many different ways. Passively, cells can be disturbed by plating them on soft substrates made of dif-

ferent polymer systems like polydimethylsiloxane (PDMS), polyacrylamide (PA) and hydrogels made from hyaluronic acid (HA). Such substrates are essential in order to study the rigidity sensing of cells. Actively, cells can be perturbed by substrate stretching [22–25] and a divers set of micro mechanical devices, including microneedles, elastic polymer pillars, optical and magnetic tweezers or AFM tips. These micromanipulators have already been applied in order to measure the micro-rheological properties of the actin cytoskeleton or to perturb the mechanical tension within the cytoskeleton and subsequently measure the response of focal adhesions [34, 35, 39, 59, 60]. In principle, all of these techniques also allow to measure the forces applied to cells.

Another method to perturb the mechanical stress within the cytoskeleton is nano-surgery of filaments by UV laser pulses. The energy deposition and the resulting disruptive effect of the laser pulse is mediated by the formation of a plasma. The plasma is initiated by thermal emission or by multiphoton ionization of electrons. Once a free electron is produced, it can absorb further photons by *inverse Bremsstrahlung absorption* while interacting with other charged particles. When its kinetic energy exceeds a certain threshold, the electron can generate another free electron via impact ionization which finally leads to an ionization avalanche and plasma formation [61]. Laser-induced plasma-mediated ablation has a long tradition in medicine as well as cell biology [61, 62]. Very recently, laser nanosurgery has been applied to dissect stress fibers to study their mechanical properties as well as the mechanosensitivity of zyxin, a protein which resides in focal adhesions and stress fibers [63, 64]. An essential contribution of this thesis is to support a mechanical model that allows to further quantify these processes [34], see Fig. 1.4.

1.4   Previous theoretical work

Several aspects of cell adhesion have been addressed by theoretical models. Especially the mechanics of the actin cytoskeleton has attracted the interest of many physicists. However, as the actin cytoskeleton is very dynamic and interacts with many different molecular factors, including actin-associated proteins and molecular motors, it is very difficult to model its mechanical properties in a general way. Modeling becomes feasible if one focuses on one of the well-characterized states of the actin cytoskeleton, for example the lamellipodium or stress fibers. Because here we are mostly interested in mature cell adhesion in culture, we will focus on the latter case. Modeling stress fibers can be approached from different perspectives. An obvious starting point are their common characteristics with muscle fibers, which is a linear sequence of sarcomeres, each containing around 300 myosin II molecular motors working collectively together as they slide the actin filaments relatively to each other. This field has been pioneered by the Huxley-model [65], which later has been modified in many regards, e.g. in regard to filament extensibility [66] or by a detailed modeling of the myosin II hydrolysis cycle [67]. In contrast to muscle fibers, stress fibers are more disordered and a complete description therefore requires a model for their assembly process from polar filaments interacting through molecular motors. Such a description has been achieved in the framework of a phenomenological theory which however does not model the details of

the underlying motor activity [68, 69]. This theory does predict different dynamical states of the system, including a stationary state of isometric contraction as observed in stress fibers.

The positive feedback loop between contractility and growth of adhesions has been modeled before in the framework of kinetic equations, but without addressing the details of force generation and its regulation by signaling pathways [70]. Similar kinetic equations have been used to model the antagonistic roles of Rho and Rac in cell adhesion, but again without addressing the details of force generation and regulation [71]. Recently, force generation has been addressed in more detail in a model for whole cell contractility and stress fiber formation [72, 73]. However, no details of the signaling pathway have been modeled except for an unspecified activation signal.

An essential part of the mechano-chemical feedback loop is the force induced growth of focal adhesion, which recently has been the subject of different modeling approaches [74–80], reviewed in [81]. However, these models have focused mainly on the mechanical and thermodynamic aspects of the growth process, neglecting the interaction of mechanics and biochemical signaling.

1.5   Outline and main results

A detailed understanding of most cell-adhesion related processes requires a model that accounts for the mutual interaction between the mechanics of the actin cytoskeleton and the biochemical regulation at focal adhesions. While several cell-adhesion phenomena have been approached from either direction, probably due to the conceptual differences between the two disciplines, theoretical models that describe the interaction of mechanics and chemistry are still rare in the literature. The ultimate goal of this thesis is to fill this gap and to build up a model that accounts for the complete mechano-chemical feedback cycle in cell adhesion. To achieve this goal we develop a model for stress fibers as well as model for the biochemical feedback with a focus on the Rho-pathway and finally demonstrate how mechanics and signaling can be coupled to each other. A major part of this thesis is also assigned for testing the complete model as well as model components by comparison with experimental data. Most importantly, we have used our mechanical model to analyze stress fiber contraction dynamics upon laser nanosurgery which lead to new insights into the mechanosensitivity of the protein zyxin. In the following we give a brief outline for each chapter.

In **Chapter 2** we develop an one dimensional viscoelastic model for stress fibers which is then solved for the boundary conditions that are appropriate to describe stress fiber contraction dynamics induced by laser release. We first introduce a discrete model which is inspired by the sarcomeric substructure of stress fibers. The fiber itself is described by a linear chain of Kelvin-Voigt bodies which, in addition, interacts viscoelasticly with its surrounding. Actomyosin contractility is accounted for by incorporating a contractile element into each Kelvin-Voigt body. This discrete model can be solved analytically for the displacements of an arbitrary number of sarcomeric units. Having this discrete model solution we then perform the continuum limit of the model. We obtain a partial differential equation as well as its continuum solution

describing stress fiber contraction dynamics. The continuum model later provides the opportunity to analyze experimental data. The solution in the continuum limit is then discussed thoroughly. It turns out that the contraction dynamics can be regarded as a retardation process but the associated spectrum of retardation times exhibit positive as well as negative amplitudes. Within a certain parameter range this can also lead to damped oscillation of inner fiber sections. Beside the time course of the tension in the fiber, we also calculate the complex modulus of the stress fiber model using three different approaches. These model predictions could be tested by future microrheology measurements.

In **Chapter 3** we apply our stress fiber model to quantify stress fiber contraction dynamics after laser nanosurgery. This project evolved from a tight collaboration with the experimental biophysics group of Ernst Stelzer at the European Molecular Biology Laboratory (EMBL) at Heidelberg. The experimental data presented within this chapter has been acquired by Julien Colombelli who designed and performed the stress fiber nanosurgery experiments. Quantification of the contraction dynamics by means of our model is utilized by resolving the displacement field along the fiber with high resolution in space and time. The innovation is to use the natural pattern of stress fibers as an intrinsic ruler during the contraction phase. We find excellent agreement between experimental data and our stress fiber model which can reproduce the complete displacement field in space and time.

By fitting the theory to the data we obtain values for the four model parameters, that is, the parameter that measures the degree of crosslink of the fiber, the average free contraction length of a sarcomeric unit as well as the typical equilibration times associated with internal and external friction. This analysis has been performed separately for stress fibers dissected in cells transfected to express either fluorescently labelled actin ($n = 86$) or α-actinin ($n = 34$). By comparing the parameter distributions from these two samples we can show that the crosslinker α-actinin not only connects actin filaments within stress fibers but also plays an essential role in crosslinking stress fibers to surrounding mechanical scaffolds. Moreover, we can discriminate between the importance of the effective fiber-internal viscosity and the viscosity of the surrounding cytosol. In regard to stress fiber contraction dynamics, we demonstrate that the latter seems to play a minor role. From the extracted model parameters we can also deduce a typical length scale over which mechanical perturbations decay along the fiber. It is also this length scale which impacts on the total contraction length of fibers, reached after mechanical re-equilibration as well as on the loss of force acting on connected focal adhesions.

Finally, we use our model to quantify the mechanosensitivity of zyxin. The model is thereby used to calculate the change in mechanical stress within the cytoskeleton upon laser release which is otherwise not accessible experimentally. The change in stress is then compared with the change in zyxin intensity. We find that zyxin intensity at focal adhesions and along stress fibers strongly correlates with mechanical stress. Furthermore, our study suggests that zyxin also relocalizes at intermediate crosslinks to the substrate that are set under high mechanical tension by the retracting fibers [34]. We hypothesize that these newly formed zyxin spots are the onset of nascent focal adhesions and that their formation might play an essential role during the intracellular

repair of the laser caused damage.

In **Chapter 4** we develop the model for the biochemical signaling cascade that is initiated at focal adhesions and is propagated along stress fibers through diffusion. Our study focuses on the Rho-pathway. We have performed an extensive literature research and compiled a list of the known rate and diffusion constants in such a way that they can be used for mathematical modeling. The developed system of reaction diffusion equations is then coupled to the contraction dynamics of stress fibers through the force-velocity relationship of myosin molecular motors. Vice versa, the resulting myosin forces are coupled back into the biochemical reactions by treating them similar to an enzyme that promotes Rho-signaling. The obtained mechano-chemically coupled system can be solved numerically. We find that the system is bistable. One stable state can be identified with a highly contractile cell whereas the other stable state corresponds to an inactive cell that failed to establish actomyosin contractility. As a first application of the model we address it to recent experiments by Peterson et al.[31]. They show that the striation pattern along stress fibers in yet unperturbed cells are wider at the center compared to the cell periphery. Upon induction of a uniformly distributed contractile drug, the bands at the periphery contract while the bands at the center surprisingly expand, amplifying the spatial differences. By simulating this drug experiment *in silico* we can reproduces the found spatial gradients in myosin activity and the resulting inhomogeneous distortion of stress fibers in qualitative agreement with experiments [58]. Most importantly, we also demonstrate that the positive biochemical and mechanical feedback has to be taken into account, in order to explain the experimental findings.

In **Chapter 5** we use our model to address cell behavior. In particular, we focus on the ability of cells to establish contractile forces on differently stiff substrates. The cellular contractile stress or the substrate deformation are considered as state variable of the model system. The substrate stiffness and a reaction parameter that accounts for the effect of a contractile drug are employed as control parameters in the bifurcation analysis. We find that bistability is not a universal feature of the model. There also exist parameter regions where either the contractile or the non-active state are the only stable fixed points. This gives rise to a threshold of substrate stiffness below which cells are not able to build up contractile forces. On stiffer substrates cells adopt a contractile state but the reached steady state forces depend only weakly on the substrate stiffness. These findings might contribute to the understanding of rigidity sensing of cells as well as to tensional homeostasis in tissue. Furthermore, we hypothesize that the potential bistability in the system gives rise to hysteresis in cell adhesion. To substantiate these ideas, we simulate cellular behavior on substrates of time dependent stiffness. The most idealized example is a cyclic varying boundary stiffness. Finally, we give some suggestions how substrates of time dependent stiffness could be realized experimentally.

Chapter 2

Viscoelastic fiber model: definition and solution

In this chapter we develop the basic concepts of our one dimensional viscoelastic stress fiber model. We first introduce a discrete model which is inspired by the sarcomeric substructure of stress fibers. The considered boundary conditions represent the situation that the fiber is released at one end and start to contract due to actomyosin contractility. The discrete model can be solved analytically for an arbitrary number of sarcomeric units. Subsequently, we perform a continuum limit of the model which results in a partial differential equation and its solution for the displacement field. The continuum description is superior for analyzing data and for coupling the model later on with the biochemical signaling. The continuum model solution is discussed by means of the spectrum of retardation times. Interestingly, within a certain parameter range, the inner sections of the fiber can exhibit damped oscillations. Finally, we calculate the stress profile along the fiber, as well as the complex modulus of the fiber model using several different approaches.

2.1 A model for stress fibers

2.1.1 The discrete stress fiber model

In spirit with the regular striation pattern of stress fibers we first introduce a discrete stress fiber model which is in its structure similar to the Kargin-Slonimsky-Rouse model (KSR model [82–84] reviewed in [85]) for long polymers in dilute solutions. The KSR model played an important role in the history of polymer physics. It proved that a retardation time spectrum can be generated by a polymer model with simple periodic structure and is not necessarily evidence for structural complexity of the polymer [85]. The model presented here is similar in its periodicity to the models suggested by Kargin and Slonimsky [82, 83] but differs in the composition of its elementary units as well as in its boundary conditions. In our model the mechanical response of each sarcomeric unit of length a is described by the Kelvin-Voigt model for viscoelastic material [86]. It consists of a dashpot with viscosity γ_{int} and a spring of stiffness k_{int} connected in parallel. These two modules represent the viscous and elastic properties of the ma-
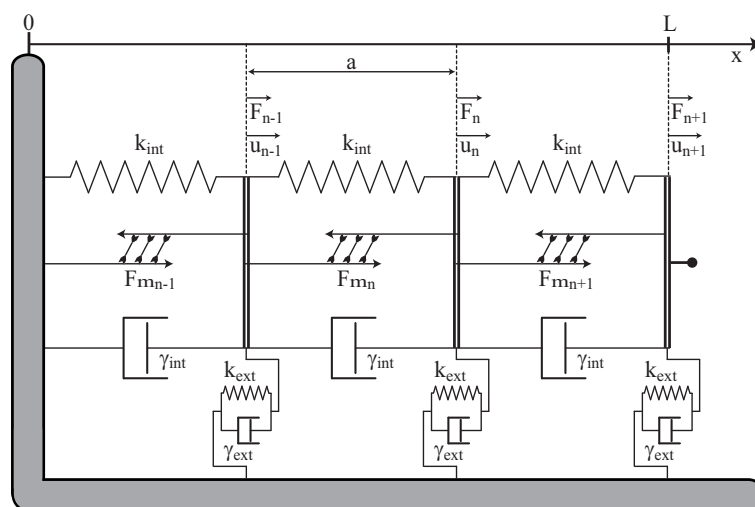
Figure 2.1: Illustration of the discrete stress fiber model. The fiber is modeled as a linear chain of Kelvin-Voigt bodies, each consisting of a spring of stiffness k_{int} and dashpot of viscosity γ_{int}. Actomyosin contractility is described by a contractile element added to each Kelvin-Voigt body along the chain. F_{m_n} represents the contractile force of the n-th molecular motor. Each element of length a represents one sarcomeric unit. Local viscoelastic interactions between the fiber elements with their surrounding are described by an additional set of external Kelvin-Voigt bodies with stiffness k_{ext} and viscosity γ_{ext}. The total length of the fiber is L. The fiber is clamped at $x = 0$ and free at $x = L$. u_n denotes the displacement of the n-th node.

terial, respectively. In stress fibers, the actin scaffold can be regarded as the elastic component. Viscous friction may arise from relative actin filament sliding, movement of solvent or bond breaking within the fiber. The Kelvin-Voigt body is the simplest viscoelastic model which in the stationary state is determined by elasticity, in contrast to the Maxwell model, which flows in the stationary limit. Thus the Kelvin-Voigt model is the appropriate choice for stress fibers, which can carry load at constant deformation over a long time. In order to cope with the contractile behavior of stress fibers, we introduce into these Kelvin-Voigt bodies a further contractile element that represents the activity of motor proteins. Its properties are given by the specific force-velocity relation of the molecular motors. A stress fiber of total length L is then represented by a linear chain of $N = L/a$ such viscoelastic and contractile elements, compare Fig. 2.1. Experimental observations [34] suggest that stress fibers do not contract unhindered within the cytoplasm upon laser dissection but interact locally with their surrounding. These interaction, e.g. mechanical crosslinks to the surrounding cytoskeleton or to intermediate contacts with the substrate, impose shear forces to the stress-fiber that counteract the retraction. In our one-dimensional model we account for these viscoelastic shear forces by additional external Kelvin-Voigt bodies each composed of a spring of stiffness k_{ext} and dashpot of viscosity γ_{ext}. The spring represents elastic interconnections to cytoplasmic components, whereas the dashpot accounts for the viscous drag within the cytosol. These external Kelvin-Voigt bodies exert forces whenever a fiber element is displaced (sheared) with respect to its initial position. The internal Kelvin-

Voigt bodies build up forces whenever a fiber element changes elongation. At each site n these external and internal forces as well as the contractile motor forces, F_m, have to balance:

$$
\begin{aligned}
0 \quad = \quad & \gamma_{int}(\dot{u}_{n+1} - \dot{u}_n) - \gamma_{int}(\dot{u}_n - \dot{u}_{n-1}) + k_{int}(u_{n+1} - u_n) \\
& - k_{int}(u_n - u_{n-1}) - \gamma_{ext}\dot{u}_n - k_{ext}u_n + F_{m_{n+1}} - F_{m_n}
\end{aligned}
\tag{2.1}
$$

The first four terms originate from the internal Kelvin-Voigt bodies. The internal frictional forces, the first two terms, arise when a sarcomeric unit changes elongation, i.e. these forces depend on the temporal change of relative displacements of neighboring sites $(\dot{u}_{n+1} - \dot{u}_n)$. The third and the fourth term account for elastic forces within the stress fiber and are proportional to the elongation of a sarcomeric unit, which is given by the relative displacement of neighboring sites $(u_{n+1} - u_n)$. The fifth and the sixth term originate from the external Kelvin-Voigt bodies. The contributions from external viscous drag depend on the local retraction velocity $\dot{u}_n$. The external harmonic restoring forces depend on the local displacement u_n of the considered site. The last two terms account for the contractile forces resulting from molecular motor activity which we model by a linearized force-velocity relationship [87]:

$$
F_{m_n} = F_s(1 - \frac{v_n}{v_0}) = F_s + \frac{F_s}{v_0}(\dot{u}_n - \dot{u}_{n-1})
\tag{2.2}
$$

F_{m_n} is the actual force exerted by the n-th motor moving with velocity v_n. v_0 is the zero-load velocity and F_s is the stall force of the motor. In the final relation we have used that the contraction velocity, v_n, of the n-th motor, can be related to the temporal change in displacement of neighboring sites according to*: $v_n = -(\dot{u}_n - \dot{u}_{n-1})$. For the moment being we assume that the stall force of motors is constant along the length of the fiber. In general, however, this is not the case. In chapter 4 we will argue that the motor activity is regulated by biochemical signals that effectively alter the stall force of the motors. In this way F_s becomes spatially dependent. Eq. (2.2) can now be used to specify the motor contributions in Eq. (2.1).

$$
\begin{aligned}
0 \quad = \quad & \tilde{\gamma}_{int}(\dot{u}_{n+1} - \dot{u}_n) - \tilde{\gamma}_{int}(\dot{u}_n - \dot{u}_{n-1}) + k_{int}(u_{n+1} - u_n) \\
& - k_{int}(u_n - u_{n-1}) - \gamma_{ext}\dot{u}_n - k_{ext}u_n
\end{aligned}
\tag{2.3}
$$

Here, we have introduced the effective internal viscosity $\tilde{\gamma}_{int} = \gamma_{int} + F_s/v_0$ which now contains motor contributions. At this point it is worth mentioning that, due to the *linearized* force velocity relation, the motor contribution Eq. (2.2) decomposes into two parts. On the one hand it effectively alters the internal viscosity $\tilde{\gamma}_{int}$ and thus will slow down the equilibration process. On the other hand, the constant contribution F_s cancels out at each node within the string and will only enter the boundary conditions. The upper equation holds for all nodes $0 < n < N$, where N is the total number of sarcomeric units. At the left end, $n = 0$, and at the right end, $n = N$, the boundary conditions have to be adopted according to the considered situation. In the following

---

*An arguable factor of 1/2 in this relation which depends on the definition of the motor velocity could be absorbed in the parameter v_0.

we will focus on the boundary conditions appropriate for the stress fiber laser cutting experiments. Here, one end of the fiber terminates at focal adhesions and thus can be considered as stationary. At the end where the stress fiber is released by the laser pulse all forces have to be balanced. From now on we will refer to the situation at the stationary end as *clamped boundary* whereas the situation at the cut we will call a *free boundary*. Throughout this manuscript we will choose the coordinate system such that the clamped end is always at the left and the free end is at the right. In total we have the following system of $N + 1$ equations:

Clamped boundary at $n = 0$:

$$u_0 = 0 \tag{2.4}$$

For $n = 1, \ldots, N-1$:

$$\tilde{\gamma}_{int}(\dot{u}_{n+1} - 2\dot{u}_n + \dot{u}_{n-1}) + k_{int}(u_{n+1} - 2u_n + u_{n-1}) - \gamma_{ext}\dot{u}_n - k_{ext}u_n = 0 \tag{2.5}$$

Free boundary at $n = N$:

$$-\tilde{\gamma}_{int}(\dot{u}_N - \dot{u}_{N-1}) - k_{int}(u_N - u_{N-1}) - \gamma_{ext}\dot{u}_N - k_{ext}u_N = F_s \tag{2.6}$$

The last equation can be deduced from Fig. 2.1 by balancing all internal and external viscoelastic forces as well as the motor forces at the terminating node, $n = N$. By examining the upper system of equations one finds that the contractile motor forces enter explicitly only at the free boundary at $n = N$. This is a direct result of assuming that the stall force of the molecular motors is uniform along the fiber. Otherwise, one would obtain additional terms $F_{s_{n+1}} - F_{s_n}$ in the equations $n = 1, \ldots, N-1$. The system of coupled first order linear differential equations (2.4)-(2.6) can be solved for the discrete displacements $u_n(t)$. In section 2.2.1 we show that there exist a closed analytical solution for an arbitrary number, N, of sarcomeric units. However it is also helpful to perform a continuum limit on the discrete model system. This results in a partial differential equation which will be derived in section 2.1.3 and its exact solution will be provided in section 2.2.2.

2.1.2 Relations between 1D and 3D viscoelastic constants

Before we perform the continuum limit of the discrete model described above, we first want to relate the parameters from the one-dimensional model to three dimensional quantities. In doing so we focus on the elastic constants. For the viscous constants corresponding relations follow immediately and are given at the end of this section. The presented one dimensional model accounts only for two elastic deformation modes, that is homogeneous uniaxial extension of the sarcomeric units or shear of the surrounding medium. These two deformation modes are depicted for one sarcomeric unit in Fig. 2.2. The deformation of an isotropic and linear elastic body exposed to homogeneous uni-axial stress, $\sigma_{xx} = F/A_{face}$, is determined by the Young's modulus E and the Poisson's ratio ν. Given this simple form of the stress tensor, the strain tensor follows as [88]:

$$u_{xx} = \sigma_{xx}/E = \frac{F}{EA_{face}} \quad \text{and} \quad u_{yy} = u_{zz} = -\nu u_{xx} \tag{2.7}$$
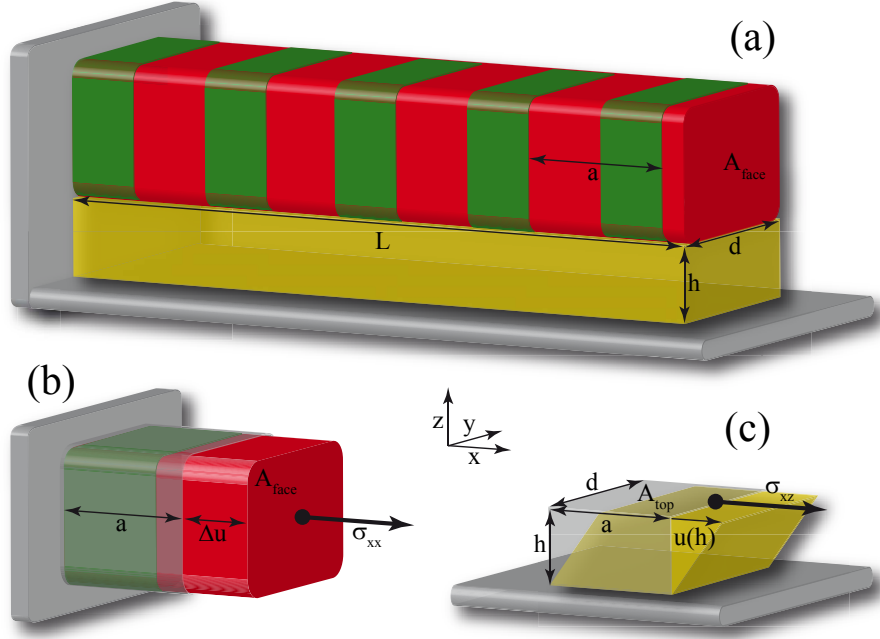
Figure 2.2: (a) A three dimensional simplistic illustration of a stress fiber. Our model accounts for two deformation modes: (b) Uniaxial extension induced by the uniform stress $\sigma_{xx} = F/A_{face}$. Here, the elongation of the sarcomeric unit is denoted by $\Delta u = u(a) - u(0)$. (c) Pure shear of the surrounding medium induced by the stress $\sigma_{xz} = F/A_{top}$. $u(h)$ denotes the displacement of the top at height h in the x-direction. In both cases F is an arbitrary force pointing in x-direction.

All off-diagonal components of the strain tensor vanish. Since our model is one-dimensional it can only account for the strain in the x-direction. The strain is homogenous, thus we can write:

$$u_{xx} = \frac{\partial u_x}{\partial x} = \frac{u_x(a) - u_x(0)}{a} = \frac{F}{EA_{face}} \tag{2.8}$$

Where $u_x(x)$ is the displacement in the x-direction (arguments (y, z) have been dropped). The upper force-extension relation can now be compared with the one-dimensional version to obtain a relation between the internal spring stiffness k_{int} of the one dimensional model and the Young's modulus:

$$u_x(a) - u_x(0) = \frac{a}{EA_{face}}F = \frac{1}{k_{int}}F \qquad \Rightarrow \qquad k_{int} = \frac{EA_{face}}{a} \tag{2.9}$$

Similarly we can deduce a relation between the external spring stiffness k_{ext} and the shear modulus G of the surrounding medium. Here, the pure shear stress is given by $\sigma_{xz} = F/A_{top}$. The resulting strain is given by [88]:

$$u_{xz} = \frac{\sigma_{xz}}{2G} = \frac{F}{2GA_{top}} \tag{2.10}$$

All other components of the strain tensor vanish, in particular the component $u_{zz} = \frac{\partial u_z}{\partial z} = 0$. Therefore the z-component of the displacement has to be constant along the z-direction: $u_z(x, y, z) = f(x, y)$. Since at the bottom, $z = 0$, the displacement vanishes, $u_z(x, y, 0) = 0$ at all position (x, y), the function $f(x, y)$ has to be identical zero and the z-component of the displacement, u_z, also vanishes. Then it follows:

$$u_{xz} = \frac{1}{2}\left(\frac{\partial u_x}{\partial z} + \frac{\partial u_z}{\partial x}\right) = \frac{1}{2}\frac{\partial u_x}{\partial z} = \frac{1}{2}\frac{u_x(h) - u_x(0)}{h} = \frac{1}{2}\frac{u_x(h)}{h} = \frac{F}{2GA_{top}} \qquad (2.11)$$

Where in the upper equation $u_x(z)$ is the displacement in the x-direction at height z (arguments (x, y) have been dropped) and h is the thickness of the sheared layer. The substitution of the derivative $\partial u_x/\partial z$ by the simple difference quotient holds true, since strain is uniform. It has also been used that the displacement at the bottom is zero, $u_x(0) = 0$. The upper final equation can now be used to derive a relation between the external spring stiffness k_{ext} of the one dimensional model and the shear modulus G:

$$u_x(h) = \frac{h}{GA_{top}}F = \frac{1}{k_{ext}}F \qquad \Rightarrow \qquad k_{ext} = \frac{GA_{top}}{h} = \frac{Gda}{h} \qquad (2.12)$$

Where d is the width of the sheared layer, compare Fig. 2.2. So far we have only discussed the elastic constants. However, similar relations follow immediately for the viscous parameters. The internal viscosity, γ_{int}, can be set in relation to the *extensional viscosity* analogous to Eq. (2.9) whereas the external viscosity, γ_{ext} and the *shear viscosity* fulfill a relation analogous to Eq. (2.12). At this point we want to stress that the quantity a in Eqs. (2.9), (2.12) is in principle an arbitrary length scale. The entities k_{int} and k_{ext} then represent the elastic properties of a fiber fragment of length a. A convenient definition is $a = 1\,\mu$m which corresponds to the average length of a sarcomeric unit $1.01 \pm 0.14\,\mu$m[†][34]. The Young's modulus of stress fibers has been measured by Deguchi et al. [89]. Using the value that they found for small deformations we can estimate the internal fiber stiffness to be $k_{int} \approx 45\,$nN$/a$. This value together with our fit values for the model parameters summarized in Tab. 3.1 and Eqs. (2.9), (2.12), (2.20) can be used to give rough estimates for the extensional viscosity of the fiber and for the shear modulus and shear viscosity of the surrounding medium.

2.1.3   The continuum stress fiber model

The discrete model described in section 2.1.1 can be transformed to a continuum equation by considering the limit for a large number of elementary units N. In this limiting process, the total length L of the stress fiber will be subdivided into incremental smaller pieces of length $a_N = L/N$. Thereby it has to be ensured that the effective viscoelastic properties of the whole chain are conserved, i.e. in each iteration step the discrete model should reflect a fiber with a certain Young's modulus E embedded in a medium with shear modulus G. This is accomplished by re-scaling the viscoelastic constant

---

[†]If not denoted otherwise, experimental measures are given as mean $\pm$ standard deviation

$(k_{N,int}, \gamma_{N,int}, k_{N,ext}, \gamma_{N,ext})$ in each iteration step according to Eq. (2.9) and Eq. (2.12):

$$
\begin{aligned}
k_{N,int} &= \frac{EA_{face}}{a_N} = \frac{aN}{L}\frac{EA_{face}}{a} = \phi_N k_{int} \\[2mm]
k_{N,ext} &= \frac{GA_{N,top}}{h} = \frac{Gda_N}{h} = \frac{L}{aN}\frac{Gad}{h} = \frac{k_{ext}}{\phi_N}
\end{aligned}
\tag{2.13}
$$

Here, we have introduced the scaling factor $\phi_N = \frac{a}{a_N} = \frac{Na}{L}$. It ensures that by dividing the chain into more and more smaller pieces, the effective Young's and shear modulus of the model is conserved. The stiffness $k_{N,int}$ represents the stiffness of an $a_N = L/N$ long piece of the fiber and increases linearly with the number of partitions N, whereas k_{int} is the stiffness of a fiber fragment of length a. In principle a is an arbitrary length scale that we have chosen to be $a = 1\,\mu$m such that it corresponds to the typical length of a sarcomeric unit of a stress fiber, compare also the discussion at the end of the previous section. While $k_{N,int}$ increases linearly with the number of partitions, $k_{N,ext}$ decreases according to $1/N$. Similarly it follows that the viscous parameter $\gamma_{N,int}$ and $\gamma_{N,ext}$ scale as $k_{N,int}$ and $k_{N,ext}$, respectively. In total one finds:

$$
\begin{aligned}
k_{N,int} &= \phi_N k_{int} &&\text{and} & \gamma_{N,int} &= \phi_N \gamma_{int} \\[2mm]
k_{N,ext} &= \frac{k_{ext}}{\phi_N} &&\text{and} & \gamma_{N,ext} &= \frac{\gamma_{ext}}{\phi_N}
\end{aligned}
\tag{2.14}
$$

These conditions on the viscoelastic constants prepare the ground for the continuum limit of Eqs. (2.4)-(2.6). To begin with the limiting procedure we first introduce the continuous spatial variable $x = na_N$, denoting the position of the n-th node within the yet discrete chain. Then Eq. (2.5) can be reformulated as:

$$
\begin{aligned}
\tilde{\gamma}_{N,int}(\dot{u}(x+a_N) - 2\dot{u}(x) + \dot{u}(x-a_N)) - \gamma_{N,ext}\dot{u}(x) &+ \ldots \\[2mm]
+ k_{N,int}(u(x+a_N) - 2u(x) + u(x-a_N)) - k_{N,ext}u(x) &= 0
\end{aligned}
\tag{2.15}
$$

Substitution of the viscoelastic parameters $(k_{N,int}, \gamma_{N,int}, k_{N,ext}, \gamma_{N,ext})$ which depend on the refinement N, by the appropriate scaling relations given in Eq. (2.14) and conducting the limit $N \to \infty$ yields:

$$
\begin{aligned}
a^2\tilde{\gamma}_{int}\lim_{N\to\infty}\left(\frac{\dot{u}(x+a_N) - 2\dot{u}(x) + \dot{u}(x-a_N)}{a_N{}^2}\right) - \gamma_{ext}\dot{u}(x) &+ \ldots \\[2mm]
+ a^2 k_{int}\lim_{N\to\infty}\left(\frac{u(x+a_N) - 2u(x) + u(x-a_N)}{a_N{}^2}\right) - k_{ext}u(x) &= 0
\end{aligned}
\tag{2.16}
$$

Since a_N is a sequence which converges to zero, the limits define the second derivative of u with respect to x. The continuum limit of the upper equation results in a partial differential equation for the displacement $u(x,t)$. The highest order term will contain mixed derivatives in x and t, namely, $\partial_x^2\dot{u}$. Similarly, the limiting process can be performed for the boundary condition at the free end. Note that at this point the

spatial variable evaluates to $x = Na_N = L$:

$$a\tilde{\gamma}_{int} \lim_{N\to\infty} \left(\frac{\dot{u}(L) - \dot{u}(L - a_N)}{a_N} \right) + \lim_{N\to\infty} \frac{a_N}{a} \gamma_{ext}\dot{u}(L) \quad +\dots$$

$$+ak_{int} \lim_{N\to\infty} \left(\frac{u(L) - u(L - a_N)}{a_N} \right) + \lim_{N\to\infty} \frac{a_N}{a} k_{ext}u(L) \quad = \quad -F_s$$

(2.17)

In each line of the equation, the first limit gives the first derivative of u with respect to x evaluated at $x = L$ and the second limit in each line vanishes as a_N converges to zero. Consequently, in the continuum representation, the stresses which originate from shearing the environment can not contribute to this boundary condition. However, note that the stresses exerted by the motors, F_s, on the boundary are unaffected during the limiting process and do contribute. Eventually our continuum model for stress fibers can be formulated in the following boundary value problem:

$$\tilde{\gamma}_{int}a^2\partial_x^2\dot{u} + k_{int}a^2\partial_x^2 u - \gamma_{ext}\dot{u} - k_{ext}u = 0 \tag{2.18}$$

With the boundary conditions:

$$u(0,t) = 0 \quad \text{and} \quad \tilde{\gamma}_{int}a\partial_x\dot{u}(L,t) + k_{int}a\partial_x u(L,t) + F_s = 0 \tag{2.19}$$

The appropriate initial conditions for the stress fiber dissection experiments are zero displacement before the cut, namely $u(x,0) = 0$. Note that the terms on the left hand side of the boundary condition at $x = L$ denote the stress within the fiber. In our one-dimensional model the elastic stress is simply proportional to the strain in x-direction, $\partial_x u$, viscous stress is proportional to the rate of strain $\partial_x \dot{u}$ and the total stress is completed by the contractile forces exerted by molecular motors F_s. Thus, the boundary conditions mean that the total stress within the fiber has to vanish at the position of the cut, i.e. these three components of the stress have to balance internally. The structure of the model equations allows us to eliminate one parameter which we have chosen to be k_{int}. So essentially, our model has only the following four parameters:

$$\kappa = \frac{k_{ext}}{k_{int}}; \qquad \delta = \frac{F_s}{k_{int}}; \qquad \tau = \frac{\tilde{\gamma}_{int}}{k_{int}} = \frac{\gamma_{int}}{k_{int}} + \frac{F_s}{v_0 k_{int}}; \qquad \tau_\epsilon = \frac{\gamma_{ext}}{k_{int}} \tag{2.20}$$

The ratio of external and internal stiffness κ is a non-dimensional parameter which can be regarded as a measure for the degree of crosslink of the fiber. The parameter δ can be understood as the free contraction length of a sarcomeric unit of initial length $a = 1\mu$m. The parameters τ and τ_ϵ represent two distinct equilibration times associated with internal and external processes, respectively. It is worth mentioning that the parameters (κ, δ) are, similar to the previous viscoelastic parameters, normalized to the length of one sarcomeric unit a, whereas the parameters (τ, τ_ϵ) are invariant under the scaling of a. To see this in the case of τ, note that the zero-force velocity of the motors scales like $v_{N,0} = v_0/\phi_N$. Formulated in terms of the parameter set depicted in Eq. (2.20), the model equation and the boundary condition at the free end are given

as:

$$\tau a^2 \partial_x^2 \dot{u} + a^2 \partial_x^2 u - \tau_\epsilon \dot{u} - \kappa u = 0 \quad \text{and} \quad \tau a \partial_x \dot{u}(L, t) + a \partial_x u(L, t) + \delta = 0 \quad (2.21)$$

The boundary condition at $x = 0$ and the initial conditions remain unchanged. We use this continuous model equation comprising the set of the four parameters $(\kappa, \delta, \tau, \tau_\epsilon)$ to describe the contraction dynamics of stress fiber after UV laser cutting. By fitting the model to the data we are able to extract values for these parameters. In the following section we will derive the solution of the stress fiber model. Thereby it is quite convenient to non-dimensionalize the model equations. We do this by introducing the non-dimensional spatial variable $\tilde{x} = x/a$, non-dimensional time $\tilde{t} = t/\tau$ and the non-dimensional ratio of the two time scales $\Gamma = \tau_\epsilon/\tau$. In this way the model equations adopt the simple form:

$$\partial_{\tilde{x}}^2 \dot{u} + \partial_{\tilde{x}}^2 u - \Gamma \dot{u} - \kappa u = 0 \quad \text{and} \quad \partial_{\tilde{x}} \dot{u}(\tilde{L}, \tilde{t}) + \partial_{\tilde{x}} u(\tilde{L}, \tilde{t}) + \delta = 0 \quad (2.22)$$

We will either use the non-dimensional formulation given in Eq. (2.22) or switch to the dimensional model equation Eq. (2.21) with parameters $(\kappa, \delta, \tau, \tau_\epsilon)$ depending on which one is more convenient in the considered situation.

Before we start to derive the general solution of the presented model we discuss the special case where $\kappa = \Gamma$. This case is easy to solve and gives preliminary insight into how the solution for the displacement roughly looks like. Substitution of the ansatz $h = \dot{u} + u$ into the partial differential equation Eq. (2.22) yields the following ordinary differential equation for h:

$$\partial_{\tilde{x}}^2 h - \kappa h = 0 \quad (2.23)$$

and the boundary conditions transform to: $h(0) = 0$ and $\partial_{\tilde{x}} h(\tilde{L}) + \delta = 0$. Solution of this ordinary differential equation for $h(\tilde{x})$ and subsequent solution of the inhomogeneous ordinary differential equation for the displacement $\dot{u} + u = h$ with the initial condition $u(\tilde{x}, 0) = 0$ yields the final solution:

$$u(\tilde{x}, \tilde{t}) = -\frac{\delta}{\sqrt{\kappa}} \frac{\sinh(\tilde{x}\sqrt{\kappa})}{\cosh(\tilde{L}\sqrt{\kappa})} \left(1 - e^{-\tilde{t}}\right) \quad \Rightarrow \quad u_{ss}(\tilde{x}) = -\frac{\delta}{\sqrt{\kappa}} \frac{\sinh(\tilde{x}\sqrt{\kappa})}{\cosh(\tilde{L}\sqrt{\kappa})} \quad (2.24)$$

The assumption $\kappa = \Gamma$ leads to a simple retardation process with a single *retardation time* τ. This term, retardation time, is derived from rheology where it is associated with viscoelastic creep, in contrast to the term, relaxation time, which is rather associated with the relaxation of viscoelastic stress. In this thesis, we will sometimes refer to τ also as the typical equilibration time of a stress fiber.

The stationary solution is denoted as $u_{ss}(\tilde{x})$. The largest, always negative displacement given by $-\frac{\delta}{\sqrt{\kappa}}$ occurs at $x = L$, that is where the fiber was released. The magnitude of the displacement decreases exponentially with increasing distance from this point. The typical length scale of this decay is given by $a/\sqrt{\kappa}$. It is important to note that the general case with arbitrary κ and Γ evolves to the same stationary solution given in Eq. (2.24). However, the dynamics during the retraction phase are more complicated for the general case. In the next section we will show that the general

solution is a superposition of infinitely many discrete retardation times. The associated retardation time spectrum is spatially dependent and may have positive as well as negative amplitudes. Under certain conditions, this even leads to solutions for the local displacements that are not monotonically decreasing in time, compare section 2.3.

2.2   Solution of the model

2.2.1   Solution of the discrete model

The discrete stress fiber model developed in section 2.1.1 constitutes a coupled system of first order linear differential equations in the displacements u_n at nodes $n = 0 \ldots N$. It is straight forward to solve these equations for a certain small number of nodes. However, it is quite challenging to find a closed solution for a general number of degrees of freedom N. Still, finding such a solution is quite appealing since it allows not only exhaustive analysis of the discrete model. Execution of the continuum limit described in the previous section will carry the discrete solution over to the solution of the continuum model described by the partial differential equation Eq. (2.18). The closed solution then also provides a simple tool for other groups to analyze their data on stress fiber experiments, since the tedious implementation of a numerical procedure to solve the boundary value problem given by Eq. (2.18) and Eq. (2.19) is no longer necessary.

Because of the unequal boundary conditions at the two ends, the derivation of the model solution is more complicated. It turned out to be fruitful to first symmetrize the problem by considering a string of length $2N+1$ with free boundary conditions at both ends (see Eq. (2.6)), that is, at each end the contractile motor forces are balanced by the internal and external viscoelastic forces, see Fig. 2.3. The solution for this boundary value problem, that is the displacements along the string, has to be an antisymmetric function with respect to the center of the string. This is because the contractile forces equally pull both terminating nodes inwards. Consequently, the displacement at the center has to be zero. The solution for the symmetric problem with $2N+1$ units thus comprises the solution for a fiber with N units with one free and one clamped end, the actual problem of interest.

The symmetric problem for a slightly simpler model has been analyzed in great detail by Gotlib and Volkenshtein [90]. Their calculations paved the way for the following derivation. In exact accordance with our considerations in section 2.1.1 we can write down the force balance equations at each node $j = 1, \ldots, 2N+1$ of the string shown in Fig. 2.3(a) and Fig. 2.3(b). The resulting $2N+1$ first order differential equations are given by:
For $j = 1$:
$$\tilde{\gamma}_{int}(\dot{u}_2 - \dot{u}_1) - \gamma_{ext}\dot{u}_1 + k_{int}(u_2 - u_1) - k_{ext}u_1 = -F_s \qquad (2.25)$$
For $j = 2, \ldots, 2N$:
$$\tilde{\gamma}_{int}(\dot{u}_{j+1} - 2\dot{u}_j + \dot{u}_{j-1}) - \gamma_{ext}\dot{u}_j + k_{int}(u_{j+1} - 2u_j + u_{j-1}) - k_{ext}u_j = 0 \qquad (2.26)$$
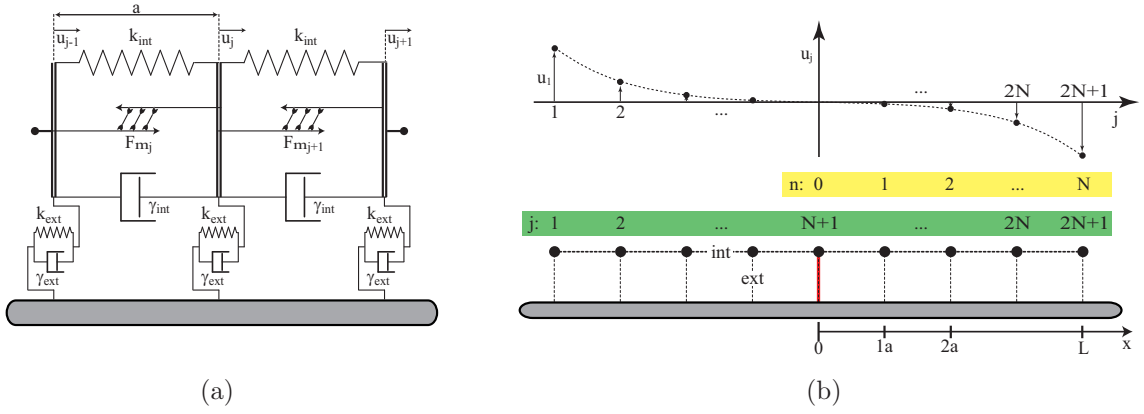
Figure 2.3: Sketch of the model with symmetric boundary conditions. (a) Stress fiber with two free ends. Viscoelastic constants and contractile motor forces are as in Fig. 2.1. (b) Lower figure illustrates the counting of the two indices n and j. The index n starts counting at the central node highlighted in red. The index j starts counting at the node which terminates the fiber at the left. Upper figure is a schematic drawing of the solution for the displacements of the nodes assuming that both ends of the fiber are free. Since the contractile forces pull both terminating nodes inwards, the solution for the displacements has to be antisymmetric about the central node. For the same reason the central node has to be stationary. In this way, the nodes at $n = 0 \dots N$ obey the actually boundary conditions of interest: clamped at $n = 0$ and free at $n = N$.

For $j = 2N + 1$:

$$- \tilde{\gamma}_{int}(\dot{u}_{2N+1} - \dot{u}_{2N}) - \gamma_{ext}\dot{u}_{2N+1} - k_{int}(u_{2N+1} - u_{2N}) - k_{ext}u_{2N+1} = F_s \qquad (2.27)$$

Here, we have again used the abbreviation for the effective internal viscosity $\tilde{\gamma}_{int} = \gamma_{int} + F_s/v_0$. By subtracting from each equation the subsequent one and introducing the relative coordinates $y_j = u_{j+1} - u_j$, we can rewrite the upper system of equations in the following compact form:

$$\boldsymbol{M}_{visc}\dot{\vec{y}} + \boldsymbol{M}_{elas}\vec{y} = \vec{F} \qquad (2.28)$$

with the $2N \times 2N$ matrix:

$$\boldsymbol{M}_{visc} = \begin{pmatrix} 2\tilde{\gamma}_{int} + \gamma_{ext} & -\tilde{\gamma}_{int} & 0 & 0 & \cdots \\ -\tilde{\gamma}_{int} & 2\tilde{\gamma}_{int} + \gamma_{ext} & -\tilde{\gamma}_{int} & 0 & \cdots \\ 0 & -\tilde{\gamma}_{int} & 2\tilde{\gamma}_{int} + \gamma_{ext} & -\tilde{\gamma}_{int} & \cdots \\ 0 & 0 & -\tilde{\gamma}_{int} & 2\tilde{\gamma}_{int} + \gamma_{ext} & \cdots \\ \vdots & \vdots & \vdots & \vdots & \ddots \end{pmatrix} \qquad (2.29)$$

The matrix $\boldsymbol{M}_{elas}$ has exactly the same form as $\boldsymbol{M}_{visc}$ but the viscous constants have to be replaced by the corresponding elastic constants. That is, $\tilde{\gamma}_{int}$ has to be substituted by k_{int} and similarly, γ_{ext} by k_{ext}. In addition we have defined the $2N$-dimensional

vectors:

$$\vec{y}(t) = \begin{pmatrix} y_1 \\ y_2 \\ \vdots \\ y_{2N-1} \\ y_{2N} \end{pmatrix} \quad \text{and} \quad \vec{F} = \begin{pmatrix} -F_s \\ 0 \\ \vdots \\ 0 \\ -F_s \end{pmatrix} \tag{2.30}$$

In the following we will solve Eq. (2.28) for the relative coordinates $y_j(t)$. At the end, the displacements $u_n(t)$ can be recovered from Eq. (2.46) once the dynamics of the relative coordinates have been determined. The force vector on the right hand side of Eq. (2.28) renders the differential equation to be inhomogeneous. In preparation for the general inhomogeneous solution of Eq. (2.28), as usual, first consider the homogeneous equation

$$\boldsymbol{M}_{visc}\dot{\vec{y}} + \boldsymbol{M}_{elas}\vec{y} = 0 \tag{2.31}$$

Let λ_l be an eigenvalue and let $\vec{v}_l$ be the associated eigenvector that obeys the eigenvalue problem:

$$(\boldsymbol{M}_{elas} - \lambda_l \boldsymbol{M}_{visc})\vec{v}_l = 0 \tag{2.32}$$

It turns out that Eq. (2.31) is solved by $\vec{y}_l(t) = \vec{v}_l e^{-\lambda_l t}$ which can be easily proven by inserting this ansatz into Eq. (2.31). Since the differential equation is linear the superposition principle holds and the general homogeneous solution is given by:

$$\vec{y}(t) = \sum_{l=1}^{2N} c_l \vec{y}_l(t) = \sum_{l=1}^{2N} c_l \vec{v}_l e^{-\lambda_l t} \tag{2.33}$$

The upper solution is primarily valid only if there are exactly $2N$ distinct eigenvalues, but we will find that this is indeed true in the considered case. A similar but slightly simpler eigenvalue problem has been treated by Gotlib and Volkenshtein [90]. The set of eigenvalues and eigenvectors appropriate for our model is given by:

$$\lambda_l = \frac{k_{ext} + 4k_{int}\sin^2\frac{\pi l}{2(2N+1)}}{\gamma_{ext} + 4\tilde{\gamma}_{int}\sin^2\frac{\pi l}{2(2N+1)}} \quad \text{and} \quad \vec{v}_l = \begin{pmatrix} \sin\frac{\pi l}{2N+1} \\ \sin\frac{\pi 2l}{2N+1} \\ \sin\frac{\pi 3l}{2N+1} \\ \vdots \\ \sin\frac{\pi 2Nl}{2N+1} \end{pmatrix} \tag{2.34}$$

It is now straight forward to show by insertion that Eq. (2.34) is indeed the solution to the eigenvalue problem defined by Eq. (2.32). For the sake of completeness and to not distract the reader from the main course of the calculation, we have removed this proof from the main text and shifted to appendix 6.2. In this appendix we also proof that the $2N$ eigenvalues are distinct, positive and non-zero and that the eigenvectors are orthogonal and their length is given by $v_l = \sqrt{(2N+1)/2}$. The fact that the eigenvalues are distinct affirms the form of the homogeneous solution given in Eq. (2.33). Later on we will also take advantage of the listed properties of the eigenvectors. In

order to determine the solution of the inhomogeneous equation Eq. (2.28) we make the common ansatz:

$$\vec{y}(t) = \sum_{l=1}^{2N} c_l(t)\vec{v}_l e^{-\lambda_l t} \tag{2.35}$$

The coefficients $c_l(t)$ which still have to be determined are now taken to be time dependent. Setting the ansatz into the inhomogeneous Eq. (2.28) yields $2N$ conditions defining the coefficients $c_l(t)$:

$$\sum_l \dot{c}_l(t) \boldsymbol{M}_{visc}\vec{v}_l e^{-\lambda_l t} + \sum_l c_l(t) e^{-\lambda_l t} \left(\boldsymbol{M}_{elas}\vec{v}_l - \lambda_l \boldsymbol{M}_{visc}\vec{v}_l\right) = \vec{F} \tag{2.36}$$

The second sum on the left hand side vanishes since its summands just constitute the previously solved eigenvalue problem: $(\boldsymbol{M}_{elas}\vec{v}_l - \lambda_l \boldsymbol{M}_{visc}\vec{v}_l) = 0$. Evaluation of the product $\boldsymbol{M}_{visc}\vec{v}_l$ and rewriting the $2N$ equations componentwise, for $j = 1, .., 2N$, yields:

$$\sum_l \dot{c}_l(t) \left(-\tilde{\gamma}_{int} \sin\frac{\pi l(j-1)}{2N+1} + (\gamma_{ext} + 2\tilde{\gamma}_{int}) \sin\frac{\pi l j}{2N+1} + \dots \right.$$
$$\left. -\tilde{\gamma}_{int} \sin\frac{\pi l(j+1)}{2N+1}\right) e^{-\lambda_l t} = F_j \tag{2.37}$$

Application of appropriate addition theorems converts the trigonometric terms to the concise expression, $j = 1, .., 2N$:

$$\sum_l \dot{c}_l(t) \sin\frac{\pi l j}{2N+1} \left(\gamma_{ext} + 4\tilde{\gamma}_{int} \sin^2\frac{\pi l}{2(2N+1)}\right) e^{-\lambda_l t} = F_j \tag{2.38}$$

The sin-factor which has been pulled out of the parenthesis in the upper equations can be identified with the j-th component of the l-th eigenvector. In order to rewrite the upper equation in a simple form it is convenient to define the $2N \times 2N$ matrix of normalized eigenvectors,

$$\boldsymbol{U} = \sqrt{\frac{2}{2N+1}}(v_1, v_2, \dots, v_{2N}) \qquad \Leftrightarrow \qquad \boldsymbol{U}_{j,l} = \sqrt{\frac{2}{2N+1}} \sin\frac{\pi l j}{2N+1} \tag{2.39}$$

The remaining terms within the sum of Eq. (2.38) only depend on the index l not on j. By defining the $2N$-dimensional vector $\vec{b}$ with components

$$b_l(t) = \sqrt{\frac{2N+1}{2}} \dot{c}_l(t) \left(\gamma_{ext} + 4\tilde{\gamma}_{int} \sin^2\frac{\pi l}{2(2N+1)}\right) e^{-\lambda_l t} \tag{2.40}$$

Eq. (2.38) can be rewritten as:

$$\boldsymbol{U}\vec{b}(t) = \vec{F} \tag{2.41}$$

This upper system of $2N$ equations has to be solved for $\vec{b}$, the solution for the coefficients $c_l(t)$ then follows by integration. Solution of Eq. (2.41) is simple because of the

special properties of the matrix $\boldsymbol{U}$. By definition, $\boldsymbol{U}$ is built up by the normalized and orthogonal eigenvectors, thus $\boldsymbol{U}^T \boldsymbol{U} = I$. Moreover, since $\boldsymbol{U}$ is obviously symmetric it even follows that $\boldsymbol{U} = \boldsymbol{U}^T = \boldsymbol{U}^{-1}$, which means that the matrix $\boldsymbol{U}$ constitutes its own inverse. With these considerations the solution of Eq. (2.41) is simply given by:

$$\vec{b}(t) = \boldsymbol{U}\vec{F} \tag{2.42}$$

The only non-zero components of $\vec{F}$ are the first and the last one, $F_1 = F_{2N} = -F_s$. Accordingly, only the first and the last column of $\boldsymbol{U}$ contributes to the result of the product with $\vec{F}$. The solution for $\vec{b}$ is then given by:

$$
\begin{aligned}
b_l(t) &= \sqrt{\frac{2}{2N+1}} \left(\sin \frac{\pi l}{2N+1} + \sin \frac{\pi 2Nl}{2N+1} \right) (-F_s) \\
&= -F_s \sqrt{\frac{2}{2N+1}} \left(1 + (-1)^{l+1} \right) \sin \frac{\pi l}{2N+1}
\end{aligned}
\tag{2.43}
$$

It turns out that all even-numbered components of $\vec{b}$ vanish and only the odd-numbered components contribute. The coefficients of interest, $c_l(t)$, now result from a simple integration of Eq. (2.40).

$$
c_l(t) =
\begin{cases}
0 & \text{if } l \text{ even} \\[2ex]
-\dfrac{4}{2N+1} \dfrac{\sin \frac{\pi l}{2N+1}}{\gamma_{ext} + 4\tilde{\gamma}_{int} \sin^2 \frac{\pi l}{2(2N+1)}} \displaystyle\int_0^t F_s(t')e^{\lambda_l t'} dt' & \text{if } l \text{ odd}
\end{cases}
\tag{2.44}
$$

Here, we have considered the more general case that the forces F_s might vary in time. This will become particularly important in conjunction with the complex modulus of the stress fiber model where we have to account for oscillating boundary forces. The final solution for the relative coordinates is given by Eq. (2.35):

$$
y_j(t) = -\frac{4}{2N+1} \sum_{l=1,3,5,\ldots}^{2N} \frac{\sin \frac{\pi l}{2N+1} \sin \frac{\pi l j}{2N+1}}{\gamma_{ext} + 4\tilde{\gamma}_{int} \sin^2 \frac{\pi l}{2(2N+1)}} \int_0^t F_s(t')e^{-\lambda_l(t-t')} dt'
\tag{2.45}
$$

The actual displacements $u_j(t)$ are recovered from the relative coordinates by evaluating the telescoping sum:

$$
\begin{aligned}
u_{2N+1} - u_1 &= \underbrace{(u_{2N+1} - u_{2N})}_{y_{2N}} + \underbrace{(u_{2N} - u_{2N-1})}_{y_{2N-1}} + \ldots + \underbrace{(u_2 - u_1)}_{y_1} \\
&= \quad\quad y_{2N} \quad\quad + \quad\quad y_{2N-1} \quad\quad + \ldots + \quad\quad y_1 \\
&= \sum_{j=1}^{2N} y_j
\end{aligned}
\tag{2.46}
$$

Since the solution has to be antisymmetric with respect to the center point at $j = N + 1$, compare Fig. 2.3(b), it must hold true that $u_{2N+1} = -u_1$ and more generally

$u_{2N+1-k} = -u_{1+k}$, such that for $k = 0, \ldots, N-1$, the displacements are given by:

$$
\begin{aligned}
u_{2N+1-k} &= \frac{1}{2} \sum_{j=1+k}^{2N-k} y_j \\
&= \frac{1}{2} \sum_{j=1}^{2N-k} y_j - \frac{1}{2} \sum_{j=1}^{k} y_j \\
&= \frac{1}{2} \sum_{l=1,3,5,\ldots}^{2N} c_l(t) e^{-\lambda_l t} \left(\sum_{j=1}^{2N-k} \sin \frac{\pi j l}{2N+1} - \sum_{j=1}^{k} \sin \frac{\pi j l}{2N+1} \right)
\end{aligned}
\tag{2.47}
$$

In the last step, we have plugged in the solution for the relative coordinates given by Eq. (2.45) and have subsequently reversed the order of summation in both terms. The two sums in parenthesis can be further simplified by rewriting the sin-functions in terms of exponential functions. The resulting geometric sums can be evaluated, since summation is finite and convergence is guaranteed. For a derivation see appendix 6.2, here, we only provide the identity:

$$
\sum_{j=0}^{n} \sin(j\alpha) = \frac{1}{2} \left(\cot(\alpha/2) - \frac{\cos(\alpha(n+1/2))}{\sin(\alpha/2)} \right)
\tag{2.48}
$$

Using this identity to simplify the upper expressions yields

$$
u_{2N+1-k} = \frac{1}{2} \sum_{l=1,3,5,\ldots}^{2N} c_l(t) e^{-\lambda_l t} \frac{\cos \frac{\pi l (k+1/2)}{2N+1}}{\sin \frac{\pi l}{2(2N+1)}}
\tag{2.49}
$$

The index of u in the upper equation runs, according to the range of k, from $(N+1)+1 \leq (2N+1)-k \leq (2N+1)$. The node $(N+1)$ just denotes the center and the node $(2N+1)$ terminates the chain at its right end. In the next step we transform the index of u such that it now runs from $n = 1, \ldots, N$ and the node $n = 1$ corresponds to the node $(N+1)+1$ in the previous counting, compare figure 2.3(b). The proper transformation is $n = N-k$. Moreover, we exchange the index of summation by $l = 2m-1$ and obtain the final solution of the discrete model:

$$
u_n(t) = -\frac{2}{2N+1} \sum_{m=1}^{N} \frac{(-1)^{m-1}}{\sin \frac{\pi(2m-1)}{2(2N+1)}} \frac{\sin \frac{\pi n(2m-1)}{2N+1} \sin \frac{\pi(2m-1)}{2N+1}}{\gamma_{ext} + 4\tilde{\gamma}_{int} \sin^2 \frac{\pi(2m-1)}{2(2N+1)}} \int_0^t F_s(t') e^{-\frac{t-t'}{\tau_{m,N}}} dt'
\tag{2.50}
$$

with the retardation times (see page 23 for an explanation of this terminology):

$$
\tau_{m,N} = \frac{1}{\lambda_{2m-1,N}} = \frac{\gamma_{ext} + 4\tilde{\gamma}_{int} \sin^2 \frac{\pi(2m-1)}{2(2N+1)}}{k_{ext} + 4k_{int} \sin^2 \frac{\pi(2m-1)}{2(2N+1)}}
\tag{2.51}
$$

It is important to note that Eq. (2.50) gives the correct result for $n = 0$, that is $u_0 = 0$.

For this reason we can extend the range of validity of Eq. (2.50) to $n = 0 \dots N$. With this solution several aspects of our stress fiber model can be investigated analytically. For example in section 2.6 we will assume cyclic boundary forces in order to study the complex modulus of the stress fiber model. For the following, however, we consider our initial problem of a freely contracting stress fiber that has been released at one end. In this case the force exerted on the boundary is the constant stall force of the molecular motors and the solution simplifies to:

$$u_n(t) = -\frac{2F_s}{2N+1} \sum_{m=1}^{N} \frac{(-1)^{m+1}}{\sin\frac{\pi(2m-1)}{2(2N+1)}} \frac{\sin\frac{\pi n(2m-1)}{2N+1}\sin\frac{\pi(2m-1)}{2N+1}}{k_{ext} + 4k_{int}\sin^2\frac{\pi(2m-1)}{2(2N+1)}} \left(1 - e^{-\frac{t}{\tau_{m,N}}}\right) \qquad (2.52)$$

2.2.2 Solution in the continuum limit

In section 2.1.3, we have discussed how the system of discrete model equations can be converted to a continuum boundary value problem by performing the appropriate continuum limit. Thereby we have assumed that the total length L of the fiber is maintained constant while the fiber itself has been subdivided into an increasing number N of shorter pieces of length $a_N = L/N$. Moreover, in order to maintain the effective modulus of the macroscopic fiber we had to re-normalize the viscoelastic constants according to Eq. (2.14).

$$
\begin{aligned}
k_{N,int} &= \phi_N k_{int} & \text{and} \qquad \gamma_{N,int} &= \phi_N \tilde{\gamma}_{int} \\
k_{N,ext} &= \frac{k_{ext}}{\phi_N} & \text{and} \qquad \gamma_{N,ext} &= \frac{\gamma_{ext}}{\phi_N}
\end{aligned}
\qquad (2.53)
$$

with the scaling factor $\phi_N = \frac{Na}{L}$. In addition we have introduced the spatial variable $x = L\frac{n}{N}$ for the position of the n-th node. The same continuum limit can be performed on the solution for the discrete model Eq. (2.52) and we will finally obtain the solution of the continuum boundary value problem Eq. (2.22). To start with the continuum limit we apply it to the retardation times:

$$\tau_{m,N} = \frac{\gamma_{N,ext} + 4\gamma_{N,int}\sin^2\frac{\pi(2m-1)}{2(2N+1)}}{k_{N,ext} + 4k_{N,int}\sin^2\frac{\pi(2m-1)}{2(2N+1)}} = \tau \frac{\Gamma L^2 + 4a^2N^2\sin^2\frac{\pi(2m-1)}{2(2N+1)}}{\kappa L^2 + 4a^2N^2\sin^2\frac{\pi(2m-1)}{2(2N+1)}} \qquad (2.54)$$

Where we have used the parameters $\kappa = k_{ext}/k_{int}$, $\tau = \tilde{\gamma}_{int}/k_{int}$, $\Gamma = \gamma_{ext}/k_{int}/\tau$, defined in section 2.1.3. Evaluation of the retardation times in the limit $N \to \infty$ yields:

$$\tau_m := \tau \frac{4\Gamma L^2 + (a\pi(2m-1))^2}{4\kappa L^2 + (a\pi(2m-1))^2} \qquad (2.55)$$

Since $1 \leq m \leq \infty$ the upper relation defines infinitely many discrete retardation times. The resulting range is bounded by the extreme values τ_1 and τ_∞:

$$\tau \leq \tau_m \leq \tau \frac{4\Gamma L^2 + a^2\pi^2}{4\kappa L^2 + a^2\pi^2} \qquad \text{or} \qquad \tau \frac{4\Gamma L^2 + a^2\pi^2}{4\kappa L^2 + a^2\pi^2} \leq \tau_m \leq \tau \qquad (2.56)$$

The first relation holds if $\kappa < \Gamma$, whereas the second holds if $\kappa > \Gamma$. For comparison, our quantification of stress fiber retraction dynamics yields the ratio $\Gamma/\kappa = 0.037$ for actin transfected cells, see section 3.1. Therefore, the latter relation in Eq. (2.56) seems to be valid for stress fibers. In the special case, $\kappa = \Gamma$, the finite range of possible values collapses to the single retardation time τ which leads to the largely simplified form of the analytical solution, discussed early in section 2.1.3, see Eq. (2.24). In general, the infinitely many retardation times give rise to a discrete spectrum of retardation times further discussed below. The limiting procedure applied in Eq. (2.54) can be carried out similarly on the remaining N-dependent terms of the discrete solution given in Eq. (2.52). The result is the solution for the continuous boundary value problem outlined in section 2.1.3:

$$u(x,t) = -8a\delta L \sum_{m=1}^{\infty} \frac{(-1)^{m+1}\sin\frac{\pi x(2m-1)}{2L}}{4\kappa L^2 + (a\pi(2m-1))^2}(1 - e^{-t/\tau_m}) \qquad (2.57)$$

First note that the sum in Eq. (2.57) is uniformly convergent for all $x \in [0,L]$ and $t \in [0,\infty]$, a majorant and convergent series is given e.g. by $\sum_{m=1}^{\infty} \frac{1}{(a\pi(2m-1))^2}$. One is now tempted to set the found solution into the partial differential equation Eq. (2.21) in order to check if the solution indeed obeys the boundary value problem. However, verification is not straight forward. While differential operators with respect to time can be dragged into the sum without any difficulties, one has to be cautious by exchanging the order of summation and spatial differentiation. The difficulties arise from the fact that each differentiation with respect to x increases the power of m of the summands and convergence worsens. As a result, only the first derivative can be derived in this way, higher derivatives can not be dragged into the sum. For the first derivative we show in appendix 6.3 that the resulting series is still uniformly convergent[‡] for $x \in [0, L - \epsilon]$ for all $\epsilon > 0$. While higher derivatives are of no particular interest in the problems we consider it is quite fortunate that the first derivative can be calculated directly. For instance, in section 3.3.2 we will make use of the closed expression for the first derivative in order to calculate the tension along the stress fiber which we also compare to experimental data. Since the second spatial derivative is not accessible, direct verification of the solution by substituting it into the partial differential equation is not feasible. At least, it is possible to validate the analytical solution Eq. (2.57) by comparing it with the numerical solution of the boundary value problem derived within the Matlab PDE-toolbox. Fig. 2.4 shows three resulting curves for the analytical solution where the infinite sum has been approximated by 5, 10 and 1000 terms, respectively. For comparison, the direct numerical solution of the boundary value problem is given as a benchmark. Fig. 2.4(a) shows the time dependent displacement $u(t)$ at constant positions $x \in \{0, 9\,\mu\text{m}, 12\,\mu\text{m}, L = 15\,\mu\text{m}\}$ and Fig. 2.4(b) shows the spatial dependence of the displacement $u(x)$ for certain time points $t \in \{0, 1\,\text{s}, 5\,\text{s}, \infty\}$. In the

---

[‡]Uniform convergence of both, the original and of the piecewise differentiated series, is a sufficient condition for exchanging summation and differentiation. The badly convergent part of the resulting series after differentiation has essentially the form $\sum_{m=1}^{\infty} \frac{z^m}{m} = -\ln(1-z)$ with $z = e^{i\pi(1+\frac{x}{L})}$. The explicit result in terms of the logarithm is valid for $|z| < 1$ and can be extended to $|z| = 1$ for all $z \neq 1$ on the unit circle. This constraint just excludes the case $x = L$, also compare appendix 6.3.
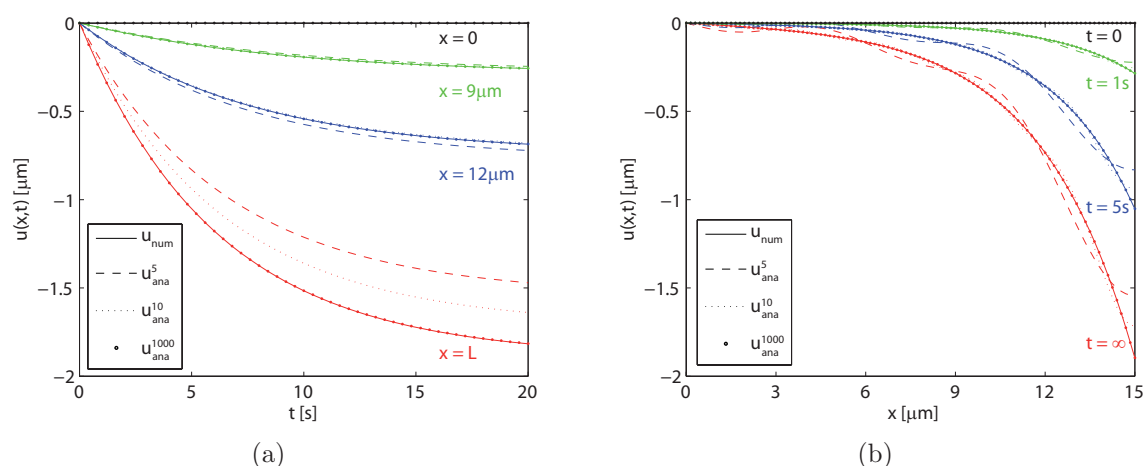
Figure 2.4: Comparison of the numerical solution from the Matlab PDE toolbox (u_{num}, solid lines) with the analytical solution calculated by Eq. (2.57). The analytical solution has been approximated by 5, 10 and 1000 terms (u_{ana}^{5} dashed lines, u_{ana}^{10} dotted lines and u_{ana}^{1000} marked by dots, respectively). (a): Plot of the time dependent displacement $u(t)$ at constant positions $x \in \{0, 9\,\mu\mathrm{m}, 12\,\mu\mathrm{m}, L\}$. (b): Plot of the spatial variations of the displacement $u(x)$ at certain time points $t \in \{0, 1\,\mathrm{s}, 5\,\mathrm{s}, \infty\}$. Used parameter values are $(\kappa, \tau, \tau_\epsilon, \delta) = (0.1, 5\,\mathrm{s}, 0.75\,\mathrm{s}, 0.6\,\mu\mathrm{m})$ and the length of the fiber was taken to be $L = 15\,\mu\mathrm{m}$.

latter plot, the *oscillating* curves for the analytical solution, approximated by only 5 or 10 terms, highlight the fact that the spatial dependence of the displacement results from a superposition of trigonometric functions, compare Eq. (2.57). These oscillations smooth out when increasing the number of considered terms which is computational not very costly. For example, conducting the sum up to a 1000 terms yields an accurate approximation of the solution and is still considerably faster than the direct numerical solution of the partial differential equation in the Matlab PDE-Toolbox.

2.2.3 Solution by inverse Laplace transform

There is yet another possibility to derive an analytical solution for the displacement field by solving an inverse Laplace transform. The resulting analytical expression is quite cumbersome and complicated to evaluate numerically. Since the concise solution given in Eq. (2.57) is superior in many aspects we only briefly sketch the alternative derivation and refer the interested reader to the detailed calculations presented in appendix 6.4.

The simple initial conditions of vanishing displacements at $t = 0$ enables the Laplace transform of the boundary value problem given in Eq. (2.22). The partial differential equation is thereby simplified to an ordinary second order differential equation which is straight forward to solve. The solution for the Laplace-transformed displacement is

given by:

$$\bar{u}(\tilde{x}, \tilde{s}) = \quad -\delta \cdot \underbrace{\frac{1}{s} \operatorname{sech}\left(\tilde{L}\frac{\sqrt{\Gamma\tilde{s}+\kappa}}{\sqrt{1+\tilde{s}}}\right)}_{=: \, \bar{g}_1(\tilde{s})} \cdot \underbrace{\frac{\sinh\left(\tilde{x}\frac{\sqrt{\Gamma\tilde{s}+\kappa}}{\sqrt{1+\tilde{s}}}\right)}{\tilde{s}\sqrt{1+\tilde{s}}\sqrt{\Gamma\tilde{s}+\kappa}}}_{=: \, \bar{g}_2(\tilde{x}, \tilde{s})} \qquad (2.58)$$

Here, $\bar{u}$ denotes the Laplace transform of the displacement which is defined by the integration $\bar{u}(\tilde{x}, \tilde{s}) = \int_0^\infty u(\tilde{x}, \tilde{t}) e^{-\tilde{s}\tilde{t}} d\tilde{t}$. In the following, overbars always denote the Laplace-transformed quantities. The variable $\tilde{s} = \gamma + i\tilde{\omega}$ is in general a complex variable with real part γ and imaginary part $\tilde{\omega}$. The above solution for $\bar{u}$ has been decomposed into the product of the two functions $\bar{g}_1(\tilde{s})$ and $\bar{g}_2(\tilde{x}, \tilde{s})$. The inverse Laplace transform can be performed on each factor separately, the inversion of the product is then given by the convolution theorem. The inversion formula for the Laplace transform is in general given by the Bromwich integral:

$$f(\tilde{t}) = \mathcal{L}^{-1}[\bar{f}(\tilde{s})](\tilde{t}) = \frac{1}{2\pi i} \int_{\gamma-i\infty}^{\gamma+i\infty} e^{\tilde{s}\tilde{t}} \bar{f}(\tilde{s}) d\tilde{s} \qquad (2.59)$$

The constant γ has to be chosen such that all singularities of the function $\bar{f}(\tilde{s})$ are on the left hand side of the integration path. For the special case where $\tilde{t} > 0$ and in addition the contour may be closed by an infinite semicircle in the left half-plane enclosing all singularities of $\bar{f}(\tilde{s})$ then the residue theorem is applicable and (see [91]):

$$f(\tilde{t}) = \sum_m \operatorname{res}(e^{\tilde{s}\tilde{t}} \bar{f}(\tilde{s}), \tilde{s}_m) \qquad (2.60)$$

where $\tilde{s}_m$ are the singularities of the function $\bar{f}(\tilde{s})$. It can be checked that Eq. (2.60) is applicable for the functions $\bar{g}_1$ and $\bar{g}_2$ that have to be inverted. The inversion problem is thus reduced to finding the residues of the two functions $e^{\tilde{s}\tilde{t}}\bar{g}_1(\tilde{s})$ and $e^{\tilde{s}\tilde{t}}\bar{g}_2(\tilde{s})$ at all occurring singularities. The function $\bar{g}_1$ has a simple pole at $\tilde{s} = 0$ and infinitely many simple poles at the roots of the hyperbolic cosine located at:

$$\tilde{s}_m = -\frac{4\tilde{L}^2\kappa + (\pi(2m-1))^2}{4\tilde{L}^2\Gamma + (\pi(2m-1))^2} \qquad (2.61)$$

In order to avoid double counting of the poles, in the upper formula, the index m runs from $m = 1, \ldots, \infty$. The residues at these simple poles are derived in appendix 6.4, here we solely give the final solution for the inversion according to Eq. (2.60):

$$g_1(\tilde{t}) = \operatorname{sech}(\tilde{L}\sqrt{\kappa}) + \sum_{m=1}^{\infty} \frac{(-1)^{m+1} 16\tilde{L}^2 \pi(2m-1)(\Gamma-\kappa)}{(4\tilde{L}^2\Gamma + (\pi(2m-1))^2)^2} \frac{e^{\tilde{t}\tilde{s}_m}}{\tilde{s}_m} \qquad (2.62)$$

In the equation above, the first term originates from the pole at $\tilde{s} = 0$ and the infinite sum accounts for the poles at $\tilde{s} = \tilde{s}_m$. The inversion of the function $\bar{g}_2(\tilde{s})$ is more involved. It has a removable singularity at $\tilde{s} = -\kappa/\Gamma$ which gives no contribution. However, at $s = -1$ it has an essential singularity. The associated residue,

$\mathrm{res}(e^{\tilde{s}\tilde{t}}\bar{g}_2(\tilde{s}), -1)$, is derived in appendix 6.4, here we again solely give the result for the inversion:

$$g_2(\tilde{x}, \tilde{t}) = e^{-\tilde{t}} \sum_{j=0}^{\infty} \frac{\tilde{t}^j}{j!} \sum_{n=0}^{\infty} \binom{n+j}{j} \frac{\tilde{x}^{2(n+j)+1}}{(2(n+j)+1)!} \Gamma^n (\kappa - \Gamma)^j \qquad (2.63)$$

The final solution for the displacement is then given by means of the convolution theorem as:

$$u(\tilde{x}, \tilde{t}) = -\delta \int_0^{\tilde{t}} g_1(\tilde{t}') g_2(\tilde{t} - \tilde{t}') d\tilde{t}' \qquad (2.64)$$

This expression which results from Eq. (2.62) to Eq. (2.64) is more difficult to evaluate than the solution previously presented in Eq. (2.57). In particular, many terms in the infinite series have to be taken into account in order to get a satisfying approximation for the solution at large x and t. In appendix 6.4, we compare the upper result numerically with the solution derived from the Matlab-PDE toolbox, see Fig. 6.1. Although little further insight to the contraction dynamics can be gained from the upper result, it is still interesting to compare the two different solutions given by Eqs. (2.62) to (2.64) and by Eq. (2.57). It turns out that the retardation times in the first derivation are, except for the signs, identical with the position of the poles in the last derivation. Thus, in both expressions there appear identical time-dependent exponential factors. However, in Eq. (2.64) there are in addition polynomial contributions in t which make it difficult to extract the retardation spectrum like we present it below by means of the other solution. Because of the functional complexity of the expressions it is not feasible to show that the two analytical solutions are indeed identical. Still, the convolution integral in Eq. (2.64) can be evaluated and the limit $t \to \infty$ can be performed. The resulting expression for the stationary solution, can be compared to the equivalent expressions found in Eq. (2.24) which yields several non-trivial mathematical identities. The interested reader is referred to appendix 6.4.

In the following, we will stick to the more concise solution given by Eq. (2.57) in order to discuss the contraction dynamics of the fiber.

2.3   Retardation time spectrum

The solution for the displacement $u(x, t)$ given in Eq. (2.57) can be understood as a spatial dependent creep function of the stress fiber model. It describes the shortening of the fiber as response to the contractile motor forces. From this point of view, the m-th coefficient in Eq. (2.57) constitutes the amplitude of the retardation time τ_m. The resulting discrete spectrum of retardation times is then given by the following parametric equations in, $m = 1, \ldots, \infty$:

$$S_m = -8a\delta L \frac{(-1)^{m+1} \sin\frac{\pi x(2m-1)}{2L}}{4\kappa L^2 + (a\pi(2m-1))^2} \quad \text{with} \quad \tau_m = \tau \frac{4\Gamma L^2 + (a\pi(2m-1))^2}{4\kappa L^2 + (a\pi(2m-1))^2} \qquad (2.65)$$

It is not very useful to eliminate the parameter m in the upper equations in order to get the explicit dependence of the amplitudes S on the retardation times τ_m. This is only convenient in the special case, $x = L$, where this relationship turns out to be linear:

$$S(\tau_m) = -\frac{2a\delta}{L\tau} \frac{\tau - \tau_m}{\kappa - \Gamma} \tag{2.66}$$

Since the range of possible retardation times is bounded according to Eq. (2.56), it follows that the spectrum for $x = L$ has only negative amplitudes and the resulting solution for the displacement at $x = L$ is always a monotonically decreasing function. However, for arbitrary x this holds not true. Inspection of Eq. (2.65) yields that in general negative as well as positive amplitudes appear simultaneously. For example, Fig. 2.5(a) and Fig. 2.5(b) show the discrete retardation spectrum at position $x = 12\,\mu$m and $x = 9\,\mu$m, respectively. The spectrum at $x = L$ is included in both figures as a reference. Since $x = L$ evaluates the numerator in Eq. (2.65) at its maximum, the resulting spectrum constitutes a lower bound for the negative amplitudes of the spectra with $x \neq L$. Similarly, the absolute value of Eq. (2.66) gives an upper bound for all positive amplitudes (not shown in the figures). Thus, the retardation spectra with $x \neq L$ oscillate around zero within an envelope for the amplitudes that decays linearly towards zero. The appearance of amplitudes with different signs gives rise to a potentially overshooting solution. Such a situation is depicted in Fig. 2.5(c). Here, the time-dependent solutions for the displacements at $x = 9\,\mu$m and $x = 12\,\mu$m overshoot before they approach their steady state values and thereby form a minimum. These characteristics turn out to be persistent for all displacements at $x \neq L$ if and only if $\kappa > \Gamma$. This is difficult to proof rigorously but in the following we will give some plausible arguments. Consider the retardation spectrum for $x = 9\,\mu$m in Fig. 2.5(b) and the corresponding solution for the displacement highlighted in Fig. 2.5(d). One finds that the smallest retardation time, $m = 1$, has the largest negative amplitude. Evidently this term equilibrates much faster than all the remaining ones and because of its large amplitude, it quickly overshoots the stationary value of the full solution, compare the dash-dot curve in Fig. 2.5(d) with the green curve representing the full solution. The next two terms, $m = 2, 3$ equilibrate considerably slower than the first term and have positive but smaller amplitudes. Hence, the sum of these three terms must exhibit a minimum at an intermediate time point, see black solid curve in Fig. 2.5(d). Together, the first three terms already give an astonishingly accurate approximation of the full solution, especially for small time scales. The remaining terms of larger retardation times with further decreasing amplitudes can be considered as corrections to the long term dynamics. The overshooting in the upper example is thus a consequence of the fact that the amplitudes decrease with increasing retardation times. It is now important to note that this feature is only given if $\kappa > \Gamma$. Then, according to Eq. (2.56) the retardation times increase with m towards their maximal value τ while the envelope of the amplitudes decreases with $1/m^2$. If the opposite is true, $\kappa < \Gamma$, then the retardation times approach τ from above and the largest amplitudes are associated with the largest retardation times. In this case, the solution for the displacements are always monotonically decreasing functions exemplified in Fig. 2.4(a) where $\Gamma/\kappa = 1.5$. In
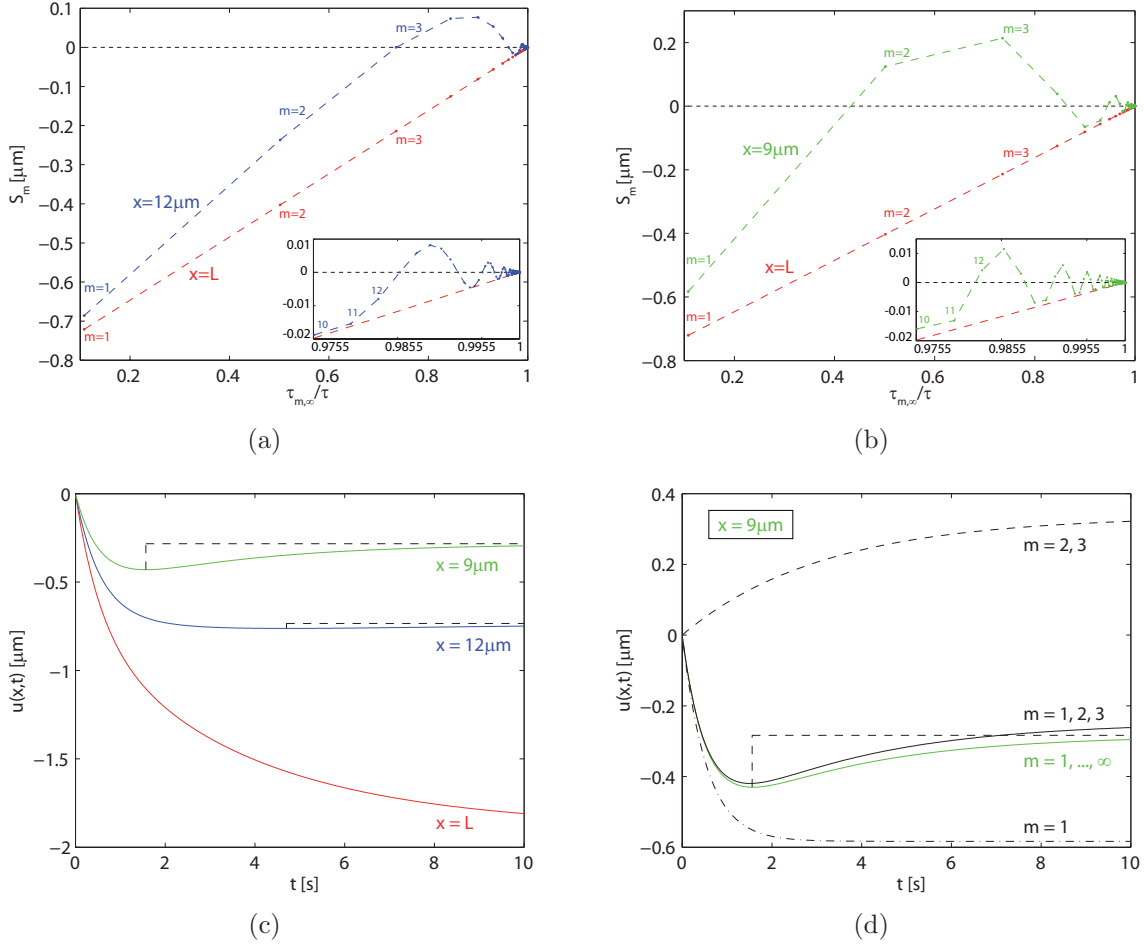
Figure 2.5: (a) Discrete spectrum of retardation times for $x = 12\,\mu$m. The discrete amplitudes are indicated by blue dots, the first three, $m = 1, 2, 3$, are numbered explicitly. The discrete spectrum for $x = L = 15\,\mu$m is included as a reference, shown in red. The inset shows a magnification of the spectra close to $\tau_m \approx \tau$ for $m \geq 10$. The first amplitudes $m = 10, 11, 12$, are numbered for clarity. (b) Same spectrum analysis as (a) but for $x = 9\,\mu$m. The spectrum for $x = L$ is again included as a reference. On sees from (a) and (b) that the spectra for $x = L$ constitutes a lower bound for all negative amplitudes. Similarly, the absolute value of Eq. (2.66) gives an upper bound for the positive amplitudes (not shown). (c) Shows the time-dependent solution for the displacement of the fiber at $x \in \{9\,\mu\mathrm{m}, 12\,\mu\mathrm{m}, L\}$. The solutions for $x \neq L$ overshoot their finally approached stationary values and thereby form a minimum highlighted by dashed lines. These characteristics are specific for $x \neq L$ when $\Gamma/\kappa < 1$, for comparison see Fig. 2.4 where $\Gamma/\kappa = 1.5$ and all solutions are monotonically decreasing. (d) Comparison of the full solution for the displacement at $x = 9\,\mu$m (green line) with the first term $m = 1$ (black dash-dot line), sum of second and third term $m = 2, 3$ (black dashed line) and the sum of the first three terms $m = 1, 2, 3$ (black solid line). The first term causes the overshoot, the subsequent terms turn it back to the finally approached stationary value and thereby form the minimum. Used parameter values are identical to the values used for Fig. 2.4, except for $\tau_\epsilon = 0.005\,$s which yields the ratio $\Gamma = \tau_\epsilon/\tau = 0.001 \ll 1$.

addition to the more technical arguments above we can also give a physical explanation for the overshooting solutions. For that purpose it is instructive to consider the time course of the viscoelastic stress or the tension along the fiber for the two extreme cases, $\kappa \ll \Gamma$ or $\kappa \gg \Gamma$. These considerations will be carried out below, in the next section.

To conclude the discussion of the retardation time spectrum we finally compare our model to the KSR-model. The emergence of a discrete retardation spectrum in our model is in contrast to the continuous spectrum obtained in the KSR-model for macromolecules [90] which considers a different continuum limit. There, the viscoelastic properties and the length a of the elementary units are kept constant while the number of units increases, similar to a polymer where the properties of each monomer are conserved. This leads to an infinitely long chain $L = Na \to \infty$. The spatial coordinate, however, remains discrete as it is a multiple of the finite length a. The two continuum limits intend to describe two different situations and thus also differ in their results. The essential differences are in summary, that the limit presented here yields a continuous spatial coordinate x with a discrete spectrum of retardation times, whereas the limit considered in the KSR-model yields a continuous spectrum of retardation times but the spatial coordinate remains discrete.

2.4   Stress fiber tension

The calculation of the viscoelastic stress within the actin cytoskeleton will play an essential role in understanding the dynamics of the mechanosensitive protein zyxin at focal adhesions and along stress fibers. This tight comparison of our model with experimental data will be subject of section 3.3. Also, the occurrence of overshooting solutions for the displacements presented above can be understood thoroughly by considering the time course of viscoelastic stress within the fiber. To further elucidate these issues, we will first explain how the viscoelastic stress within the fiber can be calculated and then we will discuss the time course of internal stresses for the two extreme cases $\Gamma \to 0$ and $\Gamma \to \infty$. Since our model is purely one-dimensional, the viscoelastic stress within the fiber is equivalent to a rope tension. It is given by:

$$\sigma(x,t) = \gamma_{int} a \partial_x \dot{u}(x,t) + k_{int} a \partial_x u(x,t) + F_m(x,t) \tag{2.67}$$

The first and the second term account for the internal viscous and internal elastic stresses, respectively. Since our model is one-dimensional the elastic stress is simply proportional to the strain in x-direction, $\partial_x u$, whereas viscous stress is proportional to the rate of strain, $\partial_x \dot{u}$. The last term results from the contractile motor forces, also compare Fig. 2.1. The latter can be expressed in terms of the continuum analog to Eq. (2.2), that is, $F_m(x,t) = F_s + a \frac{F_s}{v_0} \partial_x \dot{u}(x,t)$. The time dependent contributions of the motor forces are thus absorbed by the viscous term in the equation above changing the coefficient again to the effective internal viscosity $\tilde{\gamma}_{int} = \gamma_{int} + \frac{F_s}{v_0}$. Before cutting, we assume that the fiber is unperturbed $u(x,0) \equiv 0$. Therefore the initial tension is constant along the fiber and given by the stall force of the motors $\sigma_0 = F_s$. It is now convenient to normalize the tension by its initial value before cutting, leading to the

equation:

$$\frac{\sigma(x,t)}{\sigma_0} = \tau\frac{a}{\delta}\partial_x\dot{u}(x,t) + \frac{a}{\delta}\partial_x u(x,t) + 1 \tag{2.68}$$

where τ, δ are the model parameters defined in Eq. (2.20). The expression for the normalized tension above can be calculated from the analytical solution for the displacements given by Eq. (2.57). For that purpose, we have shown in appendix 6.3 that the first spatial derivative of the solution can be derived by simply exchanging the order of differentiation and summation. Also derivatives with respect to time do not cause any problems, see appendix 6.3 for a detailed discussion. There is yet another possibility to derive the tension within the fiber. Since inertia is neglected in our model, the tension at a certain position after cutting is also determined by the sum over all external forces that pull on this piece of the fiber. This is quite similar to a tug of war where the tension in the rope is given by the sum over the manpower:

$$\sigma(x,t) = -\frac{1}{a}\int_x^L k_{ext}u(x,t)dx - \frac{1}{a}\int_x^L \gamma_{ext}\dot{u}(x,t)dx \tag{2.69}$$

The first term constitutes the sum over all elastic forces mediated by the crosslinks and the second term accounts for the viscous friction forces exerted by the surrounding cytosol. The integration runs over the length of the considered piece of the fiber. It is a pure matter of taste to choose between the two alternatives either Eq. (2.68) or Eq. (2.69).

In the following, we use Eq. (2.68) to discuss the time course of the normalized tension for different ratios of Γ/κ. We start with the special case $\Gamma/\kappa = 1$. In this case the solution for the displacement u is particularly simple. Using Eq. (2.24) yields for the time course of tension:

$$\frac{\sigma(x,t)}{\sigma_0} = 1 - \frac{\cosh\frac{x\sqrt{\kappa}}{a}}{\cosh\frac{L\sqrt{\kappa}}{a}} = \frac{\sigma_{ss}(x)}{\sigma_0} \tag{2.70}$$

Interestingly, for this special case, the tension is not time dependent. This means that at each position along the fiber the tension drops to its final steady state value immediately after cutting. At $t = 0$ only the molecular motors and the viscous stress contributes to the tension. In the steady state the viscous forces vanish and their initial contribution is finally exactly substituted by the elastic stress. Thus, in the case $\Gamma = \kappa$, this turnover from viscous to elastic stress is at each time point and at each position along the fiber exactly balanced. In the moment of cutting, each fiber element is subject to a one-step stress history, from a constant high stress level before cutting, down to a lower constant stress level after cutting. The height of the step, however, is dependent on the position along the fiber. This one-step stress history results in a simple creep response of each segment along the fiber and the length as well as the displacement of each segment will thus change monotonically in time. This can also be read off directly from the solution, given in Eq. (2.24).

Next we discuss the case $\Gamma/\kappa \to \infty$ which is equivalent to $\tau \to 0$. In this case it is sufficient to study the tension shortly after cut at $t = 0$. Since here, τ is negligible,
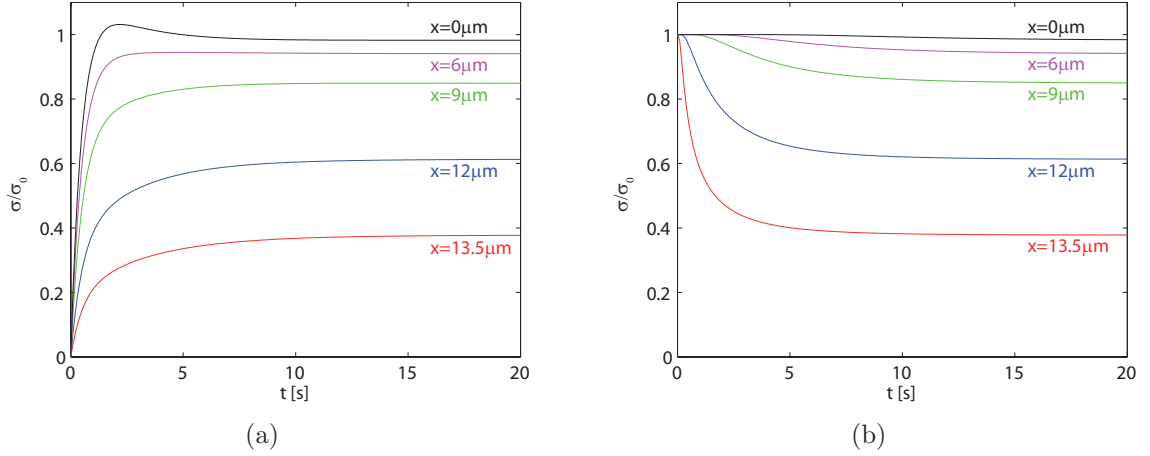
Figure 2.6: Time course of tension at certain position $x \in \{0, 6, 9, 12, 13.5\}\,\mu$m along the fiber. (a) Shows the case $\Gamma \ll \kappa$. Used parameter values are $(\kappa, \tau, \tau_\epsilon, \delta) = (0.1, 5\,\text{s}, 0\,\text{s}, 0.6\,\mu\text{m})$ which means $\Gamma = 0$. (b) Shows the case $\Gamma \gg \kappa$. Used parameter values are $(\kappa, \tau, \tau_\epsilon, \delta) = (0.1, 0.0\,\text{s}, 0.5\,\text{s}, 0.6\,\mu\text{m})$ which means $\Gamma \to \infty$. The length of the fiber was taken to be $L = 15\,\mu$m in both cases.

the viscous stress term in Eq. (2.68) cancels out. The initial elastic stress also vanishes since the initial strain is zero according to the imposed initial conditions. Thus, the stress shortly after cut is still given by the stall force of the motors. In other words, the time course of tension upon cut is continuous. After cutting, the stress decreases monotonically to its steady state value, illustrated in Fig. 2.6(b). Since the stress within each fiber segment decreases monotonically, also the change of length as well as the displacements of each segment will change monotonically in time. In the more general case of finite ratios with $1 < \Gamma/\kappa < \infty$, the time course of stress exhibits a discontinuity at the moment of cut, similar to the case where $\Gamma = \kappa$. But in contrast to the latter case, here, the sudden down step in stress does not immediately reach the steady state value. This remaining difference in stress then relaxes monotonically in time. For the same reasons as discussed before, also the displacements along the fiber then change monotonically in time. The preservation of a certain amount of stress shortly after cut is essentially due to the high external friction that arrests the fiber elements at their initial position and thereby prevents the perturbation of the cut to instantly propagate along the fiber.

The last case to discuss is $0 \le \Gamma/\kappa < 1$. To gain some intuition about the tension dynamics for this range it is instructive to study again the extreme case $\Gamma/\kappa = 0$ shortly after cut, at $t = 0$. According to the imposed initial conditions the elastic stress term again vanishes at $t = 0$ and the viscous stress term can be evaluated by applying the solution for the displacements given in Eq. (2.57):

$$
\begin{aligned}
a\frac{\tau}{\delta}\partial_x \dot{u}(x,0) &= -\frac{4}{\pi}\sum_{m=1}^{\infty}(-1)^{m+1}\frac{\cos\frac{(2m-1)\pi x}{2L}}{2m-1} \\
&= -\frac{2}{\pi}\left(\arctan(e^{i\pi\frac{x}{2L}}) + \arctan(e^{-i\pi\frac{x}{2L}})\right) = -1
\end{aligned}
\tag{2.71}
$$

In the first step we used the solution for the displacements, carried out the derivatives and set $\Gamma = 0$. To perform the second step we have expressed the cosine by exponential functions. The result can be identified with the Taylor series of the inverse tangent. The last step follows by using the definition of the inverse tangent in terms of the natural logarithm. To evaluate the arguments we have used that $0 \leq \pi \frac{x}{2L} < \frac{\pi}{2}$. The resulting viscous stress is constant along the fiber and just cancels the contributions of the contractile motor forces. Thus, at the moment of cut, the total stress drops to zero all along the fiber. As a consequence, shortly after cut, all fiber segments are subject to the full contractile motor force, as if they were contracting independently from each other. While the fiber retracts, restoring forces are built up by tensed crosslinks and the tension within the fiber starts to approach its steady state value from below, illustrated in Fig. 2.6(a). The non-monotonic stress history, namely the first instant loss of tension and the subsequent recovery of the steady state tension from below causes each fiber segment to contract to a large extend at first and then relax to its less contracted steady state length. This also results in the overshooting solutions for the displacements, discussed beforehand and illustrated in Fig. 2.5(c). These overshooting solutions are a persistent characteristic for all segments along the fiber given that $0 \leq \Gamma/\kappa < 1$. The only exception takes place at $x = L$ where the tension drops to zero after cut and remains there due to the imposed boundary conditions. In the more general case where the ratio is finite, $0 < \Gamma/\kappa < 1$, the initial loss of tension along the fiber is not complete. In this case, the external friction does not vanish completely and can sustain a certain amount of tension which is increasing with distance from the cut. Still, if $\Gamma/\kappa < 1$ the final steady state tension is then approached from below and the solutions for the time course of strain as well as for the displacements will exhibit the overshooting characteristics. Interestingly, the approach to the steady state tension is even not monotonic after the first local minimum. This is indicated by the time course of tension at $x = 0$ in Fig. 2.6(a) which exhibits a pronounced second extremum before it further approaches steady state. This is the onset of damped oscillations discussed below.

2.5 Damped oscillations without inertia

In the previous sections we have shown that there exist overshooting solutions for the displacements of inner fiber segments, if $\Gamma/\kappa < 1$. These overshooting solutions are at the beginning of damped oscillations about the approached steady state. This can be demonstrated by plotting the residual displacement, that is, the difference between the actual displacement and its steady state value, $u(t) - u_{ss}$, at $x < L$, shown in Fig. 2.7 as an inset. Two periods can be traced easily, but the amplitude decays quickly over time. In order to see how these oscillations proceed we plot the absolute value of the residual displacement in a log-log-plot, see Fig. 2.7. To ensure that these oscillations are not simply due to numerical inaccuracy we show the numerical solution, derived from the Matlab PDE toolbox and compare it to the analytical solution, calculated from Eq. (2.57) where the infinite sum has been approximated by the leading 10^5 terms. Both solutions oscillate and show 5 periods before they diverge at around $t \approx 50\,\mathrm{s}$.
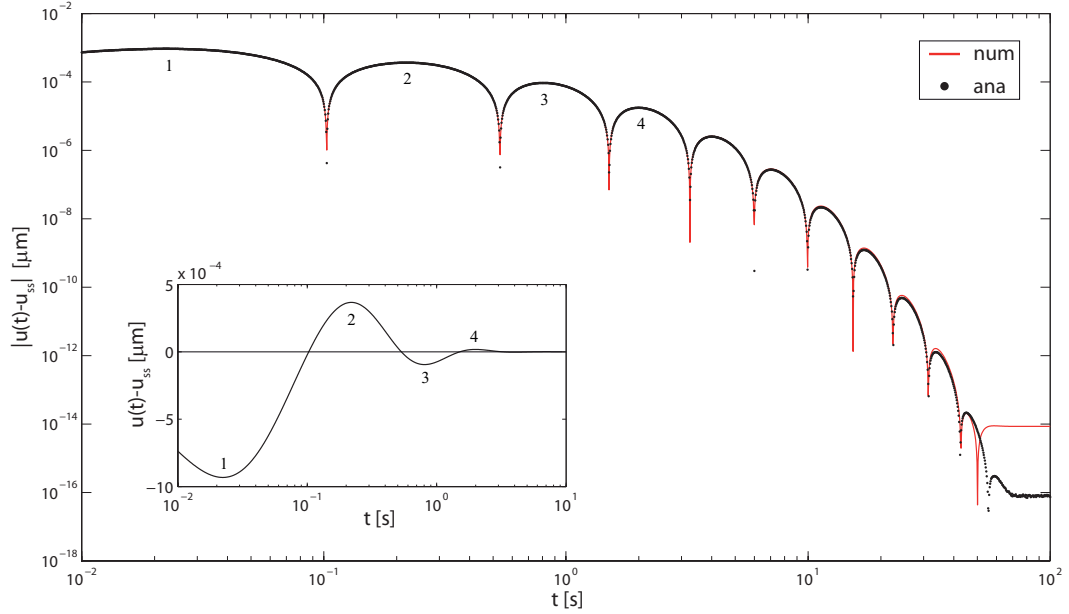
Figure 2.7: In the case of $\Gamma < \kappa$, the displacements of inner fiber segments exhibit damped oscillations around their final steady state. Here, we plot the time course of the absolute difference $|u(x,t) - u_{ss}(x)|$ on a logarithmic scale. The chosen position is $x = 1\,\mu$m. To assure that the oscillations are not due to numerical inaccuracy we compare the numerical solution (red line) to the solution calculated from Eq. (2.57) where the infinite sum has been approximated by the leading 10^5 terms (black dots). The oscillations are reliable up to $t \approx 50\,$s where the two solutions begin to diverge. In addition, we also give the difference $u(x,t) - u_{ss}(x)$ on a normal scale as an inset. For clarification we included the counting of the extremal values. Used parameters are $(\kappa, \tau, \tau_\epsilon, \delta) = (0.1, 5\,\mathrm{s}, 0\,\mathrm{s}, 0.6\,\mu\mathrm{m})$ which yields $\Gamma/\kappa = 0$. The fiber length was chosen to be $L = 100\,\mu$m.

For longer times, both solutions are not reliable any more but it is expected that a further increase in numerical precision reveals more oscillations. From the plot it can be deduced, that the amplitude decays quickly and the period time increases over time.

These oscillations are also found when plotting the viscoelastic stress. By comparing the viscoelastic stress with the strain within the fiber we find that strain lags behind stress as it is expected for a viscoelastic material exposed to cyclic forces.

As mentioned before, the oscillations occur only at inner fiber segments but the total length of the fiber decreases monotonically over time as it is expected for an over damped system. The fact that the oscillations occur at the inner segments is still surprising as the fiber is model in an over damped limit, that is, inertia is neglected. So far, we have no simple physical argument for the onset of these fiber internal oscillations. But according to our model these oscillations should be observed experimentally when a viscoelastic fiber under prestress is released in an elastic medium. Elastic, because $\Gamma/\kappa \ll 1$ essentially means that the external viscosity can be neglected and that the surrounding of the fiber rather appears to be purely elastic.

By fitting our model to stress fiber contraction dynamics after laser release we find that these conditions are likely fulfilled for stress fibers. Results are reported in the

next chapter. The cytoplasm which surrounds the stress fibers is indeed viscoelastic but the effective internal fiber viscosity is so large that $\Gamma/\kappa \ll 1$ seems to be fulfilled, see the last line in Tab. 3.1. But it is worth mentioning, that the activity of the molecular motors contribute to the fiber internal viscosity. As the motor activity can be regulated by the cell, the condition, $\Gamma/\kappa < 1$, has not to be fulfilled for every single stress fiber.

In general, these oscillations will be hard to measure experimentally, since they only occur at the inner fiber segments where the displacements are very small and hard to resolve experimentally. But there is few experimental data that at least indicate the first overshoot. For example, compare Fig. 3.2(b). Here, the inner bands, no.3 (green) and no.4 (pink) fairly follow the overshooting model solutions for the displacement.

2.6 The complex modulus of the fiber model

The mechanical properties of the cytoskeleton are intensively studied with many different experimental setups, including passive microrheology with immersed micrometer sized beads [92, 93] or active measurements like micropipette aspiration [94, 95], atomic force microscopy [96], optical or magnetic tweezers [97–100], all reviewed in [60]. With the latter techniques forces can be applied to the cytoskeleton and the resulting mechanical deformation can be measured. In case of cyclic forces, stress and strain are connected by the complex modulus, see appendix 6.1. The complex modulus of the cytoskeleton as a function of frequency has been measured in detail using magnetic tweezers [99, 100]. So far, experimental measurements have been concentrated on isotropic actin networks as it is organized for example in lamellipodia. However, little experimental or theoretical work has been performed on single actin stress fibers [89].

In the following, we will calculate the complex modulus for our stress fiber model taking three different approaches: Firstly, by a recursion rule deduced from the discrete model, secondly, by solving the continuum model for cyclic boundary forces and finally, by solving the Laplace-transformed model equation to obtain the Laplace-transformed creep compliance.

2.6.1 Recursion for the complex modulus

Appendix 6.1 provides all necessary tools to derive the complex modulus for the discrete set of springs and dashpots shown in Fig. 2.1. The needed relations are briefly recapitulated and thereby adapted to the present problem. Finally, repeated application of these relations yields an iteration rule that determines the complex modulus of the stress fiber model up to arbitrary high numbers of sarcomeric units.

The main tools to calculate the viscoelastic moduli of more complicated networks are the summation rules given by Eq. (6.10) and Eq. (6.12): When two elements are connected in series then the effective creep compliance is the sum of the individual creep compliances. And conversely, when two elements are connected in parallel their relaxation moduli are additive. Obviously, these relations hold true for their Laplace-transformed quantities, too. Multiplying the Laplace-transformed Eq. (6.12) and Eq. (6.10) by s and performing the limit according to Eq. (6.25) and Eq. (6.27)

yields equivalent relations for the complex compliance and the complex modulus:

$$J_{tot}^{* \to \to}(\omega) = J_1^*(\omega) + J_2^*(\omega) \quad \text{and} \quad G_{tot}^{* \rightrightarrows}(\omega) = G_1^*(\omega) + G_2^*(\omega) \tag{2.72}$$

The symbol $\to \to$ means that elements are connected in series and $\rightrightarrows$ denotes parallel alignment. Once, either $G^*(s)$ or $J^*(s)$ has been determined for a certain setup, the other entity can be calculated from Eq. (6.28), for example:

$$G^*(\omega) = \frac{1}{J^*(\omega)} \tag{2.73}$$

Eqs. (2.72)-(2.73) are now used to set up an iteration rule to determine the complex modulus of the discrete stress fiber model up to arbitrary high numbers of sarcomeric units. The picture Fig. 2.1 illustrates that the stress fiber model is built up by connecting internal Kelvin-Voigt bodies with external Kelvin-Voigt bodies alternating in series and in parallel. The most simple model for the stress fiber, containing only one sarcomeric unit, is a combination of a single internal Kelvin-Voigt body with complex modulus $G_{int}^*(\omega)$ and complex compliance $J_{int}^*(\omega)$ connected in parallel with an external Kelvin-Voigt body with complex modulus $G_{ext}^*(\omega)$ and complex compliance $J_{ext}^*(\omega)$. The complex modulus $G_1^*(\omega)$ for the whole sarcomeric unit is according to Eq. (2.72):

$$G_1^*(\omega) = G_{ext}^*(\omega) + G_{int}^*(\omega) \tag{2.74}$$

and Eq. (2.73) directly yields the complex compliance of the first unit:

$$J_1^*(\omega) = \frac{1}{G_1^*(\omega)} = \frac{1}{G_{ext}^*(\omega) + G_{int}^*(\omega)} \tag{2.75}$$

A further refinement of the model by an additional sarcomeric unit requires two intermediate steps: at first, an internal Kelvin-Voigt body has to be connected in series and secondly an external Kelvin-Voigt body has to be connected in parallel. According to Eq. (2.72) the effective complex compliance $J_{1.5}^*$ after the first half step, is the sum of the individual complex compliances:

$$J_{1.5}^*(\omega) = J_{int}^*(\omega) + J_1^*(\omega) \tag{2.76}$$

After this half step the complex modulus $G_{1.5}^*$ can be calculated from $J_{1.5}^*$ by means of Eq. (2.73)

$$G_{1.5}^*(\omega) = \frac{1}{J_{1.5}^*(\omega)} = \frac{1}{J_{int}^*(\omega) + J_1^*(\omega)} \tag{2.77}$$

In order to complete a full iteration step an additional external Kelvin-Voigt body has to be connected in parallel. In a parallel setup, the complex moduli are additive and the effective complex modulus G_2^* of a stress fiber with two sarcomeric units is thus given by

$$G_2^*(\omega) = G_{ext}^*(\omega) + G_{1.5}^*(\omega) = G_{ext}^*(\omega) + \frac{1}{J_{int}^*(\omega) + J_1^*(\omega)} \tag{2.78}$$
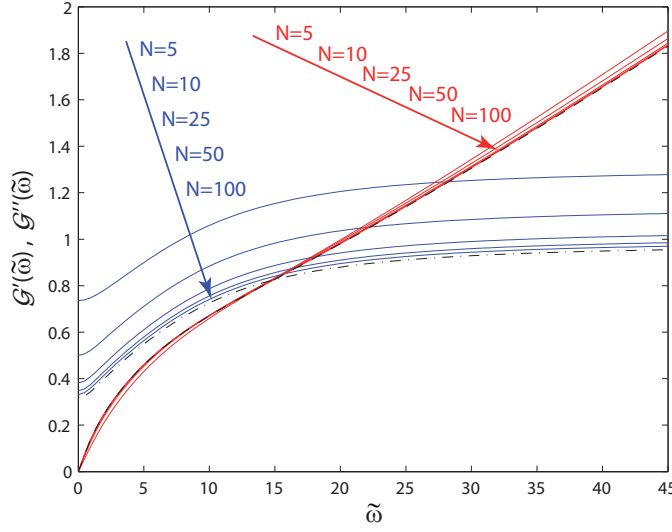
Figure 2.8: Iterated non-dimensional storage modulus $\mathcal{G}'(\tilde{\omega}) = G'/k_{int}$ (blue curves) and loss modulus $\mathcal{G}''(\tilde{\omega}) = G''/k_{int}$ (red curves) calculated from Eq. (2.85). The frequency $\tilde{\omega} = \omega\tau$ is also non-dimensional. Curves are shown for the iteration steps $N \in \{5, 10, 25, 50, 100\}$. Used parameter values are $L/a = 30$, $\kappa = 0.1$ and $\Gamma = 0.0005$. As a reference, analytical solutions for $\mathcal{G}'$ and $\mathcal{G}''$ calculated from Eq. (2.95) are shown as dash-dot and dashed black lines.

Repeated application of the relation given by Eq. (2.73) yields the complex compliance J_2^* for a stress fiber with two sarcomeric units

$$J_2^*(\omega) = \frac{1}{G_2^*(\omega)} = \frac{1}{G_{ext}^*(\omega) + \frac{1}{J_{int}^*(\omega) + J_1^*(\omega)}} \tag{2.79}$$

The presented iteration scheme can be applied for arbitrary numbers of sarcomeric units. The appropriate recursion rule for the complex compliance J_N^* of a stress fiber with N sarcomeric units is given by:

$$J_N^*(\omega) = \frac{1}{G_{ext}^*(\omega) + \frac{1}{J_{int}^*(\omega) + J_{N-1}^*(\omega)}} \quad \text{with} \quad J_1^*(\omega) = \frac{1}{G_{ext}^*(\omega) + G_{int}^*(\omega)} \tag{2.80}$$

Similarly, the recursion rule for the complex modulus is given by:

$$G_N^*(\omega) = G_{ext}^*(\omega) + \frac{1}{J_{int}^*(\omega) + \frac{1}{G_{N-1}^*(\omega)}} \quad \text{with} \quad G_1^*(\omega) = G_{ext}^*(\omega) + G_{int}^*(\omega) \tag{2.81}$$

In both cases, the recursion rule describes a terminating continued fraction. Note that $G_{int}^*(\omega)$ appears only in the initial conditions. The aim of this section is to derive the complex modulus for the continuous stress fiber model. The continuum description is appropriate when the stress fiber is composed of many sarcomeric units, say $N \to \infty$. Simple application of this limiting procedure in Eq. (2.81), however, would not lead to the correct result. In fact, the viscoelastic constants of the springs and dashpot have

to be re-scaled during the limiting procedure according to Eq. (2.14) in order to ensure that the effective viscoelastic properties of the whole chain are conserved, compare also the discussion in section 2.1.3. For convenience we again summarize the appropriate scalings of the viscoelastic constants below.

$$
\begin{aligned}
k_{N,int} &= \phi_N k_{int} &\text{and}&& \gamma_{N,int} &= \phi_N \gamma_{int} \\
k_{N,ext} &= \frac{k_{ext}}{\phi_N} &\text{and}&& \gamma_{N,ext} &= \frac{\gamma_{ext}}{\phi_N}
\end{aligned}
\tag{2.82}
$$

Where the scaling factor $\phi_N = \frac{a}{a_N} = \frac{Na}{L}$ has been introduced again. As a consequence, also the moduli of the internal and external Kelvin-Voigt bodies have to be re-scaled. In particular, when aiming at the continuum limit, the recursion rule given in Eq. (2.81) should be rewritten as:

$$
G_N^*(\omega) = G_{N,ext}^*(\omega) + \left(\cfrac{1}{J_{N,int}^*(\omega) + \cfrac{1}{G_{N,ext}^*(\omega) + ...}} \right)_{N-1} ... + G_{N,int}^*(\omega)
\tag{2.83}
$$

The fraction in parentheses is continued periodically $(N-1)$-times and terminates with $G_{N,int}^*(\omega)$. Here, the index N denotes that the complex modulus and the complex compliance of the Kelvin-Voigt bodies now become dependent on the iteration step N. For example, substituting the scaled elastic constants given in Eq. (2.14) into the expression for the complex modulus of a Kelvin-Voigt body, see Tab. 6.1, yields:

$$
G_{N,ext}^* = k_{N,ext} + i\omega\gamma_{N,ext} = \frac{1}{\phi_N}(k_{ext} + i\omega\gamma_{ext}) = \frac{k_{int}}{\phi_N}(\kappa + i\omega\tau_\epsilon) = \frac{k_{int}}{\phi_N}(\kappa + i\tilde{\omega}\Gamma) = \frac{k_{int}}{\phi_N}\mathcal{G}_{ext}^*
$$

Where the non-dimensional external complex modulus $\mathcal{G}_{ext}^*$ has been introduced. Similarly, the other moduli can be calculated.

$$
\begin{aligned}
G_{N,int}^* &= k_{int}\phi_N\mathcal{G}_{int}^* &\text{with}&& \mathcal{G}_{int}^*(\omega) &= 1 + i\omega\tau &=& 1 + i\tilde{\omega} \\[2mm]
J_{N,int}^* &= \frac{1}{k_{int}\phi_N}\mathcal{J}_{int}^* &\text{with}&& \mathcal{J}_{int}^*(\omega) &= \frac{1 - i\omega\tau}{1 + \omega^2\tau^2} &=& \frac{1 - i\tilde{\omega}}{1 + \tilde{\omega}^2} \\[2mm]
G_{N,ext}^* &= \frac{k_{int}}{\phi_N}\mathcal{G}_{ext}^* &\text{with}&& \mathcal{G}_{ext}^*(\omega) &= \kappa + i\omega\tau_\epsilon &=& \kappa + i\tilde{\omega}\Gamma \\[2mm]
J_{N,ext}^* &= \frac{\phi_N}{k_{int}}\mathcal{J}_{ext}^* &\text{with}&& \mathcal{J}_{ext}^*(\omega) &= \frac{\kappa - i\omega\tau_\epsilon}{\kappa^2 + \omega^2\tau_\epsilon^2} &=& \frac{\kappa - i\tilde{\omega}\Gamma}{\kappa^2 + \tilde{\omega}^2\Gamma^2}
\end{aligned}
\tag{2.84}
$$

Substituting these expressions into Eq. (2.83) yields the recursion rule for the complex modulus $\mathcal{G}_N^*(\tilde{\omega})$ of the stress fiber in terms of the model parameters a, L, κ, Γ:

$$
\mathcal{G}_N^*(\tilde{\omega}) = \frac{\mathcal{G}_{ext}^*(\tilde{\omega})}{\phi_N} + \left(\cfrac{1}{\cfrac{\mathcal{J}_{int}^*(\tilde{\omega})}{\phi_N} + \cfrac{1}{\frac{\mathcal{G}_{ext}^*(\tilde{\omega})}{\phi_N} + ...}} \right)_{N-1} ... + \phi_N\mathcal{G}_{int}^*(\tilde{\omega})
\tag{2.85}
$$

Note that $\mathcal{G}_N^*(\tilde{\omega})$ is non-dimensional since it is scaled by the stiffness k_{int} of one sarcomeric unit of length a. The first term $\frac{\mathcal{G}_{ext}^*(\tilde{\omega})}{\phi_N}$ which accounts for the last external linkage at the right boundary in Fig. 2.1 vanishes for increasing N according to $1/N$. Thus in the limit of large N one obtains the same result compared to a model where this terminating linkage is missing (the considered term is just cancelled out in the recursion formula). One can now use either recursion rule to numerically approximate the continuum value for the complex modulus $\mathcal{G}^*(\tilde{\omega})$ of the stress fiber model up to arbitrary high precision. Numerical calculations reveal that regarding the speed of convergence neither approach is superior to the other. Noteworthy, their arithmetic sum (obtained by reducing the first term in Eq. (2.85) by half), however, converges considerably faster. To illustrate the results, the complex valued function is decomposed numerically into its real part, the storage modulus $\mathcal{G}'(\tilde{\omega})$ and its imaginary part, the loss modulus $\mathcal{G}''(\tilde{\omega})$. The results for the iteration scheme Eq. (2.85) are illustrated in Fig. 2.8 for several iteration steps. The curves for the storage modulus are shown in blue whereas the curves for the loss modulus are shown in red. Used parameter values are given in the figure caption. For comparison, the analytical results for the storage and loss modulus, derived in the following section, are highlighted as dash-dot and dashed black line, respectively. Convergence is slow but the numerical solution for $N = 100$ iteration steps approximate the analytical results within a relative error of about 5%.

2.6.2   Closed solution from continuum limit

In the previous section a straight forward derivation of the the complex modulus for the stress fiber model was presented. However, the resulting iteration rule leads to poor convergence. Moreover, numerical evaluation of the continued fractions is quite time consuming. The presented iteration scheme is in some sense also very similar to the derivation of our model solution. We first calculated the complex modulus for a certain number N of sarcomeric units and subsequently performed the continuum limit. Instead of repeating this procedure one can of course also use the found model solution to derive a closed form of the complex modulus. For this purpose one has to slightly adapt the boundary conditions of the model. Instead of the tension free boundary conditions used so far, in the present situation, one has to impose a cyclic boundary force: $F_b(t) = f_0 e^{i\omega t}$. This time dependent boundary force can be substituted into the general solution of our discrete model Eq. (2.50):

$$u_n(t) = \frac{2f_0}{2N+1} \sum_{m=1}^{N} \frac{(-1)^{m-1}}{\sin \frac{\pi(2m-1)}{2(2N+1)}} \frac{\sin \frac{\pi n(2m-1)}{2N+1} \sin \frac{\pi(2m-1)}{2N+1}}{\gamma_{ext} + 4\tilde{\gamma}_{int} \sin^2 \frac{\pi(2m-1)}{2(2N+1)}} \int_0^t e^{i\omega t'} e^{-\frac{t-t'}{\tau_{m,N}}} dt' \qquad (2.86)$$

It is straight forward to evaluate the integration and subsequently perform the continuum limit in the same way as presented in section 2.1.3. The imposed cyclic boundary

force then results in the following solution for the displacements along the fiber:

$$u(x,t) = 8a\delta_0 L \sum_{m=1}^{\infty} \frac{(-1)^{m+1} \sin \frac{\pi x(2m-1)}{2L}}{4\kappa L^2 + (a\pi(2m-1))^2} \frac{1}{i\omega\tau_m + 1} \left(e^{i\omega t} - e^{-t/\tau_m}\right) \qquad (2.87)$$

where we have defined $\delta_0 = f_0/k_{int}$. Inspection of the time dependent terms yields that the solution for the displacements approaches a harmonic oscillation. The deviations decay exponentially in time, according to e^{-t/τ_m}. Note that the retardation times $\tau_m > 0$ for all m. As a consequence, in the limit for large times, the fiber displacements also oscillates with the same frequency ω as the force input but the constant phase shift between displacements $u(x,t)$ and $F_b(t)$ might vary spatially along the fiber. In the following, we are only interested in the response of the fiber as a whole, that is, we focus only on the displacement at $x = L$. With the above arguments, we find in the limit for large times:

$$u(L,t) = \underbrace{\left(8aL \sum_{m=1}^{\infty} \frac{1}{4\kappa L^2 + (a\pi(2m-1))^2} \frac{1}{i\omega\tau_m + 1}\right)}_{= 1/\mathcal{G}^*(\omega)} \cdot \delta_0 e^{i\omega t} \qquad (2.88)$$

By comparing the upper result with Eq. (6.24) one can simply read off the complex modulus. As in the previous section we scale it with the internal spring stiffness k_{int}. For comparison with the previous results it is also convenient to switch to the non-dimensional variables. The upper expression for the complex modulus can be separated into real and imaginary part, the storage and the loss modulus, respectively. We find

$$\mathcal{G}^*(\tilde{\omega}) = \underbrace{\frac{p(\tilde{\omega})}{p^2(\tilde{\omega}) + q^2(\tilde{\omega})}}_{= \mathcal{G}'(\tilde{\omega})} + i \underbrace{\frac{q(\tilde{\omega})}{p^2(\tilde{\omega}) + q^2(\tilde{\omega})}}_{= \mathcal{G}''(\tilde{\omega})} \qquad (2.89)$$

with

$$
\begin{aligned}
p(\tilde{\omega}) &= 8\tilde{L} \sum_{m=1}^{\infty} \frac{1}{4\kappa\tilde{L}^2 + \pi^2(2m-1)^2} \frac{1}{\tilde{\omega}^2\tilde{\tau}_m^2 + 1} \\
q(\tilde{\omega}) &= 8\tilde{L} \sum_{m=1}^{\infty} \frac{1}{4\kappa\tilde{L}^2 + \pi^2(2m-1)^2} \frac{\tilde{\omega}\tilde{\tau}_m}{\tilde{\omega}^2\tilde{\tau}_m^2 + 1}
\end{aligned}
\qquad (2.90)
$$

Where we have defined $\tilde{\tau}_m = \tau_m/\tau$. Despite the fact that this expression for the complex modulus looks more complicated than its definition given by the continued fraction in Eq. (2.85), it is easier to evaluate. Another great advantage is that this solution is already split into its real and imaginary part. In the following we will present an even more concise solution for the complex modulus. However, in this case, the storage and loss modulus can not be given explicitly.
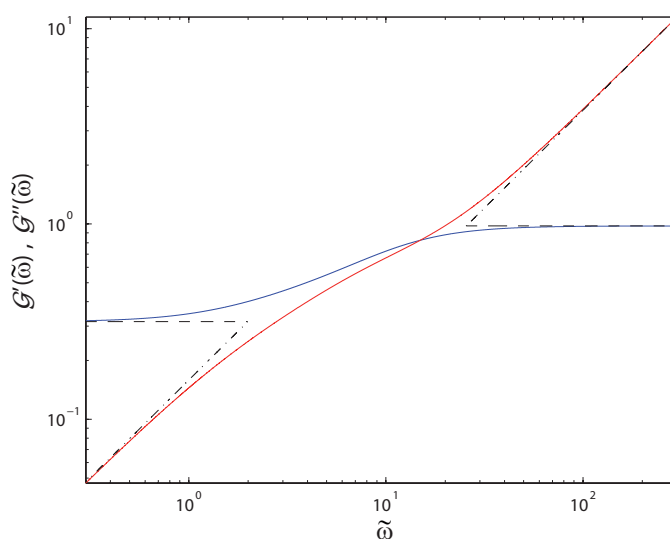
Figure 2.9: Log-log plot of the storage modulus (blue) and the loss modulus (red). The plotted moduli $\mathcal{G}' = G'/k_{int}$ and $\mathcal{G}'' = G''/k_{int}$ as well as the frequency $\tilde{\omega} = \omega\tau$ are non-dimensional quantities. The scaling at low and high frequencies is illustrated for both storage modulus (dashed black lines) and loss modulus (dash-dotted black lines). Curves were calculated from Eq. (2.95) with parameters: $\tilde{L} = 30$, $\kappa = 0.1$ and $\Gamma = 0.0005$.

2.6.3   Analytical solution by Laplace transform

In this section, the complex modulus is derived more elegantly by solving the stress fiber model equation directly for the Laplace-transformed creep compliance. This is feasible since the Laplace-transformed stress fiber equation together with the appropriate boundary conditions can be solved analytically. The calculation finally yields an analytical expression for the complex modulus which could be easily used to fit experimental data. Starting point of the derivation is the continuum stress fiber model, Eq. (2.22), expressed in non-dimensional quantities $\tilde{x} = x/a$ and $\tilde{t} = t/\tau$

$$\partial_{\tilde{x}}^2 \dot{u}(\tilde{x}, \tilde{t}) + \partial_{\tilde{x}}^2 u(\tilde{x}, \tilde{t}) - \kappa u(\tilde{x}, \tilde{t}) - \Gamma \dot{u}(\tilde{x}, \tilde{t}) = 0 \tag{2.91}$$

In general, to determine the creep compliance, the viscoelastic body under consideration is exposed to a sudden force application. Measurement of the resulting deformation then determines the creep compliance. In terms of the one dimensional stress fiber model this means that the boundary conditions have to reflect the sudden application of an external force. Solution for $u(L, t)$ then provides the creep compliance. To illustrate the appropriate boundary conditions assume the following mind experiment: Prior to cutting an external mechanical manipulator, like a magnetic bead or a cantilever, is tightly glued to the stress fiber at position $x = L$. Then at $t = 0$ the stress fiber is cut right next to the external manipulator. To hold the fiber fragment in its initial position the external pulling force has to balance the contractile inward directed motor forces. However, to deform the fiber, the externally applied force, f_{ext}, has to exceed the stall force of the motors by a certain amount, $f_{ext} = F_s + f_0$. The suddenly applied and unbalanced part of the external force f_0 will cause the stress fiber to elongate

according to $u(L, t) = f_0 J(t)$, where $J(t)$ is the creep compliance of the stress fiber. The boundary conditions at the perturbed end are given by the force balance of the internal viscoelastic and contractile forces of the stress fiber and the externally applied forces.

$$\partial_{\tilde{x}}\dot{u}(\tilde{L}, \tilde{t}) + \partial_{\tilde{x}}u(\tilde{L}, \tilde{t}) - \delta_0 = 0 \tag{2.92}$$

Where the abbreviation $\delta_0 = (f_{ext} - F_s)/k_{int} = f_0/k_{int}$ has been introduced and $\tilde{L} = L/a$. The appropriate boundary condition at the left end is $u(0, \tilde{t}) = 0$ and the initial condition is given by $u(\tilde{x}, 0) = 0$. Obviously, the additional external force does not further complicate the boundary value problem discussed in the previous sections. Laplace transform of the equations leads to a second order differential equation (also see appendix 6.4) which can be solved for the Laplace-transformed displacement:

$$\bar{u}(\tilde{x}, \tilde{s}) = \delta_0 \frac{\operatorname{sech}\left(\tilde{L}\frac{\sqrt{\Gamma\tilde{s}+\kappa}}{\sqrt{1+\tilde{s}}}\right)\sinh\left(\tilde{x}\frac{\sqrt{\Gamma\tilde{s}+\kappa}}{\sqrt{1+\tilde{s}}}\right)}{\tilde{s}\sqrt{1+\tilde{s}}\sqrt{\Gamma\tilde{s}+\kappa}} \tag{2.93}$$

The solution for $\tilde{x} = \tilde{L}$ is of particular interest since comparison with $\bar{u}(\tilde{L}, \tilde{s}) = \delta_0 \bar{\mathcal{J}}(\tilde{s})$ yields the Laplace-transformed creep compliance, non-dimensionalized with the internal spring stiffness: $\bar{\mathcal{J}}(\tilde{s}) = \bar{J}(\tilde{s})k_{int}$. Overbars denote Laplace-transformed quantities. One finds:

$$\bar{\mathcal{J}}(\tilde{s}) = \frac{\tanh\left(\tilde{L}\frac{\sqrt{\Gamma\tilde{s}+\kappa}}{\sqrt{1+\tilde{s}}}\right)}{\tilde{s}\sqrt{1+\tilde{s}}\sqrt{\Gamma\tilde{s}+\kappa}} \tag{2.94}$$

The complex modulus directly follows from the Laplace-transformed creep compliance using Eq. (6.23) and Eq. (6.25):

$$\mathcal{G}^*(\tilde{\omega}) = \lim_{\gamma \to 0} \frac{1}{\tilde{s}\bar{J}(\tilde{s})} = \frac{\sqrt{1+i\tilde{\omega}}\sqrt{i\Gamma\tilde{\omega}+\kappa}}{\tanh\left(\tilde{L}\frac{\sqrt{i\Gamma\tilde{\omega}+\kappa}}{\sqrt{1+i\tilde{\omega}}}\right)} \tag{2.95}$$

Unfortunately, it is not feasible to decompose the found complex modulus in general into its real and imaginary parts, the storage modulus $\mathcal{G}'(\tilde{\omega})$ and the loss modulus $\mathcal{G}''(\tilde{\omega})$, respectively. However, this is possible for the special case when $\Gamma/\kappa = 1$. Then, the expression for the complex modulus largely simplifies to $\mathcal{G}^*(\tilde{\omega}) = (1 + i\tilde{\omega})\sqrt{\kappa}/\tanh(\tilde{L}\sqrt{\kappa})$. The storage modulus becomes a constant, and the loss modulus is linearly dependent on the frequency. These are the simple characteristics of a single Kelvin-Voigt body! The more the ratio Γ/κ differs from unity the larger are the deviations from these simple characteristics. To further discuss the frequency dependence for the general case $\kappa/\Gamma \neq 1$, consider the limits $\tilde{\omega} \to 0$ and $\tilde{\omega} \to \infty$. In both limits, the stress fiber model again exhibits the characteristics of a Kelvin Voigt body, that is a constant storage modulus and a loss modulus linearly dependent on the frequency. The explicit values for the limit $\tilde{\omega} \to 0$ are:

$$\begin{aligned}
\mathcal{G}_0' &= \sqrt{\kappa}\coth(\tilde{L}\sqrt{\kappa}) \\
\mathcal{G}_0''(\tilde{\omega}) &= \frac{1}{4\kappa}\operatorname{csch}^2(\tilde{L}\sqrt{\kappa})\left(2\tilde{L}\kappa(\kappa - \Gamma) + \sqrt{\kappa}(\kappa + \Gamma)\sinh(2\tilde{L}\sqrt{\kappa})\right)\tilde{\omega}
\end{aligned} \tag{2.96}$$

For small frequencies, the magnitude of the constant storage modulus only depends on κ. The slope of the loss modulus, however, depends on both κ and Γ. By estimating the lower bound $\sinh(x) \geq x$, it follows that the slope of the loss modulus at low frequencies is always positive, irrespective of the precise values for Γ and κ. Similar relations are found for the limit, $\tilde{\omega} \to \infty$:

$$
\begin{aligned}
\mathcal{G}'_\infty &= \frac{1}{4\Gamma} \operatorname{csch}^2(\tilde{L}\sqrt{\Gamma}) \left(2\tilde{L}\Gamma(\Gamma - \kappa) + \sqrt{\Gamma}(\Gamma + \kappa) \sinh(2\tilde{L}\sqrt{\Gamma}) \right) \\
\mathcal{G}''_\infty(\tilde{\omega}) &= \sqrt{\Gamma} \coth(\tilde{L}\sqrt{\Gamma})\tilde{\omega}
\end{aligned}
\tag{2.97}
$$

For high frequencies, the magnitude of the storage modulus is dependent on both Γ and κ but the slope of the loss modulus is fully determined by Γ. It is also here of course true that $\mathcal{G}'_\infty \geq 0$. Furthermore, it can be shown, that the saturation level of the storage modulus for high frequencies is always larger than the value for very low frequencies, $\mathcal{G}'_\infty/\mathcal{G}'_0 \geq 1$. Similarly, the slope of the loss modulus at very low frequencies is always larger than the slope at very high frequencies, $\mathcal{G}''_0/\mathcal{G}''_\infty \geq 1$. The differences $\mathcal{G}'_\infty - \mathcal{G}'_0$ and $\mathcal{G}''_0 - \mathcal{G}''_\infty$ become minimal and vanish if and only if $\Gamma = \kappa$. This special case where the stress fiber model exhibits the simple characteristics of a Kelvin-Voigt body has been discussed beforehand, see section 2.1.3 and 2.3. The frequency dependence of the storage modulus and the loss modulus are illustrated in Fig. 2.9. The scaling behavior at low and high frequencies are shown as well. Parameter values are given in the figure caption.

2.7   Summary and discussion

In this chapter we developed a viscoelastic model for stress fibers in a discrete and a continuum description. Subsequently, we solved both versions analytically for the displacement field along the fiber. Thereby, we imposed boundary conditions that are appropriate to describe stress fiber dissection experiments. Explicit formulas have been given for the time course of the viscoelastic stress within the fiber as well as an analytical solution for the complex modulus of our stress fiber model. Furthermore, we demonstrated that, within a certain parameter range, this viscoelastic model without inertia exhibit damped oscillations of inner fiber segments. The results derived within this chapter are the basis for the mechanical part of our mechano-chemically coupled model.

By developing the stress fiber model we made strong modeling assumptions, for instance we assumed that the elastic properties of stress fibers are isotropic and the fiber mechanics can be described by linear elasticity theory. In addition, in a cellular system there always exist other processes which are of potential relevance. For example, it has been shown experimentally that the stress-strain relation of stress fibers, isolated from vascular smooth muscle cells, becomes nonlinear for large fiber elongations [89]. Moreover, on large length scales, stress fibers might not resist in equal measure to compressional as to tensile deformation. Lively discussed alternatives are cable-like characteristics with tensile but vanishing compressional resistance [101] which would

make the material intrinsically nonlinear. The proposed model is also static in the sense, that it does not account for (un-)binding of crosslinkers or (de-)polymerization of actin filaments within the stress fiber. Interestingly, these processes can also be expected to depend on the local mechanical stress within the fibers. Stress dependent polymerization kinetics of actin filaments in stress fibers haven already been considered theoretically [102]. We also neglect the exact three-dimensional geometry of the fibers.

Despite the mentioned drawbacks and limitations, the model is capable to capture the main physical characteristics of contracting stress fibers after laser release indicating that most of the modeling assumptions are fulfilled on the time and length scale of the measurement. For example, as the retraction occurs within a few second, polymerization of the actin filaments might not be a major issue. Furthermore, as stress fibers are much longer than their actual thickness, the precise geometry might play a minor role and the one-dimensional approximation might be well justified. The excellent agreement between the model and experimental data encouraged us to use the model to quantify stress fiber cutting experiments by Colombelli et al. [34]. The results of this cooperation are reported in the next chapter.

One theoretical prediction of our model worth mentioning is the frequency dependence of the complex modulus, derived analytically in section 2.6. To our knowledge, the complex modulus of a single stress fiber has not been measured yet in a living cell but there exist data on isotropic actin networks. The complex modulus of the cytoskeleton as a function of frequency has been measured over several orders of magnitudes using magnetic tweezers [99, 100] applied on human airway smooth muscle cells. Up to a frequency of about $10\,\text{Hz}$, the storage as well as the loss modulus obey a weak power law $\sim \omega^z$, with nearly the same exponent $z = 0.2$. While the storage modulus keeps the power law dependence for higher frequencies, the loss modulus deviates from these simple characteristics and approaches, but never quite attains, a power law exponent of $z = 1$. The loss modulus also crosses the curve of the storage modulus from below at very high frequencies. The latter value $z = 1$ for the loss modulus would be the characteristics of a Newtonian viscosity. This frequency dependence of the storage and loss modulus is very well described by the soft glassy rheology model [100, 103].

Our model predicts a different scaling behavior for stress fibers. For very low and high frequencies, the model exhibits the simple characteristics of a Kelvin-Voigt body, that is, a constant storage modulus, $z = 0$, and a loss modulus that is linear dependent on the frequency, $z = 1$. At intermediate frequencies, there is a cross over region between the two different Kelvin-Voigt bodies, see Fig. 2.9. In this region, the loss modulus is expected to cross the storage modulus from below and approaches a power law with $z = 1$. It is also this cross over region, $\tilde{\omega} < 10^2$, where we could expect good agreement between our model and future measurements of the complex modulus[§]. That such experiments on single stress fibers in living cells are in principle feasible, has been demonstrated by Colombelli et al. [34]. In this study an AFM tip has been used to pull cyclicly on a single stress fiber in order to measure the mechanosensitive response

---

[§]The stress fiber laser release experiments, which are well described by our model, have been performed with a time resolution of $f \sim 1\,\text{Hz}$. This yield a rough estimate for an upper bound of the non-dimensional frequency $\tilde{\omega} < 2\pi f \tau \sim 10^2$. At least up to this frequency, our model should give valuable predictions for the complex modulus of a single stress fiber.

of zyxin. However, in this setup, the direction of the pulling force was along the axis of the AFM cantilever and thus the exerted force could not be measured. By approaching the AFM cantilever from a different angle, simultaneous force measurements could be realized in the future. A more sophisticated solution would be to use zyxin as a reporter of mechanical stress within the fiber, as soon as its mechanosensitive response is understood in more detail.

Chapter 3

Quantification of stress fiber contraction dynamics

In the previous sections we have developed a linear viscoelastic model for stress fibers. In the continuum limit, the stress fiber is described by a linear partial differential equation. The imposed boundary conditions for which we derived an analytical solution correspond to the situation that the contractile fiber is released at time zero at one end, whereas the other end of the fiber is hold steady at its initial position. These theoretical considerations now prepare the ground for the quantitative analysis of experimental data obtained from stress fiber contraction dynamics after pulsed UV laser cutting. In the experiment performed by Colombelli et al. [34] stress fibers are dissected by a pulsed UV laser at varying distances from focal adhesions where the stress fibers are anchored to the glass substrate. The fiber fragment which has been cut apart starts to contract because of acto-myosin tension within the fiber. The time-dependent displacement of the fiber that is pointed towards the focal adhesion is recorded by time-laps fluorescence microscopy. An essential advantage to former studies is that the experimental setup by Colombelli et al. allows to spatially resolve the displacement field along the fibers. This is in contrast to previous studies [63] that only recorded the total contraction length of the fiber in time and thereby could not resolve essential features of the retraction dynamics.

The spatial resolution along the fiber is achieved in two different ways yielding two independent data sets that are analyzed separately. One approach takes advantage of the natural striation pattern of stress fibers. The regular pattern emerge from the sequential arrangement of myosin rich and α-actinin rich regions along stress fibers [104]. In order to visualize this sarcomeric structure, mammalian epithelial Ptk-2 cells are transfected to express the crosslinker α-actinin with a fluorescent label, the green fluorescent protein (GFP). In this way the well separated α-actinin rich regions can be tracked as bright spots under the fluorescence microscope while the fiber contracts. The obtained spatial resolution is given by the period of the sarcomeric pattern which was found to be $1.01 \pm 0.14\,\mu$m for the studied Ptk-2 cells [34]. It is important to note that this spacing of about one micron is close to the spatial resolution of the fluorescence microscope of a few hundred nanometers. While the fibers contract it becomes more and more challenging to resolve neighboring α-actinin bands that move
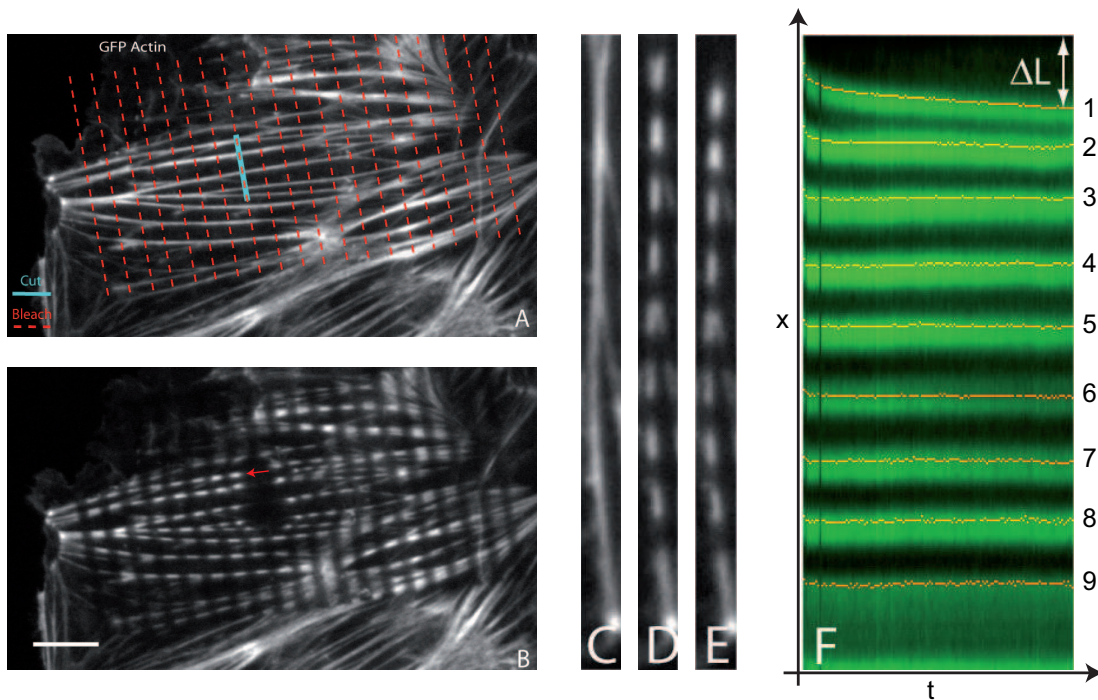
Figure 3.1: Stress fiber contraction dynamics after laser nanosurgery illustrated for a Ptk-2 cell transfected to express G-actin-EGFP. (A) Fluorescence microscopy picture of the actin cytoskeleton before cut. Stress fibers appear as rather homogeneous bright bundles. Dashed red lines indicate the bleaching pattern which is printed on the cytoskeleton prior to cut. The stripes that are aligned perpendicular to the fiber axis have a periodic spacing of $3\,\mu$m. Position of the cut is highlighted by the blue line. (B) Re-equilibrated actin cytoskeleton $120\,$s after laser surgery. Red arrow indicates the fiber which has been picked for further analysis. Scale bar denotes $5\,\mu$m. (C) Stress fiber before laser bleaching. (D) Bleached fiber shortly after cut. (E) Contracted stress fiber $120\,$s after cut. (F) Time-space kymograph reconstructed from fluorescence intensity profiles along the stress fiber. Time dependent positions of the bright spots in (D) and (E) are given as green curves in (F). The numbering of bands is illustrated on the right hand side of the figure. Red lines show the result from the edge detection later on used to fit the model, shown in Fig. 3.2. $\triangle L$ is the total contraction of the fiber after equilibration. Courtesy of Julien Colombelli.

closer to each other. Especially the application of an automatized image processing algorithm to reliably extract the position of the bands becomes increasingly difficult.

To circumvent these disadvantages an alternative technique has been developed to extract the spatial information. In the second approach cells are transfected to express the fluorescently labeled G-actin-EGFP. Accordingly, the stress fibers rather appear as homogeneously fluorescent bundles. In order to extract spatial information during the contraction phase, an artificial striation pattern is printed on the actin cytoskeleton by means of laser photobleaching. An optimal trade-off between spatial resolution and automatized processability of the achieved data was found to be a $3\,\mu$m periodic pattern printed perpendicular to the axis of the selected stress fibers before dissection.

Since in the first case α-actinin transfected cells and in the second case actin transfected cells are studied, the two experiments give independent data sets. The comparison of the two different results will give interesting insights into stress fiber mechanics. In the first half of the quantitative data analysis presented below we focus on the pure contraction dynamics of the fibers and thereby extract the distributions for the parameter values of the suggested viscoelastic stress fiber model.

In the second half, we use our model to calculate the stress distribution within the cytoskeleton and the forces that are exerted on focal adhesions that are not accessible experimentally. We then perform a case-study on the dynamics of zyxin, a protein which is localized in focal adhesions [105] as well as in stress fibers [106]. We find strong correlations between the computed forces and the translocation dynamics of zyxin. Especially the fast aggregation of zyxin at sites of increased mechanical stress suggests that a zyxin binding partner is permanently embedded into the intracellular mechanical scaffolds and that this protein changes its binding affinity to zyxin in response to mechanical stress. One likely candidate to fulfill this mechanosensitive function is α-actinin. It is the major crosslinker within stress fibers, and is furthermore an important component in the linkage between stress fibers and focal adhesions.

3.1   Data analysis yields model parameters

Stress fiber nanosurgery was performed on mammalian epithelial Ptk-2 cells either transfected to express α-actinin-EGFP or G-actin-EGFP. In the latter case, stress fibers have been patterned by means of laser photobleaching prior to cut. The distortion of the either natural or artificial striation pattern after laser surgery was recorded by time-laps fluorescence microscopy. From the time-sequence of pictures for each stress fiber a time-space kymograph of the retracting fluorescent bands was reconstructed.

This analysis revealed two remarkable features of stress fiber contraction dynamics. It turned out that stress fibers contract most in the close vicinity to the laser cut whereas sarcomeric units that are far away from the cut (more than $10\,\mu$m) are rather unaffected by the mechanical perturbations. Simultaneously, the re-equilibration of the distant subunits were found to be much faster than the ones close to the cut, compare e.g. Fig. 3.2.

In the next step an automatized edge detection was applied to the kymographs in order to retrieve the time dependent positions of the fluorescent bands. This data yields the displacement field $u(x,t)$ along the stress fiber. The stress fiber model with its solution given by Eq. (2.57) was fitted to the data to determine the free model parameters $(\kappa, \delta, \tau, \tau_\epsilon)$ defined in Eq. (2.20). In general, the model reproduces very well the non-uniform contraction along the whole fiber and over the whole observation time. Fig. 3.2 and Fig. 3.3 show a comparison between the measured kymographs and the fitted model curves for a stress fiber dissected in an actin and an α-actinin transfected cell, respectively. For the same data sets, the corresponding displacements of the numbered bands as well as the time courses for the normalized subunit widths are included in the figures. Here, normalized subunit width means the time dependent distance between two neighboring fluorescent bands normalized by their initial spacing before
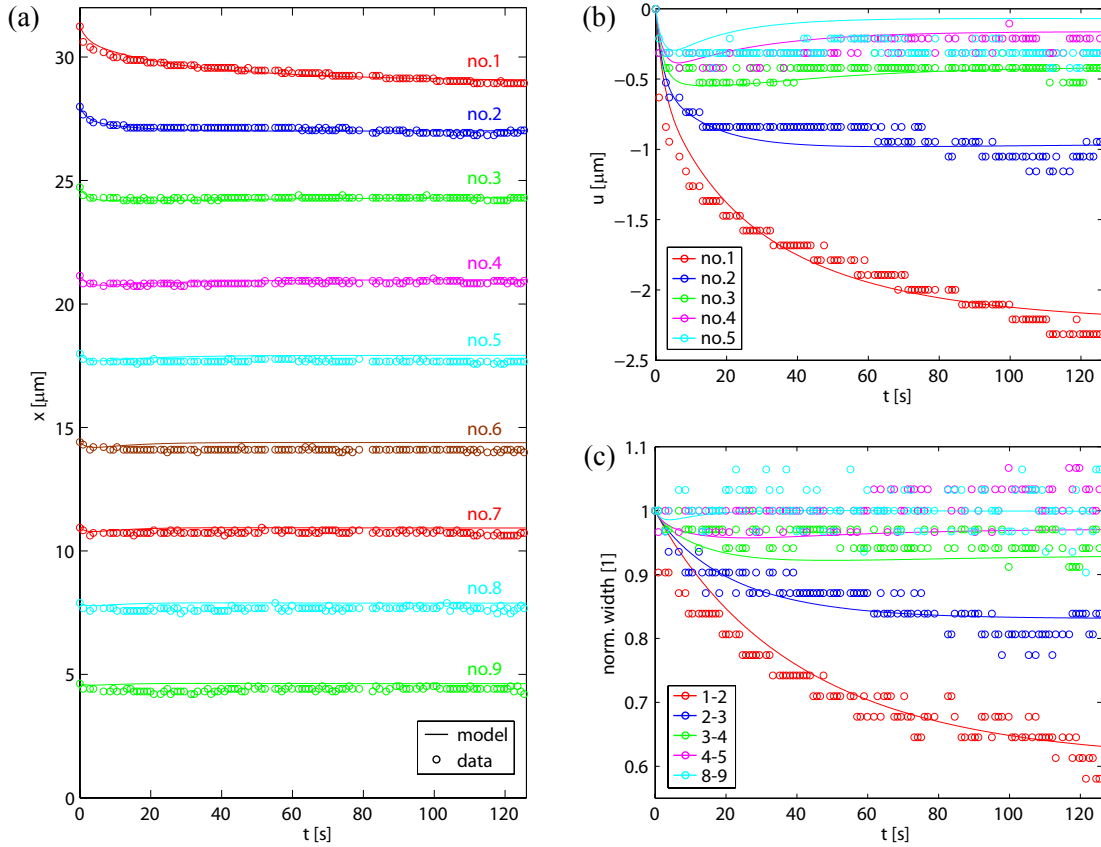
Figure 3.2: Model fit to stress fiber contraction data for the actin transfected cell previously shown in Fig. 3.1. (a) Time-space kymograph of retracting fiber, circles denote experimental data. Counting of traced bands starts at the laser cut. Band numbers are color-coded. Solid lines denote corresponding model curves. Spatial resolution of the displacement field is dictated by the period of the bleaching pattern of $3\,\mu$m. (b) Time dependent displacement of the first five bands. Bands farther away from cut remain rather unaffected, compare (a). (c) Time course of normalized subunit width, that is the distance between neighboring bands (the subunit length) normalized by their initial spacing. This quantity measures the percentile of contraction along the fiber. For example, the first subunit contracts down to about 60% of its initial length within the first 120 s. Subunits closest to cut contract most and equilibrate substantially slower than subunits far away from cut. For the fitting, only the time course data of bands 1 to 4 have been considered. Obtained fit values for the model parameters are $(\kappa, \delta, \tau, \tau_\epsilon) = (0.067, 0.58\,\mu\text{m}, 52\,\text{s}, 0.0\,\text{s})$.
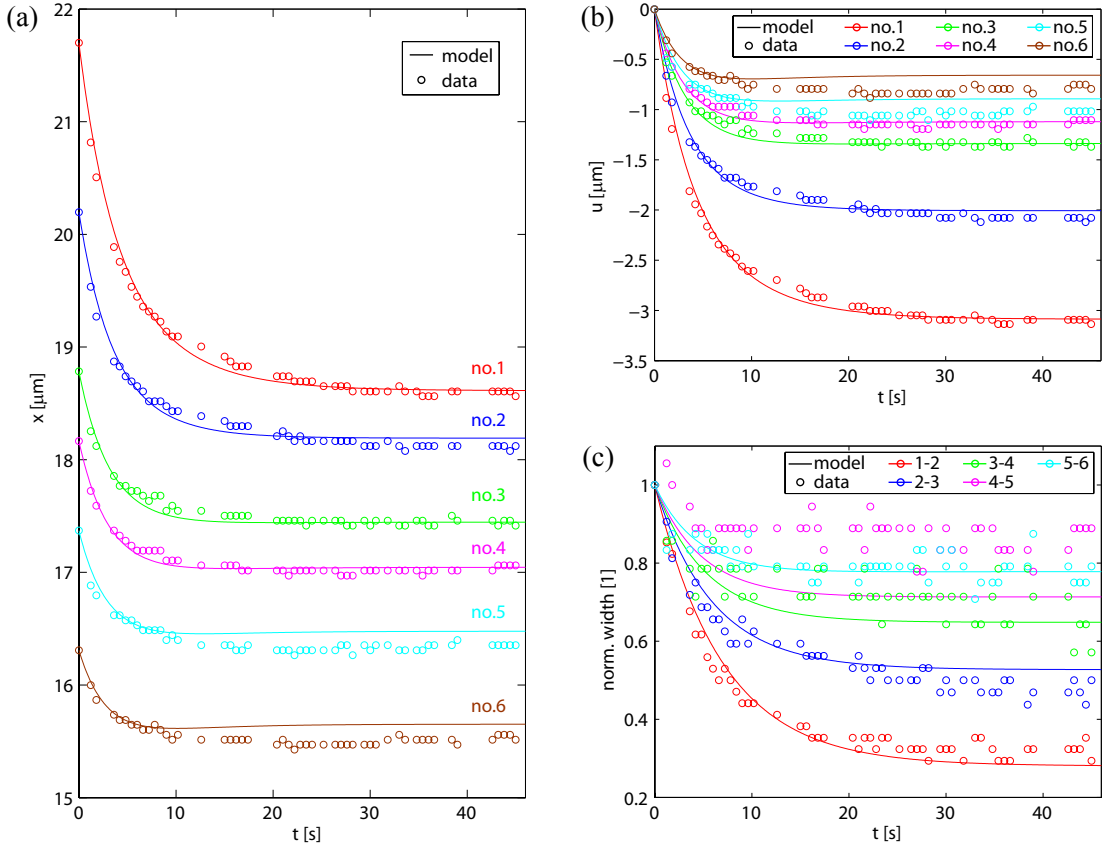
Figure 3.3: Same analysis for stress fiber contraction dynamics as in Fig. 3.2 but now for an α-actinin transfected cell. (a) Time-space kymograph of retracting fiber. The spatial resolution of the displacement field is about $1\,\mu$m and thus three times higher than for actin transfected cells. (b) Time course of bands displacement. (c) Time course of normalized subunit width. For the fitting, only the time course data of bands 1 to 4 have been considered. Obtained fit values for the model parameters are $(\kappa, \delta, \tau, \tau_\epsilon) = (0.082, 0.89\,\mu\text{m}, 7.5\,\text{s}, 0.21\,\text{s})$.

cut $\frac{u_n(t)-u_{n-1}(t)}{u_n(0)-u_{n-1}(0)}$. The initial spacing is $3\,\mu$m in case of the actin data and roughly $1\,\mu$m for the intrinsic pattern visualized in α-actinin transfected cells, compare Fig. 3.2(a) and Fig. 3.3(a). The plotted normalized subunit width also gives an approximation for the local strain within the fiber. However, the approximation is quite rough for actin transfected cells since the discretized gradient is an average over $3\,\mu$m. For the α-actinin data the spatial resolution is about $1\,\mu$m which is considerably lower than the typical length scale of about $3.6\,\mu$m over which the mechanical perturbation decays, see below. In the latter case the discrete approximation is acceptable.

In the following quantitative analysis of the stress fiber contraction dynamics we only considered the first three bands of the kymograph. In this way fitting was restricted to a region within the first $10\,\mu$m of the stress fiber where most of the contraction happens. Bands that are farther away from cut are rather stationary and do not provide distinct information, see e.g. Fig. 3.2. As fit routine we used the function "lsqnonlin" of the Matlab optimization-toolbox (version 1.0.4), which is a specialized

algorithm to solve nonlinear least-squares data-fitting problems. To check for local minima, we started the global optimization algorithm ten times with random initial sets of positive parameter values $(\kappa, \delta, \tau, \tau_\epsilon)$. For virtually all stress fibers and all runs the algorithm converged to the same fiber specific least-squares minimum defining one set of parameter values $(\kappa, \delta, \tau, \tau_\epsilon)$.

In total we analyzed 86 stress fibers from actin transfected cells and 34 stress fibers from α-actinin transfected cells. From fits to these data sets, we were able to deduce the distributions of the four parameters for the two differently transfected cell types separately. The distributions of parameters are visualized in terms of boxplots, see Fig. 3.4. In addition, we performed an extensive statistical analysis of the parameter distributions and compared the results found for the differently transfected cells. Mean values and standard deviations are summarized in Tab. 3.1. We also give the median and the interquartile range as well as the median absolute deviation about the median (MAD) which are more robust measures for distributions with outliers as it is the case for κ, τ and τ_ϵ. The MAD, a robust measure of scale, is defined as MAD = 1.4826 median$\{|x_i - \text{median}\{x_j\}|\}$. The prefactor is chosen such that the MAD is comparable with the standard deviation [107]. For the sake of clarity, however in the text, we only present mean values and standard deviations for the model parameters.

For actin transfected cells we find an average stiffness ratio $\kappa = 0.035 \pm 0.034$. The average contraction length of a sarcomeric unit, of initial length $a = 1\,\mu$m, is about $\delta = (0.66 \pm 0.36)\,\mu$m. This means that a freely contracting uncrosslinked sarcomeric unit would contract on average down to 340 nm. Interestingly, this obtained value comes very close to the length of myosin minifilaments measured to be $(393 \pm 33)\,$nm for smooth muscle cells [32] which gives a natural lower bound for this minimal length of a totally contracted sarcomeric unit. The typical timescale for contraction is dictated by $\tau = (29 \pm 27)\,$s. It is associated to the effective internal friction forces to which, for example, relative filament sliding as well as the molecular motors contribute, see Eq. (2.20) for its definition. The timescale τ is considerably larger than the second timescale $\tau_\epsilon = (0.13 \pm 0.23)\,$s in the system. The latter is associated to external friction resulting from viscous drag within the surrounding cytosol. The found parameter values suggest that this model term can be regarded as a higher order correction, further elucidated in the following.

The stress fiber model equation, written in non-dimensional from, is given by $\partial_{\tilde{x}}^2 \dot{u} + \partial_{\tilde{x}}^2 u - \Gamma \dot{u} - \kappa u = 0$, compare Eq. (2.22). The last two terms, which originate from viscoelastic interactions with the surrounding, bear the non-dimensional coefficients κ and $\Gamma = \tau_\epsilon/\tau$, both are smaller than unity. Values for Γ, derived from the distributions for τ and τ_ϵ are also given in Tab. 3.1. Since the resulting distribution for Γ is strongly skewed, that is, it has large positive outliers which distort the mean, we only give the median and the MAD for this quantity. While the parameter κ is roughly of order $\mathcal{O}(10^{-1})$ the parameter Γ is of order $\mathcal{O}(10^{-3})$, two orders of magnitude smaller than κ. For the sake of completeness, the values for the median and the MAD of the ratio Γ/κ are also itemized in Tab. 3.1. The median is as expected of order $\mathcal{O}(10^{-2})$ indicating that the model term, which is proportional to $\dot{u}$, plays a minor role and can be regarded as a higher order correction term. In general, we find that a model which neglects this term and thus has only the three parameters (κ, δ, τ) yield similar good fit results.
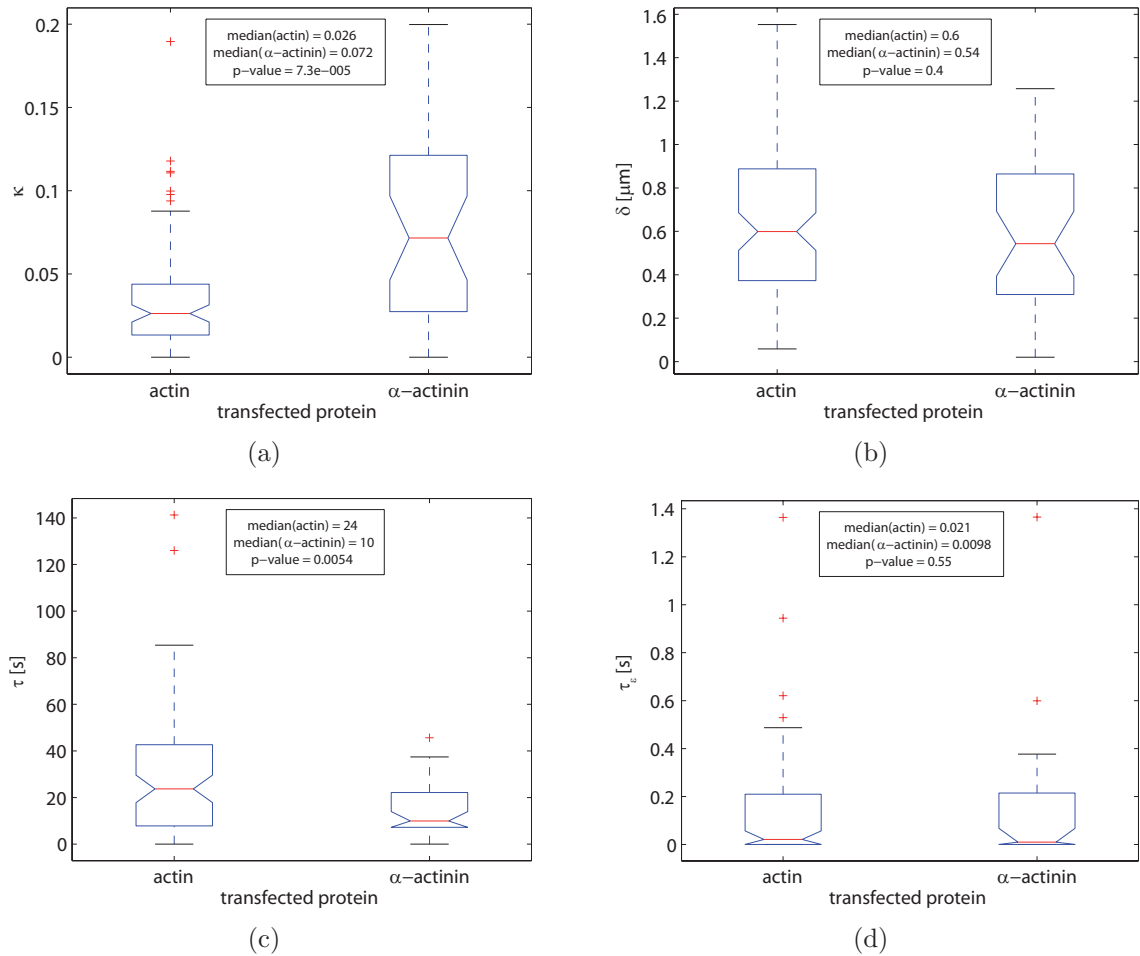
Figure 3.4: Comparison of model parameter distributions for differently transfected cells using boxplots. In total we analyzed 86 stress fibers from actin transfected cells and 34 stress fibers from α-actinin transfected cells. Each stress fiber yields one set of parameters (κ, δ, τ, τ_ϵ). The red center line of the boxes gives the median of the distribution, the lower hinge denotes the first quartile, the upper hinge denotes the third quartile. The notches around the median denote a 95% confidence interval for the median. The whiskers extend from the box out to the most extreme data value within 1.5 times the interquartile range. Outliers that do not fall into this range are highlighted with red crosses. By applying a Wilcoxon rank sum test or so called Mann-Whitney U-test we find that the crosslink parameter κ is significantly higher ($p = 0.000073$) and the time scale τ is significantly lower ($p = 0.0054$) for stress fibers observed in α-actinin transfected cells compared to actin transfected cells. The remaining parameters seem to be independent of the transfected protein. The distributions for the parameter τ_ϵ are strongly antisymmetric with a maximum close to zero and a long tail reaching out for large positive values.

parameter		actin mean $\pm$ std	α-actinin mean $\pm$ std	p-value (t-test)	
κ	[1]	0.035 ± 0.034	0.078 ± 0.059	0.0000014	yes
δ	[μm]	0.66 ± 0.36	0.59 ± 0.33	0.35	no
τ	[s]	29 ± 27	15 ± 11	0.0029	yes
τ_ϵ	[s]	0.13 ± 0.23	0.15 ± 0.27	0.72	no
		($q_{25\%}$, median, $q_{75\%}$)	($q_{25\%}$, median, $q_{75\%}$)	p-value (U-test)	
κ	[1]	$(0.013, 0.026, 0.044)$	$(0.027, 0.072, 0.12)$	0.000073	yes
δ	[μm]	$(0.37, 0.60, 0.89)$	$(0.31, 0.54, 0.86)$	0.40	no
τ	[s]	$(7.8, 24, 43)$	$(7.2, 10, 22)$	0.0054	yes
τ_ϵ	[s]	$(0.0, 0.021, 0.21)$	$(0.0, 0.01, 0.21)$	0.55	no
		median$\pm$MAD	median$\pm$MAD	p-value (U-test)	
κ	[1]	0.026 ± 0.023	0.072 ± 0.068	0.000073	yes
δ	[μm]	0.60 ± 0.36	0.54 ± 0.40	0.40	no
τ	[s]	24 ± 24	10 ± 8.7	0.0054	yes
τ_ϵ	[s]	0.021 ± 0.032	0.010 ± 0.015	0.55	no
Γ	[10^{-3}]	1.2 ± 1.7	0.42 ± 0.62	0.53	no
Γ/κ	[1]	0.037 ± 0.055	0.012 ± 0.018	0.71	no

Table 3.1: Model parameter values obtained from fits to the data (86 fibers of actin transfected cells and 34 fibers from α-actinin transfected cells). We give mean and standard deviation in the first table, median and interquartile range in the second table as well as median and the median absolute deviation about the median (MAD = 1.4826 median$\{|x_i - \text{median}\{x_j\}|\}$) in the lowest table. For every model parameter we determine two separate distributions one for each transfected protein. To compare the two distributions for each model parameter we applied a t-test for differences in the means as well as a Wilcoxon rank sum test or so called Mann-Whitney U-test for differences in the medians. Both tests indicate that the crosslink parameter κ is significantly higher and the time scale τ is significantly lower for α-actinin transfected cells. The other two parameters δ and τ_ϵ are rather independent of the transfected protein. In the last table we also included median and MAD for the derived non-dimensional parameter $\Gamma = \tau_\epsilon/\tau$ and Γ/κ. Note that $\Gamma/\kappa \ll 1$. The Young's modulus of stress fibers measured by Deguchi et al. [89] and the values for $\tau, \kappa, \tau_\epsilon$ can be used to also give rough estimates for the extensional viscosity of the fiber, the shear modulus and shear viscosity of the surrounding medium, respectively. See discussion in section 2.1.2.

Obtained parameter values for stress fibers cut in α-actinin transfected cells, also summarized in Tab. 3.1, are of similar magnitude compared to actin-transfected cells. However, the mean values of the two parameters κ and τ differ significantly from the respective values obtained from actin-transfected cells.

In order to compare the parameter samples from the actin- and the α-actinin transfected cells we applied a t-test for differences in the means as well as a Wilcoxon rank sum test, or so called Mann-Whitney U-test, for differences in the medians. The U-test is more appropriate for the present case of non-parametric distributions. Both tests indicate that the crosslink parameter κ is significantly higher (U-test: p=0.000073; t-test: p=0.0000014) and the time scale τ is significantly lower (U-test: p=0.0054; t-test: p=0.0029) for the α-actinin transfected cells. The remaining parameters δ and τ_ϵ seem to be independent of the transfected protein.

The differences for differently transfected cells regarding the crosslink parameter κ are plausible. The transfection for α-actinin is definitely accompanied by an over-expression of α-actinin[*]. The α-actinin is known as crosslinker between actin filaments not only within stress fibers but also between adjacent actin filaments. It also plays an important role in the linkage between stress fibers and integrin mediated adhesion clusters. Thus, transfection with α-actinin presumably increases the mechanical links from stress fibers to their environment including the surrounding actin cytoskeleton as well as integrin mediated contacts to the substrate. This higher degree of crosslink is reflected by the significantly higher value of κ in α-actinin transfected cells compared to actin-transfected cells.

The difference in the time scale $\tau = \gamma_{int}/k_{int} + \delta/v_0$, however, lacks such a straight forward explanation. The contraction length of sarcomeric units δ is independent of the transfection (compare values in Tab. 3.1). The same can be assumed for the maximal velocity of the motors v_0. Therefore, in terms of our simple model, we conclude that the ratio of internal friction over stress fiber stiffness γ_{int}/k_{int} is reduced when α-actinin is over expressed. A change in the friction coefficient γ_{int} could come along with an over expression of α-actinin if the latter simultaneously replaces other crosslinker proteins within stress fibers with different binding and unbinding kinetics.

3.1.1 Correlations between model parameters

Studying the correlation between the two parameters τ and δ yield another opportunity to test modeling assumptions. According to their definition the two model parameters τ and δ are linear dependent:

$$\tau = \frac{\tilde{\gamma}_{int}}{k_{int}} = \frac{\gamma_{int}}{k_{int}} + \frac{\delta}{v_0} \tag{3.1}$$

The relationship originated from the fact that the effective internal friction coefficient, $\tilde{\gamma}_{int} = \gamma_{int} + \frac{F_s}{v_0}$ has contributions from motor activity, denoted by $\frac{F_s}{v_0}$. In this way the motor activity contributes to the equilibration time τ. The above linear relationship between τ and δ implies that these two parameters are correlated with a correlation coefficient $\rho(\tau, \delta) = 1$ according to the model. The correlation coefficient is defined as:

$$\rho(\tau, \delta) = \frac{\mathrm{Cov}(\tau, \delta)}{\sqrt{\mathrm{Cov}(\tau, \tau)\mathrm{Cov}(\delta, \delta)}} \tag{3.2}$$

where $\mathrm{Cov}(x, y) = \langle xy \rangle - \langle x \rangle \langle y \rangle$ denotes the covariance of x and y. Fig. 3.5(a) and Fig. 3.5(b) show a correlation plot of the parameters τ and δ for actin and α-actinin transfected cells, respectively. The deduced values for the correlation coefficient are $\rho(\tau, \delta) = 0.40$ for actin transfected cells and $\rho(\tau, \delta) = 0.60$ for α-actinin transfected cells. In order to get an estimate of the variance of the correlation coefficient we performed a bootstrap analysis of the data: From the given sample of (τ, δ), n=1000 random samples of the same length ($N = 86$ for actin and $N = 34$ for α-actinin

---

[*]The transfected fluorescently labeled α-actinin is available additionally to the basal expression of α-actinin.
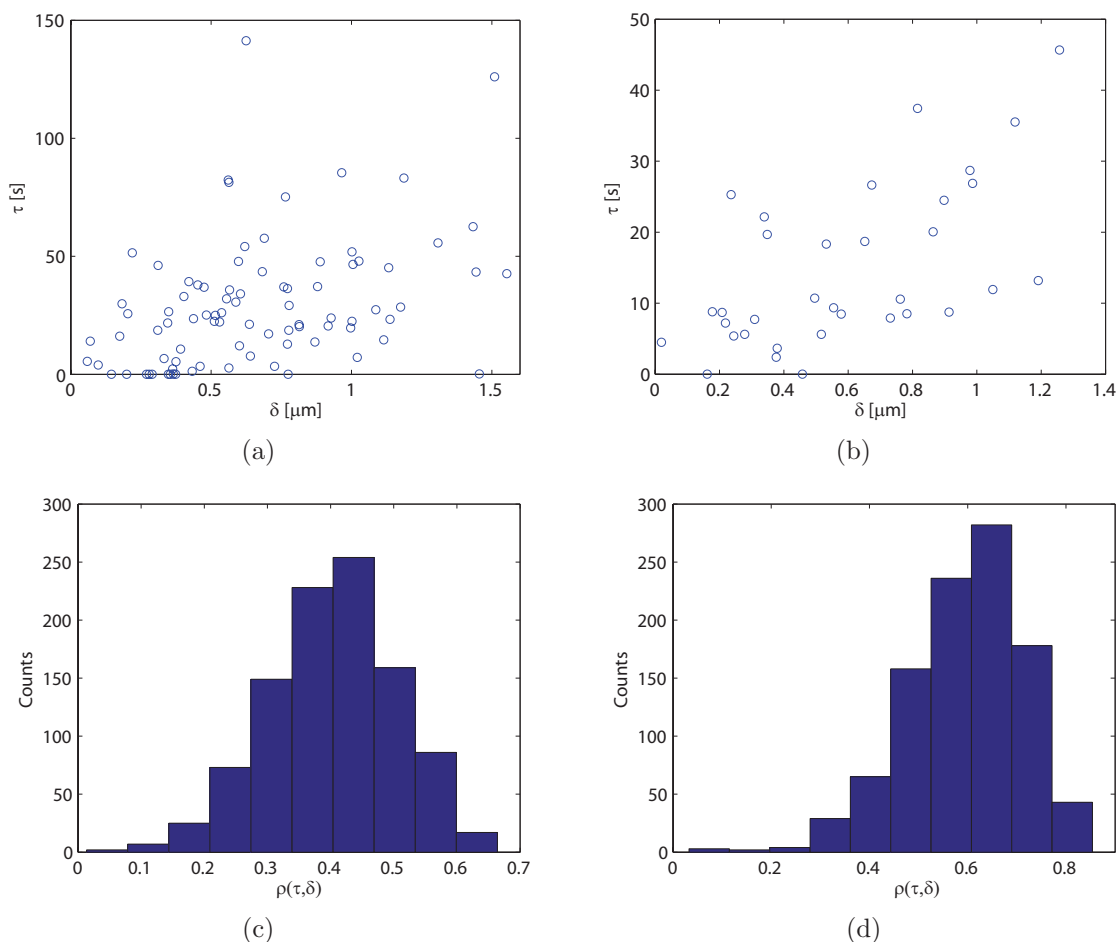
Figure 3.5: Correlation plot for the model parameters τ and δ for actin transfected cells (a) and for α-actinin transfected cells (b). Figure (c) shows a bootstrap analysis (1000 drawn samples) of the correlation coefficient $\rho(\tau, \delta)$ for actin-transfected cells which yields $\rho = 0.40 \pm 0.10$, (d) same analysis for α-actinin transfected cells which yields $\rho = 0.59 \pm 0.12$.

transfected cells) are drawn by allowing repetitions. The correlation coefficient is then calculated for each random sample and averaged over all samples. The average value for the correlation coefficient is $\rho(\tau, \delta) = 0.40 \pm 0.10$ for actin transfected cells and $\rho(\tau, \delta) = 0.59 \pm 0.12$ for α-actinin transfected cells. The results of the bootstrap analysis are illustrated in Fig. 3.5(c) and Fig. 3.5(d). To obtain a p-value for testing the hypothesis of no correlation ($\rho = 0$), the correlation coefficient is transformed to a quantity that is distributed as Student's t [107]:

$$t = \rho \sqrt{\frac{\nu}{1 - \rho^2}} \tag{3.3}$$

with $\nu = N - 2$ degrees of freedom, where N is the number of measurements. For actin transfected cells we find $p = 0.00014$ (with $\rho = 0.40$, $N = 86$) and for α-actinin transfected cells we find $p = 0.00024$ (with $\rho = 0.59$, $N = 34$). The small p-values

for both data sets ($p \ll 0.05$) support the hypothesis that the two parameters τ and δ are indeed correlated as expected from the model. However, due to the high variance in the data the 86 and 34 parameter pairs from the differently transfected cells, still do not provide a satisfactory statistical basis. Therefore, a clear statement can not be made by means of the currently available data. A convincing proof would require further measurements.

3.2 Total contraction length

Once cut and for times $t \gg \tau$ the stress fiber approaches a new mechanical equilibrium. To describe the stationary state, all time dependent model terms have to be neglected. The resulting model simplifies to a second order ordinary differential equation that is straight forward to solve. The solution for the stationary state displacement $u_{ss}(x)$ has been derived in the previous model chapter and is given below for convenience, compare Eq. (2.24):

$$u_{ss}(x) = -\frac{\delta}{\sqrt{\kappa}} \frac{\sinh(\sqrt{\kappa}x/a)}{\cosh(\sqrt{\kappa}L/a)} \tag{3.4}$$

In the following we briefly discuss the properties of the solution for the two extreme cases of a rather uncrosslinked fiber (small κ) and of a highly crosslinked fiber (large κ). In the case of a rather uncrosslinked fiber it holds that $a/\sqrt{\kappa} \gg L$ and the spatial dependence of the stationary displacement simplifies to $u_{ss}(x) \approx -\delta\,x/a$. Evidently, this linear dependence in x means that the contraction becomes uniform along an uncrosslinked stress fiber, each sarcomeric subunit contracts independently of all the other units down to the same final equilibrium length. The percentage of final contraction is simply given by δ/a. However, in the opposite case of a highly crosslinked fiber where $a/\sqrt{\kappa} \ll L$, the stationary solution Eq. (3.4) is well approximated by

$$u_{ss}(x) \approx -\frac{\delta}{\sqrt{\kappa}} e^{-(L-x)\sqrt{\kappa}/a} \tag{3.5}$$

According to the approximation given above, the mechanical perturbation of cutting a crosslinked stress fiber decays exponentially from the laser-released edge on a typical length scale given by $a/\sqrt{\kappa}$. As a consequence, if the fiber fragment length $L \gg a/\sqrt{\kappa}$, then the part of the fiber close to the focal adhesions remains unaffected by the nanosurgery, in particular the stress exerted by the stress fiber on the adhesion is rather unchanged, see discussion below. Assuming $\kappa = 0.035$ and $a = 1\,\mu$m we find that this typical length scale amounts to $a/\sqrt{\kappa} \approx 5.4\,\mu$m for stress fibers in actin transfected cells, and $a/\sqrt{\kappa} \approx 3.6\,\mu$m for stress fibers in α-actinin transfected cells. Eq. (3.4) also provides the total contraction length of the stress fiber after equilibration as a function of the initial fiber length L:

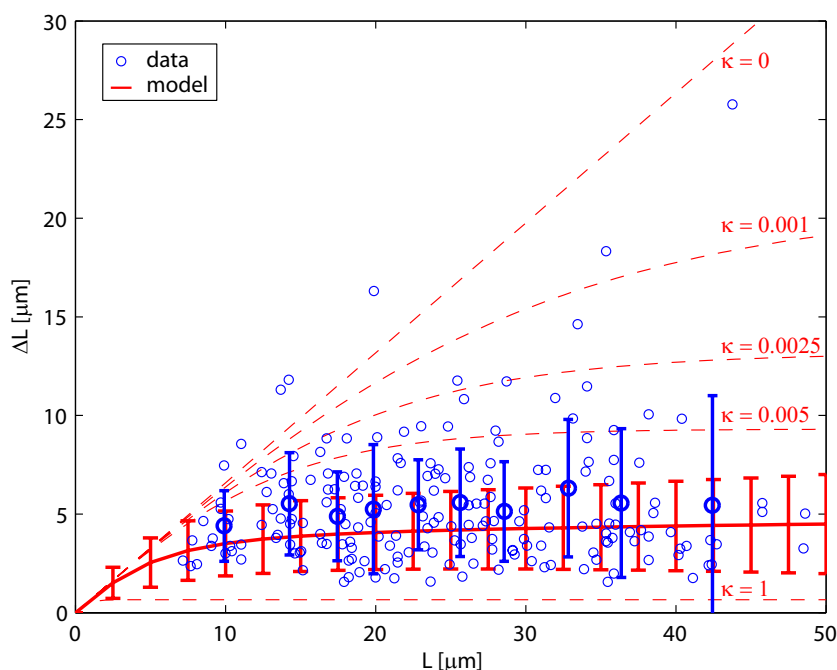$$\triangle L(L) = |u_{ss}(L)| = \frac{\delta}{\sqrt{\kappa}} \tanh(\sqrt{\kappa}L/a) \tag{3.6}$$

Figure 3.6: Total contraction length $\triangle L$ in dependence on initial fiber length L of the cut fragment. Small blue circles show 197 data points for stress fibers cut in actin-EGFP transfected Ptk-2 cells. Large bold circles with bars in blue show mean and standard deviation for the measured data. Each bin contains about 20 data points. Red solid line denotes mean model curve calculated from Eq. (3.6) averaged over 86 parameter pairs (κ, δ). Each parameter pair was obtained by fitting stress fibers dissected in actin-transfected Ptk-2 cells, also used for Tab. 3.1. Red bars show standard deviation to the model mean. Good agreement between experiment and model is found. Note that the total contraction length quickly saturates for large fibers with $L > 10 \, \mu$m which can be explained by stress fibers being crosslinked to their environment. For comparison, a few model curves (red dashed lines) with $\kappa \in \{1, 0.005, 0.0025, 0.001, 0\}$ are included. Here, we assumed $\delta = 0.66 \, \mu$m, the mean value taken from Tab. 3.1. The case $\kappa = 0$, which results in a linear relationship between $\triangle L$ and L, corresponds to a freely contracting stress fiber. The obtained mean model curve $\triangle L(L)$ would correspond to an average $\kappa \approx 0.034$.

Each parameter set $(\kappa, \delta, \tau, \tau_\epsilon)$ obtained from fits to kymographs provides one curve $\triangle L(L)$. Of course, for this steady state analysis, the parameters τ and τ_ϵ are irrelevant, and each curve is readily defined by the parameter pair (κ, δ), which can be seen explicitly in the above equation. In order to compare the model prediction with the measured data we averaged the 86 curves derived from the previously described actin sample. In Fig. 3.6 we show the sample average model curve $\langle \triangle L(L) \rangle_{actin}$ in red. Red bars denote standard deviation from the model mean. The model results are compared to the measured contraction length of 197 stress fibers observed in actin transfected Ptk-2 cells indicated as small blue circles in Fig. 3.6. In addition, large bold circles with bars in blue show mean and standard deviation for the measured data. A comparison yields that the model predictions agree very well with the measured

data. We find that $\triangle L$ first increases with L and then saturates for longer fibers with $L \gg a/\sqrt{\kappa} \approx 5.4\,\mu\text{m}$, as suggested by the model. The value of the saturation level is given by $\delta/\sqrt{\kappa}$, according to the model see Eq. (3.6). A saturation level of about $(4.5 \pm 2.5)\,\mu\text{m}$ deduced from the sample average model curve in Fig. 3.6 is also in good agreement with the experimental data. The fact that the total contraction of the fibers becomes independent of their length for large L can be attributed to their high degree of crosslink, in our model measured by the parameter κ. For comparison, we include the expected dependence of the total contraction length assuming a completely uncrosslinked stress fiber, $\triangle L(L) = \delta\,L/a$, deduced from Eq. (3.6) when $\kappa \to 0$, shown as red dashed line in Fig. 3.6. In this special case, the contraction length $\triangle L$ is expected to be proportional to the initial fiber length L which is clearly contradictory to the found saturation. As a reference we additionally include model curves for some intermediate values of κ, also shown as dashed red lines in Fig. 3.6.

The same analysis for the total contraction length has been performed for the α-actinin data, reported in [34]. Consistent with the results for the actin data, we find that also in α-actinin transfected cells the total contraction length of the fibers is rather independent of their initial length. The saturation value for the contraction length of about $(2.4\pm1.3)\,\mu\text{m}$ was found to be lower compared to stress fibers in actin transfected cells. This is consistent with the higher values for the crosslink parameter κ found for the α-actinin sample. Note that the other relevant parameter δ is rather independent of the transfected protein and thus does not contribute to the differences in the saturation levels.

3.3   Zyxin dynamics upon laser surgery

In the following the proposed stress fiber model will be used to calculate the induced changes of mechanical stress in the actin-cytoskeleton upon laser nanosurgery which are hard to measure experimentally. The intention is to correlate these changes in stress with changes in zyxin concentration easily measured by means of fluorescence microscopy. For this purpose, we used Ptk-2 cells and 3T3 fibroblasts transfected with zyxin EGFP and actin-cherry constructs. Fig. 3.7 shows typical stress fibers in a double transfected Ptk-2 cell that has been cut sequentially in different locations. First, we released a $14\,\mu\text{m}$ long centerpiece by two simultaneous laser cuts along the same bundle Fig. 3.7(a-b). After a $18\,\text{s}$ contraction phase, we performed a second cut that dissected the fragment in its middle as well as a neighboring control fiber, see Fig. 3.7(c-d). This experiment revealed three distinct translocation processes of zyxin:

1. Zyxin quickly dissociates from focal adhesions after the corresponding stress fiber has been cut. This can be seen by the naked eye comparing zyxin intensities at the very left adhesions in Fig. 3.7(k-l).

2. Zyxin also dissociates from stress fibers where it co-localizes with α-actinin and forms regular striation patterns, see Fig. 3.7(k). These zyxin striation patterns fade away after laser release, compare Fig. 3.7(k-l).
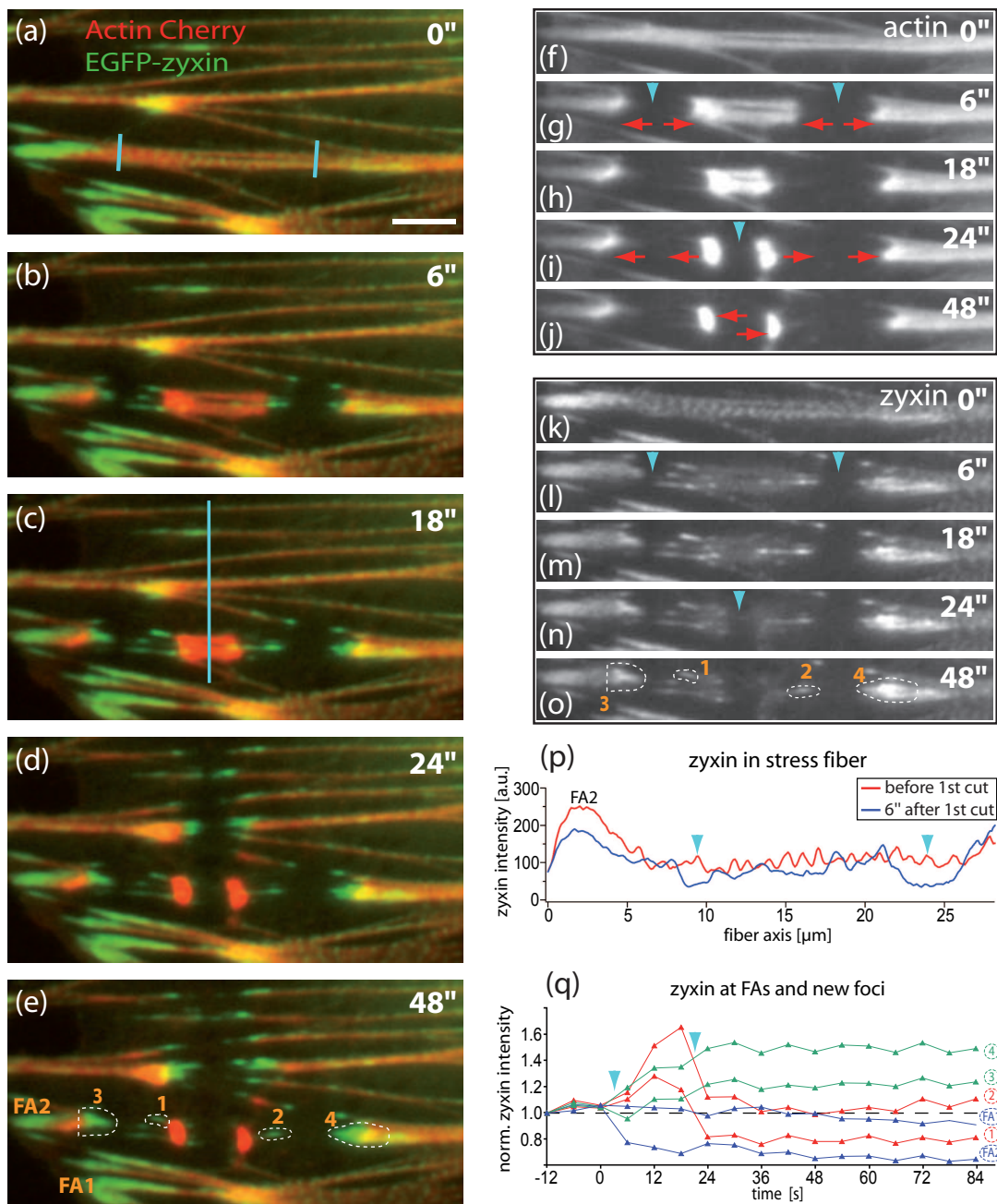
Figure 3.7: Analysis of zyxin dynamics in a Ptk-2 cell transiently transfected with zyxin-EGFP (shown in green) and actin-cherry (shown in red) constructs. (a-e) Snapshots of retracting fibers at 0 s, 6 s, 18 s, 24 s, and 48 s. Scale bar denotes 5 μm. (a) At first, two simultaneous laser pulses (indicated by blue lines) release a 14 μm centerpiece. (c) After 18 s of contraction, this central fragment is cut a second time in its middle together with a neighboring control fiber. (d)-(e) Show final equilibration. (f-j) And (k-o) show separate actin and zyxin channel, respectively. Blue arrows highlight position of cuts, red arrows indicate direction of fiber retraction. (p) Comparison of zyxin intensity along the stress fiber before and after initial cuts showing that the striation pattern is quickly lost. (q) Time course of zyxin intensity at focal adhesions FA1, FA2 and selected regions 1, 2, 3, 4 highlighted in (e) and (o). Results are discussed in the main text. Courtesy of Julien Colombelli.

3. In contrast to the previous two observations zyxin aggregates at distinct positions along the fiber fragments preferentially close to the position of the cut. These arising foci of high zyxin intensity are found to be stationary with respect to the substrate and do not retract with the stress fiber, follow encircled areas (1-4) highlighted in Fig. 3.7(o).

All of these observations can be explained consistently by assuming that zyxin is recruited by a mechanical scaffold protein (e.g. like α-actinin) in a force dependent manner. The dissociation of zyxin from focal adhesions and stress fibers are then related to a loss of exerted stress at focal adhesions and to a loss of mechanical tension in the fibers upon laser release. The emergence of new foci of high zyxin intensity could be explained by crosslinks that get increasingly tensed by the retracting fiber and then recruit zyxin. The three observations listed above that exemplify the mechanosensitivity of zyxin are further investigated in the following.

3.3.1 Zyxin dynamics at focal adhesions

Focal adhesions connected to a cut stress fiber experienced a quick loss of zyxin intensity. This can be deduced from Fig. 3.7(q) showing the time course of the normalized zyxin intensity at certain spots defined in Fig. 3.7(e,o). Zyxin intensity at focal adhesion (FA2) connected to the cut fiber sharply drops after the first laser cut indicated by the left blue arrow in Fig. 3.7(q). In contrast, zyxin intensity at the control focal adhesion (FA1), which is not connected to the cut fiber, remains unaffected. We further quantified this zyxin intensity loss in dependence on the distance, L, between cut and associated focal adhesion. In total, we analyzed 71 fibers in Ptk-2 cells and 88 fibers in 3T3 fibroblasts, shown in Fig. 3.8 as small blue circles and triangles, respectively. Data points represent the zyxin intensity loss normalized by the initial intensity, I_0, at the focal adhesion before cut:

$$\triangle I = \frac{I_0 - I_{ss}}{I_0} \tag{3.7}$$

In the equation above I_{ss} denotes the zyxin intensity at focal adhesion in the stationary state approached after cut and $\triangle I$ is the resulting normalized intensity loss. For both cell lines we found that zyxin loss is about 40% when the fibers are dissected close to the adhesions but losses turn out to be smaller if the cut is placed farther away from the adhesion. For instance, loss was found to be below 10% for very large fiber fragments, compare Fig. 3.8 for $L > 30\,\mu$m. To test whether this intensity loss is related to a loss of stresses exerted on the focal adhesions, we used our model to calculate the expected normalized force loss at focal adhesions in dependence on the fiber fragment length L. The normalized force loss $\triangle F$ is defined analogous to the intensity loss as:

$$\triangle F = \frac{F_0 - F_{ss}}{F_0} \tag{3.8}$$

where F_0 is the initial force exerted by the stress fiber on the adhesion prior to cut and F_{ss} denotes the force exerted in the new mechanical equilibrium after cut. We assume that the stress fiber is in mechanical equilibrium before the cut, that is, all
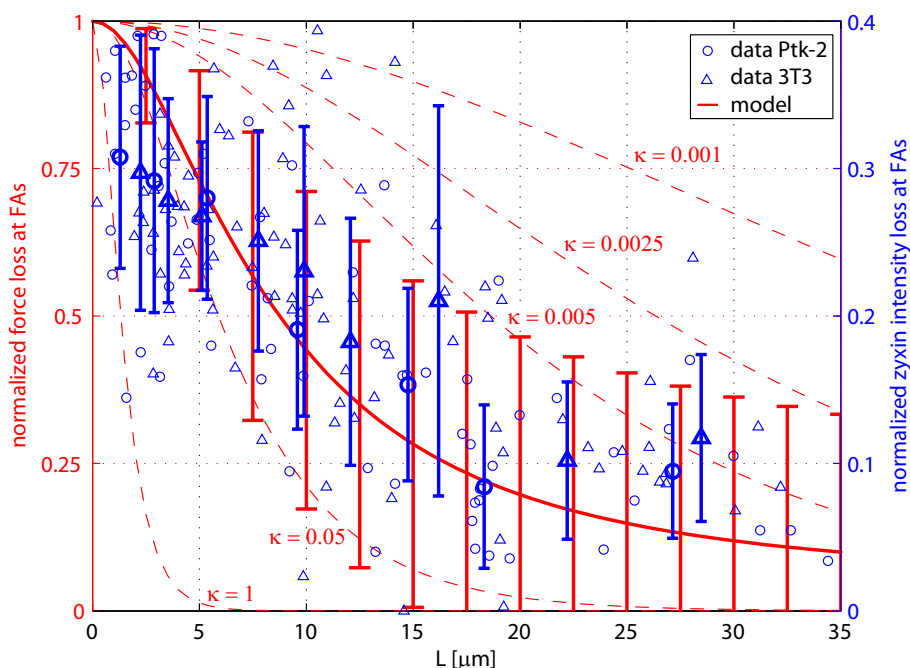
Figure 3.8: Normalized force loss at focal adhesions (red) compared to normalized zyxin intensity loss at focal adhesions (blue). Both quantities are plotted as function of the initial fiber length L. Zyxin loss at focal adhesions was measured for 71 fibers in Ptk-2 cells transfected with zyxin-EGFP and actin-cherry constructs shown as small blue circles and for 88 dissected fibers in 3T3 fibroblasts, transfected with the same constructs, shown as small blue triangles. Same but large blue symbols with bars indicate mean and standard deviation for bins of about 10 points of the respective data. Most zyxin dissociates from focal adhesion if the cut is placed close to the adhesion (L is small). Normalized force loss at focal adhesions has been calculated from Eq. (3.10) for the 86 values of κ, also used for Tab. 3.1. Averaged curve is shown as red solid line, red bars denote standard deviation to the model mean. For comparison, a few model curves (red dashed lines) with $\kappa \in \{1, 0.05, 0.005, 0.0025, 0.001\}$ are included. This analysis suggests that zyxin intensity in focal adhesions is correlated to the applied mechanical stresses.

motors operate at their stall force such that $F_0 \equiv F_s$. The force exerted by the fiber on the focal adhesion in the stationary state after cut has contributions from the elastic stress within the fiber as well as contributions from the molecular motors. The viscous forces, of course, vanish in the stationary state. Thus, F_{ss} is given by, also compare Eq. (2.68):

$$F_{ss} = ak_{int}\partial_x u_{ss}(0) + F_s \tag{3.9}$$

The first term is the elastic stress within the fiber evaluated at the focal adhesion and the second term accounts for the contractile forces of the molecular motors that are stalled in the stationary state. The stationary solution for the displacements u_{ss} is given by Eq. (3.4). Eventually, the normalized force loss at the focal adhesion is found to be:

$$\triangle F(L) = \text{sech}(\sqrt{\kappa}L/a) \tag{3.10}$$

The normalized force loss at the focal adhesion depends only on the crosslink parameter κ and the initial length of the fiber fragment L. In accordance with Eq. (3.5) we find that the mechanical integrity around the focal adhesion remains unperturbed when $L \gg a/\sqrt{\kappa}$. This typical length scale has been determined beforehand to be $a/\sqrt{\kappa} \approx 5.4 \mu m$ for actin transfected cells. In order to compare the model prediction with the measured data we averaged over 86 curves for $\triangle F(L)$, each defined by one value for κ. The 86 values for κ are taken from the previously described actin parameter sample also used for Tab. 3.1. In Fig. 3.8 we show the sample average curve for the expected normalized force loss, $\langle \triangle F(L) \rangle_{actin}$, compared with the measured normalized intensity loss of zyxin at focal adhesions in Ptk-2 cells and 3T3 fibroblasts. The agreement between model predictions and experimental data suggests a close relationship between zyxin concentration in focal adhesions and the applied forces.

3.3.2 Zyxin dissociation from stress fibers

Along stress fibers zyxin co-localizes with α-actinin and thereby forms a regular striation pattern which can be seen in Fig. 3.7(a,k). The resulting intensity profile of zyxin along the stress fiber is shown as red curve in Fig. 3.7(p). The striation pattern causes the periodic intensity peaks at the middle of the fiber in the region of $10\,\mu$m to $25\,\mu$m. These peaks in zyxin intensity are lost within $6\,$s after cut which can be deduced from the corresponding intensity profile shown as blue line in Fig. 3.7(p). The fast dissociation of zyxin along the released stress fiber fragment suggests a similar underlying mechanism in stress fibers compared to focal adhesions. We propose that the loss in zyxin is correlated to the loss of tension in the fiber. By means of our model, the viscoelastic stresses within the fiber can be calculated. The tension σ within the fiber, normalized by the initial tension before cut σ_0, is given by Eq. (2.68). In the following, we use this equation to calculate the normalized tension and compare it to the normalized zyxin intensity along the fiber. Fig. 3.9(b) shows a color coded kymograph of the normalized zyxin intensity along the laser released central stress fiber fragment of Fig. 3.7. The corresponding color coded kymograph for the normalized tension along the same fiber fragment, calculated from Eq. (2.68), is shown in Fig. 3.9(c). After cut, the tension within the fiber fragment quickly drops to very low values. Simultaneously, the zyxin-banding pattern along the stress fiber is exposed to a sharp intensity loss, compare the regions marked with a $(+)$ and a $(-)$ sign in Fig. 3.9(b,c). The dynamic response in zyxin intensity is remarkable fast and correlates qualitatively with the loss in tension after cut. However, note that the zyxin response to cut is more complex than a simple loss of intensity along the fiber. The emergence of new foci of high zyxin intensity after cut marked by $(*)$ in Fig. 3.9(b) can not be explained by the above considerations. We hypothesize that these new zyxin spots originate from crosslinks that get highly tensed by the retracting fiber and thereby recruit zyxin in a force dependent manner. It is only the superposition of all these effects that can reproduce the full kymograph in Fig. 3.9(b).
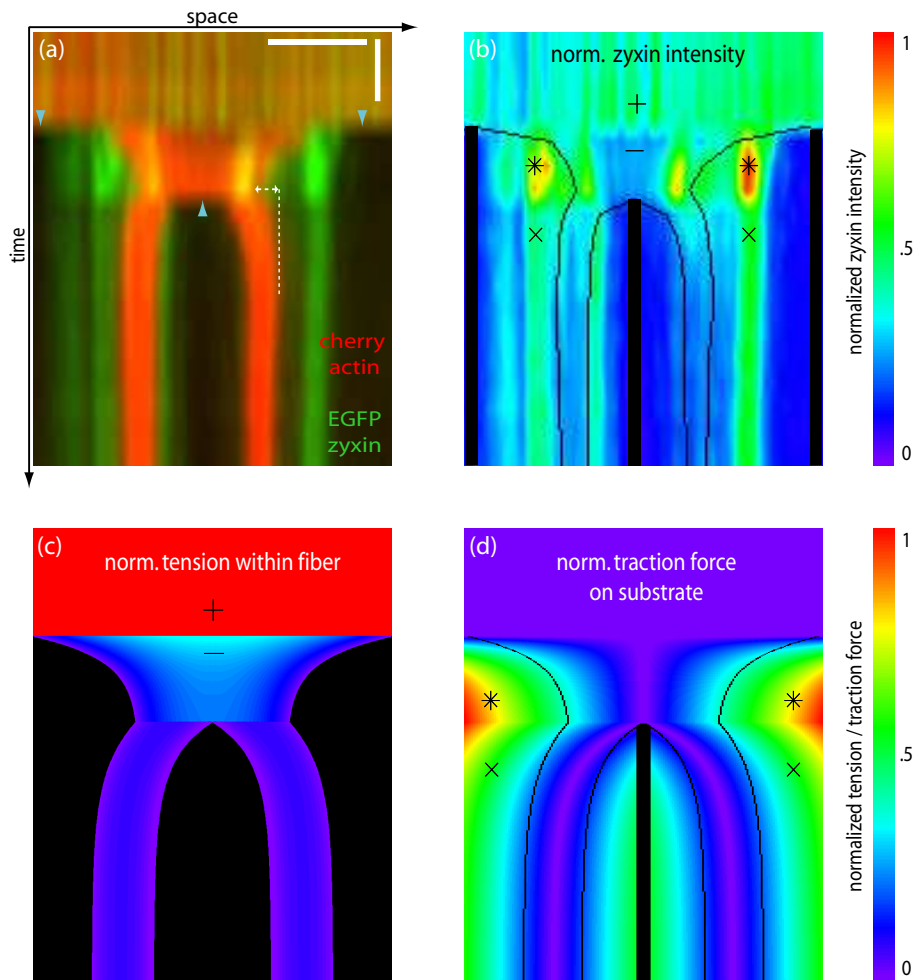
Figure 3.9: (a) Time space kymograph of the cut sequence shown in Fig. 3.7(a-e). Actin is shown in red, zyxin is shown in green. Cuts are indicated by blue arrows. White dashed lines mark the $1 \, \mu$m snap-back for one fiber fragment after the second cut, indicating the relaxation of tension in crosslinks previously strained after the first cut. Scale bar denotes $5 \, \mu$m horizontally and $10 \, $s vertically. (b) Normalized zyxin intensity. Thin black lines indicate the position of retracting fiber edges whereas thick black bars cover regions of induced laser damage. Note that appearing zyxin spots lie preferentially behind the retracting fiber and are stationary with respect to the substrate. (c) Tension within the stress fiber, normalized by the tension before cut. Large loss of tension immediately after cut compares to a simultaneous loss of zyxin intensity highlighted as $(+)$ and $(-)$ in (b,c), respectively. (d) Traction forces exerted on the substrate by the crosslinks, normalized by the maximal occurring value. The buildup of high traction forces close to the fiber edges after the first cut corresponds to the emergence of zyxin spots of high intensity, marked as $(*)$ in (b,d). Subsequently, the second cut releases tension in the strained crosslinks followed by a decrease in zyxin intensity at the preformed clusters, denoted by $(\times)$ in (b, d). Used model parameters are: $(\kappa, \delta, \tau, \tau_\epsilon)=(0.01, 0.70 \, \mu\text{m}, 5 \, \text{s}, 0.1 \, \text{s})$.

3.3.3   Zyxin recruitment at tensed crosslinks

In contrast to the loss of zyxin patterns on released fiber fragments, we observed that zyxin relocalizes at random spots along the fiber axis, for example marked as regions (1-4) in Fig. 3.7(e,o). Interestingly, these zyxin spots are immobile with respect to the substrate which can be deduced from the image sequence Fig. 3.7(l-o). After forming close to the fiber tips, their intensity steadily increases in time while the stress fiber fragments retract. The respective time courses of the normalized zyxin intensities at theses areas are shown as red and green curves in Fig. 3.7(q). After performing the second cut on the central fiber fragment at $18\,\mathrm{s}$, however, we observed a decreasing intensity in areas (1,2). In contrast, the intensity further increased at the areas (3,4) that obviously remained unaffected by the second cut, compare red and green curves in Fig. 3.7(q).

All of these observations can be explained consistently by assuming that the new zyxin spots originate at crosslinks that get highly tensed by the retracting fiber and thereby recruit zyxin in a force dependent manner. The existence of such tensed crosslinks that pull on the retracting fiber is also the most reasonable explanation for the reversed movement of the two fiber fragments created after the second cut at $18\,\mathrm{s}$. We highlight this remarkable snap back of the two central fragments by red arrows in Fig. 3.7(i). It becomes even more evident in Fig. 3.9(a) showing the kymograph of the cut sequence. The contours of the fiber fragments are shown in red (actin-cherry signal). After the second cut, the fragments are pulled apart, indicated by an increasing distance between the two wide red lines. Consistently, the center of mass of each created fragment is displaced backwards. We also indicate this reversed movement over a distance of about $1\,\mu\mathrm{m}$ with a white arrow in Fig. 3.9(a). The snap back is very likely caused by the relaxation of a tensed crosslink, but its nature remains elusive. Since it can be stretched up to $1\,\mu\mathrm{m}$, evidently, it can not be realized by a single protein but rather a longer filament or biopolymer. For instance, a few single actin filaments that are strongly coupled to the surrounding might be pulled out of the stress fiber and serve as this micrometer long and highly tensed tether.

In order to correlate the zyxin dynamics with the change of tension in the crosslinks along the stress fiber, we simulated the sequence of laser cuts with our model. Subsequently, we produced a kymograph of the traction forces transmitted by the crosslinks to the substrate given by $F_{trac}(x,t) = -k_{ext}u(x,t)$, shown in Fig. 3.9(d) and compared it to the measured kymograph of normalized zyxin intensity along the stress fiber fragments, shown in Fig. 3.9(b). The thick black bars cover regions of laser damage. In both figures, thin black lines indicate the position of the retracting fiber edges. The time course of the fiber edges including the snap back of the fiber fragments after the second cut are very well reproduced by our model.

Comparison of Fig. 3.9(b,d) also yields a remarkable correlation between the increase of zyxin at regions (1,2) with an increase in crosslink tension upon the first cut, highlighted with (∗) in Fig. 3.9(b,d). Subsequently, after the second cut, we can correlate the decrease of zyxin with the release of tension at the same location highlighted with (×) in Fig. 3.9(b,d). The remarkable correlation of modeled crosslink tension with zyxin translocation dynamics support our hypothesis that the emerging high in-

tensity spots result from a mechanosensitive recruitment of zyxin at tensed crosslinks presumably anchored to the underlying substrate.

Colombelli at al.[34] further investigated these new zyxin spots by correlative live fluorescent and transmission electron microscopy [108] and convincingly showed that zyxin localizes within the first 50 nm above the glass substrate. The new zyxin spots were found to be strikingly similar to focal adhesions. For instance, the zyxin nucleation points also recruit the protein vinculin, which is a core focal adhesion component. Noteworthy, vinculin was not detected along stress fibers before dissection. These observations suggest that the emerging zxin foci are the onset of new focal adhesion sites along the retracting stress fiber induced by a force dependent mechanism.

3.4   Summary and discussion

In this chapter we studied stress fiber contraction dynamics induced by laser nanosurgery with our stress fiber model. We find excellent agreement between experimental data and the model which can reproduce the complete displacement field in space and time. By fitting our model to the data we can extract the four model parameters $(\kappa, \delta, \tau, \tau_\epsilon)$ summarized in Tab. 3.1. They reflect physical properties of stress fibers.

The parameter $\kappa = 0.035$, which is a measure for the degree of crosslink of the fibers, sets a typical length scale $a/\sqrt{\kappa} \approx 5.4\,\mu$m over which the mechanical perturbation propagates along the fiber. This length scale has an impact on the total contraction length of short fibers as well as on the loss of force at connected focal adhesions. This model term (proportional to κ) which accounts for elastic external interactions, is essential to understand the nonhomogeneous contraction of the fibers, that is, strong contraction close to the cut, and rather no contraction far away from the cut.

The parameter $\delta = 0.66\,\mu$m denotes the maximal free contraction length of a sarcomeric unit of initial length $1\,\mu$m. Thus, the resting length of the sarcomeric unit is found to be 340 nm. This is in agreement with the natural lower bound given by the length of myosin minifilaments of (393 ± 33) nm measured for smooth muscle cells [32]. The parameter δ together with the parameter κ also determines the saturation level for the total contraction length of very long fibers to be $\delta/\kappa \approx 4.5\,\mu$m.

Finally, we extracted the two time scales, $\tau = 29$ s and $\tau_\epsilon = 0.13$ s which are associated with internal and external friction, respectively. Together, they determine the dynamics of the retardation process. However, the ratio $\tau_\epsilon/\tau = \Gamma \ll 1$ is very small and thus the model term, which accounts for the external friction forces (proportional to τ_ϵ), can be neglected in good approximation. In regard to stress fiber contraction dynamics, the viscosity of the surrounding cytosol thus plays only a minor role and the time scale for contraction is solely given by fiber-internal friction. This friction can be associated with relative filament sliding, movement of solvent within the fiber, (un-)binding kinetics of fiber internal crosslinkers, and contributions from molecular motors.

The retraction of stress fibers within the cytoplasm is actually a three dimensional contact mechanics problem. By making reasonable assumptions for the geometry of the fibers as well as for the interface to the surrounding viscoelastic medium, one could

also use the parameters $\tau, \kappa, \tau_\epsilon$ to give rough estimates for the expected extensional viscosity of the fiber, the shear modulus and shear viscosity of the surrounding medium, respectively. These considerations and the derivation of the needed relations are carried out in section 2.1.2.

The parameter values summarized above have been obtained by analyzing stress fibers in actin transfected cells. We performed the same analysis also on α-actinin transfected cells. This enabled us to investigate the impact of an enhanced α-actinin expression on stress fiber mechanics. The parameter distributions for both samples have been tested for differences in the mean as well as for differences in the median. We found that an increase in α-actinin expression leads to a significant increase in κ and decrease in τ. The remaining two parameters are rather unaffected by α-actinin over expression.

α-actinin is known as a crosslinker between actin filaments and also mediates the connection between stress fibers and focal adhesions. Thus, the over expression of α-actinin is likely to cause an increase of crosslinks between stress fibers and their surrounding. In this way, it explains an increase in the crosslink parameter κ.

The significant change in the time scale τ lacks such a straight forward explanation. A likely possibility is that other types of crosslinker proteins within the stress fiber are substituted by α-actinin. Since the bulk concentration of α-actinin is enhanced in these cells, this leads to a higher chemical potential of α-actinin in the cytosol. This in turn, might promote the substitution process. If the replaced crosslinker and α-actinin have different binding and unbinding kinetics then the exchange could lead to an alteration of the fiber-internal viscoelastic properties. More specifically, in order to explain the observations, the exchange must lead to a decrease of the internal friction coefficient of the fiber.

The observations that (1) stress fibers contract only in the vicinity of the cut, (2) the total contraction length saturates for long fibers and (3) the force loss at focal adhesions is dependent on the length of the associated fiber fragment, all result from the fact that stress fibers are considerably crosslinked to their surrounding. This degree of crosslink is measured by the parameter κ. But what is the major mechanical scaffold to which stress fibers are elastically crosslinked? Possible candidates are cytoskeletal components, in particular neighboring actin filaments, or the underlying substrate. The latter case is possible since the considered cells are very flat and the stress fibers are in close contact with the plasma membrane. We hypothesize that the major contribution of the elastic restoring forces acting on the retracting stress fibers arise from such intermediate contacts to the glass substrate. These contacts might be mediated by small integrin clusters that are still undetectable in fluorescence. This transmembrane linkage could function in a similar way to what is observed in muscle cells, where costameres (α-actinin rich protein complexes) connect sarcomeres with the extracellular matrix at the z-disk. Thereby, traction forces are transmitted to the cellular environment [109].

Such a linkage could also explain our observation that retracting stress fibers initiate zyxin rich foci, which are stationary with respect to the substrate. We suggest that these initial crosslinks to the substrate are stretched by the retracting fiber. The increased tension in the crosslinks then causes a mechanosensitive response that recruits zyxin. This protein recruitment is a reinforcement of the initially small integrin

based contacts which then might mature to focal adhesions, in agreement with previous studies [39, 59]. This hypothesis has been further tested by correlative live fluorescent and transmission electron microscopy and Colombelli et al. [108] convincingly showed that zyxin localizes within the first 50 nm above the glass substrate. The new zyxin spots were also found to recruit the protein vinculin, which is a core focal adhesion component.

The reinforcement of the mechanical anchor points can be regarded as a sophisticated repair or healing process on subcellular scale. The laser dissection causes a mechanical instability within the cytoskeleton. This mechanical disequilibrium demands quick repair to avert further damage to the cell. A force balance within the cytoskeleton is reestablished by reattaching the dissected fiber to the substrate. Thereby, the underlying force dependent mechanism has to be much faster than the typical timescale for stress fiber contraction, $\tau \approx 29\,\text{s}$. The fast association and dissociation dynamics of zyxin on a timescale below 6 s definitely fulfill this necessary condition.

To further discriminate between the importance of cytoskletal crosslinks and crosslinks to the substrate, we can suggest several control experiments for future studies. One possibility would be a systematic measurement of the total contraction length in dependence on the length of the cut across several neighboring stress fibers. If the fibers are strongly connected to each other, one would expect that the retraction is largest in the middle of the transverse cut and vanishes at the edges. The expected profile could be calculated by a model that accounts for several parallel stress fibers which elastically interact with their nearest neighbors. Another possibility would be the application of microstructured substrates. They could be biofunctionalized in such a way that the cell can form focal adhesions only on adhesive patches. However, the surface in between these patches should be passivated such that the stress fibers can not interconnect to the substrate by integrin mediated adhesion. If the intracellular cyoskeletal crosslinks are indeed negligible, then, in terms of our model, the crosslink parameter is expected to vanish. This would have the following consequences: (1) a homogenous contraction of stress fibers all along their length, (2) the total contraction length would increase linear with the fiber length and (3) the force loss at focal adhesions would be independent of the position of the cut.

We also applied our model to further quantify the mechanosensitivity of zyxin. The model is thereby used to calculate the change in mechanical stress within the cytoskeleton upon laser release which is otherwise not accessible experimentally. The change in stress was then compared with the change in zyxin intensity at focal adhesions and along stress fibers. In both situations we find that the localization of zyxin correlates with tension. Moreover, Colombelli et al. [34] could show that the mechanosensitive recruitment of zyxin is reversible by pulling cyclically on a stress fiber with an AFM cantilever. Similar mechanosensitive responses of zyxin along stress fibers and focal adhesions have also been reported in previous studies [64, 110, 111].

The question is, could there be a single mechanism underlying zyxin-recruitment at focal adhesions and stress fibers? Moreover, which is the protein that resides in the mechanical scaffolds and recruits zyxin in a mechanosensitive manner? A likely candidate for this mechanosensitive protein is the crosslinker α-actinin. It serves as main crosslinker in stress fibers and mediates also the linkage between stress fibers

and focal adhesions. In both situations α-actinin is subject to the mechanical tension and thus is predestined as a mechanosensor. Zyxin and α-actinin co-localize at focal adhesions and along stress fibers and α-actinin is also the main binding partner of zyxin [106, 112, 113]. Interestingly, the binding site on α-actinin involves two spectrin-like subdomains [114] and an interaction occurs only when α-actinin dimerizes [113]. Notably, spectrin domains are known to have unique flexible properties [115]. The flexibility of spectrins and their redundant organization along α-actinin (8 domains in a dimer) could therefore serve as a docking platform, which mechanically regulates the number and activity of zyxin binding sites. Further analysis of zyxin and α-actinin binding partners will be necessary to determine the exact number of proteins involved in the mechanosensitive recruitment of zyxin.

One possibility to further quantify the mechanosensitive recruitment of zyxin would be to perform stress fiber laser surgery in cells plated on flexible substrates. The contractile cellular stress, exerted through the focal adhesion on the substrate, could then be determined by traction force microscopy [116, 117]. In this way, the change of stress upon cut could be measured explicitly and could be compared to the model predictions and to the induced zyxin dynamics. This would provide a further test for our stress fiber model as well as a refined correlation between forces and zyxin dynamics.

Chapter 4

Coupling of mechanics and biochemistry

In the previous chapter we developed a model for stress fibers. Thereby we assumed that the viscoelastic properties of the fibers as well as the activity of the molecular motors are uniform along the whole fiber length. The model has then been used to study the pure mechanics of stress fiber contraction after laser release and by comparing calculated stresses with zyxin intensity we found that the molecular composition of focal adhesions is dependent on the applied stress. This is evidence for the widely accepted notion that mechanical stresses are involved in determining the biochemical signaling state of focal adhesions. The transduction of mechanical stress into a biochemical signal could happen for example by a force induced conformational change of single proteins or protein complexes into a high or low affinity state to possible binding partners. In a similar way forces could alter the enzymatic activity of kinases or phosphatases that are located in the adhesion contact. Although the precise mechanism has not yet been revealed some proteins that are probably involved in mechanotransduction have been identified, for example talin [41, 42], p130Cas [118] and integrin [43]. In this spirit, focal adhesions can be understood as localized spots where chemical as well as mechanical information is processed collectively. Outgoing signals then contribute to complex cellular processes like cell cycle control, apoptosis and the regulation of the actin cytoskeleton. In particular, the Rho-pathway controls the activity of myosin II molecular motors and thereby the contractility of stress fibers. The altered actomyosin forces are then transmitted to the adhesion sites and change the biochemical signaling. Consequently, focal adhesions and stress fibers are connected by a biochemical and mechanical feedback loop which is the focus of our study in this chapter. Due to the complexity of the signaling network at focal adhesions, which we briefly depict in the first section, we constrain our biochemical modeling to the Rho-pathway. This part of the signaling network has been studied thoroughly by experimentalists. We conducted an extensive survey of the relevant literature and collected the measured rate and diffusion constants in such a way that they now can be used for mathematical modeling. The coupling between the biochemical signaling pathway and the mechanical stress fiber model proceeds by introducing a spatially varying fraction of active molecular motors. The local activation level is thereby determined by the outcome

of the signaling pathway. The whole system of reaction-diffusion equations for the signal transduction and the partial differential equation for the mechanical part can be solved simultaneously. By feeding the force resulting from the mechanical model back into the activation of the signaling pathway, we obtain for the first time a model for the closed mechano-chemical feedback cycle. As a first application of our model, we simulate a drug experiment *in silico* and we show that it predicts heterogenous contraction of stress fibers in good agreement with experimental findings by Peterson et al. [31]. Furthermore we study the case of cells embedded in soft tissues and make valuable predictions for the capability of cells to establish stresses in soft environments. These model predictions could be tested in future experiments. In general, our work shows how models for the coupling of biochemistry and mechanics can be devised in a meaningful way.

4.1   Biochemical signaling at focal adhesions

First evidence for localized adhesion spots between cultured fibroblasts and the substrate was provided in the early seventies by electron microscopy [119]. At that time focal adhesions were described as electron-dense plaques where the plasma membrane comes 30 nm close to the substrate which compares to an average spacing of about 60 nm. Also filamentous structures connected to the adhesion plaque have been discovered, the fingerprint of actin stress fibers. Subsequently, focal adhesions have been investigated by interference reflection microscopy [120–122] which enabled live cell imaging of focal adhesions. In motile cells they were found to be rather stationary with respect to the substrate demonstrating their role as mechanical anchor points to the extracellular matrix. The integrin receptor family, which mainly mediates this transmembrane linkage between the extracellular matrix and the actin cytoskeleton, has been recognized in the mid-eighties [123]. However, only few components like vinculin [124–126], talin [127, 128] and α-actinin [104] were known to reside in the intracellular dense protein plaque which mediates the connection between integrin and actin filaments. In the following years the knowledge about the composition of integrin mediated adhesion has been extended primarily by immunofluorescence studies. Till to date the pace of discovery in this field of research has not slowed down. By 2001 about 50 proteins have been found either stably or transiently associated to integrin mediated contacts [36, 129]. Within about six years the number of known components increased to 90, reported by Zaidel-Bar et al. [38] after an extensive literature research also including the usage of large protein-protein interaction databases such as BIND [130] and HPRD [131]. In addition to these intrinsic components that physically reside in the adhesion plaque another 66 external interaction partners have been identified that can affect or conversely can be effected by the plaque proteins without being associated to the mechanical scaffold. The entity of all 156 components together with their known 690 interactions has been termed *integrin adhesome* in obvious analogy to the genome. Fig. 4.1 depicts the state-of-the-art interaction network between the 90 intrinsic adhesion components. The links in the network represent either non-directional binding interactions or directional signaling interactions. The latter are further subdivided into
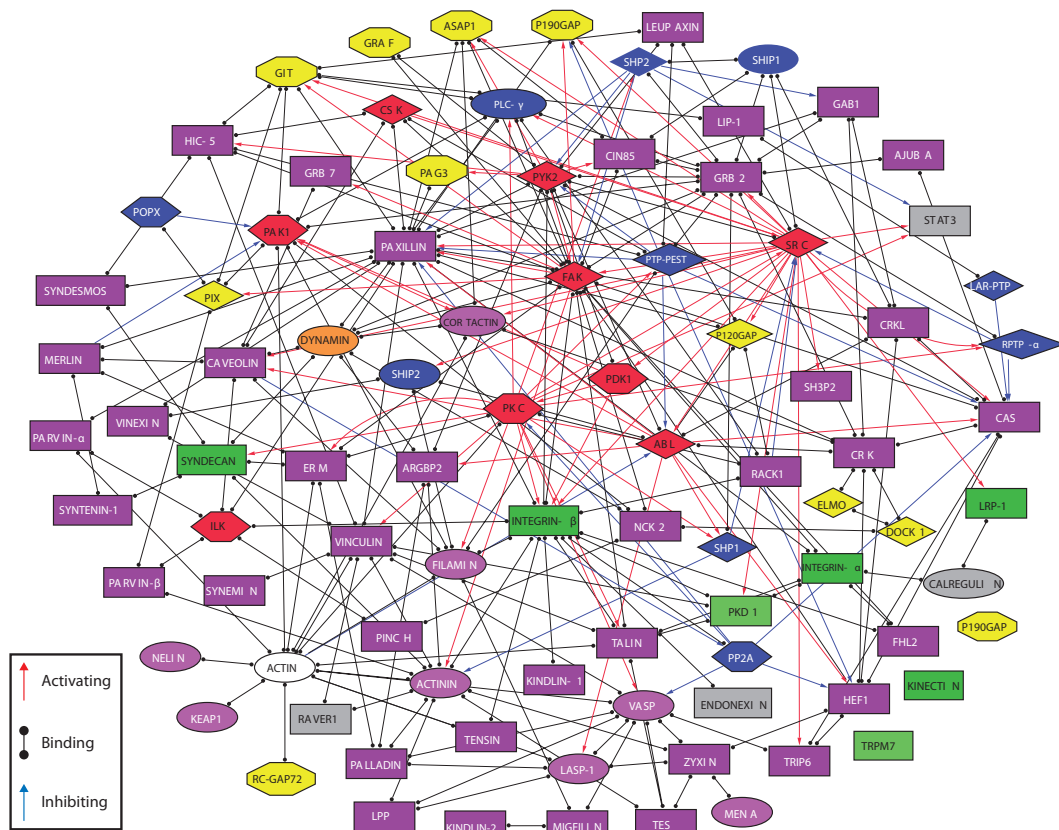
Figure 4.1: Interactions between all intrinsic components of the adhesome. Black lines with full circles at their ends denote non-directional binding interactions, blue arrows represent directional inhibition (for example, dephosphorylation, G-protein inactivation or proteolysis) and red arrows represent directional activation (for example, phosphorylation or G-protein activation) interactions. The nodes are shape- and colour-coded according to the function of the proteins. For more details, including a list of the peripheral components, see [38] where the figure and caption were taken from.

either activating or inhibiting interactions classified according to the performed molecular modification, see [38]. Each component shown in Fig. 4.1 potentially interacts also with external components (not included in the figure) that are in turn part of various signaling pathways which regulate complex cellular processes such as differentiation, cell cycle control, apoptosis as well as cell migration including the regulation of the actin cytoskeleton. An illustrative overview of the outgoing signaling pathways at focal adhesions is given for example by the KEGG database (Kyoto Encyclopedia of Genes and Genomes) [132]. Due to the vast complexity of the resulting network a system-wide quantitative model seems to be neither feasible nor reasonable at the present stage. At this point it is worth mentioning that the links in the presented network describe protein-protein interactions in a merely qualitative manner. Quantitative measurements of the chemical rate constants for the respective enzymatic reactions have been reported only in rare cases. It is mainly for this reason that we focus our biochemical modeling on the Rho-pathway where most of the chemical reaction parameters such
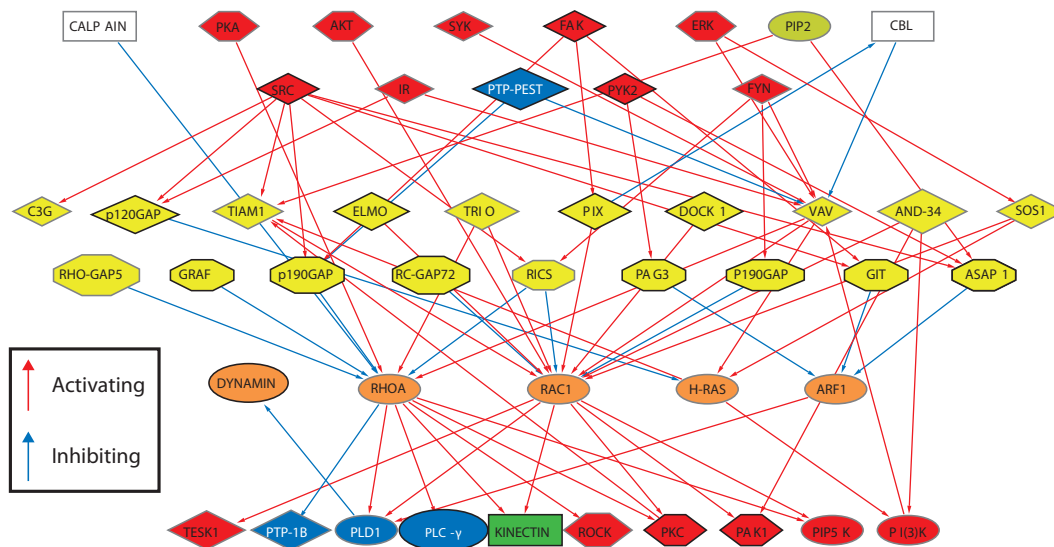
Figure 4.2: Regulation of GTPases at integrin mediated adhesions. The GTPases (mainly RhoA and Rac1) are upregulated by guanine nucleotide exchange factors (GEFs, yellow diamonds) and downregulated by GTPase-activating proteins (GAPs, yellow octagons). Regulators of GEFs and GAPs are mainly kinases shown at the top. The main substrates of GTPases are shown at the bottom. This figure was taken from [38].

as rate and Michaelis-Menten constants have been measured. The important role of Rho-GTPases in cell adhesion has been revealed in 1992 by Ridley and Hall. They demonstrated by microinjection of the respective proteins into cells, that the assembly of stress fibers and focal adhesions is regulated by a small GTPase called Rho [47]. Rho has many isoforms, but the one mainly associated with focal adhesions is RhoA, which for simplicity in the following we refer to as Rho. In a companion paper of the same year, Ridley and Hall showed together with coworkers that another small GTPase called Rac stimulates the formation of lamellipodia as they appear in cell migration [46]. The main isoform associated with focal adhesions is Rac1 which for simplicity in the following we will refer to as Rac. While Rho mainly acts through activation of actomyosin contractility, the main effect of Rac is activation of actin polymerization, in particular activation of the actin nucleation factor Arp2/3. It has been reported later that activation of Rac downregulates Rho, leading to disassembly of stress fibers and focal adhesions [133]. In many situations, Rho and Rac can be regarded as antagonists, switching the cytoskeleton between different structural states [45]. They are part of a larger family of small GTPases, called the Rho-family, which for example also includes Cdc42, which stimulates the formation of filopodia and maintains cell polarity [134]. Apart from regulation of the actin cytoskeleton, the small GTPases from the Rho-family have many other functions in the cell, for example in cell cycle control and differentiation.

　　Although the small GTPases from the Rho-family are simple molecular switches, they are regulated by many different factors. In general, GTPases are upregulated by guanine nucleotide exchange factors (GEFs) which convert the inactive Rho-GDP form to the active Rho-GTP form by exchanging GDP for GTP. They are downregulated

by GTPase-activating proteins (GAPs), which stimulate Rho-GTPase activity, thus leading to GTP-hydrolysis and transformation of the active Rho-GTP into the inactive Rho-GDP. For the 20 members of the Rho-family, 60 different GEFs and 70 different GAPs as well as more than 60 different downstream targets have been identified [135]. Fig. 4.2 illustrates this complex regulation network for GTPases at integrin mediated adhesions. The GEFs (yellow diamonds) and GAPs (yellow octagons) are mainly regulated by kinases of which the most important ones, FAK and SRC are bound to the adhesion plaque. The various signals from GAPs and GEFs are gathered and then compete at Rho-GTPases for activation or inhibition. Most of the integrin related signaling is evidently carried out through RhoA and Rac1. The remaining GTPases depicted in Fig. 4.2 seem to play only a minor role. Still, at the current stage of affairs, there is no way how this complex network can be modeled in full detail. However, certain parts of this network have been well characterized by biochemical assays, in particular different parts of the Rho-mediated signal transduction pathway leading from focal adhesions to actomyosin contractility.

In combination with our mechanical stress fiber model we focus on the role of Rho as stabilizing factor for mature adhesion. During recent years, it has been shown that Rho is the central component of a mechano-chemical feedback loop which regulates mature adhesion. In detail, it has been shown that application of force on focal adhesions triggers their growth in a Rho-dependent manner [39] (reviewed in [37, 45]). Two main downstream targets of Rho leading to stress fiber formation have been identified. The formin mDia leads to actin polymerization, while the Rho-associated kinase ROCK leads to phosphorylation of myosin light chain and thus to increased motor activity. Together these effects lead to formation of and contractility in stress fibers and therefore to increased force levels at focal adhesions. In this way, a positive feedback loop is closed for upregulation of mature adhesion characterized by focal adhesions and stress fibers. This mechano-chemical feedback loop is schematically depicted in Fig. 1.3. An essential part of this feedback loop is the growth of focal adhesions under force, which recently has been the subject of different modeling approaches [74–79] (reviewed in [81]). However, these models have focused mainly on the mechanical and thermodynamic aspects of the growth process, neglecting the interaction of mechanics and biochemical signaling. Our biochemical reaction diffusion model for the Rho-pathway will be developed in section 4.3. Next, we will give a summary of experiments by Peterson et al. [31] who used the drug calyculin A in order to interfere with this biochemical signaling pathway.

4.2   Description of inhibition experiments

Although being less ordered than muscle on the level of electron microscopy, stress fibers do exhibit a similar periodic organization of alternating α-actinin and myosin II rich bands. The resulting striation pattern can be revealed under the microscope by transfecting cells with fluorescently labelled proteins. Fig. 4.3(A-C) shows such a gerbil fibroma cell, where the green regions correspond to the actin crosslinker α-actinin while the red regions correspond to myosin II molecular motors. These striation

patterns have been used as an intrinsic ruler in our previously presented study of laser dissected stress fibers. In a similar manner, Peterson et al. [31] used these structures to investigate the effect of biochemical drugs on stress fiber contraction dynamics. The induced drug, calyculin A, is a serine/threonine phosphatase inhibitor that increases the phosphorylation level of the myosin II regulatory myosin light chain (MLC) via the Rho-pathway [56, 57] and thus increases stress fiber contractility. More details of how the drug interferes with Rho-signaling are presented in the next section, see also Fig. 4.4. The drug (5 nM) was put into the medium and subsequently got internalized by the cells. It can be expected that the drug thereby was homogeneously distributed within the cell body. Upon actomyosin stimulation, stress fibers contracted in total length by 16% within 30-40 min after induction of the drug. However, measurements of mean sarcomere lengths in α-actinin transfected 3T3 fibroblasts revealed that the induced strain was not uniform along the fiber. This is a counterintuitive result given a homogeneously distributed drug. At the cell periphery sarcomeres shortened by 30-40% (average over 40 sarcomeres in 7 cells) but in contrast sarcomeres at the cell center were simultaneously stretched by 50% (average over 20 sarcomeres in 4 cells). Here, cell periphery was defined as the part of the fiber within 5-7 μm distance to a focal adhesion and the center was defined as a 10 μm segment on either side of the fiber midpoint. The exact time courses of the mean striation width in the two regions are shown in Fig. 4.3(D-E) for control and stimulation experiments, respectively. Noteworthy, mean sarcomere widths already differed between the two regions prior to stimulation. The differences then increased upon calyculin A induction. Similar results have been reported for stimulation with LPA, another agent that also stimulates MLC phosphorylation via the Rho-pathway. In order to check whether the strong spatial gradients in the striation pattern result from a gradient in myosin activity, Peterson et al. measured the fluorescence intensity of MLC as well as the fraction of MLC phosphorylated on Ser19, both before and after stimulation. The degree of MLC-phosphorylation is a measure for the local myosin activity. In general, they found more MLC associated to peripheral compared to central parts of the fibers, before as well as after drug stimulation. More importantly, they observed that more phosphorylated MLC was localized at the cell periphery after stimulation. Furthermore, they determined the ratio of fluorescence intensity of phosphorylated MLC to total MLC in the respective regions and found that, after stimulation, this ratio was higher in the periphery. Together these observations suggest that the nonuniform distortions of the striation patterns indeed result from a gradient in MLC phosphorylation levels. The emergence of this chemical gradient, however, is not coherent with the uniformly distributed stimulus.

To resolve this inconsistency, we argue that the mechano-chemical coupling at focal adhesions has to be taken into account. According to our suggestion the chemical gradient occurs due to the following mechanism: The induction of the drug first homogeneously increases the contractility along the stress fibers leading also to higher boundary forces exerted on the focal adhesions located at the peripheral fiber tips. Subsequently, the increased mechanical stress at focal adhesions triggers additional Rho-signaling. The stimulating Rho-signal then diffuses back into the cell and thereby gets degraded. Thus the part of the stress fiber close to the adhesion gets more stimu-
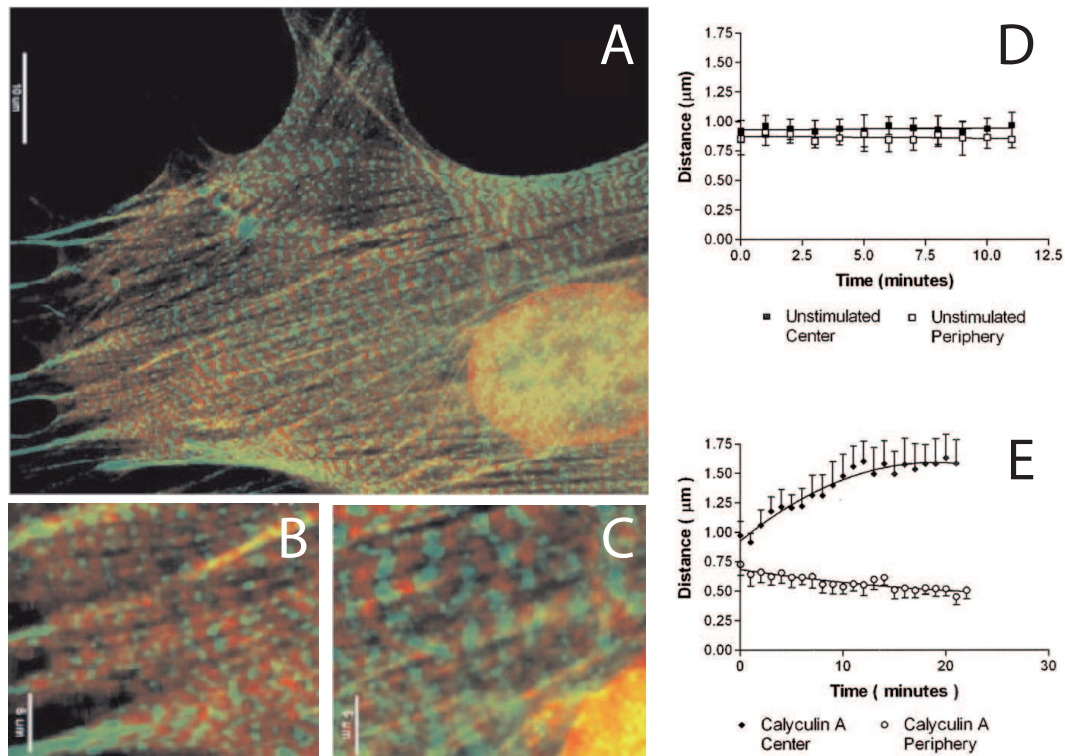
Figure 4.3: (A) Peterson et al. [31] studied the deformation of stress fibers in fibroblasts by using fluorescently labelled α-actinin (in green) and myosin light chain (in red). These two components arrange sequentially along the stress fibers and thereby form regular striation patterns. Myosin contractility was stimulated with the drug calyculin A. Then an inhomogeneous striation pattern results: stress fibers contract at the cell periphery (B) but expand at the cell center (C). These results were quantified by time course measurements of the mean pattern bandwidths in the respective regions. Compared with the control (D), stimulation of contractility leads to very strong spatial gradients (E) on the time scale of tens of minutes.

lated in contrast to the central part which is hardly reached by the diffusive Rho-signal. The strong motors at the periphery then contract the fiber at the expense of the weakly contractile central fragment. In order to further quantify these ideas we developed a model for the Rho-pathway, presented below, and showed how this biochemical model can be coupled to our slightly altered stress fiber model. The whole coupled system of reaction diffusion equations and the stress fiber equation can be solved simultaneously. The numerical results for the *in silico* drug experiments are finally compared with the experimental measurements.

4.3 Reaction diffusion model for the Rho-pathway

In Fig. 1.3 we introduce a coordinate system for our one-dimensional model: the stress fiber extends along the positive x-direction and the endpoints at $x = 0$ and $x = L$ correspond to two focal adhesions. Because the two focal adhesions are treated as equivalent,
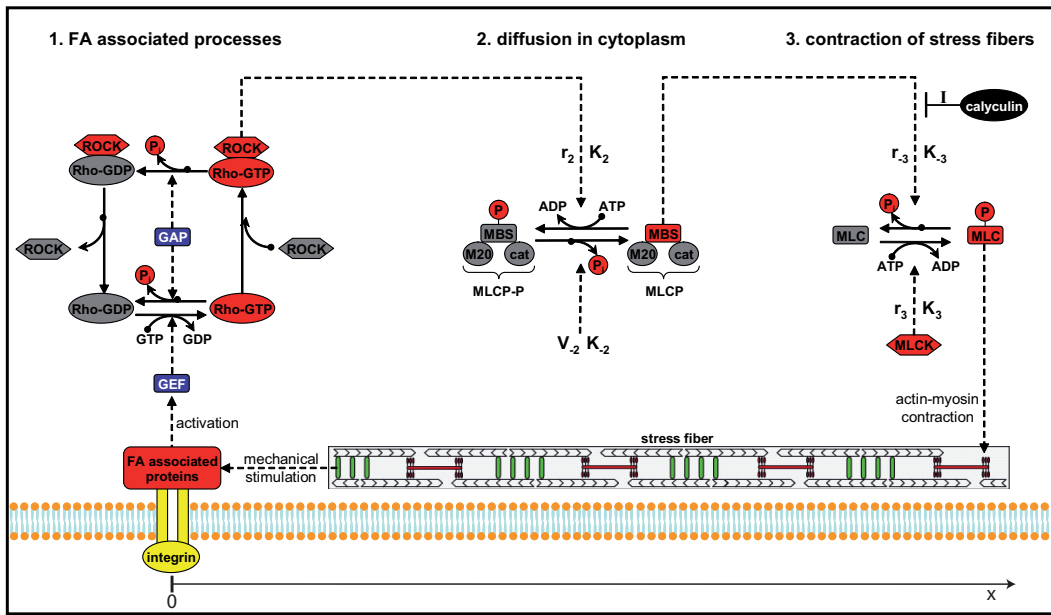
Figure 4.4: Signaling pathway that controls myosin contractility depicted in its appropriate spatial context: mechanical cues are transduced to various biochemical signals at focal adhesions, however, the precise mechanisms have not been resolved yet. One possible mechanism is that a Rho-GEF is activated by a mechanosensitive process at focal adhesions. Rho-GEF then promotes Rho-GTP loading and subsequent complexation with Rho-associated kinase (ROCK) which gets activated. Active ROCK is able to phosphorylate myosin light chain phosphatase (MLCP) at its myosin-binding subunit (MBS). MLCP and MLCP-P are freely diffusible in the cytoplasm and thus can reach the myosins in the stress fibers. Increased phosphorylation of MLCP to MLCP-P by ROCK effectively leads to increased phosphorylation of myosin light chain (MLC), thus increasing myosin contractility.

our model has inflection symmetry around $x = L/2$. In Fig. 4.4, we schematically depict the biochemical part of our model in the spatial context of the focal adhesion at $x = 0$ (by symmetry, the same description applies to the one at $x = L$). Three compartments have to be considered: the focal adhesion, the cytoplasm and the stress fiber. In our model, each of these compartments corresponds to one or two important biochemical components. The reaction pathway is a linear sequence of activating or inhibiting enzyme reactions initiated at focal adhesions, transmitted through the cytoplasm by diffusion and resulting in spatially dependent myosin activation in the stress fiber. In the following we discuss each reaction step in detail and show how these processes are translated into reaction-diffusion equations. The abbrevations used for the biochemical components are compiled in Tab. 4.1, together with a short description of their functions. The model equations are summarized in Tab. 4.2.

Our modeling of the biochemical signaling pathway starts with the activation of Rho at focal adhesions. The Rho-protein has a lipophilic end serving as an anchor for lipid membranes [136]. Complexation with guanine nucleotide dissociation inhibitors (GDIs) shields the hydrophobic parts of the Rho-protein and makes it inactive as well as soluble in the cytoplasm [137]. It is expected that Rho is released from these complexes

Abbreviation	full name	function
GDP/GTP	guanosine diphosphate/ guanosine triphosphate	small molecule without and with a third phosphate group, energy source of conformational changes
GEF	guanine nucleotide exchange factor	activates GTPases by exchanging GDP for GTP
GAP	GTPase-activating protein	stimulates GTP-hydrolysis, converting active GTPases (GTP-bound) to their inactive (GDP-bound) form
GDI	guanine nucleotide dissociation inhibitor	binds to inactive form of GTPases, the complex is soluble in the cytoplasm
MLC	myosin light chain	subunit of myosin II molecular motors, regulates myosin binding to actin filaments
MLCK	myosin light chain kinase	phosphorylates MLC
MLCP	myosin light chain phosphatase	dephosphorylates MLC
MLCP-P	phosphorylated MLCP	inactive form of MLCP
MBS	myosin-binding subunit	subunit of MLCP whose phosphorylation makes MLCP inactive
ROCK	Rho-associated kinase	ROCK phosphorylates MLCP at its myosin-binding subunit (MBS)
I	effect of calyculin	inhibits MLCP from dephosphorylating myosin, thus enhancing contractility

Table 4.1: Abbreviations and full names of the biochemical components. For each component, a short description of its function is given.

at focal adhesions. More importantly, focal adhesions are known to recruit different Rho-GEFs, thus activating Rho at the focal adhesions, compare Fig. 4.2. The active Rho is then able to bind Rho-associated kinase (ROCK) and thereby activate its kinase activity [138]. Since the active ROCK is bound to Rho-GTP, we assume in our model that these components are not diffusible but are localized to the focal adhesions. For the same reason, we neglect the direct interaction of ROCK and myosin, which has been reported to occur *in vitro*. Active ROCK phosphorylates the diffusible myosin light chain phosphatase (MLCP) at its myosin-binding subunit (MBS). MLCP and its antagonistic partner myosin light chain kinase (MLCK) are the main regulators of myosin contractility in the context we are interested in. Both enzymes interact with the regulatory myosin light chain subunit (MLC) of the myosins. Depending on the respective activities, MLC gets either phosphorylated or dephosphorylated. MLC, in turn, controls the myosin binding to actin filaments. Only if MLC is phosphorylated, myosin is able to bind actin filaments and perform its ATPase cycle that converts chemical energy into mechanical work, e.g. contraction of stress fibers [139]. By phosphorylating MLCP, ROCK effectively enhances the phosphorylation level of MLC. In

Model equations

$$\frac{\partial \text{ROCK}(t)}{\partial t} = \frac{r_1 F_b(t)(\text{ROCK}_{\text{tot}} - \text{ROCK}(t))}{K_1 + (\text{ROCK}_{\text{tot}} - \text{ROCK}(t))} - \frac{V_{-1}\text{ROCK}(t)}{K_{-1} + \text{ROCK}(t)} \quad \text{(m1)}$$

$$\frac{\partial \text{MLCP}(x,t)}{\partial t} = \frac{V_{-2}\text{MLCP-P}(x,t)}{K_{-2} + \text{MLCP-P}(x,t)} + D\frac{\partial^2 \text{MLCP}(x,t)}{\partial x^2} \quad \text{(m2)}$$

$$\frac{\partial \text{MLCP-P}(x,t)}{\partial t} = -\frac{V_{-2}\text{MLCP-P}(x,t)}{K_{-2} + \text{MLCP-P}(x,t)} + D_p\frac{\partial^2 \text{MLCP-P}(x,t)}{\partial x^2} \quad \text{(m3)}$$

$$\frac{\partial n(x,t)}{\partial t} = \frac{V_3\left(1 - n(x,t)\right)}{K_3 + \left(1 - n(x,t)\right)} - \frac{r_{-3}\text{MLCP}(x,t)n(x,t)}{K_{-3}I + n(x,t)} \quad \text{(m4)}$$

$$\left(\frac{\partial}{\partial x}\tilde{\gamma}(x,t)\frac{\partial}{\partial x}\frac{\partial}{\partial t} + \frac{\partial}{\partial x}k(x)\frac{\partial}{\partial x}\right)u(x,t) = -\frac{1}{a}\frac{\partial}{\partial x}F_s(x,t) \quad \text{(m5)}$$

Boundary conditions at $x = 0, L$

$$\frac{\partial \text{MLCP}(x,t)}{\partial x} = \pm\frac{R_2}{D}\frac{\text{ROCK}(t)\text{MLCP}(x,t)}{K_2 + \text{MLCP}(x,t)} \quad \text{(bc2)}$$

$$\frac{\partial \text{MLCP-P}(x,t)}{\partial x} = \mp\frac{R_2}{D_p}\frac{\text{ROCK}(t)\text{MLCP}(x,t)}{K_2 + \text{MLCP}(x,t)} \quad \text{(bc3)}$$

$$u(x,t) = 0 \qquad \text{stiff boundaries} \quad \text{(bc5)}$$

Abbreviations

$F_s(x,t) = F_{max}\, n(x,t)$

$\tilde{\gamma}(x,t) = \gamma(x) + F_s(x,t)/v_0$

$F_b(t) = a\tilde{\gamma}(0,t)\partial_x\partial_t u(0,t) + ak(0)\partial_x u(0,t) + F_s(0,t)$

Table 4.2: Summary of model equations. Eqs. (m1-m4) describe successive biochemical signaling events: (m1) focal adhesion associated activation of ROCK; (m2) and (m3) phosphorylation and diffusion of MLCP and dephosphorylation and diffusion of MLCP-P; (m4) regulation of the active fraction of the myosins, which is identified with the phosphorylated fraction of MLC. Eq. (m5) is the mechanical model equation for stress fibers, where $u(x,t)$ is the displacement along the fiber. The boundary conditions for the partial differential Eqs. (m2), (m3), (m5) are given by (bc2), (bc3), (bc5), respectively. In Eq. (bc2), (bc3), the upper (lower) sign is valid for the left $x = 0$ (right $x = L$) boundary. For the sake of clarity, we have introduced the listed abbreviations for the stall force F_s, the effective viscosity $\tilde{\gamma}$ and the force exerted on the boundary F_b. The presented results have been derived with the assumptions that: (I) The diffusion properties of the phosphorylated and unphosphorylated form of the phosphatase are the same, hence $D = D_p$. (II) The viscoelastic properties of the stress fiber do not vary in space, therefore $k(x) \to k$ and $\tilde{\gamma}(x,t) \to \gamma + F_{max}\, n(x,t)/v_0$.

this way, Rho-activation leads to increasing myosin contractility in stress fibers.

Our model for the biochemical reaction-diffusion system assumes that each enzyme stimulation follows Michaelis-Menten kinetics [140]. In Michaelis-Menten kinetics, production first increases linearly with educt concentration and then saturates at a maximal production velocity if educt concentration exceeds the value set by the Michaelis-Menten constant. The precise molecular process corresponding to the conversion of force into a biochemical signal at focal adhesions has not been identified yet. However, it is expected that mechanical forces exerted on focal adhesions eventually initiate the loading of Rho-GTP leading to ROCK activation. Due to the lack of information we lump the focal adhesion associated processes into one equation that effectively describes the conversion of ROCK into its activated form (presumably complexed with Rho-GTP). The mechanical force F_b that stimulates the activation is treated as an enzyme in the framework of Michaelis-Menten kinetics:

$$\frac{\partial \mathrm{ROCK}(t)}{\partial t} = \frac{r_1 F_b(t)(\mathrm{ROCK_{tot}} - \mathrm{ROCK}(t))}{K_1 + (\mathrm{ROCK_{tot}} - \mathrm{ROCK}(t))} - \frac{V_{-1}\mathrm{ROCK}(t)}{K_{-1} + \mathrm{ROCK}(t)} \tag{4.1}$$

The variable ROCK denotes the activated form of ROCK and we assume that the overall concentration of ROCK is constant at $\mathrm{ROCK_{tot}}$. The force exerted by the stress fiber on the focal adhesion, $F_b(t)$, stimulates the conversion of ROCK into its activated form with maximum velocity $r_1 F_b(t)$ and Michaelis-Menten constant K_1. The parameter r_1 is equivalent to a rate constant but relates mechanical force to a chemical reaction. For this reason the units of r_1 are given as [nM/s nN]. The force $F_b(t)$ will depend on the stress fiber deformation. The second term accounts for the degradation of activated ROCK to its inactive form, with maximum velocity V_{-1} and Michaelis-Menten constant K_{-1}. Since we expect ROCK in its active form to be associated with focal adhesions, we omit diffusive contributions to this equation.

One main effector of ROCK is MLCP, which we regard as a diffusible compound leading to a reaction-diffusion equation:

$$\frac{\partial \mathrm{MLCP}(x,t)}{\partial t} = \frac{V_{-2}\mathrm{MLCP\text{-}P}(x,t)}{K_{-2} + \mathrm{MLCP\text{-}P}(x,t)} + D\frac{\partial^2 \mathrm{MLCP}(x,t)}{\partial x^2} \tag{4.2}$$

Here, the variables MLCP-P and MLCP denote the phosphorylated and unphosphorylated form of myosin light chain phosphatase, respectively. The first term accounts for the dephosphorylation of MLCP-P with maximum velocity V_{-2} and Michaelis-Menten constant K_{-2}. The second term allows for the diffusion of the phosphatase with diffusion constant D. The phosphorylation level of MLCP is also regulated by the active form of ROCK which catalyzes the reverse reaction, that is the conversion of the phosphatase into its phosphorylated form. However, ROCK is only active in the vicinity of focal adhesions located at each end of the stress fiber. Therefore this source term can be incorporated into the boundary conditions for Eq. (4.2), in the sense that the diffusive flux into the boundary has to balance the conversion into its inactive form:

$$D\frac{\partial \mathrm{MLCP}(x=0,t)}{\partial x} = \frac{R_2\mathrm{ROCK}(t)\,\mathrm{MLCP}(x=0,t)}{K_2 + \mathrm{MLCP}(x=0,t)} \tag{4.3}$$

The same relation, but with opposite sign is valid at the other end at $x = L$, compare Tab. 4.2. The reaction is again modeled with Michaelis-Menten kinetics, where $R_2 = r_2 v_b$ is the product of a rate constant r_2 with an effective volume v_b of the focal adhesion in which the reaction takes place. K_2 is the usual Michaelis-Menten constant. For the phosphorylated form of the phosphatase (MLCP-P) equations similar to Eq. (4.2) and Eq. (4.3) are valid, but with opposite signs of the source terms and a diffusion constant which in principle can be different, see Tab. 4.2. MLCP together with MLCK regulate the phosphorylation level of MLC. Since myosin in stress fibers form mini-filaments, which are bound to actin filaments, we neglect diffusion of this compound, leading to the rate equation for the phosphorylated fraction n of MLC:

$$\frac{\partial n(x,t)}{\partial t} = \frac{V_3 \left(1 - n(x,t)\right)}{K_3 + \left(1 - n(x,t)\right)} - \frac{r_{-3} \mathrm{MLCP}(x,t) n(x,t)}{K_{-3} \, I + n(x,t)} \tag{4.4}$$

By allowing only the ratio of the phosphorylated fraction to vary, we assume that the overall amount of myosin in the stress fibers is fixed. MLC is phosphorylated by MLCK with a maximum velocity $V_3 = r_3 \mathrm{MLCK}$ and respective Michaelis-Menten constant K_3. Here we assume that the concentration of MLCK is constant within the cell. The kinase is antagonized by MLCP that dephosphorylates MLC with a rate constant r_{-3} and Michaelis-Menten constant K_{-3}. The factor I is an inhibition parameter defined below. Since MLCP has spatial dependent source terms and is diffusible, the inhibition of MLC by the phosphatase will vary in space.

To complete the biochemical modeling we have to specify how the induction of calyculin is treated in our model. Calyculin is an inhibitor of MLCP and thereby enhances the phosphorylation level of MLC. We model the interaction of calyculin with its target MLCP as a competitive inhibition leading to the additional factor I in the last term of Eq. (4.4) [151]. In the presence of calyculin $I > 1$ (in absence of the drug: $I = 1$) which effectively increases the Michaelis-Menten constant K_{-3} and thus decreases the rate of MLC dephosphorylation. Hence more myosin motors will be activated and cell contractility is stimulated. The induction of the drug is then modeled by switching instantaneously the inhibition parameter from $I = 1$ to $I = 3$. Thereby, we omit the time delay caused by the internalization of the drug.

The used parameter values for the reaction-diffusion system are based on an extensive survey of the literature and are summarized in Tab. 4.3. If a range of values is reported in the literature, we chose an intermediate value for this parameter. If no value could be found in the literature, we made reasonable assumptions based on similar parameters in other systems. No attempt was made to fit the parameters to some target function.

We first analyze the properties of this reaction diffusion system assuming that the boundary force exerted on the focal adhesions is held at a constant level. This would be the case if the myosin forces were in a stationary state and not regulated by the biochemical signals emerging from focal adhesions. We impose artificial initial conditions that all components (ROCK, MLCP-P and n) are at zero activation level but set the boundary force to $5\,\mathrm{nN}$, a typical force observed for fibroblasts [40]. This mechanical stimulation triggers the accumulation of active ROCK at focal adhesions, see

Time dependent reaction variables				
Abbreviation	Meaning	Used value	Reference values	Ref.
ROCK	activated form of ROCK	$0\ldots5\,$nM	$\gtrsim 1\,$nM	[138]
MLCP	unphosphorylated form of MLCP	$0\ldots1.2\,\mu$M	$1.2\pm0.3\,\mu$M	[141]
MLCP-P	phosphorylated form of MLCP	$0\ldots1.2\,\mu$M	$1.2\pm0.3\,\mu$M	[141]
n	fraction of active myosin	$0\ldots1$	[MLC-P]/[myosin]	
Reaction constants				
MLCK	myosin light chain kinase	$0.1\,\mu$M	$\gtrsim 100\,$nM	[142]
M	myosin concentration	$30\,\mu$M	$25\ldots30\,\mu$M	[143]
K_1	Michaelis constant	$5\,$nM	(no value)	
K_{-1}	Michaelis constant	$4.7\,$nM	(no value)	
K_2	Michaelis constant	$0.1\,\mu$M	$0.10\pm0.01\,\mu$M	[138]
K_{-2}	Michaelis constant	$15\,\mu$M	(no value)	
K_3*M	Michaelis constant	$20\,\mu$M	$52.1\pm7.1\,\mu$M	[144]
			$34.5\pm2.8\,\mu$M	[138]
			$18\,\mu$M	[145]
			$7.7\ldots96.0\,\mu$M	[146]
			$19\ldots53\,\mu$M	[142]
			$20\,\mu$M	[147]
$K_{-3}*$M	Michaelis constant	$10\,\mu$M	$10\,\mu$M	[148]
r_1	rate constant	$0.3\,$nM/s nN	(no value)	
V_{-1}	maximum velocity	$1.8\,$nM/s	(no value)	
r_2	rate constant	$2.4\ $1/s	$2.36\pm0.10\ $1/s	[138]
R_2	maximum velocity	$4.8\,\mu$m/s	r_2*v_b	
V_{-2}	maximum velocity	$0.1\,\mu$M/s	(no value)	
r_3*M	rate constant	$10\ $1/s	$2.00\pm0.36\ $1/s	[144]
			$3.85\pm0.095\ $1/s	[138]
			$5.17\ $1/s	[145]
			$7.37\ldots171.3\ $1/s	[146]
			$70\ldots100\ $1/s	[142]
			$4.64\ $1/s	[147]
V_3*M	maximum velocity	$1.0\,\mu$M/s	r_3*MLCK$*$M	
$r_{-3}*$M	rate constant	$21\ $1/s	$21\ $1/s	[148]
D	diff. const. of MLCP & MLCP-P	$14\,\mu$m^2/s	$10\ldots100\,\mu$m^2/s	[149]
v_b	effect. react. vol. of FAs	$2.0\,\mu$m	(no value)	
I	inhibition parameter	$1\rightarrow3$	(no value)	
Parameters of mechanical model				
F_{max}	stall force	$50\,$nN	(no value)	
v_0	maximum motor velocity	$1.0\,\mu$m/s	$\approx 0.1\ldots1\,\mu$m/s	[150]
a	sarcomeric length	$1.0\,\mu$m	$1.0\,\mu$m	[31]
k	spring stiffness	$45\,$nN/μm	$45.7\,$nN/a	[89]
γ	viscosity	$45\,$nN s/μm	$\approx \tau k = 45.7\,$nN s/a	[63, 89]
L	fiber length	$50\,\mu$m	$\approx 20\ldots80\,\mu$m	

Table 4.3: Model parameters based on literature search. We have set the model parameters such that they fit into the reported range. The equation for the phosphorylated fraction of MLC is normalized to the total myosin concentration denoted by M. In order to make the involved reaction constants comparable to the literature values we give K_3, K_{-3}, r_3 ,r_{-3} and V_3 scaled with M. Eq. (4.1) translates mechanical forces into biochemical activation. For this reason the units of the rate constant r_1 are given as [nM/s nN]. The typical equilibration time τ of stress fibers is of the order of a few seconds, see Tab. 3.1. Therewith, we roughly estimate the viscosity value as $\gamma \approx \tau k$, using $\tau = 1\,$s. Myosin activation by calyculin is modeled as competitive inhibition of the phosphatase. The inhibition parameter I is switched instantaneously from $I = 1$ to $I = 3$. Some of the reported values have been measured for the interactions of protein fractions and not for the native proteins. Furthermore, the experiments have been carried out on proteins extracted from different species.
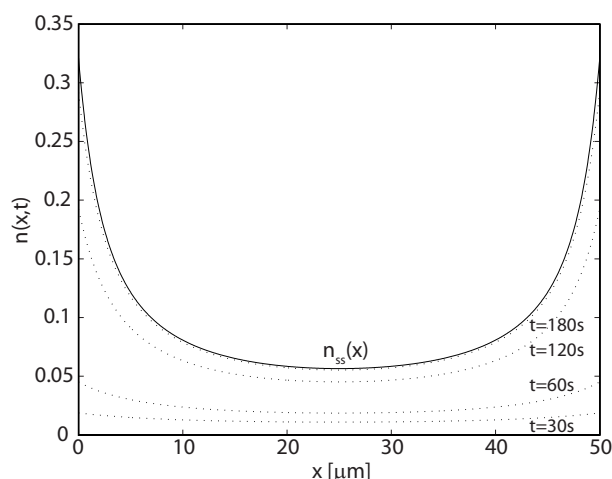
Figure 4.5: Spatial dependence of the active myosin fraction $n(x,t)$ at four different time points $t \in \{30\,\mathrm{s}, 60\,\mathrm{s}, 120\,\mathrm{s}, 180\,\mathrm{s}\}$ as well as for the steady state, $n_{ss}(x)$: We solve the biochemical model implying the artificial initial conditions that all components are at zero activation level, but set the boundary force to $5\,\mathrm{nN}$. Because of this mechanical trigger at focal adhesions, MLC gets preferentially activated at the boundaries via the Rho-pathway leading to a steady increase of the myosin activation level. Due to diffusible compounds in the Rho-pathway, the increased activation level is smoothed out towards the center of the cell.

Eq. (4.1), creating a sink for the active form of MLCP. Thus in those boundary regions MLCK dominates and increases MLC phosphorylation. Closer to the center of the cell MLC rather remains in its unphosphorylated form. The width of the interfacial region of intermediate MLC-phosphorylation level is mainly determined by the competition between diffusiveness and degradation of the phosphatase. The faster the diffusion, the wider the intermediate region. On a typical timescale of a few minutes all components equilibrate to their steady state concentration profile, where MLC is highly phosphorylated at the boundaries, but is poorly activated at the center of the stress fiber. In Fig. 4.5 we show the typical equilibration of the phosphorylated fraction of MLC, $n(x,t)$, as obtained from a solution of the full system of biochemical reaction-diffusion equations. Below we will argue that this phosphorylation profile of MLC implies a spatially varying myosin motor activation leading to an inhomogeneous stress fiber contraction.

4.4   The altered stress fiber model

Stress fiber contraction dynamics upon stimulation with the drug calyculin will be described by the model developed earlier in section 2.1.1. However, the model has to be slightly modified to cope with the present situation. On the one hand, the myosin motor activity can not be assumed to be constant along the fiber which will give rise to spatially varying contractile myosin stresses. On the other hand, the fibers are clamped at both ends by focal adhesions which prevents large displacements of fiber elements.
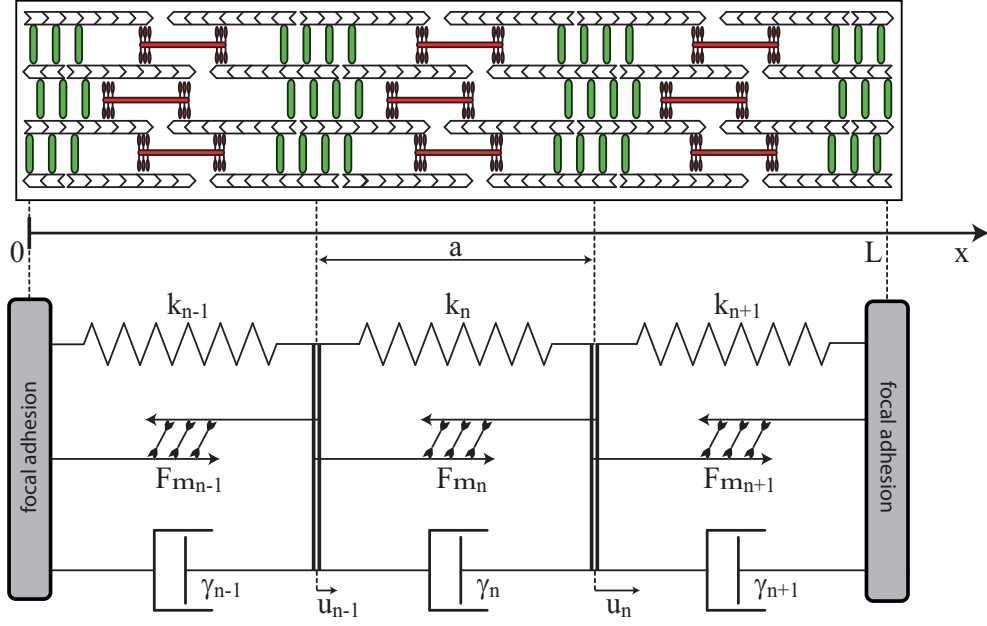
Figure 4.6: We model a stress fiber as a string of viscoelastic and contractile elements such that the spring stiffness k_n, the viscosity γ_n and the motor force F_{m_n} can vary spatially. E.g. the latter will vary spatially due to different myosin activity at the periphery compared to the center. The displacement of a certain site n is denoted by u_n. In the following, we assume clamped ends as boundary conditions, namely $u(0,t) \equiv 0$ and $u(L,t) \equiv 0$ where L is the total length of the fiber.

This is in contrast to stress fiber laser surgery experiments where the fibers retract over several micrometers and the external coupling, particularly the elastic crosslinks to the surrounding, becomes important. In the present situation, due to the small absolute displacements, we neglect these external viscoelastic interaction terms. Also because of this simplification we no longer have to distinguish between the internal and external viscoelastic properties of the fiber. Thus we can drop the lengthy indices and define $k = k_{int}$, $\gamma = \gamma_{int}$ and $\tilde{\gamma} = \tilde{\gamma}_{int}$. Analog to the derivation presented earlier we start with a discrete chain of Kelvin-Voigt bodies each of which contains an additional contractile element. A schematic representation of the model is given in Fig. 4.6. At each site n all spring forces, viscous drags and the forces built up by motor proteins have to balance:

$$0 = \gamma_{n+1}(\dot{u}_{n+1} - \dot{u}_n) - \gamma_n(\dot{u}_n - \dot{u}_{n-1}) + k_{n+1}(u_{n+1} - u_n)$$
$$-k_n(u_n - u_{n-1}) + F_{m_{n+1}} - F_{m_n}$$
(4.5)

In contrast to the previous discussion, we allow that the spring stiffness, the viscosity as well as the motor force vary spatially. The continuum limit of the above equation can be performed according to the scheme presented in section 2.1.3. The result is given by:

$$a^2 \left(\frac{\partial}{\partial x} \gamma(x) \frac{\partial}{\partial x} \frac{\partial}{\partial t} + \frac{\partial}{\partial x} k(x) \frac{\partial}{\partial x} \right) u(x,t) + a \frac{\partial F_m(x,t)}{\partial x} = 0 \qquad (4.6)$$
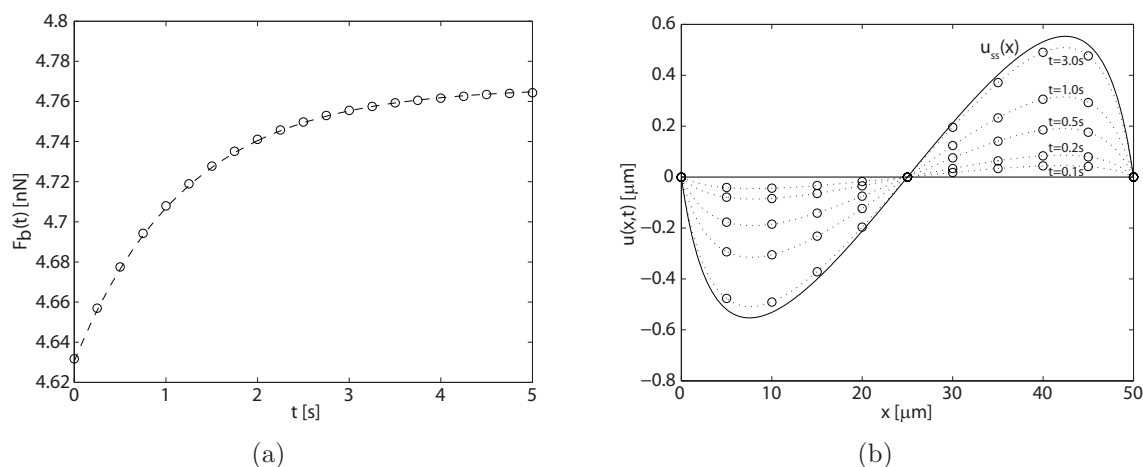
(a)

(b)

Figure 4.7: (a) Time course of boundary force $F_b(t)$. The solution of the Volterra equation, Eq. (4.11), indicated by circles, was calculated by applying an iteration rule further explained in the main text. The dashed line is the boundary force deduced from direct numerical solution of Eq. (4.9), which we include for comparison. For the assumed initial condition $\partial_x u(x,0) \equiv 0$, the boundary force increases from its non-zero value at $t = 0$, given by Eq. (4.15) and quickly saturates at larger values. (b) We first analyze the solution of the mechanical equation Eq. (4.9) by assuming a steady state myosin activation level, $n_{ss}(x)$, shown in Fig. 4.5. For this simplifying case where the myosin activation level is not time dependent, Eq. (4.9) can be solved both numerically and analytically. Fig. 4.7(b) shows the analytical solution Eq. (4.10), indicated by circles, whereas the direct numerical solution of Eq. (4.9) is indicated by dotted lines. The solution is given at time points $t \in \{0.1\,\mathrm{s}, 0.2\,\mathrm{s}, 0.5\,\mathrm{s}, 1.0\,\mathrm{s}, 3.0\,\mathrm{s}\}$ as well as for the steady state $u_{ss}(x)$, assuming the initial condition $\partial_x u(x,0) \equiv 0$ and the boundary conditions $u(0,t) \equiv 0$ and $u(L,t) \equiv 0$.

Note that the leading differential operator ∂_x acts on $\gamma(x)$ and $u(x,t)$. The same holds for the second term. If k did not vary spatially, it would simplify to the Laplacian $k\partial_x^2$ as it appeared in the previous chapter. The contractile force F_m can be described again by a linearized force-velocity relation and in this way becomes depended on the displacement $u(x,t)$. The contraction velocity, which enters the force-velocity relation, is given in the discrete picture as $v_n = -(\dot{u}_n - \dot{u}_{n-1})$, see also the discussion in section 2.1.1. Accordingly, in the continuum limit the contraction velocity is determined by $v(x,t) = -a\partial_x \dot{u}(x,t)$. This found expression for the contraction velocity is inserted into the force-velocity relation Eq. (2.2) leading to:

$$F_m(x,t) = F_s(x,t)\left(1 + \frac{a}{v_0}\frac{\partial}{\partial x}\dot{u}(x,t)\right) \tag{4.7}$$

In contrast to Eq. (2.2), here the stall force is not constant but depends on the phosphorylated fraction $n(x,t)$ of MLC along the stress fiber. This is due to the fact that along a myosin minifilament and depending on MLC phosphorylation, a larger or smaller fraction of myosin heads is able to bind to actin and perform ATP-cycles. The more

myosin heads are active the larger the maximum force that the bundle can exert to the actin filaments. In our model we regard the ensemble of myosins within a cross section of a stress fiber as one large contractile unit with an effective stall force that depends linearly on the active fraction n of myosin heads:

$$F_s(x,t) = F_{max}\, n(x,t) \tag{4.8}$$

The effective stall force, $F_s(x,t)$, would reach the maximum force F_{max} if all myosins within this cross section would be working ($n = 1$). In the following we set $F_{max} = 50\,\text{nN}$ which will result in boundary forces exerted by the fiber of about $5\,\text{nN}$ which corresponds to typical values observed in experiments [40]. Eq. (4.6) together with Eq. (4.7) and Eq. (4.8) lead to the final model equation for the stress fiber

$$\left(\frac{\partial}{\partial x}\tilde{\gamma}(x,t)\frac{\partial}{\partial x}\frac{\partial}{\partial t} + \frac{\partial}{\partial x}k(x)\frac{\partial}{\partial x} \right) u(x,t) = -\frac{1}{a}\frac{\partial}{\partial x}F_s(x,t) \tag{4.9}$$

where we have again introduced the effective viscosity $\tilde{\gamma}(x,t) = \gamma(x) + F_s(x,t)/v_0$, similar to proceedings in section 2.1.1, although here the effective viscosity varies spatially. Interestingly, only the variation of the motor force appears on the right hand side of the equation. As a consequence, a homogeneous motor activity will not contribute to the displacements within the string. To obtain some intuition for this equation, assume that the spatially varying stall force is given for example by the steady state solution n_{ss} of the reaction diffusion system, depicted in Fig. 4.5, such that $F_s(x) = F_{max}n_{ss}(x)$. For this simplifying case where the stall force does not vary in time, Eq. (4.9) can be integrated and the time dependent solution for $u(x,t)$ is given by:

$$u(x,t) = u(0,t) + \int_0^x dx' \left(\partial_{x'}u(x',t_0)e^{-\frac{t-t_0}{\tau(x')}} - \frac{F_s(x')}{ak(x')}\left(1 - e^{-\frac{t-t_0}{\tau(x')}}\right) \right.$$
$$\left. + \frac{1}{a\tilde{\gamma}(x')}e^{-\frac{t-t_0}{\tau(x')}}\int_{t_0}^t F_b(t')e^{\frac{t'-t_0}{\tau(x')}}dt' \right) \tag{4.10}$$

Here, we have set $\tau(x) = \tilde{\gamma}(x)/k(x)$, the typical equilibration time with which perturbations decay at a certain position. For example the initial conditions $\partial_x u(x,t_0)$ can be regarded as perturbations to the steady state and they decay with $\exp(-t/\tau(x))$. The three integration constants can be identified as the displacement at the left boundary $u(0,t)$, the force exerted to the left boundary $F_b(t)$, and the initial strain along the fiber, $\partial_x u(x,t_0)$. They are determined by the boundary and initial conditions. Experiments by Peterson et al. [31] are arranged with cells on stiff substrates to which the ends of the stress fiber are connected by focal adhesions. Therefore, the appropriate boundary conditions are clamped ends, namely $u(0,t) \equiv 0$ and $u(L,t) \equiv 0$. From the second condition one is able to calculate the missing integration constant $F_b(t)$ for any initial condition $\partial_x u(x,t_0)$. The force on the left boundary $F_b(t)$ is given as solution of an inhomogeneous Volterra equation of the first kind:

$$\int_{t_0}^t K(t-t')F_b(t')dt' = g(t) \tag{4.11}$$

with the kernel

$$K(t - t') = \int_0^L dx' \frac{1}{a\tilde{\gamma}(x')} e^{-\frac{t-t'}{\tau(x')}}$$

(4.12)

and the inhomogeneous part $g(t)$ dependent on the initial condition $\partial_x u(x, t_0)$:

$$g(t) = \int_0^L dx' \left(\frac{F_s(x')}{ak(x')} \left(1 - e^{-\frac{t-t_0}{\tau(x')}} \right) - \partial_{x'} u(x', t_0) e^{-\frac{t-t_0}{\tau(x')}} \right)$$

(4.13)

In order to solve the integral equation Eq. (4.11) for $F_b(t)$, we calculate its time derivative, leading to:

$$F_b(t) = \frac{\dot{g}(t)}{K(0)} - \frac{1}{K(0)} \int_{t_0}^t \dot{K}(t - t') F_b(t') dt'$$

(4.14)

This equation yields an explicit expression for the initial force F_b at $t = t_0$:

$$F_b(t_0) = \frac{\dot{g}(t_0)}{K(0)} \neq 0$$

(4.15)

By inspection of the kernel Eq. (4.12) and the inhomogeneous part Eq. (4.13) one finds that the initial force on the boundary has a finite value, even for the initial condition $\partial_x u(x, t_0) \equiv 0$. Eq. (4.14) also yields an iteration rule for the time course of $F_b(t)$, by applying a quadrature, where $F_b(t_0)$ from Eq. (4.15) is used as a starting value. The solution for $F_b(t)$ is shown in Fig. 4.7(a). The boundary force is rising from its initial value and then quickly saturates at about 4.8 nN. The result for $F_b(t)$ can then be set into the general solution (Eq. (4.10)) for the displacement $u(x, t)$ along the fiber. Fig. 4.7(b) shows this solution by using the steady state activation level for the myosins ($F_s(x) = F_{max} n_{ss}(x)$), shown in Fig. 4.5, and assuming the initial condition $\partial_x u(x, t_0) \equiv$ 0 as well as the boundary conditions $u(0, t) \equiv 0$ and $u(L, t) \equiv 0$. Beside the analytical solution, indicated by circles, we also included the direct numerical solution of Eq. (4.9) for comparison. The numerical solution was derived by using the MATLAB algorithm "pdepe". The sinusoidal shape of the function u results from stronger contractile motors close to the boundaries causing the fiber elements to displace into the direction of the boundaries. Hence the displacement u is positive (negative) along the right (left) half of the fiber. It is worth noting that the mechanical equilibration of the stress fiber occurs within seconds in contrast to the biochemical system which equilibrates over minutes.

4.5   The coupled feedback system

We already argued that the system of focal adhesions and stress fibers exhibits a closed biochemical and mechanical positive feedback loop. Despite this fact the previous results were derived under the assumption that the mechanically triggered biochemical signals at FAs originate from a constant force. In order to model the full biological system, the varying boundary forces have to be fed back into the equation describing the mechanotransduction Eq. (4.1). Since the stress fiber model does not include any

crosslinks (e.g. intermediate contacts to the substrate) the tension σ within the fiber has to be constant and therefore equals the boundary forces:

$$F_b(t) = \sigma(x=0) = a\tilde{\gamma}(0,t)\partial_x\partial_t u(0,t) + ak(0)\partial_x u(0,t) + F_s(0,t) \qquad (4.16)$$

This relation now connects the biochemical signaling to the mechanical deformation of the stress fiber. Thus, the coupled system of reaction equations Eq. (4.1) to Eq. (4.4), and the mechanical equation Eq. (4.9) have to be solved simultaneously. This can be done numerically by using the MATLAB algorithm "pdepe". The whole system of equations and the used parameter values are summarized in Tab. 4.2 and Tab. 4.3, respectively.

By performing a steady state analysis, described in great detail in chapter 5, we find that this system of equations exhibits two stable steady states for the used parameter values: the first state is characterized by a generally low activation level $n_{ss}(x)$ of the myosin motors resulting in marginal boundary forces, whereas in the second state myosin motors are non-uniformly activated and the exerted forces reach a few nN. This bistability is characteristic for a positive feedback system [16]. The first "non-active" state would correspond to cells that failed to establish mechanical stress whereas the second "active" state corresponds to cells that are well adhered to the substrate. In order to simulate the drug experiments by Peterson et al. [31], we start with the system residing in this active state and then we perturb the system at t=0 by triggering the stimulation with calyculin. This is modeled by instantaneously switching the inhibition parameter from $I = 1$ to $I = 3$, thereby omitting the time delay caused by the internalization of the drug. The stimulation with calyculin reduces the phosphatase activity and elevates the myosin activation level everywhere leading to a quick increase in the boundary forces exerted by the stress fiber. The time course of the force exerted on the focal adhesions is shown in Fig. 4.8(a). Subsequently, the positive mechanical feedback triggers additional signaling at focal adhesions activating myosin motors preferentially at the cell periphery. This results in strong spatial gradients in myosin motor activity, see Fig. 4.8(b). The strong peripheral motors then contract the fiber at the expense of the central regions where the fiber has to elongate. This can be further analyzed by using the numerical solution for the displacement $u(x,t)$. The steady states of the displacement u_{ss} before and after stimulation with calyculin are shown in Fig. 4.9(a).

The stimulation strongly increases the displacement along the fiber resulting in substantial contraction of the fiber close to the boundaries but in expansion around the cell center. This finding becomes more apparent in the shown striation pattern calculated from the displacement after stimulation (upper string) compared to the striation pattern of a completely undistorted fiber (lower string). The bands close to the boundaries have been contracted whereas the bands around the center have been expanded, compare Fig. 4.10. We have to stress the fact that the presented stress fiber model is continuous, thus the model cannot distinguish between α-actinin bands or MLC bands. The color code in Fig. 4.9(a) and Fig. 4.10 is therefore arbitrary. We also derive the local relative change of density within the fiber which is given in general as the negative trace of the strain tensor $\delta\rho_{rel} = (\rho - \rho_0)/\rho_0 = -\text{tr}(u_{ij})$. Since the model is one dimensional this simplifies to $\delta\rho_{rel} = -\partial_x u(x,t)$, plotted in Fig. 4.9(b). The
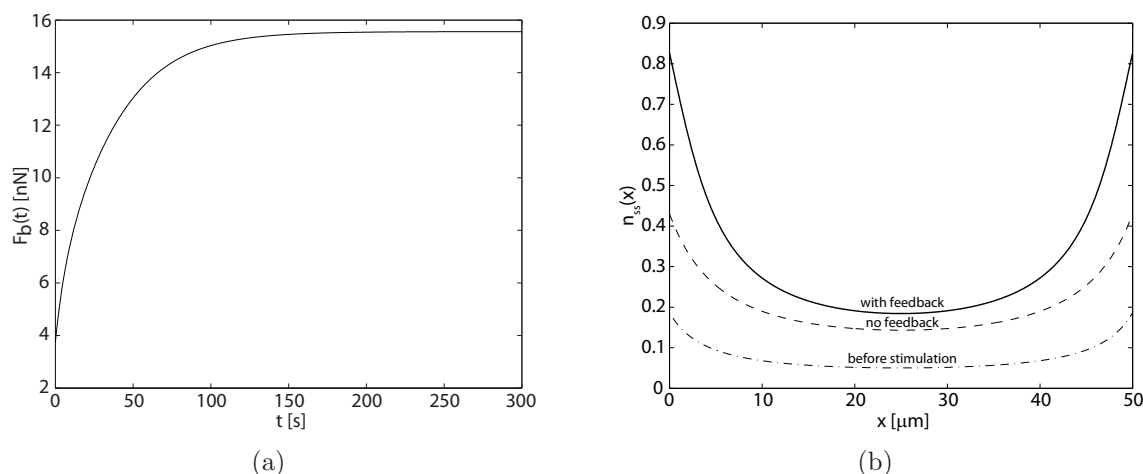
(a)   (b)

Figure 4.8: (a) At $t = 0$ calyculin is added to the system. Then myosin motors along the filament get activated and further increase the tension within the fiber. The time course of the force $F_b(t)$ transduced to the boundaries is shown. (b) Steady state profile of the active myosin fraction before stimulation with the drug (dash-dotted line), after stimulation including the mechanical feedback (solid line) and after stimulation but neglecting the mechanical feedback (dashed line). For the latter case, homogeneous induction of the drug causes an almost uniform elevation of myosin activity. Slight differences between center and periphery persist but rather marginally extend, whereas the closed feedback system results in an amplification of the spatial differences of myosin activation.

local relative change of bandwidth at a certain position within the fiber, is then simply given by: $(w(x,t) - w_0)/w_0 = -\delta\rho_{rel}(x,t) = \partial_x u(x,t)$. The figure shows that the inhomogeneous motor activity causes a contraction of the bands of about 55% close to the fiber ends (the relative change in density is positive), whereas the pattern expands up to 15% at the middle of the fiber (the relative change in density is negative).

The experimental time course data for the sarcomere length shown in Fig. 4.3 is intrinsically averaged over a certain area in the peripheral and central regions of the cell. In order to compare the model results with the experimental finding we therefore define similar central (center $\pm 10\,\mu$m) and peripheral (edges $\pm 10\,\mu$m) regions of the cell, indicated by vertical lines in Fig. 4.9(b). The expected sarcomere length at a certain position along the fiber is given by

$$w(x,t) = w_0 + u(x + w_0, t) - u(x,t) \ \ \text{or} \ \ w(x,t) = w_0\left(1 + \partial_x u(x,t)\right) \ \ \text{for} \ \ w_0 \ll L \ \ (4.17)$$

In the following analysis this measure is averaged over the defined central and peripheral regions, respectively. The deduced time courses for the mean pattern bandwidths in the distinct regions are shown in Fig. 4.10. The expected steady state striation patterns are illustrated as insets. Upon stimulation with calyculin, the peripheral mean bandwidth shrinks from its initial value of about $0.97\,\mu$m down to $0.83\,\mu$m, whereas in the central regions, the bands elongate from about $1.03\,\mu$m up to $1.13\,\mu$m. Interestingly the inital mean bandwidth at the center and periphery yet differ in the initial unperturbed steady
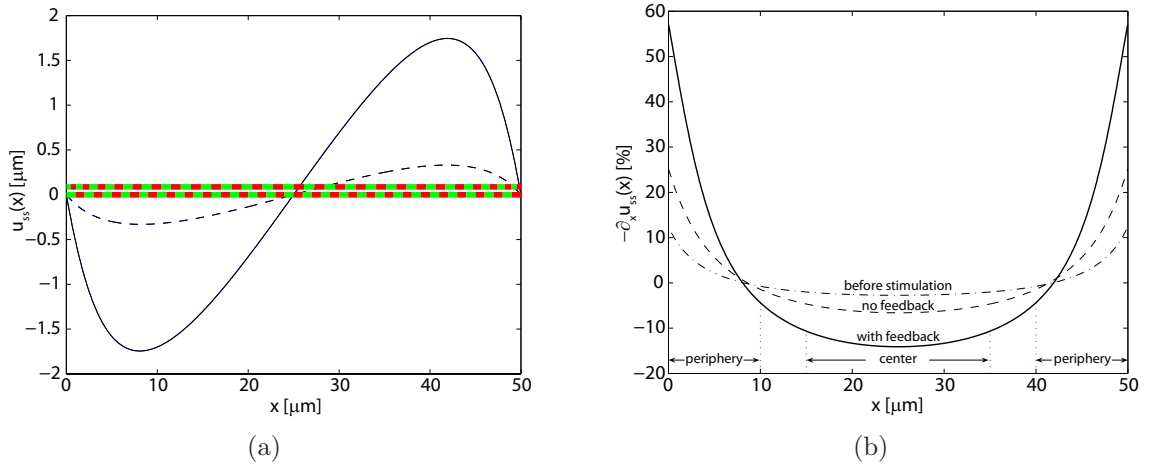
Figure 4.9: (a) Steady state solution of the displacement $u_{ss}(x)$ along the fiber before (dashed line) and after (solid line) stimulation with calyculin. The stimulation strongly increases the deformation of the fiber resulting in substantial distortion of the expected striation pattern (upper line) compared to the striation pattern of a completely undistorted fiber (lower line). The upper striation pattern was calculated from the displacement data. The bands close to the boundaries have been contracted (about 55%) whereas the bands around the center have been expanded (about 15%). (b) Relative change in density along the fiber in the steady state before stimulation with the drug (dashed-dotted line), after stimulation with the drug including the feedback (solid line) and after stimulation but neglecting the mechanical feedback (dashed line). Positive values correspond to a compression of the fiber, whereas negative values indicate elongation. In case of the closed feedback (solid line) the fiber strongly contracts close to the boundaries up to 55% but elongates at the center about 15%. In order to compare the model results with the experimental findings, we arbitrarily define central (center $\pm 10\,\mu$m) and peripheral (edges $\pm 10\,\mu$m) regions of the cell, indicated by vertical lines.

state of the cell ($1.03\,\mu$m compared to $0.97\,\mu$m). This results from the fact that the unperturbed fiber already exerts moderate forces on the focal adhesions which results in slight spatial gradients in myosin activation. These gradients then sharpen upon stimulation with calyculin, see Fig. 4.8(b) and Fig. 4.9(b). The model results agree qualitatively with the experimental findings by Peterson et al. [31] and the quantitative measurements are within the same order of magnitude, compare Fig. 4.3. It is worth mentioning that the amplitude of contraction or elongation of the fiber scales inversely with the fiber stiffness k: the softer the fiber, the stronger the mechanical deformation will be. Thus, a lower k value would simply explain the reported higher values for sarcomere contraction of about 30-40%. In our calculation we used $k = 45\,\text{nN}/\mu$m, a value reported by Deguchi et al [89]. The experimentally measured equilibration time of the stress fiber upon stimulation is about 20 min (Fig. 4.3) which compares to about 3 min for the model results. These quantitave difference originate from two model simplifications. First, we lump the focal adhesion associated processes into one equation and thereby shortcut the activation of ROCK and neglect prior activation steps of e.g. Rho-Gef or Rho-GTPase. Considering these steps would cause an additional
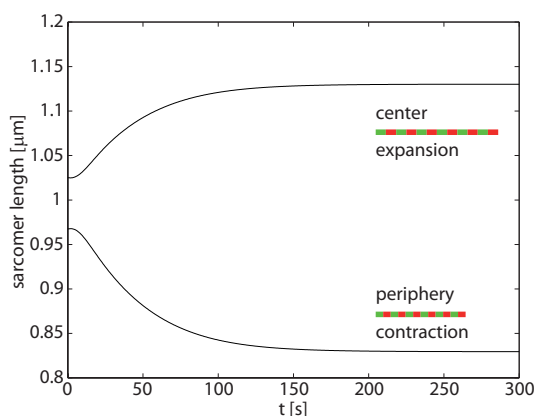
Figure 4.10: Time courses of the mean bandwidth of the fiber in the center (upper curve) and in the periphery of the cell (lower curve). The shown values are averages of the bandwidths at the center $\pm 10\,\mu$m for the central region and at the edges $\pm 10\,\mu$m for the peripheral region. The defined intervals are also shown in Fig. 4.9(b). The expected steady state striation patterns for the two distinct regions are shown as insets. These results agree qualitatively with the experimental findings by Peterson et al., shown in Fig. 4.3.

time delay. Secondly, the stimulation with calyculin happens instantaneously in the model omitting the time delay caused by the internalization of the drug. Refining the model and eliminating these simplifications will further decrease the differences in equilibration times.

To highlight the importance of the mechanical feedback we also include the expected results for a system neglecting this feedback shown as dashed lines in Fig. 4.8(b) and Fig. 4.9(b). Here the homogeneous induction of the drug causes an almost uniform elevation of myosin activation within the cell. Slight differences between cell center and cell periphery would persist but rather marginally extend (Fig. 4.8(b)). In fact stimulation also here leads to amplified distortions of the striation pattern. However, the changes in bandwidths are significantly smaller compared to the system incorporating the feedback (Fig. 4.9(b)). Thus, the closed biochemical and mechanical feedback loop is an essential feature required to describe the strong distortions of striation patterns upon homogenous drug induction.

4.6 Summary and outlook

In this chapter, we presented for the first time a mathematical model for the closed mechano-chemical feedback loop triggering the upregulation of focal adhesions and stress fibers which is typical for cell culture on stiff substrates. In regard to the biochemical part, we presented a reaction-diffusion model for Rho-signaling from focal adhesions towards stress fibers. Our modeling is based on an extensive review of the literature, which provides the list of diffusion and reaction constants summarized in Tab. 4.3.

In regard to the mechanical part, we extended the stress fiber model presented in

chapter 2, in order to take into account the spatial varying viscoelastic and contractile properties of the sarcomeric units. These variations result from spatial gradients of the biochemical signal that regulates the myosin activity along stress fibers. The biochemical signal couples into the stress fiber equations by altering the stall forces of the molecular motors. The established actomyosin forces are transmitted back to focal adhesions where they are treated similar to an enzyme that catalyzes Rho activation.

Combining the two model parts in the described way results in a complete model for the mechano-chemical feedback loop of interest [58]. By solving the complete model numerically, we can reproduce several experimental findings by Peterson et al. [31]. By means of our model, we can explain the slight differences in the mean pattern bandwidth at the center and periphery of unperturbed cells, as well as the unexpected sharpening of the spatial gradients upon stimulation with a homogenously distributed drug. According to our model, the observed contraction of sarcomeric units at the periphery, and their elongation at the center, result from a spatial gradient in myosin activity, which is induced by the diffusive biochemical signal. Such spatial differences in myosin light chain phosphorylation have indeed been found in experiments by Peterson et al. [31]. Most importantly, we also demonstrate that the positive mechano-chemical feedback has to be taken into account, in order to explain the experimental findings.

In general, our work shows how coupling of mechanics and biochemistry can be devised in a meaningful way. Furthermore, our model can be addressed to other issues in the context of cell adhesion. For example, we find that the described positive feedback loop can lead to bistability between highly contractile cells and cells that fail to establish actomyosin contractility. The bistability in the model system will be discussed thoroughly in the next chapter where we focus on cellular behavior on soft substrates and implications for the rigidity sensing of cells.

In order to close the mechano-chemical feedback loop in a concise way we neglected several aspects which might play a role in the considered system. They are discussed below and should be regarded as starting points for future model refinements.

Although in principle possible, our model does not account for certain spatial variations in mechanical properties along stress fibers. For example, mDia, a down stream target of Rho, regulates actin polymerization and thereby might locally change the mechanical properties of stress fibers. The (de-)polymerization of actin filaments could in addition depend on the local stress within the fiber [102]. As described above, Rho also regulates the phosphorylation level of MLC and in this way controls binding of myosin heads to actin filaments. Myosin, arranged in minifilaments, can be regarded as a crosslinker of actin filaments when MLC is phosphorylated. Thus, a lower phosphorylation level of MLC, as it is found experimentally at the center of the cell, might also locally change the rigidity of stress fibers.

Furthermore, myosins or crosslinkers can also unbind from actin filaments and dissociate from stress fibers. In order to account for such processes, one would have to consider further rate equations for the on- and off-kinetics of these proteins. Another aspect which we have neglected in our presented model is the fact that, over long time scales, focal adhesions are not stationary with respect to the substrate. It has been shown that force induced growth of focal adhesions is preferentially in the direction of the applied force, that is usually towards the center of the cell [39]. In addition,
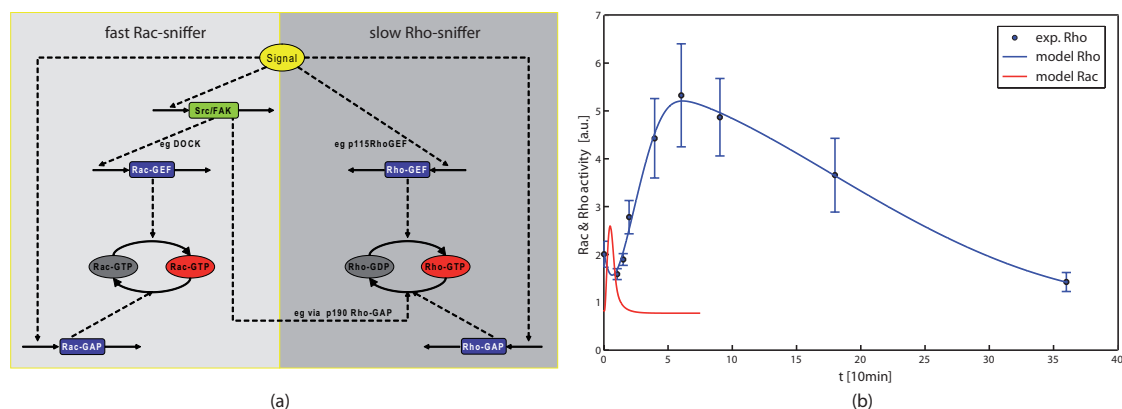
Figure 4.11: A brief outlook on the double sniffer model. (a) Suggestion for the reaction network which regulates Rac and Rho activity during early cell spreading. Protein names are included when reactions are known from the literature . The reaction network has been implemented in Copasi [152] in terms of rate equations. (b) Best model fit to the measured times courses of Rho-GTPase activity. Experimental time course of Rho-activity has been reproduced from [153]. Del Pozo et al. [154] reported a transient increase in Rac within 20 min after cell spreading. Model curves are given as solid lines and are in agreement with the experimental data.

focal adhesions detach at their back end. This leads to an effective movement of focal adhesions towards the center of the cell. Simultaneously, while the fiber is shortening, tension is expected to be released in the stress fiber which in turn changes the initiation of signals at focal adhesions.

The presented biochemical pathway can also be understood only as a first attempt to account for one major aspect in cell adhesion, that is the maturation of focal adhesions and contraction of stress fibers in a Rho dependent manner. As described in the introduction of this chapter, the regulatory network at focal adhesions is far more complicated as the considered Rho-GTPase pathway. For instance, it has been shown, that not only Rho-GEFs are associated with the adhesion plaque but also certain GAPs, which deactivate Rho. This interplay between activating and deactivating factors during early cell spreading leads to (1) an initial deactivation of Rho-activity, (2) a subsequent increase in Rho-activity and (3) a downregulation of Rho-activity on the long term [153], see Fig. 4.11(b). It remains elusive which of these processes are induced by chemical signals or depend on mechanical stress. Rac-activation has also been measured and shows a fast transient increase in early cell spreading [154]. The time course of Rac and Rho-activation can be understood in terms of rate equations (no spatial coordinate, no mechanics) assuming that Rac-activation as well as Rho-activation can be described by a sniffer motive [16]. In addition, the fast Rac-sniffer presumably inhibits the slow Rho-sniffer and causes the early decrease in Rho-activation. The reaction network is illustrated in Fig. 4.11(a) and the best model fit to the data is shown in Fig. 4.11(b).

This reaction network is a suggestion for a further refinement of the biochemical signaling which originates at focal adhesions. However, before this network can be incorporated in future studies of the mechano-chemical feedback system, detailed ex-

perimental analysis is required. Such experiments should be aimed at (1) measuring the missing reaction constants (reducing the number of free parameters) and (2) at resolving the relative contributions from chemical or mechanical factors that lead to Rho-GTPase activation.

Chapter 5

Cellular response to stiffness

In the previous chapter we have developed a reaction diffusion system for the Rho-GTPase pathway and presented how the biochemical signaling interacts with the stress fiber contraction mechanics. The resulting mechano-chemically coupled system essentially constitutes a positive feedback and we have demonstrated that accounting for this simple regulatory motive is sufficient to understand the inhomogeneous contraction of stress fibers upon stimulation with a drug. In general, positive feedback systems also have the potential to show bistability. The emergence of bistability within our model has been noted previously but now will be investigated in more detail. In contrast to the previous chapter where we have focused on spatial and temporal variation of the stress fiber deformation, here, we will focus on the boundary force as a state variable. In this way we are able to perform a stability analysis of the model. As boundary force we understand the force that the fibers exert at their terminating ends on the focal adhesions. In addition, we will generalize our model to the case of deformable boundaries representing soft substrates. The substrate stiffness will then serve as a control parameter in the stability analysis. Finally, we will discuss the consequences of the intrinsic bistability and how it effects the capability of cells to establish a contractile state on a soft substrate. Furthermore, we will point out several possibilities how the model predictions could be tested in future experiments.

5.1 Bifurcation analysis

In this section we search for the different fixed points of the mechano-chemically coupled system defined in the previous chapter. All equations and their coupling to each other remain the same. We also reuse the parameter values presented in Tab. 4.3 except that two values are marginally changed to $K_{-1} = 7\,\mathrm{nM}$ (formerly $4.7\,\mathrm{nM}$) and $V_{-1} = 1.7\,\mathrm{nM/s}$ (formerly $1.8\,\mathrm{nM/s}$). The values for these two parameters are not known from the literature and are chosen to be within a reasonable range compared to similar parameters in our model. More importantly, we introduce more general boundary conditions for the mechanical stress fiber equations to account for the case that cells are exposed to a soft substrate. In such a situation, at each fiber end, the viscoelastic stress within the fiber has to be balanced by the elastic restoring forces from the
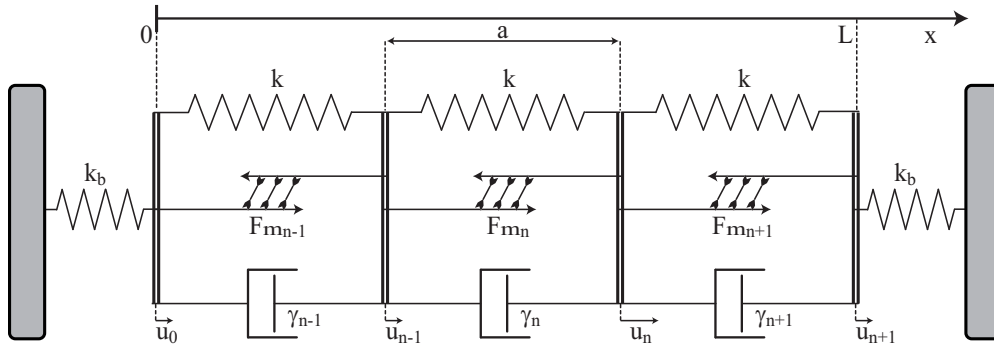
Figure 5.1: Same fiber model as it was introduced in the previous chapter. The elasticity of the substrate is accounted for by an additional spring of stiffness k_b connected in series at each end of the fiber. Other viscoelastic interactions of the fiber with its surrounding will be neglected in this chapter.

substrate:

$$\text{at} \quad x = 0, L: \qquad a\tilde{\gamma}\partial_x \dot{u}(x,t) + ak\partial_x u(x,t) + F_s = \pm k_b u(x,t) \qquad (5.1)$$

In our one-dimensional model, the soft substrate is accounted for by an additional harmonic spring k_b connected in series at each end of the fiber, see Fig. 5.1. The upper sign is valid for $x = 0$, the lower for $x = L$. These boundary conditions are similar to the ones used to describe the stress fiber nanosurgery experiments. There, all internal viscoelastic forces had to balance at the position of the cut. Such a situation is described by a free boundary and obtained by setting $k_b = 0$ in the above equation. In contrast, a clamped boundary is obtained by performing the limit $k_b \to \infty$. In this way, all types of boundary conditions used so far are contained in the upper formulation.

The boundary stiffness k_b modeled by a simple spring accounts effectively for the stiffness of the substrate. In general, one would have to solve the full contact mechanics problem to obtain an accurate value for this effective stiffness k_b. Not only the size, but also the geometry of the adhesion plays an important role in these contact mechanics problems [155]. However, given a certain geometry, the effective stiffness k_b is expected to be proportional to the substrate stiffness. The stiffness of the substrate should be understood as the Young's modulus, E, or the shear modulus, G, of an isotropic elastic material. These two elastic moduli are proportional to each other $G = E/(2 + 2\nu)$. The proportional constant involves Poisson's ratio ν which evaluates to 0.5 if the material is incompressible. The latter is roughly true for most materials that are used as substrates for cells. The measurement of either one thus determines the other. A common material that is used for cell experiments is for example polydimethylsiloxane (PDMS) whose mechanical properties are tunable during preparation. There exist also standard techniques to finally measure the achieved shear or Young's modulus of the prepared substrates. In this spirit, the substrate stiffness can be used as a physical parameter in a biological experiment that is easy to control and easy to measure.

These are the main reasons for choosing the non-dimensional ratio of substrate stiffness over internal fiber stiffness, k_b/k, as a control parameter in the following steady
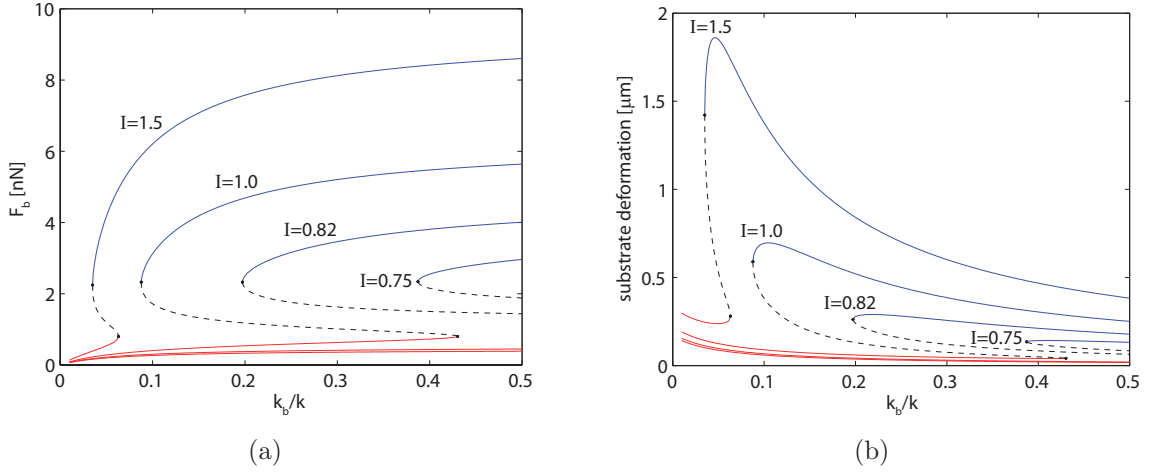
Figure 5.2: (a) Bifurcation diagrams for the exerted boundary force F_b reached in the steady state. The varied parameter is the non-dimensional stiffness ratio k_b/k. Bifurcation diagrams are given for different values of the inhibiting factor $I \in \{0.75, 0.82, 1.0, 1.5\}$. The stable upper branch (blue) corresponds to a highly contractile cell, the stable lower branch (red) corresponds to a non-active cell. The unstable branch is shown as dashed line. Saddle node bifurcation points are highlighted as black dots. When decreasing I, first the lower bifurcation point and later also the upper bifurcation point is lost within the considered window for the stiffness ratio. A three-dimensional representation of this plot is given in Fig. 5.3. (b) Equivalent bifurcation diagrams for the substrate deformation reached in the steady state. The color coding is as in (a).

state analysis of our model. The second parameter which we have chosen to vary is the factor of inhibition, I, which we introduced previously to account for the inhibitory effects of calyculin on myosin light chain phosphatase. Since calyculin inhibits the phosphatase ($I > 1$) it effectively increases myosin light chain phosphorylation and thereby enhances actomyosin contractility. As a consequence values for $I > 1$ ($I < 1$) lead to higher (lower) myosin activity. $I = 1$ corresponds to the unperturbed system. Compared to the substrate stiffness, however, this reaction parameter is much less controllable in experiments.

In general, the stationary model solution comprises the complete displacement field along the stress fiber as well as the concentration profiles of all biochemical components. In order to have a simple measure of the approached steady state we introduce the absolute value of the boundary force F_b as a state variable. This force is equivalent to the tension within the fiber and can be calculated by using either side of Eq. (5.1). Another interesting measure is the deformation of the substrate which is simply given by the absolute value of displacements at the boundaries $|u(0,t)| = |u(L,t)|$. It is important to note that in the steady state, the mapping from the complete solution onto one of these two state variables is bijective. This is true because the boundary force fully determines the steady state activation profile which in turn defines the steady state deformation of the fiber. However, such a bijective mapping is of course not possible during the equilibration process. Here, the same boundary force may originate from differently deformed fibers.

Fig. 5.2(a) shows the bifurcation diagram for the boundary force F_b. The upper blue and the lower red branch represent the stable fixed points of the model for different values of the stiffness ratio k_b/k. The unstable branch is indicated as dashed line. It connects to the stable branches at two saddle node bifurcation points, marked by black dots. The stable upper branch corresponds to a highly contractile cell whereas the stable lower branch corresponds to a non-active cell that fails to establish a contractile state. Both branches increase monotonically with the substrate stiffness. Thus, the stiffer the substrate the higher will be the exerted forces in the contractile or even in the non-active state. However, it is important to note that the upper branch quickly saturates at a certain force level for high stiffness ratios. The stiffness range between the two bifurcation points (if both exist) defines the region of bistability. On softer substrates the non-active state is the only stable fixed point whereas on stiffer substrates all cells are forced into the contractile state.

We have calculated this bifurcation diagram for different values of the inhibiting factor I. From Fig. 5.2(a) it can be deduced that for all considered values of the inhibiting factor there exist a critical stiffness ratio below which the upper stable branch vanishes. As a consequence, on very soft substrates, cells can not establish a highly contractile state. This critical value, which depends on the inhibiting factor, is just given by the stiffness ratio of the upper left bifurcation point. When the factor I is decreased, both bifurcation points move to higher stiffness ratios. For $I = 0.82$ and for lower values, the lower right bifurcation point is lost within the considered stiffness window. The upper left bifurcation point will be also lost for slightly lower values of I and the lower branch which corresponds to the non-active state is the only remaining attractor. These results are not surprising since decreasing I leads to an increase in phosphatase activity and subsequently to a decrease in myosin contractility. Thus, if I is low, the positive feedback is suppressed.

Fig. 5.2(b) shows the bifurcation diagram for the substrate deformation. It essentially contains the same information as the bifurcation diagram for the boundary force since the substrate deformation is simply given by F_b/k_b. Nevertheless, this representation reveals some notable features. For example, the upper stable branch exhibits a maximum at an intermediate stiffness ratio. This is because on the one hand the contractile forces sharply decrease with decreasing substrate stiffness as the left bifurcation point is approached, compare Fig. 5.2(a). Thus, also the resulting deformations decrease in the vicinity of the left bifurcation point. On the other hand, the exerted forces saturate for large stiffness ratios. As a consequence, the deformations roughly decay proportional to $1/k_b$ for high stiffness ratios.

This nicely depicts the dilemma experimentalists have to face when they perform experiments with cells on soft substrates and want to measure the resulting substrate deformations. They are "caught between a rock and a soft place": On a very stiff substrate, cells are able to build up high forces but since the substrate is so stiff the caused displacements are very small and hardly measurable. On the other hand, if the substrate is very soft, cells can not exert large forces, thus the substrate deformations are also very small and hardly measurable. There is only a small window of suitable substrate stiffness over which cells reach a contractile state and the substrate is still soft enough to allow for measurable deformations.

The bifurcation diagram for the substrate deformation has also been calculated for different values of the inhibiting factor I. One can deduce from the figure that the maximum of the upper branch is more pronounced when the factor of inhibition is high. When I decreases also the maximum decreases and simultaneously shift to higher stiffness ratios.

5.1.1   State diagram

In the previous section we have calculated the fixed points of our model and thereby used the stiffness ratio k_b/k as a control parameter. By simultaneously varying a second parameter, the factor of inhibition I, we obtained the family of bifurcation diagrams shown in Fig. 5.2(a) or Fig. 5.2(b). This analysis can be performed more thoroughly by systematically sampling the two-dimensional parameter space $(k_b/k, I)$. The stable and unstable branches then become surfaces defined over the parameter plane $(k_b/k, I)$ illustrated in Fig. 5.3 from two different view points. Over a certain domain of the parameter space this surface folds over on itself. If the system resides in the upper branch and is pushed to the edge by an appropriate parameter change it is forced to drop onto the lower branch. This large jump corresponds to a catastrophic change of the system [156]. In the present situation the jump means the transition from the contractile to the non-active state.

The two folds where the surface bends over just define the two bifurcation curves. These curves are the parameterized positions of the two bifurcation points. Their projections onto the parameter plane are illustrated as dashed lines in Fig. 5.3. This projection yields the two-dimensional stability diagram for the model sketched up again in Fig. 5.4(b). There, the position of the bifurcation point that terminates the lower branch is shown in red. The curve for the other bifurcation point is shown in blue. The two bifurcation curves divide the parameter plane $(k_b/k, I)$ into three regions. Each region is labelled according to the existing fixed points. Both, in the lower and upper regions there exists only one stable fixed point which corresponds to a non-active cell or a contractile cell, respectively. In the region of intermediate values for I there exist three fixed points two of which are stable and one is unstable. It is in this parameter region where the model system becomes bistable and the two phases of contractile and non-active cells coexist. In this parameter range, in principle, transition between these two states could be provoked by a large enough perturbation from the steady state.

It is noteworthy that both bifurcation curves are bounded below. This can be shown by calculating the bifurcation diagram for the case of an infinitely stiff substrate and using the factor of inhibition I as the only control parameter. The resulting diagram is shown in Fig. 5.4(a). Within a certain range of the parameter I the systems still exhibits bistability. Thus, the position of the two bifurcation points in Fig. 5.4(a), more precisely their I-coordinate, determines the asymptotes for the bifurcation curves in Fig. 5.4(b) in the limit of high substrate stiffness. The found asymptotes, namely $I = 0.68 \pm 0.01$ (blue) and $I = 0.91 \pm 0.01$ (red), are given as dashed lines in Fig. 5.4(b). The fact that the blue bifurcation curve is bounded below has the following consequences: There exists a certain value of the inhibition factor, that is $I = 0.68 \pm 0.01$, below which the only stable fixed point is the non-active state irrespective of the substrate stiffness. This
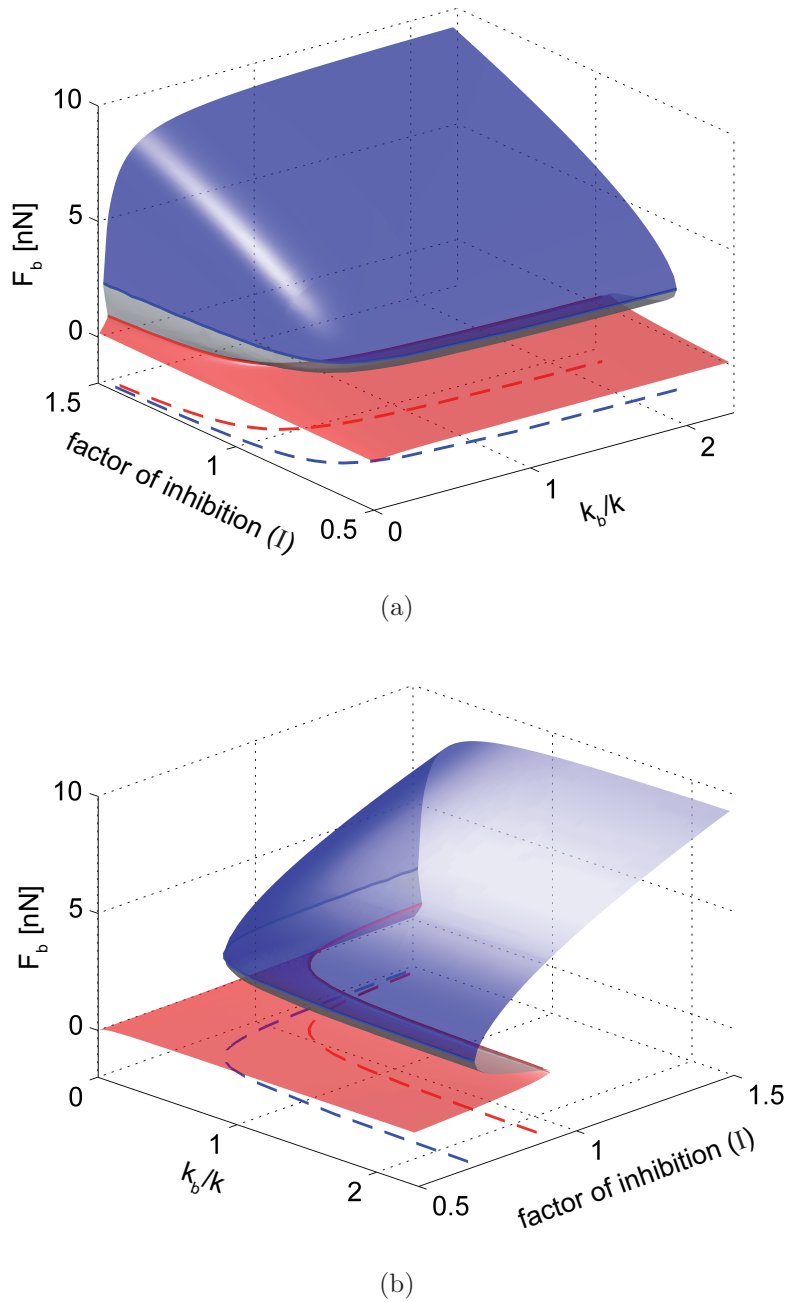
(a)

(b)

Figure 5.3: Three dimensional bifurcation diagram of the steady state boundary force F_b depicted from two different view points (a) and (b). The varied parameters are the factor of inhibition I and the stiffness ratio k_b/k. The colored planes represent: the stable upper branch (blue), the stable lower branch (red) and the unstable branch (grey). The boarder line between the stable branches and the unstable branch defines two bifurcation curves highlighted by red and blue solid lines. Projections of these two curves onto the parameter plane are shown as dashed lines of respective color. The bifurcation curves are bounded below at $I = 0.68 \pm 0.01$ (blue) and $I = 0.91 \pm 0.01$ (red).
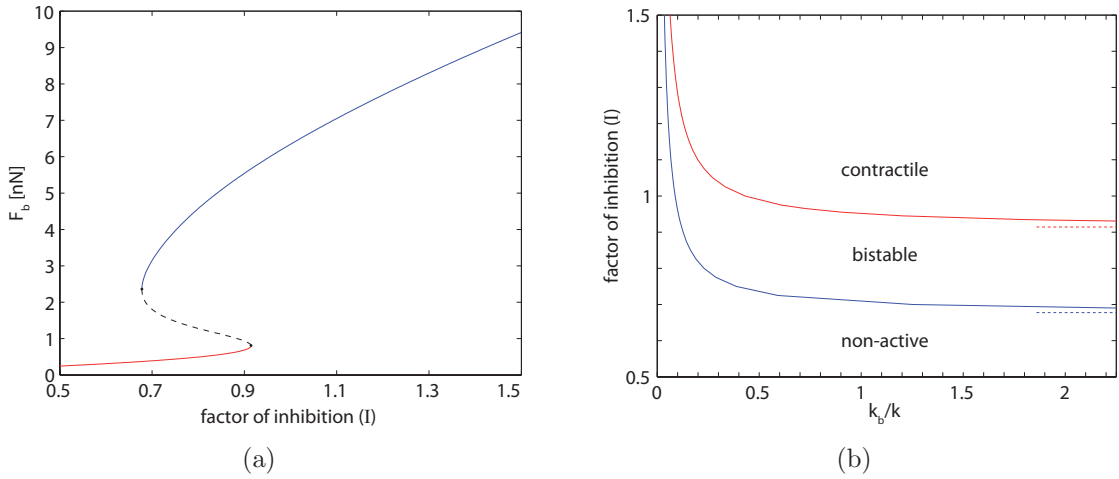
(a)   (b)

Figure 5.4: (a) Bifurcation diagram of the steady state boundary force F_b for the case of an infinitely stiff substrate. The varied parameter is the factor of inhibition I. The stable upper branch (blue) again corresponds to a highly contractile cell whereas the stable lower branch (red) corresponds to a non-active cell. The unstable branch that connect the two saddle node bifurcation points is shown as dashed line. The two bifurcation points (black dots) are located at $(0.68 \pm 0.01, 2.36 \pm 0.05)$ and $(0.91 \pm 0.01, 0.81 \pm 0.01)$. (b) Stability diagram: The two bifurcation curves divide the parameter plane into three regions. Each region is labelled according to the existing fixed points. In the bistable region, there exist three fixed points: one is unstable, and the other two correspond to the non-active and the contractile state, respectively. Both bifurcation curves are bounded below, their asymptotes are given by the position of the bifurcation points in (a) and are included as dashed lines of respective color.

is due to the fact that decreasing I leads to an increase of the phosphatase activity and subsequently to a decrease in myosin contractility. Thus, if I falls below this critical value, the positive feedback is suppressed to such an extend that a contractile state is no longer possible.

It can be deduced from Fig. 5.4(b) that for very low stiffness ratios, k_b/k, the two bifurcation curves seem to converge. However it is not clear if they simultaneously diverge to infinity or if they mutually annihilate in a cusp point at a finite value for I. In order to determine the location of a possible cusp point we steadily increased the parameter I and subsequently screened for the two saddle-node bifurcations. The highest value for the inhibiting factor that still allowed differentiation between the two bifurcation points was $I = 19.7$ where the upper left bifurcation point (blue) was found to be located at $(k_b/k, F_b) = (2.3463 \cdot 10^{-3} \pm 10^{-7}, 1.13 \pm 0.02)$ and the lower right (red) at $(k_b/k, F_b) = (2.3464 \cdot 10^{-3} \pm 10^{-7}, 1.06 \pm 0.02)$. For even higher values of I the two bifurcation points could no longer be separated and no bifurcation could be detected. However, this might be simply due to insufficient numerical precision. On the basis of our numerical study a clear statement cannot be made and a more thorough investigation of the stationary system would be necessary to determine the location of a possible cusp point.

So far we have studied the stability of our model only under variations of the

two parameters k_b/k and I. However, due to the simple structure of the biochemical pathway, it is just a sequence of activating or inhibiting enzyme reactions, the above-mentioned properties of the model seem to be qualitatively true for small variations in every other reaction parameter. For example the role of I could also be taken over by a parameter which in contrast inhibits the positive feedback. This would only invert the I-axis but the qualitative shape of the surfaces would remain unchanged. We have verified this explicitly for a small set of parameters.

5.2 Probing hysteresis in cell adhesion

The existence of bistability within a certain range of substrate stiffness gives rise to the possibility of hysteresis in cell adhesion. In the following we suggest and analyze three experiments that should allow to probe such a hysteresis cycle. Finally, we discuss how these experiments could be realized.

5.2.1 Cyclic varying stiffness

In order to reconstruct a hysteresis cycle, the system has to be prepared initially in one of the two stable states, say the highly contractile state. By reducing the substrate stiffness sufficiently slowly, that the system can adapt and remain in a quasi steady state, it will follow the upper stable branch until it reaches the bifurcation point. Here, the upper branch becomes unstable and the system is forced into the non-active state. When the control parameter is increased again, the system will stay on the lower branch while it passes below the left bifurcation point. Subsequently, it will reach the right bifurcation point, where the lower branch becomes unstable. Thus, the system is finally forced again onto the upper branch and the hysteresis cycle is closed.

If one had full control over the system, a very well-defined experiment would be to expose the cells to a cyclic varying substrate stiffness. Thereby, the range over which the stiffness varies has to exceed the bistable region. Furthermore, the period of the oscillation should be much larger than the typical equilibration time of the system, if one wants to assure that the system essentially follows the stable branches as the control parameter is varied over time. We have simulated this experiment with COMSOL Multiphysics for a cyclic stiffness ratio of the following form:

$$k_b(t)/k = 10^{-2} + 10 \left(\frac{1}{2} + \frac{1}{2} \cos \omega t \right) \tag{5.2}$$

The upper function describes a sinusoidal oscillation of amplitude 5 with offset of 5 and angular frequency $\omega = 2\pi/T$, where T is the period of the oscillation. At $t = 0$ it starts at its maximum and reaches its minimum $k_b/k = 10^{-2}$ at $t = T/2$. The system response to this cyclic mechanical input has been calculated for different periods T. The resulting time course of the exerted boundary forces are illustrated in Fig. 5.5. As expected, for very large periods, the system follows essential the bifurcation diagram, see $T = 1\,\mathrm{d}$ in Fig. 5.5. The area of the hysteresis cycle first increases with the angular frequency and reaches a maximum for $T = 4300\,\mathrm{s}$, the red curve in Fig. 5.5. For
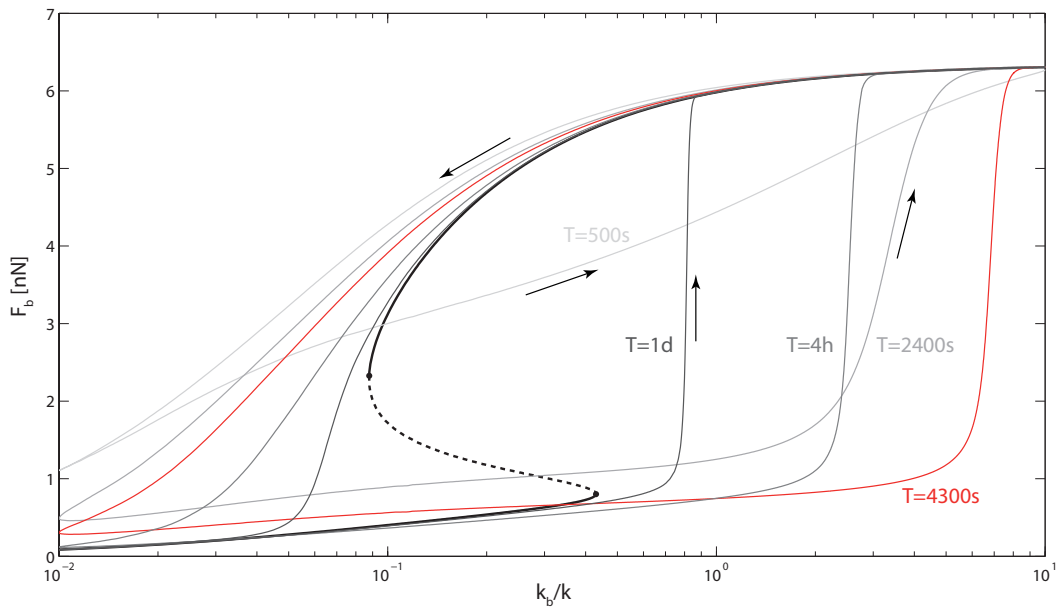
Figure 5.5: Time course of contraction forces for a cyclic varying substrate stiffness with period $T \in \{500\,\text{s}, 2400\,\text{s}, 4300\,\text{s}, 4\,\text{h}, 1\,\text{d}\}$. The area of the hysteresis cycle reaches its maximum at $T = 4300\,\text{s} \pm 100\,\text{s}$ highlighted in red. If the cycle has a very large period, then the time course of the force approaches the stable branches of the bifurcation diagram (black and fat lines). Arrows indicate the direction of rotation. The assumed factor of inhibition is $I = 1.0$, representing a biochemically unperturbed system.

very high angular frequencies the hysteresis cycle tightens up again. The resulting dependence of the encircled area on the period T is further illustrated in Fig. 5.6(b). As noticed before, the function exhibits a clear maximum at $T = 4300\,\text{s} \pm 100\,\text{s}$. For very large T, the function is bounded below by the area encircled in the bifurcation diagram (the quasi steady state cycle). In addition, the function also shows a faint maximum for very small T. This is partially due to the fact that, in this regime, the trajectories do not close up on itself after the first cycle, compare Fig. 5.6(a).

The maximum in encircled hysteresis area around $T = 4300\,\text{s}$ results from the interplay of different time scales. If the angular frequency is very low, both, the biochemical environment, as well as the mechanical state of the fiber follow in a quasi steady state. If the frequency increases, the biochemistry begins to lag behind the varying mechanical input. For example, when the stiffness decreases in time, the biochemistry conserves the passed activity and the system can maintain higher forces on the soft substrates than actually appropriate. However, the overall exposure time to the soft environment is large enough to cool the system down, close to the inactive state. Thus, a similar lagging occurs when the stiffness subsequently increases in time. This is not the case, if the angular frequency is high, $T < 4300\,\text{s}$. Then, the exposure time to the soft environment is not large enough to fully cool the system down. As a consequence it can maintain an anomalous high contractile state even until it leaves again the soft environment, see e.g. $T = 500\,\text{s}$ in Fig. 5.5. This is the reason why the hysteresis cycle tightens again for further increasing frequencies.
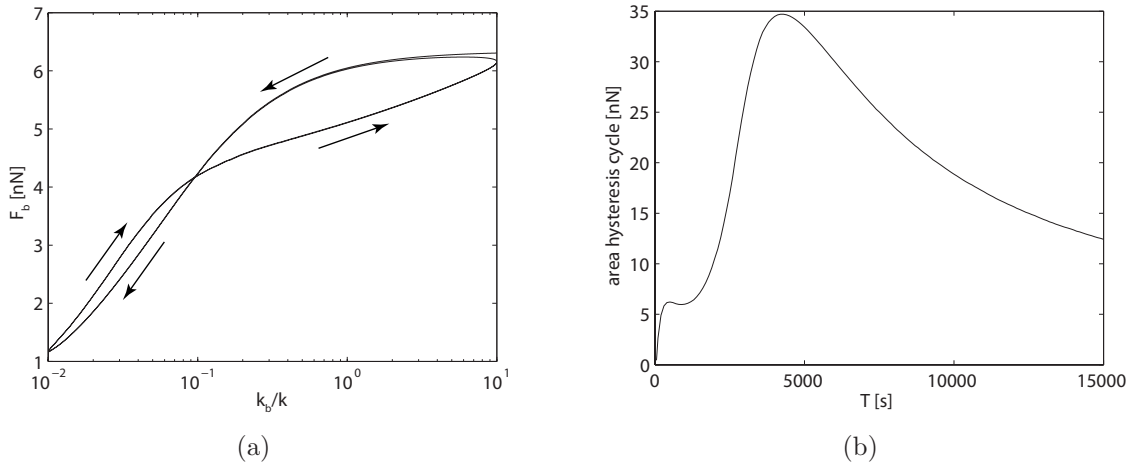
(a)   (b)

Figure 5.6: (a) Time course of the boundary force for two cycles in substrate stiffness with period $T = 240\,\text{s}$. The first cycle is not closed but the second cycle settles down to the first trajectory. (b) Area of the first hysteresis cycle in the force in dependence on the period T, compare also Fig. 5.5. The main maximum is reached for $T = 4300\,\text{s} \pm 100\,\text{s}$. The lower maximum is partially due to the fact that first cycles are not closed for small periods, compare (a).
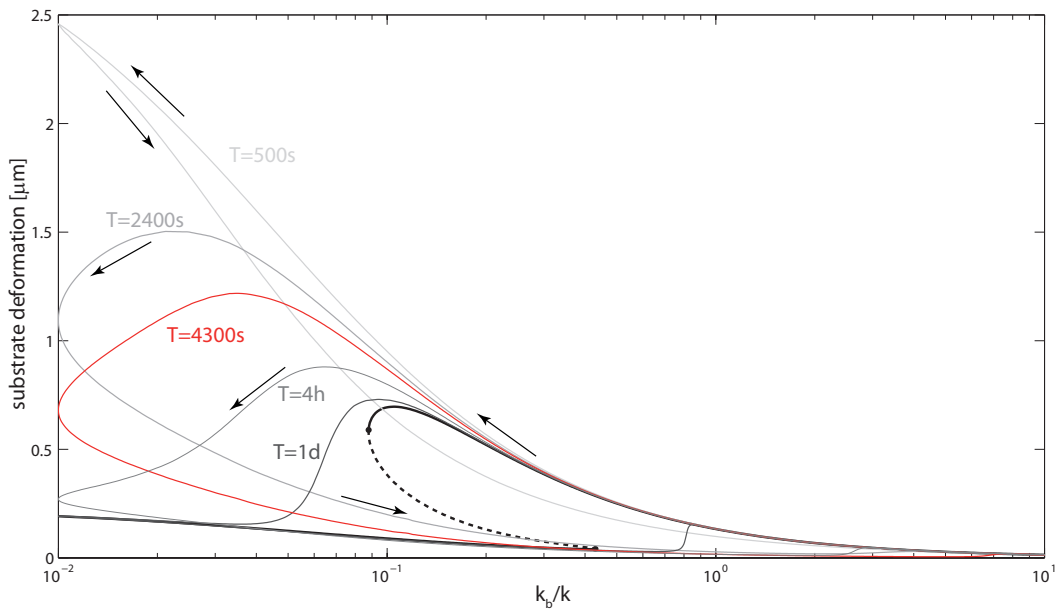

Figure 5.7: Time course of the substrate deformation for a cyclic varying substrate stiffness with periods as in Fig. 5.5. The curve highlighted in red corresponds to the largest hysteresis cycle in the force diagram Fig. 5.5. In the cycles with $T \in \{2400\,\text{s}, 4300\,\text{s}, 4\,\text{h}, 1\,\text{d}\}$, the deformation reaches its maximum shortly before the stiffness ratio passes through its minimum. Similar to the findings in Fig. 5.10, the deformation curves for fast cycles exhibit large excursions to very high values. Arrows indicate the direction of rotation.
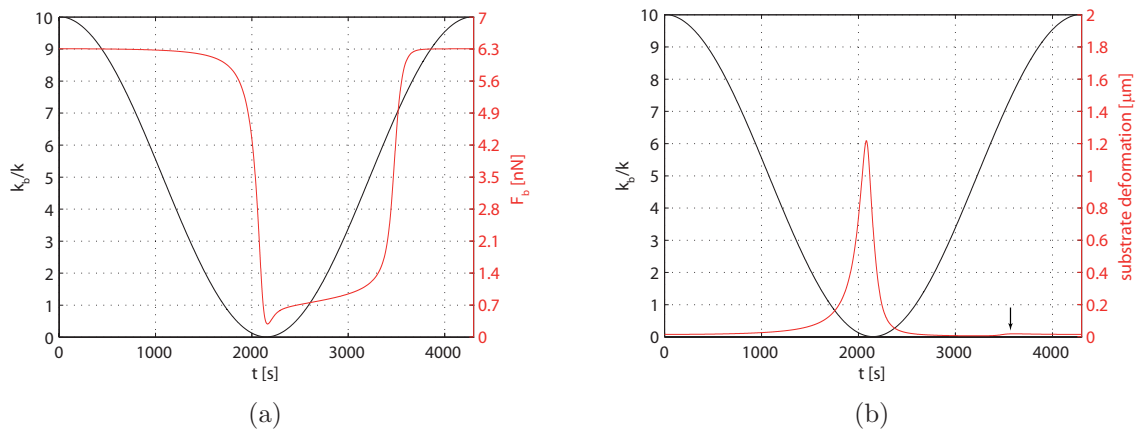
Figure 5.8: (a) Time course of the boundary force (red) for cyclic substrate stiffness (black) with period $T = 4300\,\text{s}$. The force response to the sinusoidal input is also a periodic function but has a more complicated shape. (b) Time course of the deformation (red) for the same mechanical input as in (a). The deformation response is again a periodic function. It shows two extremal values. The main maximum is reached shortly before the stiffness reaches its minimum. The faint second maximum, indicated by the arrow, is reached when the system is forced onto the upper stable branch by the increasing substrate stiffness.

For very high angular frequencies (not included in Fig. 5.5) another time scale comes into play: If the softening of the boundaries is very quick, even the fiber mechanics are not fast enough to follow the loosening boundaries. As a consequence, the contractile motor forces are expended on working against the internal viscosity rather than on deforming the external spring. The forces on the boundaries are thus low despite the fact that the myosins are highly activated. An exemplary trajectory of the boundary forces for such a high frequency is given in Fig. 5.6(a). Since the stiffening of the boundaries is faster than the mechanical equilibration, the increase in stiffness causes an additional tension in the fiber. This is the reason for the twist in the shown trajectory.

It is also instructive to analyze the trajectory of substrate deformations, shown in Fig. 5.7 for the same angular frequencies as used for Fig. 5.5. Also here, the area of the hysteresis cycle first increases with the angular frequency, reaches a maximum (not necessarily at the same T-value as the force) and then decreases again with increasing frequency. In the latter case, when the frequency is very high, the system maintains anomalous high forces on soft substrates. This combination of high forces and low stiffness leads to very large deformations. This can be deduced from the trajectories for $T < 4300\,\text{s}$ which undergo large excursions away from the steady state branch. It is also noteworthy that the deformation trajectories reach a maximum shortly before the stiffness passes through its minimal value.

To conclude this section we finally compare the time course of the boundary forces to the mechanical input. This comparison is shown in Fig. 5.8(a) for $T = 4300\,\text{s}$. In contrast to the input function, the force response is not a harmonic oscillation. This is due to the non-linear reaction terms in the biochemical equations. If the model was linear, the output could be expected to be also harmonic. Although the force

response lags behind the stiffness input over most of the time, both functions reach their minimum and maximum virtually in phase. This is different for the time course of deformations shown in Fig. 5.8(b). As discussed earlier, the maximum in deformation is interestingly reached shortly before the stiffness reaches its minimal value. To see this, compare also Fig. 5.7. Beside this main maximum the time course of deformation exhibit a second faint maximum. The latter occurs when the system is forced from the non-active state to the contractile state during increasing stiffness.

5.2.2   Spreading and linear softening

The previously simulated experiment is very well defined theoretically but experimentally difficult to realize as it presupposes accurate control over the substrate stiffness. In the following we will model two different experiments. They require in some sense only minimal control over the substrate stiffness but the combination of both still allows to test for hysteresis in cell adhesion. These theoretical ideas can be realized experimentally with available techniques, discussed in the last section.
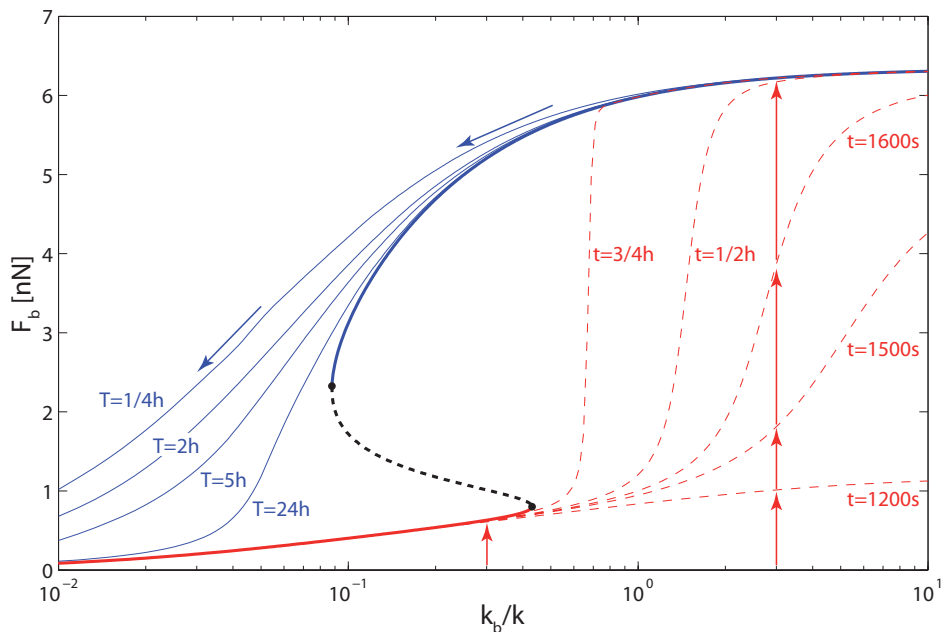

Figure 5.9:   Simulation of two different experiments to probe the hysteresis cycle. (1) Lower red curves simulate the buildup of force up to the time $t \in \{1200\,\text{s}, 1500\,\text{s}, 1600\,\text{s}, 1800\,\text{s}, 2700\,\text{s}\}$ for cells exposed to a constant but different substrate stiffness. Cells are considered to be in a totally non-active state at $t = 0$. Depending on the degree of stiffness, cells remain either in a non-active state or reach a contractile state. Red arrows indicate the direction of single cell trajectories. (2) Upper blue curves depict the expected time course of the boundary forces if the substrate stiffness is reduced linearly over the time span $T \in \{0.25\,\text{h}, 2\,\text{h}, 5\,\text{h}, 24\,\text{h}\}$. The starting point is an active cell on a stiff substrate which is forced into a non-active state by the steadily decreasing stiffness. Blue arrows indicate the direction of single cell trajectories in this situation.
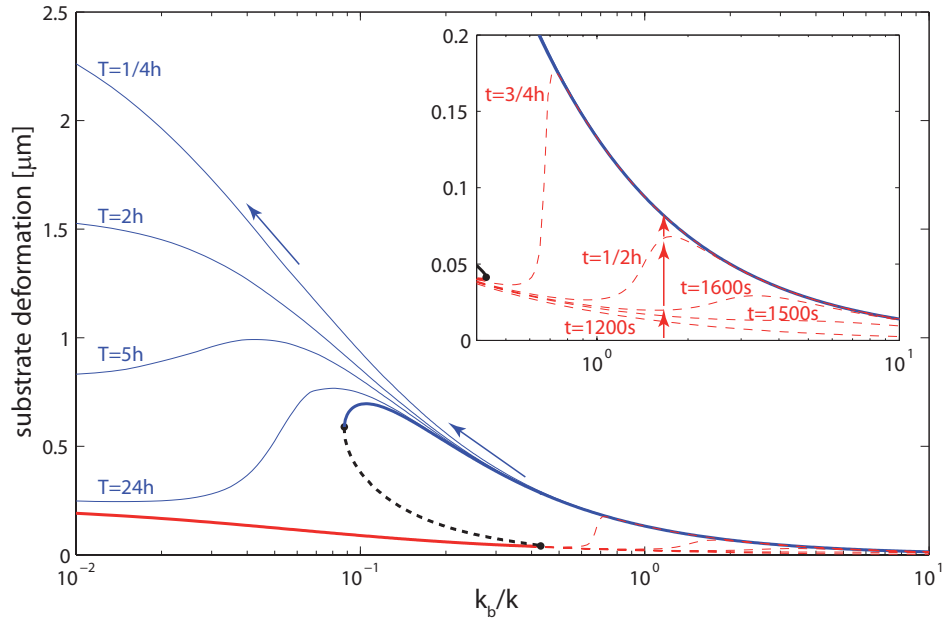
Figure 5.10: Same analysis like in Fig. 5.9 but now illustrated for the substrate deformation. Upper blue curves describe the time course of the substrate deformation if the substrate stiffness is reduced linearly over time. If the stiffness is reduced quickly, anomalous high forces can be maintained on comparably soft substrates leading to large deformations, see $T \in \{0.25\,\mathrm{h}, 2\,\mathrm{h}, 5\,\mathrm{h}\}$. If the mechanics change very slowly, then the biochemistry has time to adapt and deformations rather follow the steady state curve, see $T = 24\,\mathrm{h}$. Lower red curves, also enlarged in the inset, simulate the buildup of substrate deformations up to the time $t \in \{1200\,\mathrm{s}, 1500\,\mathrm{s}, 1600\,\mathrm{s}, 1800\,\mathrm{s}, 2700\,\mathrm{s}\}$ for cells exposed to a constant but different substrate stiffness. Cells are considered to be in a totally non-active state at $t = 0$. Depending on the degree of stiffness, cells remain either in a non-active state or reach a contractile state. Blue and red arrows indicate the direction of single cell trajectories.

To reproduce the presumed hysteresis cycle it is only essential to have an experimental technique for reducing the substrate stiffness over time. This is because the system has to be prepared initially in an active state on a stiff substrate in order to explore the upper stable branch by subsequently softening the substrate. In contrast, in order to explore the lower branch, one can simply take advantage of the fact that initial cell spreading starts in a low contractile state. To reconstruct the lower stable branch it is thus sufficient to prepare differently soft substrates and let the cells start to adhere. On very soft substrates, the finally reached contractile forces will be bounded above by the lower stable branch. Only on stiff substrates, where the contractile state is the only stable fixed point, the upper branch will be reached.

This experiment has been simulated by means of our model. As initial condition, we assumed that the biochemical components are all equilibrated for zero boundary force. That is, we have set $F_b(t) = 0$ in Eq. (4.1) and let the biochemical components evolve to their steady state. The resulting concentration profiles are then taken as initial conditions for the subsequent simulation. This situation is meant to represent a

cell, formerly in suspension where no forces could be built up, that starts to adhere to the substrate at $t = 0$. The results are illustrated in Fig. 5.9. The red curves show the expected boundary forces built up within the time t by cells seeded on differently stiff substrates.

To clarify the course of the experiment, two single cell trajectories are illustrated by red arrows. On a soft substrate, $k_b/k = 0.3$, the system settles down in the non-active state (left red arrow in Fig. 5.9). On a stiff substrate, $k_b/k = 3$, the system is forced onto the upper branch which is the only stable fixed point (series of red arrows on the right hand side of Fig. 5.9). Thereby, the red curves indicate the time needed to reach a certain boundary force. In other words, every red curve is reconstructed from an ensemble of experiments each of which is performed on a differently stiff substrates. The time courses of the established boundary forces on a certain substrate stiffness are illustrated in Fig. 5.11(a). We find that the stiffer the substrate the faster is the equilibration process and the higher is the force reached in the steady state. As discussed earlier, cells on very soft substrate, (see $k_b/k = 0.46$), can not establish high contraction forces and are kept in the non-active state.

To explore the upper branch in Fig. 5.9, softening of the substrate is required as the system resides in the contractile state. The most simple process would be a linear decrease of substrate stiffness over time. This experiment has been simulated and the results are shown as blue curves in Fig. 5.9. Each curve gives the trajectory of the boundary force as the stiffness is reduced linearly form $k_b/k = 10$ to $k_b/k = 10^{-2}$ over the period T. Only if the stiffness is changed very slowly ($T = 1\,\mathrm{d}$), the trajectory closely follows the stable branches in a quasi steady state. For this case, the hysteresis cycle is found to be closed. If the decay in stiffness is fast, the system can conserve the myosin activity and maintain higher forces. These findings are qualitatively similar to the ones presented in the previous section.

We also calculate the corresponding substrate deformations, shown in Fig. 5.10. If the stiffness is reduced quickly (blue curves), anomalous high forces can be maintained on comparably soft substrates leading to large deformations, see curves for $T \leq 5\,\mathrm{h}$. If the stiffness is reduced slowly, then the deformation exhibit a maximum shortly before the stiffness reaches its minimum, see $T \geq 5\,\mathrm{h}$. Similar findings have been reported for cyclic stiffness, see corresponding discussion in section 5.2.1. During cell spreading (red curves) the deformations on each substrate are expected to increase monotonically in time, see Fig. 5.11(b). However, the reached deformation at a certain time point, of course, varies with the stiffness of the substrate. Interestingly, the deformation exhibits a maximum for intermediate stiffness. This maximum then increases and shifts to lower stiffness ratios with increasing time, compare e.g. the two curves $t = 0.5\,\mathrm{h}$ and $t = 0.75\,\mathrm{h}$ in the inset of Fig. 5.10. In the steady state, the largest deformation is reached on substrates that are slightly stiffer than the critical stiffness defined by the lower right bifurcation point, compare also Fig. 5.11(b).

5.2.3   Using biochemical stimulation

All experiments discussed above require substrates of time dependent stiffness. Usage of such substrates would allow to test bistability in cell adhesion by varying a well
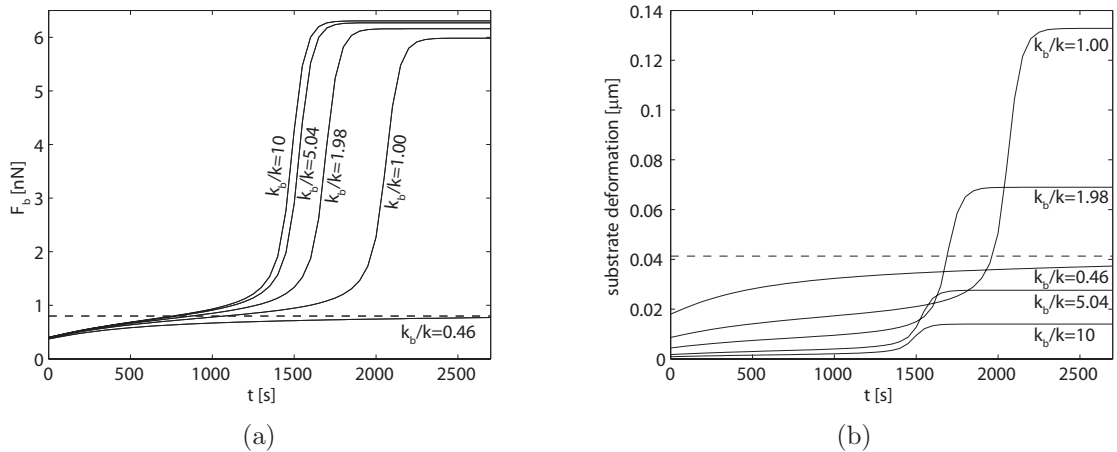
Figure 5.11: (a) Time course of the boundary forces established by cells on substrates with different stiffness: $k_b/k \in \{0.46, 1.00, 1.98, 5.04, 10\}$. The stiffer the substrate the faster is the equilibration process and the higher is the force reached in the steady state. Cells on the softest substrate, $k_b/k = 0.46$, can not establish high contraction forces and are kept in the non-active state. The reached steady state forces of cells in the contractile state only differ within a few percent. (b) Time course of the substrate deformation caused by cells on different rigidities. Stiffness ratios are the same as in (a). The equilibration is also faster on stiffer substrates but the highest deformations are reached on intermediately stiff substrates. Dashed line gives the y-coordinate of the lower bifurcation point in both figures.

defined and accurately measurable physical quantity, e.g. the Young's modulus of the substrate. Here, we want to discuss a simple alternative to circumvent such elaborate substrates by using a contractile drug like calyculin. The great disadvantage of such an experiment is, however, that the precise value of the control parameter is difficult to quantify.

In our model, the effect of calyculin is described by the factor of inhibition I which essentially increases myosin activity. In section 5.1 and 5.1.1 we have shown that cells, exposed to a high concentration of this drug, are expected to reach a contractile state even on very soft substrates. This can now be used to explore the stable upper branch of the bifurcation diagram in the chemically unperturbed situation. To reproduce the complete bifurcation diagram for the unperturbed situation ($I = 1.0$), one has to perform two different experiments. In the first experiment, the spreading of unperturbed cells on different rigidities has to be conducted. Thereby the reached steady state forces have to be recorded. This experiment has been described in detail in the previous section. It reveals the complete lower stable branch as well as parts of the upper stable branch over the high stiffness regime. The discovered parts are indicated by the upward pointing arrows in Fig. 5.12. The upper stable branch over the bistable region is the only inaccessible part of the bifurcation diagram. To discover this part, is the subject of the second experiment. Here, the cells are exposed to a high drug concentration during spreading, that is e.g. $I = 1.5$. Thus, they will populate the stable branches of the bifurcation diagram shown in Fig. 5.12 for $I = 1.5$. If the effect of the drug is
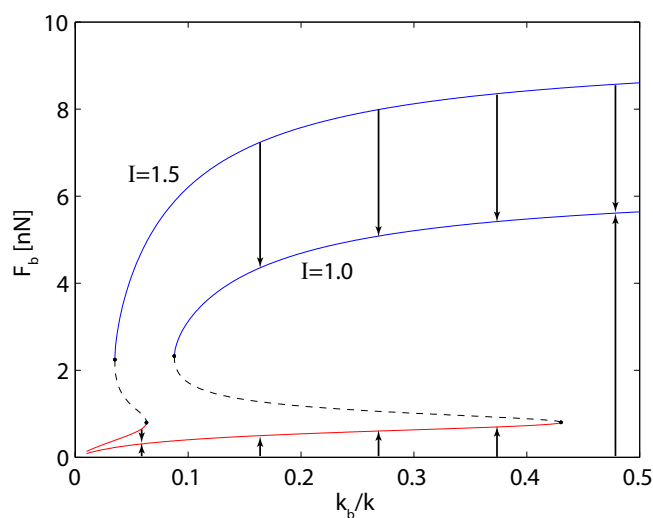
Figure 5.12: Probing the hysteresis cycle by using a contractile drug. Cells exposed e.g. to calyculin are expected to reach a contractile state even on very soft substrates ($I = 1.5$). When the effect of the drug is decreased again, they are expected to relax to the unperturbed steady state ($I = 1.0$). In this way, the upper stable branch can be probed within the bistable region. Downward pointing arrows indicate cell trajectories when the effect of the drug is reduced. Upward pointing arrows indicate trajectories for unperturbed cell spreading.

subsequently reduced, for example by washing it out, the cells will relax to the stable states of the unperturbed situation, $I = 1.0$. The trajectories of cells on differently stiff substrates are indicated by the downward pointing arrows in Fig. 5.12. Most importantly, cells plated on substrates of intermediate stiffness, $k_b/k \in [0.1, 0.4]$, will settle down on the upper stable branch over the bistable region. If the initial stimulation with the drug is strong enough, such that the lower right bifurcation point of the stimulated system is left of the bistable region of the unperturbed system, then, combining the results from both experiments should reproduce the complete bifurcation diagram of the unperturbed system.

5.2.4   Experimental realization

To conclude this section, we will finally discuss how the experiments described above can be turned into reality. There are at least two possibilities to mimic substrates of time dependent stiffness. On the one hand, there exist certain polymer systems whose stiffness can be tuned over time. On the other hand, micromanipulators can perform a similar task if applied appropriately. Both methods will be briefly discussed below.

Polymer systems with time dependent stiffness

Typical polymer systems used as elastic substrates in cell adhesion experiments are for example polydimethylsiloxane (PDMS), polyacrylamide (PA) and hydrogels made from hyaluronic acid (HA). In contrast to PDMS or PA, the latter HA is a natural component
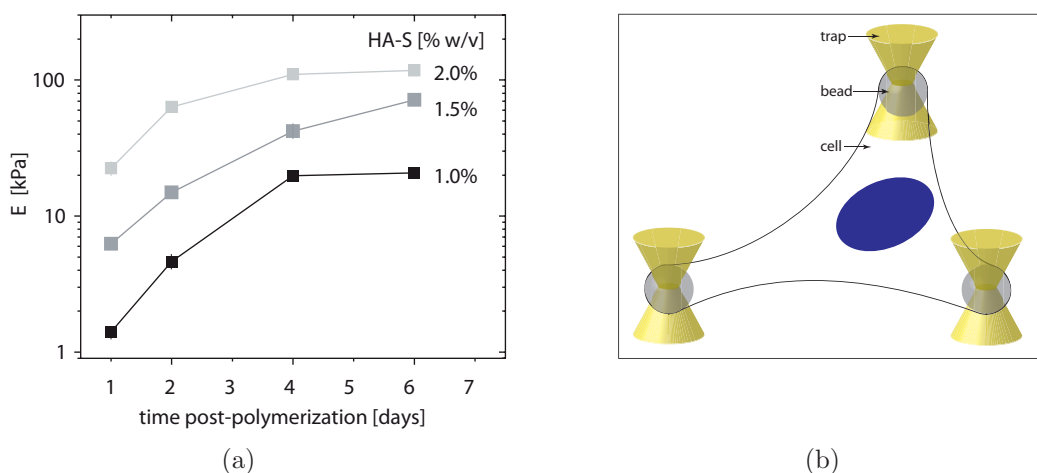
(a)   (b)

Figure 5.13: (a) Development of the Young's modulus E of PEG-DA crosslinked HA-S hydrogels, polymerized at three different HA-S concentrations. Stiffness has been measured with AFM. It increases over time due to auto-crosslinking of the remaining free thiol groups. Saturation in stiffness is reached after 6 days. Figure and caption has been taken from [160]. (b) Cell adhered to optical trapped micro beads. The stiffness of the traps could be precisely controlled by varying the laser power. Also force measurements could be performed with high precision. The severe drawback is, however, that the maximal trap force of optical tweezers ($\approx 100\,\mathrm{pN}$) is roughly one order of magnitude below cellular contraction forces ($> 1\,\mathrm{nN}$). Thus, it might be inevitable to substitute the elegant optical traps by other mirco-manipulators in such an experiment.

of the extracellular matrix. HA is a linear polysaccharide of glucuronic acid and N-acetylglucosamine. Its mechanical properties can be tuned by adding thiol groups to the HA polymer (HA-S). This modification allows for crosslinks in between HA polymers or to additives like polyethylene glycol diacrylate (PEG-DA) [157–160]. By varying the concentrations of the two components, the stiffness of this polymer system is tunable in the range of 0.1-150 kPa. It is also this polymer mixture, HA-S and PEG-DA, which exhibits a well characterized time dependent change in the Young's modulus. It results from the progressive formation of disulfide bonds which in turn increase the stiffness of the hydrogel over time. This process lasts for days and finally leads to an overall increase in stiffness of about one order of magnitude. The development of the substrate stiffness has been measured by atomic force microscopy [160]. Results are illustrated in Fig. 5.13(a). More importantly, the stiffness can also be reduced again by breaking up the previously formed crosslinks. The appropriate chemical agent is dithiothreitol (DTT) which reduces the disulfide bonds (Florian Rehfeldt et al., personal communication). In addition, collagen type I can be attached to the surface of this hydrogel in order to promote cell adhesion. Thus, this polymer mixture provides all necessary features in order to perform the experiments described in section 5.2.1 and 5.2.2.

Optical tweezers

Instead of using elaborated polymer mixtures as described above, one might also be able to use micro-manipulators to tune the stiffness of the cellular environment. A very convenient technique would be holographic optical tweezers. In a straight forward setup, a cell would be caught by at least two trapped micro beads that are functionalized appropriately for cell adhesion. The stiffness of the trap could be simply controlled by the laser power and the forces exerted by the cells could be deduced from the displacement of the beads from the center of the traps. Both, imposed stiffness and cellular force response could be measured with high precision. However, there is this severe problem that the force of optical tweezers is roughly $1\,\mathrm{pN}$ per $10\,\mathrm{mW}$ on micron sized beads [161]. For a typical laser power of a few W this is still too low to resist contractile stress fibers which exerts forces on the order of nN. In addition, the usage of more than one trap splits up the laser power on different foci which further decreases the stiffness of each trap. Still, there might be experimental solutions to the raised concerns. For example one can think of an experimental setup where a single laser trap is sufficient (one end of the cell is glued to a solid support, the other to the trapped bead). This allows to focus the full laser power on a single bead. It might also be possible to substitute the optical trap by other micro manipulators such as glass micro needles or magnetic tweezers. Both techniques can exert forces in the nN range. Moreover, the stiffness of the micro needle for example could be controlled by fixating it at different lengths/positions.

5.3   Summary and discussion

In this chapter we applied our full mechano-chemical model to investigate cellular behavior on soft substrates. In particular, we focused on the ability of cells to establish contractile forces in dependence on substrate rigidity. Due to the positive feedback, our model is potentially bistable. The two stable fixed points correspond to a highly contractile and a non-active cell state, respectively. However, we find that bistability is not a universal feature of the model. There also exist parameter regions where either the contractile or the non-active state are the only stable fixed points. This gives rise to a threshold of substrate stiffness below which cells are not able to build up contractile stress. On stiffer substrates cells adopt a contractile state but the reached steady state force depends only weakly on the substrate stiffness. Such a mechanism might contribute to tensional homeostasis in tissue [162, 163], which denotes the process when cells actively maintain a set level of prestress in their matrix. Finally, we also hypothesized that the potential bistability in the system gives rise to hysteresis in cell adhesion. To prove these predictions experimentally requires substrates of time dependent stiffness and we made several suggestions how such experiments could be realized in the future.

So far there are only few experiments reported in the literature that systematically measured contractile forces of single cells over a wide range of stiffness. Saez et al. [8] used micro arrays of elastic polymer pillars to measure the forces exerted by clusters of 10-20 cells. The stiffness offered to the cells has been varied by changing the height

or the radius of the pillars. This study showed that the forces exerted by cell clusters are proportional to the pillar stiffness. This scaling behavior was observed over two orders of magnitude. Although qualitatively in line with our theoretical predictions, our model rather suggests a threshold in stiffness and a sharp transition from low contractile forces to high contractile forces on stiff substrates. This discrepancy might result from the fact that Saez et al. studied clusters of cells. Cells in close contact to each other have been reported to respond less sensitive to substrate rigidity than single cells [6, 9]. Thus, for cells in contact with each other, such a sharp transition might be smoothed out, leading to the rather linear dependence between cellular forces and substrate stiffness.

Several single cell experiments on flat substrates of varying stiffness have been performed [7, 9] but in these studies no traction forces have been quantified. Instead, morphology changes have been reported like the spread area or the detection of focal adhesions and stress fibers under the light microscope. Yeung et al. [9] showed that single fibroblasts and endothelial cells exhibit an abrupt change in spread area at a Young's modulus of around 3 kPa. In addition, no actin stress fibers are seen in fibroblasts on soft surfaces, and the appearance of stress fibers is abrupt and complete also around 3 kPa. This sudden change in cellular response and presumably also in the cellular stress is consistent with our model predictions. Interestingly, cells were also found to spread faster on stiff substrates, which is also in agreement with our model that predicts faster buildup of forces on stiff substrates. Nevertheless, future measurements of the cellular traction forces are essential to further substantiate the agreement between the model and experimental data.

An intriguing aspect of our model is the way in which different stress fibers might cooperate inside a living cell. Conceptually it is easy to generalize our model to describe a system in which many stress fibers share the signaling input and many focal adhesions share the mechanical output. Such a model might contribute to a further understanding of cell orientation along the axis of highest rigidity on anisotropic substrates. In connection with a model for cell motility this might also lead to a detailed understanding of cellular durotaxis. However, this would require a theoretical description of the actin cytoskeleton which allows for both morphologies, Rho-induced actin stress fibers as well as Rac-induced lamellipodia as they occur in motile cells. Detailed modeling of the dynamics of such an actomyosin system remains a challenge for future theoretical studies.

Chapter 6

Appendices

6.1 Introduction to linear viscoelasticity

For the sake of completeness, we give in this appendix a brief introduction into linear viscoelasticity theory. The course of derivation follows closely the lecture series by Allen Pipkin [164]. Since we aim to model stress fibers that can be regarded as linear strings we restrict the description for simplicity to one dimension. However, once the theory is established in one dimension it can, in principle, be generalized to higher dimensions.

6.1.1 Relaxation modulus and creep compliance

The stress in a pure elastic body at a certain time point, say t_0, is given by the present strain in the system. In contrast, it is important to note, that in a viscoelastic material the current stress is a result of the full strain history for $t < t_0$. In order to derive a general relation between stress and strain in a viscoelastic body we first consider the stress relaxation as response to a one-step strain history $u(t) = u_0 \theta(t)$ where $u(t)$ is the strain, $\theta(t)$ is the Heaviside unit step function $\theta(t < 0) = 0$ and $\theta(t \geq 0) = 1$. The constant u_0 is the hight of the step. After a sudden application of the strain the stress in the material will relax. For symmetry reasons (assuming the material is isotropic) the imposed stress $f(t)$ relaxes according to an asymmetric function:

$$f(t) = G(t)u_0 + \mathcal{O}(u_0^3) \tag{6.1}$$

Where the higher order terms can be neglected, assuming that the step size is small enough such that linearization still holds. Similarly, if the material is subject to a one-step stress history $f(t) = f_0 \theta(t)$, the strain will relax according to the asymmetric function

$$u(t) = J(t)f_0 + \mathcal{O}(f_0^3) \tag{6.2}$$

The time dependent coefficients $G(t)$ and $J(t)$ of the linear terms are called *stress relaxation modulus* and *creep compliance*, respectively. Their functional form will depend on the properties of the underlying material.

One dimensional combinations of springs and dashpots provide simple models for

viscoelastic materials. The relations derived above can be carried over by substituting the strain (amount of shear) with the elongation of the element and the stress with the applied force. The force extension relation of a spring is given by

$$f(t) = ku(t) \tag{6.3}$$

Where k is the spring stiffness. When subject to a sudden elongation $u(t) = u_0\theta(t)$ the resistance force of the spring will be $f(t) = k\theta(t)u_0$. Comparison with Eq. (6.1) yields the relaxation modulus of a spring:

$$G(t) = k\theta(t) \tag{6.4}$$

Vice versa, if the spring is subject to a sudden force $f(t) = f_0\theta(t)$ it will elongate according to $u(t) = 1/kf(t) = 1/k\theta(t)f_0$ and comparison with Eq. (6.2) yields the creep compliance of a spring

$$J(t) = \frac{1}{k}\theta(t) \tag{6.5}$$

The resistance force of a dashpot is proportional to the rate of its elongation

$$f(t) = \gamma\dot{u}(t) \tag{6.6}$$

Where γ is the viscosity of the dashpot. When subject to a sudden elongation $u(t) = u_0\theta(t)$ the resistance force of the dashpot will be $f(t) = \gamma\delta_{dirac}(t)u_0$, where the time derivative of the Heaviside function yields the Dirac-δ function. Comparison with Eq. (6.2) yields the relaxation modulus of the dashpot

$$G(t) = \gamma\delta_{dirac}(t) \tag{6.7}$$

To obtain a relation between the force and the elongation, Eq. (6.6) has to be integrated $u(t) = \frac{1}{\gamma}\int_{-\infty}^{t} f(\tau)d\tau$. When subject to the force history $f(t) = f_0\theta(t)$ the dashpot will elongate according to $u(t) = \frac{1}{\gamma}\int_{-\infty}^{t} f_0\theta(\tau)d\tau = \frac{t}{\gamma}\theta(t)f_0$. Comparison with Eq. (6.2) yields the creep compliance of the dashpot

$$J(t) = \frac{t}{\gamma}\theta(t) \tag{6.8}$$

These basic relations can now be used as a starting point to calculate the relaxation modulus or the creep compliance for more complicated models. When two elements are connected in series, the applied tensile force f_0 is the same in both elements and the total elongation $u_{tot}^{\rightarrow\rightarrow}(t)$ is the sum of individual elongations.

$$u_{tot}^{\rightarrow\rightarrow}(t) = u_1(t) + u_2(t) = J_1(t)f_0 + J_2(t)f_0 \tag{6.9}$$

Here, the symbol $\rightarrow\rightarrow$ means that elements are connected in series. As a result the effective creep compliance of two elements placed in series is the sum of the individual creep compliances:

$$J_{tot}^{\rightarrow\rightarrow} = J_1(t) + J_2(t) \tag{6.10}$$

In contrast, if two elements are connected in parallel their elongation u_0 is identical and the applied force $f_{tot}^{\rightrightarrows}(t)$ is shared.

$$f_{tot}^{\rightrightarrows}(t) = f_1(t) + f_2(t) = G_1(t)u_0 + G_2(t)u_0 \tag{6.11}$$

Here, the symbol $\rightrightarrows$ denotes parallel alignment of elements. Thus, the effective relaxation modulus of two elements connected in parallel is the sum of the individual relaxation moduli:

$$G_{tot}^{\rightrightarrows} = G_1(t) + G_2(t) \tag{6.12}$$

We will see later on that the Laplace transform of J(t) and G(t) are tightly coupled to each other. It is due to this relation that, if one of the two quantities has been determined, the missing one can be calculated, provided that the involved inversion of the Laplace transform is feasible. The creep compliance and the relaxation modulus for some simple models are illustrated in Tab. 6.1. In particular, the properties of the Kelvin-Voigt body are of importance for this study.

6.1.2 Stress-relaxation and creep integral

In the previous paragraph the relaxation modulus $G(t)$ and the creep compliance $J(t)$ were derived. The merit of these response functions in a certain viscoelastic problem is comparable to the Greensfunction of a linear differential equation: Once, the single-step response function $G(t)$ or $J(t)$ is known, one can calculate the response of the system to an arbitrary strain or stress history. This results from the fact that any physical strain or stress history can be approximated arbitrary well by a sum of step functions. For example, let $u(t)$ be the imposed strain history. Approximation by N step functions yields:

$$u(t) \approx \sum_{i=1}^{N} \theta(t - t_i)\Delta u_i \tag{6.13}$$

Where Δu_i is the hight of the i-th step at time t_i. Due to the linear approximation, the total stress $f(t)$ is the superposition of the N stresses caused by each discrete strain step i.

$$f(t) \approx \sum_i G(t - t_i)\Delta u_i = \sum_i G(t - t_i)\frac{\Delta u_i}{\Delta t_i}\Delta t_i \tag{6.14}$$

A large number of steps leads to the continuous *stress-relaxation integral*:

$$f(t) = \int_{-\infty}^{t} G(t - t')\dot{u}(t')dt' \tag{6.15}$$

An equivalent relation follows when a certain stress history is given from which the strain has to be calculated. One finds the *creep integral*

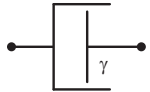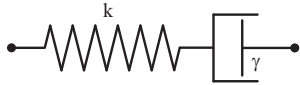$$u(t) = \int_{-\infty}^{t} J(t - t')\dot{f}(t')dt' \tag{6.16}$$

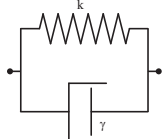| Generic viscoelastic models						
Schematic	$G(t)$	$J(t)$	$\bar{G}(s)$	$\bar{J}(s)$	$G^*(\omega)$	$J^*(\omega)$
	$k\theta(t)$	$\dfrac{1}{k}\theta(t)$	$\dfrac{k}{s}$	$\dfrac{1}{ks}$	k	$\dfrac{1}{k}$
	$\gamma\delta_{dirac}(t)$	$\dfrac{t}{\gamma}\theta(t)$	γ	$\dfrac{1}{s^2\gamma}$	$i\omega\gamma$	$-\dfrac{i}{\omega\gamma}$
	$ke^{-t/\tau}\theta(t)$	$\left(\dfrac{1}{k}+\dfrac{t}{\gamma}\right)\theta(t)$	$\dfrac{k\gamma}{k+s\gamma}$	$\dfrac{1}{ks}+\dfrac{1}{s^2\gamma}$	$\dfrac{\omega^2\gamma^2 k+i\omega\gamma k^2}{k^2+\omega^2\gamma^2}$	$\dfrac{1}{k}-\dfrac{i}{\omega\gamma}$
	$k\theta(t)+\gamma\delta_{dirac}(t)$	$\dfrac{1}{k}(1-e^{-t/\tau})\theta(t)$	$\dfrac{k}{s}+\gamma$	$\dfrac{1}{sk+s^2\gamma}$	$k+i\omega\gamma$	$\dfrac{k-i\omega\gamma}{k^2+\omega^2\gamma^2}$

Table 6.1: Overview of generic viscoelastic models: spring, dashpot, Maxwell body and Kelvin-Voigt body. Respectively, the relaxation modulus $G(t)$, the creep compliance $J(t)$, the same but Laplace-transformed quantities $\bar{G}(s)$ and $\bar{J}(s)$ as well as the complex modulus $G^*(\omega)$ and the complex compliance $J^*(\omega)$ are given. For the sake of clarity the time scale $\tau = \gamma/k$ was introduced. Knowing e.g. the relaxation modulus for the spring and the dashpot all other entries can be calculated from Eqs. (6.10),(6.12),(6.19),(6.21),(6.23),(6.25) and (6.27).

6.1.3   Sinusoidal deformation

A standard experiment for characterizing the viscoelastic properties of a material is to set it under sinusoidal deformation. Measurement of the phase shift between stress and strain as well as the ratios of their amplitudes determines the so called dynamic modulus or complex modulus. In this paragraph the theory behind such an experiment is described. But first we assume that the material is subject to an oscillating deformation with an exponentially increasing amplitude

$$u(t) = u_0 e^{\gamma t + i\omega t} = u_0 e^{st} \tag{6.17}$$

where s is a complex variable with a positive real part $\gamma > 0$ and its positive imaginary part denotes the radian frequency ω. The amplitude of the oscillation is exponentially growing according to $u_0 e^{\gamma t}$. Later, the limit $\gamma \to 0$ recovers the sinusoidal deformation with constant amplitude, the case we are actually interested in. The stress-relaxation integral Eq. (6.15) determines the stress provoked in the material

$$
\begin{aligned}
f(t) = \int_{-\infty}^{t} G(t - \tau)\dot{u}(\tau)d\tau &= u_0 s \int_{-\infty}^{t} G(t - \tau)e^{s\tau}d\tau \\
&= u_0 s \int_{0}^{\infty} G(\tau)e^{s(t-\tau)}d\tau \\
&= s\bar{G}(s)u_0 e^{st}
\end{aligned}
\tag{6.18}
$$

Where we abbreviated the Laplace transform of $G(t)$ by $\bar{G}(s)$

$$\bar{G}(s) = \int_{0}^{\infty} G(t)e^{-st}dt \tag{6.19}$$

According to Eq. (6.18), the stress also oscillates with exponentially increasing amplitude given by $|s\bar{G}(s)|u_0 e^{\gamma t}$ and frequency ω but with the constant phase shift $\arg(s\bar{G}(s))$ to the strain. Similarly, if the stress was initially given by $f(t) = f_0 e^{st}$, then the strain follows from the creep integral Eq. (6.16)

$$u(t) = s\bar{J}(s)f_0 e^{st} \tag{6.20}$$

Where, $\bar{J}(s)$ is the Laplace transform of the creep compliance $J(t)$.

$$\bar{J}(s) = \int_{0}^{\infty} J(t)e^{-st}dt \tag{6.21}$$

Now assume we have initially started with the input: $u_{in}(t) = u_0 e^{st}$. According to Eq. (6.18) this provokes the stress $f_{out}(t) = s\bar{G}(s)u_0 e^{st}$ in the material. It is now legitimate to ask, what would be the expected strain regarding the stress $f_{out}(t)$ as the input, that is $f_{in}(t) \equiv f_{out}(t)$. Of course, the resulting strain has to be equivalent to

the initial input $u_{in}(t)$! From Eq. (6.20) we find

$$u_{out}(t) = s\bar{J}(s)f_{in}(t) = s\bar{J}(s)s\bar{G}(s)u_0e^{st} \stackrel{!}{=} u_{in}(t) \qquad (6.22)$$

The last identity in the upper string of equations yields an important relation between the Laplace transforms of the relaxation modulus and the creep compliance

$$s\bar{J}(s)s\bar{G}(s) = 1 \qquad (6.23)$$

In principle, it allows to calculate e.g. G(t), given J(t), or vice versa, as long as the involved Laplace transform and its inversion are feasible. In order to get a relation between stress and strain for sinusoidal oscillations one has to perform the limit $\gamma \to 0$ in Eq. (6.18). Then the applied strain becomes $u(t) = u_0e^{i\omega t}$ and the provoked stress is given by

$$f(t) = G^*(\omega)u(t) \qquad (6.24)$$

The complex constant $G^*(\omega)$ is called the complex modulus, defined through the limiting process

$$G^*(\omega) = \lim_{\gamma \to 0} s\bar{G}(s) = \lim_{\gamma \to 0} (\gamma + i\omega)\bar{G}(\gamma + i\omega) \qquad (6.25)$$

Similarly, if the stress is the input

$$u(t) = J^*(\omega)f(t) \qquad (6.26)$$

Here, the complex constant $J^*(\omega)$ is called the complex compliance and equivalent to the complex modulus it is defined through the limiting process:

$$J^*(\omega) = \lim_{\gamma \to 0} s\bar{J}(s) \qquad (6.27)$$

With the same arguments as for exponentially increasing amplitudes of the input one can derive a relation equivalent to Eq. (6.23) but now for the complex compliance and complex modulus:

$$G^*(\omega)J^*(\omega) = 1 \qquad (6.28)$$

To see how the complex modulus $G^*(\omega)$ and the complex compliance $J^*(\omega)$ can be related to measurable quantities, we write the complex modulus in polar form $G^*(\omega) = |G^*(\omega)|e^{i\varphi}$. Then the relation between sinusoidal stress and strain, Eq. (6.24), becomes

$$f(t) = G^*(\omega)u(t) = |G^*(\omega)|u_0e^{i\omega t + i\varphi} \qquad (6.29)$$

Thus, in order to determine the absolute value of the complex modulus one has to measure the amplitudes of stress and strain. The absolute value is then given by the ratio of the amplitudes

$$|G^*(\omega)| = \frac{|f(t)|}{|u(t)|} \qquad (6.30)$$

The argument of the complex modulus can be determined by measuring the phase shift, φ, between stress and strain. φ is also called the *loss angle*. Experimentally, it has

been found that the strain always lags behind the stress, therefore $0 < \varphi < \pi/2$. Once G^* has been constructed Eq. (6.28) delivers J^* which can be expressed as:

$$J^*(\omega) = \frac{1}{|G^*(\omega)|} e^{-i\varphi} \tag{6.31}$$

It is also convenient to divide the complex modulus into real and imaginary part

$$G^*(\omega) = G'(\omega) + iG''(\omega) \tag{6.32}$$

The real part $G'(\omega)$ is called the *storage modulus* whereas the imaginary part $G''(\omega)$ is called the *loss modulus*. The names result from the fact that the first quantity amounts the part of the energy that is elastically stored whereas the second gives is a measure for the part of the energy that is dissipated by viscous friction. The total work performed by a little change in strain is given by

$$dW(t) = f(t)du(t) = G^*(\omega)u(t)du(t) = d\left(\frac{1}{2}G'(\omega)u^2(t)\right) + \left(\frac{G''(\omega)}{\omega}\dot{u}^2(t)\right) dt \tag{6.33}$$

The first term is a perfect differential and can be regarded as change of the stored elastic energy whereas the second term amounts the energy that is dissipated in time dt.

6.2   Proofs for eigenvalues and eigenvectors

In section 2.2.1 we have used the eigenvalues and eigenvectors given by

$$\lambda_l = \frac{k_{ext} + 4k_{int}\sin^2\frac{\pi l}{2(2N+1)}}{\gamma_{ext} + 4\tilde{\gamma}_{int}\sin^2\frac{\pi l}{2(2N+1)}} \quad \text{and} \quad \vec{v}_l = \begin{pmatrix} \sin\frac{\pi l}{2N+1} \\ \sin\frac{\pi 2l}{2N+1} \\ \sin\frac{\pi 3l}{2N+1} \\ \vdots \\ \sin\frac{\pi 2Nl}{2N+1} \end{pmatrix} \tag{6.34}$$

without proofing that this system indeed solves the eigenvalue problem (also compare Eq. (2.29) and Eq. (2.30))

$$(\boldsymbol{M}_{elas} - \lambda_l \boldsymbol{M}_{visc})\vec{v}_l = 0 \tag{6.35}$$

In this appendix we first catch up on this proof and later on verify certain properties of the eigenvalues and eigenvectors which we have claimed in the main text. These are:

(1) The eigenvalues are distinct, positive and non-zero.

(2) The eigenvectors are orthogonal and their length is given by $v_l = \sqrt{(2N+1)/2}$

In order to verify the given eigenvalues and eigenvectors we first rewrite the matrix $\boldsymbol{M}_{elas} - \lambda_l \boldsymbol{M}_{visc}$ as:

$$\boldsymbol{M}_{elas} - \lambda_l \boldsymbol{M}_{visc} = \begin{pmatrix} 2B-A & -B & 0 & 0 & \cdots \\ -B & 2B-A & -B & 0 & \cdots \\ 0 & -B & 2B-A & -B & \cdots \\ 0 & 0 & -B & 2B-A & \cdots \\ \vdots & \vdots & \vdots & \vdots & \ddots \end{pmatrix} \tag{6.36}$$

Where $B = k_{int} - \lambda_l \tilde{\gamma}_{int}$ and $A = -k_{ext} + \lambda_l \gamma_{ext}$. Now, one can use the expression for the eigenvalues given in Eq. (6.34) to express A in terms of B. It turns out that

$$A = 4B\sin^2\frac{\pi l}{2(2N+1)} \tag{6.37}$$

This relation allows to pull out a factor B from the matrix given in Eq. (6.36) and application of common addition theorems yields ($\cos 2\alpha = 1 - 2\sin^2\alpha$):

$$\boldsymbol{M}_{elas} - \lambda_l \boldsymbol{M}_{visc} = B\begin{pmatrix} 2\cos\left(\frac{\pi l}{2N+1}\right) & -1 & 0 & \cdots \\ -1 & 2\cos\left(\frac{\pi l}{2N+1}\right) & -1 & \cdots \\ 0 & -1 & 2\cos\left(\frac{\pi l}{2N+1}\right) & \cdots \\ \vdots & \vdots & \vdots & \vdots & \ddots \end{pmatrix} =: B\boldsymbol{M}_l$$

According to Eq. (6.35) it remains to be shown that the product $\boldsymbol{M}_l\vec{v}_l$ vanishes for all $l = 1, \ldots, 2N$. The m-th component of the vector which results from this product is

given below. It simplifies to zero after application of the common addition theorem: $2 \cos \alpha \sin \beta = \sin(\alpha + \beta) + \sin(\beta - \alpha)$.

$$- \sin \left(\frac{\pi(m-1)l}{2N+1} \right) + 2 \cos \left(\frac{\pi l}{2N+1} \right) \sin \left(\frac{\pi ml}{2N+1} \right) - \sin \left(\frac{\pi(m+1)l}{2N+1} \right) = 0 \quad (6.38)$$

In total we have shown that the system of eigenvalues and eigenvector Eq. (6.34) indeed obeys the eigenvalue equation Eq. (6.35).

We go on to proof claim (1) that the eigenvalues are distinct, positive and non-zero. The fact that the eigenvalues are positive and non-zero follows directly by inspection of Eq. (6.34) and by noting that all viscoelastic constants are positive, negative values would not be physical. It remains to be shown that there are no multiple eigenvalues. This can be seen after reformulating the expression for the eigenvalues as:

$$\lambda_l = \frac{k_{int}}{\tilde{\gamma}_{int}} + k_{int} \frac{\frac{k_{ext}}{k_{int}} - \frac{\gamma_{ext}}{\tilde{\gamma}_{int}}}{\gamma_{ext} + 4\tilde{\gamma}_{int} \sin^2 \frac{\pi l}{2(2N+1)}} \quad (6.39)$$

Since $1 \le l \le 2N$, it holds for the argument of the sin-function that $0 < \frac{\pi l}{2(2N+1)} < \frac{\pi}{2}$. In this interval, the sin-function increases monotonically and is single-valued. For this reason, the eigenvalues, λ_l, are also single-valued. The eigenvalues increase monotonically with l if $\frac{k_{ext}}{k_{int}} < \frac{\gamma_{ext}}{\tilde{\gamma}_{int}}$ and decrease monotonically for increasing l if the opposite inequality holds.

In the next step we deliver the proof for claim (2) that the eigenvectors are orthogonal and their length is given by $v_l = \sqrt{(2N+1)/2}$. To show this in a convenient way we consider the matrix of normalized eigenvectors, $\boldsymbol{U}$, which is also used in the main text:

$$\boldsymbol{U} = \sqrt{\frac{2}{2N+1}}(v_1, v_2, \ldots, v_{2N}) \quad \Leftrightarrow \quad \boldsymbol{U}_{j,l} = \sqrt{\frac{2}{2N+1}} \sin \frac{\pi lj}{2N+1} \quad (6.40)$$

By means of this matrix, the statement to be shown can be recapitulated as $\boldsymbol{U}^T \boldsymbol{U} = I \Leftrightarrow (\boldsymbol{UU})_{k,m} = \delta_{k,m}$. The second relation follows since $\boldsymbol{U}$ is obviously symmetric. In the following we will evaluate the square of the matrix $\boldsymbol{U}$ componentwise:

$$
\begin{aligned}
(\boldsymbol{UU})_{k,m} &= \sum_{j=1}^{2N} \boldsymbol{U}_{k,j} \boldsymbol{U}_{j,m} \\
&= \frac{2}{2N+1} \sum_{j=1}^{2N} \sin \frac{\pi kj}{2N+1} \sin \frac{\pi jm}{2N+1} \\
&= \frac{1}{2N+1} \sum_{j=1}^{2N} \left(\cos \frac{\pi j(k-m)}{2N+1} - \cos \frac{\pi j(k+m)}{2N+1} \right)
\end{aligned} \quad (6.41)
$$

The finite sums over the cos-functions can be evaluated. For an arbitrary angle α one finds:

$$
\begin{aligned}
\sum_{j=0}^{n} \cos(j\alpha) &= \Re \sum_{j=0}^{n} \left(\cos(j\alpha) + i\sin(j\alpha) \right) \\
&= \Re \sum_{j=0}^{n} \left(e^{i\alpha} \right)^{j} \\
&= \Re \left(\frac{1 - e^{i\alpha(n+1)}}{1 - e^{i\alpha}} \right) \\
&= \frac{1}{2} \left(1 + \frac{\sin(\alpha(n+1/2))}{\sin(\alpha/2)} \right)
\end{aligned}
\tag{6.42}
$$

Where $\Re(z)$ denotes the real part of the complex variable z. If instead the imaginary part is taken, a similar relation is obtained for the sin-function which we also use in section 2.2.1 of the main text:

$$
\sum_{j=0}^{n} \sin(j\alpha) = \frac{1}{2} \left(\cot(\alpha/2) - \frac{\cos(\alpha(n+1/2))}{\sin(\alpha/2)} \right)
\tag{6.43}
$$

Application of Eq. (6.42) in order to simplify Eq. (6.41) finally yields:

$$
\begin{aligned}
(\boldsymbol{UU})_{k,m} &= \frac{1}{2(2N+1)} \left(\sin\left((k-m)\pi\right) \cot \frac{(k-m)\pi}{2(2N+1)} + \dots \right. \\
&\left. - \sin((k+m)\pi) \cot \frac{(k+m)\pi}{2(2N+1)} + \cos((k+m)\pi) - \cos((k-m)\pi) \right)
\end{aligned}
\tag{6.44}
$$

There are two cases, namely $k = m$ and $k \neq m$, that have to be considered. At first, assume that $k = m$. In this case, the last two terms in Eq. (6.44) just cancel out each other. The sin-function in the second term evaluates to zero while the cotangent gives a finite value: since $0 < \frac{(k+m)\pi}{2(2N+1)} < \pi$, the poles are just spared. Thus, also this term vanishes. It is only the first term that gives a real contribution, it evaluates to:

$$
(\boldsymbol{UU})_{k,k} = \frac{1}{2(2N+1)} \lim_{m \to k} \frac{\sin\left((k-m)\pi\right)}{\sin \frac{(k-m)\pi}{2(2N+1)}} = \lim_{m \to k} \frac{\cos\left((k-m)\pi\right)}{\cos \frac{(k-m)\pi}{2(2N+1)}} = 1
\tag{6.45}
$$

The upper equation constitutes that all diagonal components of $\boldsymbol{U}^2$ are unity. Now assume that $k \neq m$. In this case the first as well as the second term in Eq. (6.44) vanish since the sin-function evaluates to zero while the co-tangent yields finite values. The last two terms further simplify to:

$$
\begin{aligned}
(\boldsymbol{UU})_{k,m \neq k} &= \frac{1}{2(2N+1)} \left((-1)^{k+m} - (-1)^{k-m} \right) \\
&= \frac{1}{2(2N+1)} (-1)^{k-m} \left((-1)^{2m} - 1 \right) = 0
\end{aligned}
\tag{6.46}
$$

The upper equation constitutes that all off-diagonal components of $\boldsymbol{U}^2$ vanish. The combination of Eq. (6.45) and Eq. (6.46) yields $(\boldsymbol{U}\boldsymbol{U})_{k,m} = \delta_{k,m}$ which was to be demonstrated. In total we have shown that all eigenvectors are of length $v_l = \sqrt{(2N+1)/2}$ and form a complete orthogonal basis.

6.3   Uniform convergence of first derivative

The calculation of the tension within the stress fiber requires the evaluation of the first spatial derivative of the displacement, Eq. (2.57). In this appendix we deliver the proof that this derivative can be calculated by changing the order of differentiation and summation in Eq. (2.57). This change in order is in general not legitimate unless the series obeys certain conditions. For instance, it is sufficient, if the series shows the following properties:

Theorem 1: Let f_m be continuously differentiable complex functions in $\mathbb{D}$ that obey the following conditions:

(1) the series $\sum_{m=1}^{\infty} f_m$ converges uniformly in $\mathbb{D}$;

(2) the series $\sum_{m=1}^{\infty} f_m'$ converges also uniformly in $\mathbb{D}$.

Then, the function defined by $f := \sum_{m=1}^{\infty} f_m$ is differentiable in $\mathbb{D}$ and its derivative is given by: $f' := \sum_{m=1}^{\infty} f_m'$.

There exist sharper theorems that pose weaker conditions on the functions f_m but the given theorem is sufficient for our purpose. The series of interest that constitutes the solution for the displacement, Eq. (2.57), is obviously uniformly convergent for all $x \in [0, L]$ and $t \in [0, \infty]$. A majorant and convergent series is given e.g. by $\sum_{m=1}^{\infty} \frac{1}{(a\pi(2m-1))^2}$. However, it is more challenging to prove the uniform convergence of the piecewise differentiated series with respect to the spatial variable x:

$$u'(x,t) = -4a\pi\delta \sum_{m=1}^{\infty} \underbrace{\frac{2m-1}{4\kappa L^2 + (a\pi(2m-1))^2}}_{=:\,f_m} \underbrace{(-1)^{m+1}(1 - e^{-t/\tau_m}) \cos\frac{\pi x(2m-1)}{(2L)}}_{=:\,a_m(x)} \quad (6.47)$$

In order to proof the uniform convergence of this series, we apply the Dirichlet-Criteria depicted in the following theorem:

Theorem 2 (The Dirichlet-Criteria): Let f_m be real and let a_m be complex functions on $\mathbb{D}$ that obey the following conditions for $m \in \mathbb{N}$:

(1) $f_m(x)$ is monotonically decreasing for all $x \in \mathbb{D}$;

(2) f_m converges uniformly in $\mathbb{D}$ to zero;

(3) There exists an upper bound M such that $\|\sum_{m=1}^{n} a_m\|_{\mathbb{D}} \leq M$ for all n. Here, $\|g\|_{\mathbb{D}}$ denotes the supremum norm of g with respect to $\mathbb{D}$, that is $\|g\|_{\mathbb{D}} := \sup\{|g(x)|, x \in \mathbb{D}\}$.

Then, the series $\sum_{m=1}^{\infty} a_m f_m$ converges uniformly in $\mathbb{D}$.

In Eq. (6.47) we have already separated the summands into the two factors f_m and $a_m(x)$. The functions f_m obviously fulfill the conditions (1) and (2) required by the

Dirichlet-Criteria. The condition (3) on the functions a_m remain to be shown. The domain, $\mathbb{D}$, over which this is possible has to be limited to $x \in [0, L-\epsilon]$ with $0 < \epsilon < L$:

$$
\begin{aligned}
\left\| \sum_{m=1}^{n} a_m(x) \right\|_{\mathbb{D}} &= \left\| \sum_{m=1}^{n} (-1)^{m+1}(1 - e^{-t/\tau_m}) \cos \frac{\pi x(2m-1)}{2L} \right\|_{x \in [0,L-\epsilon]} \\
&\leq \left\| \sum_{m=1}^{n} (-1)^{m+1} \cos \frac{\pi x(2m-1)}{2L} \right\|_{x \in [0,L-\epsilon]} \\
&= \frac{1}{2} \left\| \sum_{m=1}^{n} e^{i\pi(m+1)} \left(e^{i\pi \frac{x}{2L}(2m-1)} + e^{-i\pi \frac{x}{2L}(2m-1)} \right) \right\|_{\mathbb{D}} \\
&\leq \frac{1}{2} \left\| \sum_{m=1}^{n} e^{i\pi m(1+\frac{x}{L})} \right\|_{\mathbb{D}} + \frac{1}{2} \left\| \sum_{m=1}^{n} e^{i\pi m(1-\frac{x}{L})} \right\|_{\mathbb{D}} \\
&= \frac{1}{2} \left\| \frac{1 - e^{i\pi(1+\frac{x}{L})(n+1)}}{1 - e^{i\pi(1+\frac{x}{L})}} - 1 \right\|_{\mathbb{D}} + \frac{1}{2} \left\| \frac{1 - e^{i\pi(1-\frac{x}{L})(n+1)}}{1 - e^{i\pi(1-\frac{x}{L})}} - 1 \right\|_{\mathbb{D}} \\
&\leq \frac{1}{2} \left\| \frac{1}{\sin \frac{\pi(1+\frac{x}{L})}{2}} \right\|_{x \in [0,L-\epsilon]} + \frac{1}{2} \left\| \frac{1}{\sin \frac{\pi(1-\frac{x}{L})}{2}} \right\|_{x \in [0,L-\epsilon]} \\
&\leq \frac{1}{2} \left| \frac{1}{\sin\left(\pi - \frac{\pi\epsilon}{2L}\right)} \right| + \frac{1}{2} \left| \frac{1}{\sin \frac{\pi\epsilon}{2L}} \right| \\
&= \frac{1}{\sin \frac{\pi\epsilon}{2L}} =: M
\end{aligned}
\tag{6.48}
$$

The very first inequality holds true since t and τ_m are both positive. The exponential factor therefore varies within the bounds $[0, 1]$. In the second to last step the two x-dependent terms have been evaluated at their maximal values within the domain $\mathbb{D}$ which are reached at $x = L - \epsilon$, respectively. The last line defines the upper bound M which is neither dependent on x nor on n and thus fulfills the requirements (3) of the Dirichlet-Criteria. In total we have shown that the first spatial derivative of the displacement field $u(x, t)$ can be calculated by piecewise differentiation within the interval $x \in [0, L - \epsilon]$ with $\epsilon > 0$. Note that for $\epsilon = 0 \Leftrightarrow x = L$ the upper bound M diverges and the calculation breaks down. Therefore it is indeed necessary to constrain the spatial variable to $x \in [0, L - \epsilon]$ with $\epsilon > 0$. This constraint, however, is not further hindering. The first spatial derivative is of interest only in connection with the viscoelastic stress within the stress fiber. Eq. (6.47) allows to calculate the tension for all $x < L$ whereas the tension at $x = L$ is set to zero by the imposed boundary conditions. In this way, the tension can be calculated analytically along the whole fiber. It is also noteworthy that the upper calculation breaks down for higher spatial derivatives. Each differentiation step contributes an additional factor $(2m - 1)$ to the functions f_m. Already in case of the second derivative the functions f_m no longer converge to zero and condition (3) of the Dirichlet-Criteria can not be fulfilled anymore.

In contrast, derivatives with respect to time pose no problems because convergence of the functions f_m to zero is sustained.

6.4   Solution by inverse Laplace transform

In the main text (see section 2.2.3) we have briefly discussed how an analytical expression for the displacements can be derived by solving an inversion problem. This appendix complements the calculations presented in the main text and provides some further derivation details. In the following we express all equations in terms of the non-dimensional quantities $\tilde{x} = x/a$, $L = L/a$, $\tilde{t} = t/\tau$, $\tilde{s} = s/\tau$ and $\tilde{\omega} = \omega/\tau$. For the sake of clarity, however, we omit to furnish the variables with the tilde.

The simple initial conditions of vanishing displacements at $t = 0$ enables the Laplace transform of the boundary value problem given in Eq. (2.22). Transformation simplifies the model equation to the following second order differential equation:

$$(1 + s)\partial_x^2 \bar{u}(x, s) - (\kappa + s\Gamma)\bar{u}(x, s) = 0 \tag{6.49}$$

Here, $\bar{u}(x, s) = \int_0^\infty u(x,t)e^{-st}dt$ denotes the Laplace transform of the displacement. In the following and throughout the manuscript, overbars always denote the Laplace-transformed quantities. The variable $s = \gamma + i\omega$ is in general a complex variable with real part γ and imaginary part ω. Similarly, the boundary conditions transform according to:

$$\bar{u}(0, s) = 0 \quad \text{and} \quad (1 + s)\bar{u}(L, s) + \frac{\delta}{s} = 0 \tag{6.50}$$

Eq. (6.49) and Eq. (6.50) describe an ordinary differential equation with appropriate boundary conditions which is straight forward to solve. The solution for the Laplace-transformed displacement is given by:

$$\bar{u}(x, s) = \quad -\delta \cdot \underbrace{\frac{1}{s}\operatorname{sech}\left(L\frac{\sqrt{\Gamma s + \kappa}}{\sqrt{1 + s}}\right)}_{=: \ \bar{g}_1(s)} \cdot \underbrace{\frac{\sinh\left(x\frac{\sqrt{\Gamma s + \kappa}}{\sqrt{1 + s}}\right)}{\sqrt{1 + s}\sqrt{\Gamma s + \kappa}}}_{=: \ \bar{g}_2(x, s)} \tag{6.51}$$

The solution in real space is now given by the inverse Laplace transform of the upper equation. The inversion problem will be divided into two parts. The two functions, $\bar{g}_1(s)$ and $\bar{g}_2(x, s)$ defined above, will be inverted separately. The inverse Laplace transform of $\bar{u}$, the product of these two functions, is then given by the convolution theorem. The inversion formula for the Laplace transform is in general given by the Bromwich integral:

$$f(t) = \mathcal{L}^{-1}[\bar{f}(s)](t) = \frac{1}{2\pi i}\int_{\gamma - i\infty}^{\gamma + i\infty} e^{st}\bar{f}(s)ds \tag{6.52}$$

The constant γ has to be chosen such that all singularities of the function $\bar{f}(s)$ are on the left hand side of the integration path. For the special case where $t > 0$ and in addition the contour may be closed by an infinite semicircle in the left half-plane enclosing all singularities of $\bar{f}(s)$ then the residue theorem is applicable and (see [91]):

$$f(t) = \sum_m \operatorname{res}(e^{st}\bar{f}(s), s_m) \tag{6.53}$$

Where s_m are the singularities of the function $\bar{f}(s)$. It has to be checked that the two functions, $\bar{g}_1$ and $\bar{g}_2$ fulfill the conditions mentioned above. Then, the inversion problem is solved by finding the residues of the two functions $e^{st}\bar{g}_1(s)$ and $e^{st}\bar{g}_2(s)$ at all occurring singularities. Since we are only interested in solutions for $t > 0$ it remains to be shown, that the occurring singularities of the two functions can be encircled by a closed contour. Thereby caution is in principle advised since the roots, occurring in both functions, could necessitate the introduction of cut lines into the complex plane that are not allowed to cross and potentially prohibit an enclosing contour. Fortunately, for both functions, no cut lines have to be introduced which can be seen directly when expressing the occurring hyperbolic functions by their Taylor series. The function $\bar{g}_1$ contains a hyperbolic secant which is an even function, thus its Taylor series contains only even powers. The roots which appear in the argument of the hyperbolic secant are thus converted to polynomials with integer powers in s and essentially no roots have to be calculated. Similar arguments hold true for the function $\bar{g}_2$. The hyperbolic sine is an odd function, its Taylor series contains only terms of odd powers. Since the arguments of the hyperbolic sine contains roots, this term alone would require a cut line. However, $\bar{g}_2$ contains the same roots which appear in the argument of the hyperbolic sine also as pre-factors. These pre-factors convert the half-integral powers within the Taylor series to integer powers and no roots have to be calculated. Thus, for both functions, no cut lines have to be introduced and the Laplace inversion of the two functions $\bar{g}_1$ and $\bar{g}_2$ can be performed using residues calculus according to Eq. (6.53). In the following, we will derive the inversion for the two functions separately and at the end merge them by the convolution theorem to obtain the final solution for the displacement.

The function $\bar{g}_1$ has a simple pole at $s = 0$ with residue $\mathrm{res}(e^{st}\bar{g}_1(s), 0) = \mathrm{sech}\left(L\sqrt{\kappa}\right)$. In addition, every root of the hyperbolic cosine contributes a singularity. The roots r_m of the hyperbolic cosine are $r_m = i(2m - 1)\pi/2$ with $m \in \mathbb{Z}$. Therefore the poles of the hyperbolic secant, s_m are located at:

$$s_m = -\frac{L^2\kappa - r_m^2}{L^2\Gamma - r_m^2} = -\frac{4L^2\kappa + (\pi(2m-1))^2}{4L^2\Gamma + (\pi(2m-1))^2} \tag{6.54}$$

Notice that $s_m = s_{-m+1}$. In order to avoid double counting of the poles, in Eq. (6.54), m has to be constraint to $m = 1, \ldots, \infty$. To calculate the associated residues we expand the hyperbolic cosine in the denominator about its roots s_m. Expansion yields:

$$
\begin{aligned}
e^{st}\bar{g}_1(s) &= \frac{1}{\cosh\left(\frac{L\sqrt{\Gamma s + \kappa}}{\sqrt{1+s}}\right)} \cdot \frac{e^{st}}{s} \\[2mm]
&= \frac{1}{\frac{(-1)^{m+1}(\pi^2(2m-1)^2 + 4L^2\Gamma)^2}{16\pi L^2(2m-1)(\Gamma - \kappa)}(s - s_m) + \mathcal{O}\left((s - s_m)^2\right)} \cdot \frac{e^{st}}{s} \\[2mm]
&= \underbrace{\frac{16\pi L^2(-1)^{m+1}(2m-1)(\Gamma - \kappa)}{(\pi^2(2m-1)^2 + 4L^2\Gamma)^2(s - s_m)}}_{\text{simple pole at } s = s_m} \cdot \underbrace{\frac{1}{1 + \mathcal{O}(s - s_m)}}_{\text{holomorphic}} \cdot \frac{e^{st}}{s}
\end{aligned}
\tag{6.55}
$$

The first factor on the right hand side of the upper equation is a function with a simple pole at $s = s_m$. It is multiplied with a function which is holomorphic at $s = s_m$. In this situation, the residue of the product is given by the residue of the function with the simple pole, multiplied with the value of the holomorphic function at the singularity. Thus, the residue at $s = s_m$ is given by:

$$\mathrm{res}(e^{st}\bar{g}_1(s), s_m) = 16\pi L^2 \frac{(-1)^{m+1}(2m-1)(\Gamma - \kappa)}{(\pi^2(2m-1)^2 + 4L^2\Gamma)^2} \frac{e^{ts_m}}{s_m} \tag{6.56}$$

According to Eq. (6.53) the inverse of the function $\bar{g}_1(s)$ is now given by the sum over all residues.

$$g_1(t) = \mathrm{sech}(L\sqrt{\kappa}) + 16\pi L^2 \sum_{m=1}^{\infty} \frac{(-1)^{m+1}(2m-1)(\Gamma - \kappa)}{(\pi^2(2m-1)^2 + 4L^2\Gamma)^2} \frac{e^{ts_m}}{s_m} \tag{6.57}$$

The first term originates from the simple pole at $s = 0$ and the infinite sum accounts for the residues at $s = s_m$. Values for s_m are given by Eq. (6.54). It is interesting to note, that the position of the poles s_m are, except for the signs, identical with the eigenvalues that arise in the other derivation. The inverse of both give the retardation times of the model. The inversion of the second function $\bar{g}_2$ is a bit more involved since $\bar{g}_2$ has an essential singularity at $s = -1$. Note that the singularity at $s = -\kappa/\Gamma$ is removable and has not to be considered! It is convenient to first perform the variable transformation $s \rightarrow s - 1$ and calculate the residue of the function $\bar{g}_2(s-1)$ at $s = 0$ instead. The final result is then obtained using the substitution rule of the Laplace transform: $g(t) = e^{-at}\mathcal{L}^{-1}[\bar{g}(s-a)]$ where in the present case $a = 1$. The course of the calculation is as follows: The hyperbolic sine and the exponential function will be expressed in terms of their Taylor series. Subsequently, the product of these two series will be reordered such that the terms of order s^{-1}, which constitute the residue, can be read off. The Taylor series of the hyperbolic sine is given by:

$$\sinh(z) = \sum_{n=0}^{\infty} \frac{z^{2n+1}}{(2n+1)!} = z + \frac{z^3}{3!} + \frac{z^5}{5!} + \frac{z^7}{7!} + ... \tag{6.58}$$

Performing the previously announced variable transformation $s \rightarrow s - 1$ on $\bar{g}_2$ and evaluating the hyperbolic sine at its actual argument yields:

$$\sinh\left(\frac{x\sqrt{\Gamma s + \kappa - \Gamma}}{\sqrt{s}}\right) = \sum_{n=0}^{\infty} \frac{x^{2n+1}(\Gamma s + \kappa - \Gamma)^{\frac{2n+1}{2}}}{(2n+1)! s^{\frac{2n+1}{2}}} \tag{6.59}$$

To complete the function $\bar{g}_2$ the additional pre-factors have to be taken into account. They can be pulled into the series and the formerly half-integral powers cancel to common polynomials in s:

$$
\begin{aligned}
\bar{g}_2(s-1) = \frac{\sinh\left(\frac{x\sqrt{\Gamma s + \kappa - \Gamma}}{\sqrt{s}}\right)}{\sqrt{s}\sqrt{\Gamma s + \kappa - \Gamma}} &= \sum_{n=0}^{\infty} \frac{x^{2n+1}(\Gamma s + \kappa - \Gamma)^n}{(2n+1)! s^{n+1}} \\
&= \sum_{n=0}^{\infty} \frac{x^{2n+1}}{(2n+1)! s^{n+1}} \sum_{k=0}^{n} \binom{n}{k}(\Gamma s)^{n-k}(\kappa - \Gamma)^k
\end{aligned}
\tag{6.60}
$$

In the last step, we have evaluated the polynomials by means of the binomial formula which now allows to reorder the double sum and collect terms of the same powers in s:

$$
\begin{aligned}
\bar{g}_2(s-1) = \quad & +\frac{x^1}{1!}\binom{0}{0}\Gamma^0(\kappa-\Gamma)^0\frac{1}{s} \\
& +\frac{x^3}{3!}\binom{1}{0}\Gamma^1(\kappa-\Gamma)^0\frac{1}{s} + \frac{x^3}{3!}\binom{1}{1}\Gamma^0(\kappa-\Gamma)^1\frac{1}{s^2} \\
& +\frac{x^5}{5!}\binom{2}{0}\Gamma^2(\kappa-\Gamma)^0\frac{1}{s} + \frac{x^5}{5!}\binom{2}{1}\Gamma^1(\kappa-\Gamma)^1\frac{1}{s^2} + \frac{x^5}{5!}\binom{2}{2}\Gamma^0(\kappa-\Gamma)^2\frac{1}{s^3} \\
& +\frac{x^7}{7!}\binom{3}{0}\Gamma^3(\kappa-\Gamma)^0\frac{1}{s} + \frac{x^7}{7!}\binom{3}{1}\Gamma^2(\kappa-\Gamma)^1\frac{1}{s^2} + \frac{x^7}{7!}\binom{3}{2}\Gamma^1(\kappa-\Gamma)^2\frac{1}{s^3} + \dots
\end{aligned}
$$

In the equation above, terms of same power in s, are arranged column-wise. In the following each column will be merged to a separate sum:

$$
\begin{aligned}
\bar{g}_2(s-1) = \quad & \frac{1}{s}\sum_{n=0}^{\infty}\frac{x^{2n+1}}{(2n+1)!}\binom{n}{0}\Gamma^n(\kappa-\Gamma)^0 + \frac{1}{s^2}\sum_{n=0}^{\infty}\frac{x^{2(n+1)+1}}{(2(n+1)+1)!}\binom{n+1}{1}\Gamma^n(\kappa-\Gamma)^1 \\
& +\frac{1}{s^3}\sum_{n=0}^{\infty}\frac{x^{2(n+2)+1}}{(2(n+2)+1)!}\binom{n+2}{2}\Gamma^n(\kappa-\Gamma)^2 + \dots \\
= \quad & \sum_{j=0}^{\infty}\frac{1}{s^{j+1}}\sum_{n=0}^{\infty}\binom{n+j}{j}\frac{x^{2(n+j)+1}}{(2(n+j)+1)!}\Gamma^n(\kappa-\Gamma)^j = \sum_{j=0}^{\infty}\frac{d_j}{s^{j+1}}
\end{aligned}
$$

Where we defined the coefficients d_j to short cut the calculation:

$$
d_j = \sum_{n=0}^{\infty}\binom{n+j}{j}\frac{x^{2(n+j)+1}}{(2(n+j)+1)!}\Gamma^n(\kappa-\Gamma)^j \tag{6.61}
$$

In order to calculate the proper residue, the series expansion for the function $\bar{g}_2$ derived above has to be multiplied with the exponential factor e^{st}. Collection of all terms of order s^{-1} then yields the searched residue. Multiplication of the two series gives:

$$
\bar{g}_2(s-1)\cdot e^{st} = \left(\frac{d_0}{s} + \frac{d_1}{s^2} + \frac{d_2}{s^3} + \mathcal{O}(1/s^4)\right) \cdot \left(1 + st + \frac{(ts)^2}{2!} + \frac{(ts)^3}{3!} + \mathcal{O}(s^4)\right)
$$

$$
\begin{aligned}
= \quad & \boxed{\frac{d_0 t^0}{0!}\frac{1}{s}} + \frac{d_0 t^1}{1!} + \frac{d_0 t^2}{2!}s + \frac{d_0 t^3}{3!}s^2 + \dots \\
& +\frac{d_1 t^0}{0!}\frac{1}{s^2} + \boxed{\frac{d_1 t^1}{1!}\frac{1}{s}} + \frac{d_1 t^2}{2!} + \frac{d_1 t^3}{3!}s + \frac{d_1 t^4}{4!}s^2 + \dots \\
& +\frac{d_2 t^0}{0!}\frac{1}{s^3} + \frac{d_2 t^1}{1!}\frac{1}{s^2} + \boxed{\frac{d_2 t^2}{2!}\frac{1}{s}} + \frac{d_2 t^3}{3!} + \frac{d_2 t^4}{4!}s + \frac{d_2 t^5}{5!}s^2 + \dots
\end{aligned} \tag{6.62}
$$

The highlighted column determines the residue at $s = 0$ which constitutes the inverse Laplace transform of the function $\bar{g}_2(s-1)$. The coefficients d_j are given by Eq. (6.61). To obtain the inverse Laplace transform of the unshifted function $\bar{g}_2(s)$ the substitution

rule of the Laplace transform has to be applied:

$$
\begin{aligned}
g_2(t) &= \mathcal{L}^{-1}[\bar{g}_2(s)] = e^{-t}\mathcal{L}^{-1}[\bar{g}_2(s-1)] = e^{-t}\,\mathrm{res}(\bar{g}_2(s-1)e^{st},0) \\
&= e^{-t}\sum_{j=0}^{\infty}\frac{t^j}{j!}d_j = e^{-t}\sum_{j=0}^{\infty}\frac{t^j}{j!}\sum_{n=0}^{\infty}\binom{n+j}{j}\frac{x^{2(n+j)+1}}{(2(n+j)+1)!}\Gamma^n(\kappa-\Gamma)^j
\end{aligned}
\tag{6.63}
$$

Eq. (6.57) and Eq. (6.63) give the inverse Laplace transform of the two functions $\bar{g}_1$ and $\bar{g}_2$. The inversion of the Laplace-transformed displacement, which is essentially the product of $\bar{g}_1$ and $\bar{g}_2$, is then given by the convolution theorem as: $u(x,t) = -\delta\int_0^t g_1(t')g_2(t-t')dt'$. Insertion of the derived functions g_1 and g_2 finally yields the analytical solution for the displacement along the fiber:

$$
\begin{aligned}
u(x,t) = -\delta\int_0^t &\left[\left(\mathrm{sech}(L\sqrt{\kappa}) + 16\pi L^2\sum_{m=1}^{\infty}\frac{(-1)^{m+1}(2m-1)(\Gamma-\kappa)}{(\pi^2(2m-1)^2+4L^2\Gamma)^2}\frac{e^{t's_m}}{s_m}\right)\right. \\
&\left.\cdot e^{-(t-t')}\sum_{j=0}^{\infty}\frac{(t-t')^j}{j!}\sum_{n=0}^{\infty}\binom{n+j}{j}\frac{x^{2(n+j)+1}\Gamma^n}{(2(n+j)+1)!}(\kappa-\Gamma)^j\right]dt'
\end{aligned}
\tag{6.64}
$$

The expression above can be evaluated numerically, however many terms of the infinite series have to be taken into account to get a satisfactory approximation for the solution. Especially displacements at large x and intermediate time points t are difficult to evaluate. Fig. 6.1 shows a pointwise comparison of the above solution with the numerical solution obtained from the Matlab PDE-toolbox. Thereby, the upper limits of the infinite series have been approximated by either 5, 10 or 50 yielding the solutions u_{ana}^5 dashed lines, u_{ana}^{10} dotted lines and u_{ana}^{50} marked by dots, respectively. Calculation of the solution by the above expression is much slower than by Eq. (2.57). The latter turned out to be even faster than the numerical solution in the Matlab-PDE toolbox.

The convolution integral in Eq. (6.64) can be readily calculated after exchanging the order of summation and integration. The occurring two integrals that have to be solved are of the form:

$$
\int_0^t (t-t')^j e^{-(t-t'-\alpha t')}dt' = \frac{j!e^{\alpha t}}{(1+\alpha)^{j+1}} - e^{-t}\sum_{k=0}^{j}\frac{j!t^{j-k}}{(j-k)!(1+\alpha)^{k+1}}
\tag{6.65}
$$

In one integral α vanishes and in the other integral $\alpha = s_m$. Evaluation of the convolution in Eq. (6.64) finally yields an analytical expression that only contains infinite series, that are straight forward to calculate. More importantly, the resulting solution decomposes into a stationary and several time-dependent contributions which vanish exponentially for large times. The remaining stationary contribution is given by:

$$
u_{ss}(x) = -\delta\,\mathrm{sech}(L\sqrt{\kappa})\sum_{j=0}^{\infty}(\kappa-\Gamma)^j\sum_{n=0}^{\infty}\binom{n+j}{j}\frac{x^{2(n+j)+1}\Gamma^n}{(2(n+j)+1)!}
\tag{6.66}
$$

The above result has to be mathematically identical with previously found expressions for the stationary solution in Eq. (2.24) and Eq. (2.57). By comparing these results
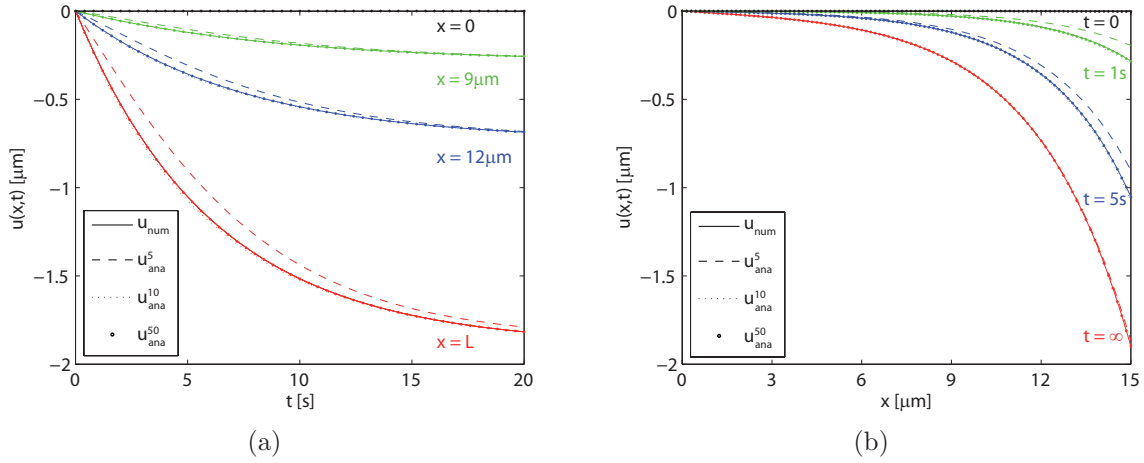
(a)   (b)

Figure 6.1: Comparison of the numerical solution from the Matlab PDE toolbox (u_{num}, solid lines) with the analytical solution calculated by Eq. (6.64). In the analytical solution the upper limits of all infinite sums have been approximated by 5, 10 and 50 (u_{ana}^5 dashed lines, u_{ana}^{10} dotted lines and u_{ana}^{50} marked by dots, respectively). (a) Plot of the time dependent displacement $u(t)$ at constant positions $x \in \{0, 9\,\mu\text{m}, 12\,\mu\text{m}, L\}$. (b) Plot of the spatial variations of the displacement $u(x)$ at certain time points $t \in \{0, 1\,\text{s}, 5\,\text{s}, \infty\}$. Used parameter values are identical with Fig. 2.4: $(\kappa, \tau, \tau_\epsilon, \delta) = (0.1, 5\,\text{s}, 0.75\,\text{s}, 0.6\,\mu\text{m})$ and $L = 15\,\mu\text{m}$.

the following mathematical identities can be deduced:

$$
\begin{aligned}
\frac{\sinh(x\sqrt{\kappa})}{\sqrt{\kappa}} &\overset{!}{=} 8L\cosh(L\sqrt{\kappa}) \sum_{m=1}^{\infty} \frac{(-1)^{m+1}\sin\frac{\pi x(2m-1)}{2L}}{4\kappa L^2 + (\pi(2m-1))^2} \\
\frac{\sinh(x\sqrt{\kappa})}{\sqrt{\kappa}} &\overset{!}{=} \sum_{j=0}^{\infty}(\kappa-\Gamma)^j \sum_{n=0}^{\infty} \binom{n+j}{j} \frac{x^{2(n+j)+1}\Gamma^n}{(2(n+j)+1)!}
\end{aligned}
\tag{6.67}
$$

The last identity is particularly interesting. Note, that the right hand side of the last equation depends on the parameter Γ in a complicated manner. The left hand side, however, does not depend on Γ. The only assumptions made to derive this identity were that the occurring parameters κ, Γ, x are all positive. Beside these constraints, the given identity must hold true for all positive Γ. The identity is easy to verify for the special case $\Gamma = \kappa$ where only the $j = 0$ term survives. The remaining series is just the Taylor series for the hyperbolic sine, compare Eq. (6.58). In addition the identity has been checked numerically for a few different sets of non-trivial parameter values.

Bibliography

[1] V. Vogel and M. Sheetz. Local force and geometry sensing regulate cell functions. *Nature reviews. Molecular Cell Biology*, 7:265–75, 2006.

[2] C. E. Morris. Mechanosensitive ion channels in eukaryotic cells. In Nicholas Sperelakis, editor, *Cell Physiology Source Book: A Molecular Approach*, pages 668–681,. Academic Press: SanDiego CA, 1998.

[3] B. Martinac. Mechanosensitive ion channels: Molecules of mechanotransduction. *Journal of Cell Science*, 117(12):2449–2460, 2004.

[4] K. W. Foster, J. Saranak, N. Patel, G. Zarilli, M. Okabe, T. Kline, and K. Nakanishi. A rhodopsin is the functional photoreceptor for phototaxis in the unicellular eukaryote Chlamydomonas. *Nature*, 311(5988):756–759, 1984.

[5] C. A. Erickson. Embryonic fibroblast motility and orientation can be influenced by physiological electric fields. *The Journal of Cell Biology*, 98(1):296–307, 1984.

[6] C.-M. Lo, H.-B. Wang, M. Dembo, and Y.-L. Wang. Cell movement is guided by the rigidity of the substrate. *Biophysical Journal*, 79:144–152, 2000.

[7] R. J. Pelham and Y. Wang. Cell locomotion and focal adhesions are regulated by substrate flexibility. *Proceedings of the National Academy of Sciences*, 94(25):13661–13665, 1997.

[8] A. Saez, A. Buguin, P. Silberzan, and B. Ladoux. Is the mechanical activity of epithelial cells controlled by deformations or forces? *Biophysical Journal*, 89(6):52–54, 2005.

[9] T. Yeung, P. C. Georges, L. A. Flanagan, B. Marg, M. Ortiz, M. Funaki, N. Zahir, W. Ming, V. Weaver, and P. A. Janmey. Effects of substrate stiffness on cell morphology, cytoskeletal structure, and adhesion. *Cell Motility and the Cytoskeleton*, 60(1):24–34, 2005.

[10] B. M. Gumbiner. Cell adhesion: The molecular basis of tissue architecture and morphogenesis. *Cell*, 84:345–357, 1996.

[11] S. Huang and D. E. Ingber. The structural and mechanical complexity of cell-growth control. *Nature Cell Biology*, 1:E131–E138, 1999.

[12] M. H. Zaman, L. M. Trapani, A. L. Sieminski, D. MacKellar, H. Gong, R. D. Kamm, A. Wells, D. A. Lauffenburger, and P. Matsudaira. Migration of tumor cells in 3D matrices is governed by matrix stiffness along with cell-matrix adhesion and proteolysis. *Proceedings of the National Academy of Sciences*, 103(29):10889–10894, 2006.

[13] D. E. Discher, P. Janmey, and Y.-L. Wang. Tissue cells feel and respond to the stiffness of their substrate. *Science*, 310:1139–1143, 2005.

[14] U. S. Schwarz. Soft matters in cell adhesion: Rigidity sensing on soft elastic substrates. *Soft Matter*, 3:263–266, 2007.

[15] T. Lecuit and P. F. Lenne. Cell surface mechanics and the control of cell shape, tissue patterns and morphogenesis. *Nature Reviews. Molecular Cell Biology*, 8(8):633–644, 2007.

[16] J. J. Tyson, K. C. Chen, and B. Novak. Sniffers, buzzers, toggles and blinkers: Dynamics of regulatory and signaling pathways in the cell. *Current Opinion in Cell Biology*, 15(2):221–231, 2003.

[17] B. N. Kholodenko. Cell signalling dynamics in time and space. *Nature Reviews. Molecular Cell Biology*, 7(3):165–176, 2006.

[18] A. Saez, M. Ghibaudo, A. Buguin, P. Silberzan, and B. Ladoux. Rigidity-driven growth and migration of epithelial cells on microstructured anisotropic substrates. *Proceedings of the National Academy of Sciences*, 104(20):8281–8286, 2007.

[19] J. L. Tan, J. Tien, D. M. Pirone, D. S. Gray, K. Bhadriraju, and C. S. Chen. Cells lying on a bed of microneedles: An approach to isolate mechanical force. *Proceedings of the National Academy of Sciences*, 100(4):1484–1489, 2003.

[20] A. J. Engler, S. Sen, H. L. Sweeney, and D. E. Discher. Matrix elasticity directs stem cell lineage specification. *Cell*, 126(4):677–689, 2006.

[21] I. B. Bischofs and U. S. Schwarz. Cell organization in soft media due to active mechanosensing. *Proceedings of the National Academy of Sciences*, 100(16):9274–9279, 2003.

[22] M. Eastwood, V. C. Mudera, D. A. McGrouther, and R. A. Brown. Effect of precise mechanical loading on fibroblast populated collagen lattices: Morphological changes. *Cell Motility and the Cytoskeleton*, 40:13–21, 1998.

[23] A. M. Collinsworth, C. E. Torgan, S. N. Nagda, R. J. Rajalingam, W. E. Kraus, and G. A. Truskey. Orientation and length of mammalian skeletal myocytes in response to a unidirectional stretch. *Cell and Tissue Research*, 302(2):243–251, 2000.

[24] V. P. Shirinsky, Antonov A. S., K. G. Birukov, A. V. Sobolevsky, Y. A. Romanov, N. V. Kabaeva, G. N. Antonova, and V. N. Smirnov. Mechano-chemical control of human endothelium orientation and size. *The Journal of Cell Biology*, 109(1):331–339, 1989.

[25] K. Kurpinski, J. Chu, C. Hashi, and S. Li. Anisotropic mechanosensing by mesenchymal stem cells. *Proceedings of the National Academy of Sciences*, 103(44):16095–16100, 2006.

[26] D. Kong, B. Ji, and L. Dai. Stability of adhesion cluster and cell reorientation under lateral cyclic tension. *Biophysical Journal*, pages 4034–4044, 2008.

[27] R. De, A. Zemel, and S. A. Safran. Dynamics of cell orientation. *Nature Physics*, 3(9):655–659, 2007.

[28] D. E. Ingber. Mechanobiology and diseases of mechanotransduction. *Annals of Medicine*, 35(8):564–577, 2003.

[29] M. J. Paszek, N. Zahir, K. R. Johnson, J. N. Lakins, G. I. Rozenberg, A. Gefen, C. A. Reinhart-King, S. S. Margulies, M. Dembo, D. Boettiger, et al. Tensional homeostasis and the malignant phenotype. *Cancer Cell*, 8(3):241–254, 2005.

[30] B. Alberts, A. Johnson, J. Lewis, M. Raff, K. Roberts, and P. Walter. *Molecular biology of the cell*. Garland Science, New York, 4th edition, 2002.

[31] L. J. Peterson, Z. Rajfur, A. S. Maddox, C. D. Freel, Y. Chen, M. Edlund, C. Otey, and K. Burridge. Simultaneous stretching and contraction of stress fibers in vivo. *Molecular Biology of the Cell*, 15(7):3497–3508, 2004.

[32] K. M. Trybus and S. Lowey. Assembly of smooth muscle myosin minifilaments: Effects of phosphorylation and nucleotide binding. *The Journal of Cell Biology*, 105(6):3007–3019, 1987.

[33] T. D. Pollard and W. C. Earnshaw. *Cell biology*. Saunders, Philadelphia, 4th edition, 2004.

[34] J. Colombelli, A. Besser, H. Kress, E. G. Reynaud, P. Girard, E. Caussinus, U. Haselmann, J. V. Small, U. S. Schwarz, and E. H. K. Stelzer. Mechanosensing in actin stress fibers revealed by a close correlation between force and protein localization. *Journal of Cell Science*, in press.

[35] D. Choquet, D. P. Felsenfeld, and M. P. Sheetz. Extracellular matrix rigidity causes strengthening of integrin-cytoskeleton linkages. *Cell*, 88(1):39–48, 1997.

[36] B. Geiger, A. Bershadsky, R. Pankov, and K.M. Yamada. Transmembrane crosstalk between the extracellular matrix and the cytoskeleton. *Nature Reviews Molecular Cell Biology*, 2:793–805, 2001.

[37] A. Bershadsky, N. Q. Balaban, and B. Geiger. Adhesion-dependent cell mechanosensitivity. *Annual Review of Cell and Developmental Biology*, 19:677–95, 2003.

[38] R. Zaidel-Bar, S. Itzkovitz, A. Ma'ayan, R. Iyengar, and B. Geiger. Functional atlas of the integrin adhesome. *Nature Cell Biology*, 9(8):858–867, 2007.

[39] D. Riveline, E. Zamir, N. Q. Balaban, U. S. Schwarz, B. Geiger, Z. Kam, and A. D. Bershadsky. Focal contact as a mechanosensor: Externally applied local mechanical force induces growth of focal contacts by a mDia1-dependent and ROCK-independent mechanism. *The Journal of Cell Biology*, 153:1175–1185, 2001.

[40] N. Q. Balaban, U. S. Schwarz, D. Riveline, P. Goichberg, G. Tzur, I. Sabanay, D. Mahalu, S. Safran, A. Bershadsky, L. Addadi, and B. Geiger. Force and focal adhesion assembly: A close relationship studied using elastic micro-patterned substrates. *Nature Cell Biology*, 3:466–472, 2001.

[41] S. E. Lee, R. D. Kamm, and M. R. K. Mofrad. Force-induced activation of Talin and its possible role in focal adhesion mechanotransduction. *Journal of Biomechanics*, 40(9):2096–2106, 2007.

[42] A. del Rio, R. Perez-Jimenez, R. Liu, P. Roca-Cusachs, J. M. Fernandez, and M. P. Sheetz. Stretching single talin Rod molecules activates vinculin binding. *Science*, 323(5914):638–641, 2009.

[43] J. C. Friedland, M. H. Lee, and D. Boettiger. Mechanically activated integrin switch controls $\alpha5\beta1$ function. *Science*, 323(5914):642–644, 2009.

[44] G. Giannone and M. P. Sheetz. Substrate rigidity and force define form through tyrosine phosphatase and kinase pathways. *Trends in Cell Biology*, 16(4):213–223, 2006.

[45] K. Burridge and K. Wennerberg. Rho and Rac take center stage. *Cell*, 116(2):167–179, 2004.

[46] A. J. Ridley, H. F. Paterson, C. L. Johnston, D. Diekmann, and A. Hall. The small GTP-binding protein Rac regulates growth factor-induced membrane ruffling. *Cell*, 70(3):401–410, 1992.

[47] A. J. Ridley and A. Hall. The small GTP-binding protein Rho regulates the assembly of focal adhesions and actin stress fibers in response to growth factors. *Cell*, 70(3):389–399, 1992.

[48] E. Neumann, M. Schaefer-Ridder, Y. Wang, and P. H. Hofschneider. Gene transfer into mouse lyoma cells by electroporation in high electric fields. *The EMBO Journal*, 1(7):841–845, 1982.

[49] C. L. Cepko, B. E. Roberts, and R. C. Mulligan. Construction and applications of a highly transmissible murine retrovirus shuttle vector. *Cell*, 37(3):1053–1062, 1984.

[50] P. L. Felgner, T. R. Gadek, M. Holm, R. Roman, H. W. Chan, M. Wenz, J. P. Northrop, G. M. Ringold, and M. Danielsen. Lipofection: A highly efficient, lipid-mediated DNA-transfection procedure. *Proceedings of the National Academy of Sciences*, 84(21):7413–7417, 1987.

[51] R. Y. Tsien. The green fluorescent protein. *Annual Reviews in Biochemistry*, 67(1):509–544, 1998.

[52] J. Lippincott-Schwartz and G. H. Patterson. Development and use of fluorescent protein markers in living cells. *Science*, 300(5616):87–91, 2003.

[53] N. C. Shaner, R. E. Campbell, P. A. Steinbach, B. N. G. Giepmans, A. E. Palmer, and R. Y. Tsien. Improved monomeric red, orange and yellow fluorescent proteins derived from discosoma sp. red fluorescent protein. *Nature Biotechnology*, 22:1567–1572, 2004.

[54] A. F. Straight, A. Cheung, J. Limouze, I. Chen, N. J. Westwood, J. R. Sellers, and T. J. Mitchison. Dissecting temporal and spatial control of cytokinesis with a myosin II inhibitor. *Science*, 299(5613):1743–1747, 2003.

[55] W. H. Moolenaar, L. A. van Meeteren, and B. N. G. Giepmans. The ins and outs of lysophosphatidic acid signaling. *BioEssays*, 26(8):870–881, 2004.

[56] H. Ishihara, B. L. Martin, D. L. Brautigan, H. Karaki, H. Ozaki, Y. Kato, N. Fusetani, S. Watabe, K. Hashimoto, D. Uemura, and D. J. Hartshorne. Calyculin-A and okadaic acid: Inhibitors of protein phosphatase activity. *Biochemical and Biophysical Research Communications*, 159(3):871–877, 1989.

[57] L. Chartier, L. L. Rankin, R. E. Allen, Y. Kato, N. Fusetani, H. Karaki, S. Watabe, and D. J. Hartshorne. Calyculin-A increases the level of protein phosphorylation and changes the shape of 3T3 fibroblasts. *Cell Motility and the Cytoskeleton*, 18(1):26–40, 1991.

[58] A. Besser and U. S. Schwarz. Coupling biochemistry and mechanics in cell adhesion: A model for inhomogeneous stress fiber contraction. *New Journal of Physics*, 9:425, 2007.

[59] R. Paul, P. Heil, J. P. Spatz, and U. S. Schwarz. Propagation of mechanical stress through the actin cytoskeleton toward focal adhesions: Model and experiment. *Biophysical Journal*, 94(4):1470–1482, 2008.

[60] M. R. K. Mofrad. Rheology of the cytoskeleton. *Annual Review of Fluid Mechanics*, 41(1):433–53, 2009.

[61] A. Vogel and V. Venugopalan. Mechanisms of pulsed laser ablation of biological tissues. *Chemical Reviews*, 103(2):577–644, 2003.

[62] K. R. Strahs and M. W. Berns. Laser microirradiation of stress fibers and intermediate filaments in non-muscle cells from cultured rat heart. *Experimental Cell Research*, 119(1):31–45, 1979.

[63] S. Kumar, I. Z. Maxwell, A. Heisterkamp, T. R. Polte, T. P. Lele, M. Salanga, E. Mazur, and D. E. Ingber. Viscoelastic retraction of single living stress fibers and its impact on cell shape, cytoskeletal organization, and extracellular matrix mechanics. *Biophysical Journal*, 90(10):3762–3773, 2006.

[64] T. P. Lele, J. Pendse, S. Kumar, M. Salanga, J. Karavitis, and D. E. Ingber. Mechanical forces alter zyxin unbinding kinetics within focal adhesions of living cells. *Journal of Cellular Physiology*, 207(1):187–94, 2006.

[65] A. F. Huxley. Muscle structure and theories of contraction. *Progress in Biophysics and Biophysical Chemistry*, 7:255–318, 1957.

[66] S. M. Mijailovich, J. J. Fredberg, and J. P. Butler. On the theory of muscle contraction: Filament extensibility and the development of isometric force and stiffness. *Biophysical Journal*, 71:1475–84, 1996.

[67] T. A. J. Duke. Molecular model of muscle contraction. *Proceedings of the National Academy of Sciences*, 96:2770–2775, 1999.

[68] K. Kruse and F. Jülicher. Actively contracting bundles of polar filaments. *Physical Review Letters*, 85(8):1778–1781, 2000.

[69] K. Kruse and F. Jülicher. Self-organization and mechanical properties of active filament bundles. *Physical Review E*, 67(5):051913, 2003.

[70] I. L. Novak, B. M. Slepchenko, A. Mogilner, and L. M. Loew. Cooperativity between cell contractility and adhesion. *Physical Review Letters*, 93(26):268109, 2004.

[71] G. Civelekoglu-Scholey, A. Wayne Orr, I. Novak, J.-J. Meister, M.A. Schwartz, and A. Mogilner. Model of coupled transient changes of Rac, Rho, adhesions and stress fibers alignment in endothelial cells responding to shear stress. *Journal of Theoretical Biology*, 232(4):569–585, 2005.

[72] V. S. Deshpande, R. M. McMeeking, and A. G. Evans. A bio-chemo-mechanical model for cell contractility. *Proceedings of the National Academy of Sciences*, 103(38):14015–14020, 2006.

[73] V. S. Deshpande, R. M. McMeeking, and A. G. Evans. A model for the contractility of the cytoskeleton including the effects of stress-fibre formation and dissociation. *Proceedings of the Royal Society A: Mathematical, Physical and Engineering Sciences*, 463(2079):787–815, 2007.

[74] A. Nicolas, B. Geiger, and S. A. Safran. Cell mechanosensitivity controls the anisotropy of focal adhesions. *Proceedings of the National Academy of Sciences*, 101(34):12520–12525, 2004.

[75] A. Nicolas and S. A. Safran. Elastic deformations of grafted layers with surface stress. *Physical Review E*, 69(5):051902, 2004.

[76] T. Shemesh, B. Geiger, A. D. Bershadsky, and M. M. Kozlov. Focal adhesions as mechanosensors: A physical mechanism. *Proceedings of the National Academy of Sciences*, 102(35):12383–12388, 2005.

[77] A. Besser and S. A. Safran. Force-induced adsorption and anisotropic growth of focal adhesions. *Biophysical Journal*, 90(10):3469–3484, 2006.

[78] D. R. B. Aroush and H.D. Wagner. Shear-stress profile along a cell focal adhesion. *Advanced Materials*, 18(12):1537–1540, 2006.

[79] A. Nicolas and S. A. Safran. Limitation of cell adhesion by the elasticity of the extracellular matrix. *Biophysical Journal*, 91(1):61–73, 2006.

[80] A. Nicolas, A. Besser, and S. A. Safran. Dynamics of cellular focal adhesions on deformable substrates: Consequences for cell force microscopy. *Biophysical Journal*, 95(2):527–539, 2008.

[81] A. Bershadsky, M. Kozlov, and B. Geiger. Adhesion-mediated mechanosensitivity: A time to experiment, and a time to theorize. *Current Opinion in Cell Biology*, 18(5):472–481, 2006.

[82] V. A. Kargin and G. L. Slonimsky. *Doklady Akademii Nauk SSSR*, 62:239–242, 1948.

[83] V. A. Kargin and G. L. Slonimsky. *Zurnal Fiziceskoj Chimii*, 23:563–571, 1949.

[84] P. E. Rouse. A theory of the linear viscoelastic properties of dilute solutions of coiling polymers. *The Journal of Chemical Physics*, 21:1272–1280, 1953.

[85] G. V. Vinogradov and A. Ya. Malkin. *Rheology of polymers: Viscoelasticity and flow of polymers*. Springer-Verlag, Berlin, 1980.

[86] Y. C. Fung. *Biomechanics: Mechanical properties of living tissues*. Springer Verlag, New York, 1993.

[87] J. Howard. *Mechanics of motor proteins and the cytoskeleton*. Sunderland, Sinauer Associates, 2001.

[88] L. D. Landau and E. M. Lifschitz. *Lehrbuch Der Theoretischen Physik VII, Elastizitätstheorie*. Akademie Verlag, Berlin, 7th edition, 1991.

[89] S. Deguchi, T. Ohashi, and M. Sato. Tensile properties of single stress fibers isolated from cultured vascular smooth muscle cells. *Journal of Biomechanics*, 39:2603–2610, 2006.

[90] Yu. Ya. Gotlib and M. V. Volkenshtein. *Zurnal Techniceskoj Fiziki*, 23:1936–1948, 1953.

[91] George B. Arfken and Hans J. Weber. *Mathematical methods for physicists*. Harcourt/Academic Press, San Diego, 5th edition, 2001.

[92] B. Schnurr, F. Gittes, F. C. MacKintosh, and C. F. Schmidt. Determining microscopic viscoelasticity in flexible and semiflexible polymer networks from thermal fluctuations. *Macromolecules*, 30(25):7781–7792, 1997.

[93] F. C. MacKintosh and C. F. Schmidt. Microrheology. *Current Opinion in Colloid & Interface Science*, 4(4):300–307, 1999.

[94] R. M. Hochmuth. Micropipette aspiration of living cells. *Journal of Biomechanics*, 33(1):15–22, 2000.

[95] D. E. Discher, D. H. Boal, and S. K. Boey. Simulations of the erythrocyte cytoskeleton at large deformation. II. Micropipette aspiration. *Biophysical Journal*, 75(3):1584–1597, 1998.

[96] J. Alcaraz, L. Buscemi, M. Grabulosa, X. Trepat, B. Fabry, R. Farre, and D. Navajas. Microrheology of human lung epithelial cells measured by atomic force microscopy. *Biophysical Journal*, 84(3):2071–2079, 2003.

[97] A. R. Bausch, F. Ziemann, A. A. Boulbitch, K. Jacobson, and E. Sackmann. Local measurements of viscoelastic parameters of adherent cell surfaces by magnetic bead microrheometry. *Biophysical Journal*, 75(4):2038–2049, 1998.

[98] A. R. Bausch, W. Moller, and E. Sackmann. Measurement of local viscoelasticity and forces in living cells by magnetic tweezers. *Biophysical Journal*, 76(1):573–579, 1999.

[99] B. Fabry, G. N. Maksym, J. P. Butler, M. Glogauer, D. Navajas, and J. J. Fredberg. Scaling the microrheology of living cells. *Physical Review Letters*, 87(14):148102, 2001.

[100] B. Fabry, G. N. Maksym, J. P. Butler, M. Glogauer, D. Navajas, N. A. Taback, E. J. Millet, and J. J. Fredberg. Time scale and other invariants of integrative mechanical behavior in living cells. *Physical Review E*, 68(4):41914, 2003.

[101] I. B. Bischofs, F. Klein, D. Lehnert, M. Bastmeyer, and U. S. Schwarz. Filamentous network mechanics and active contractility determine cell and tissue shape. *Biophysical Journal*, 95(7):3488–3496, 2008.

[102] M. R. Stachowiak and B. O'Shaughnessy. Kinetics of stress fibers. *New Journal of Physics*, 10(025002):025002, 2008.

[103] P. Sollich, F. Lequeux, P. Hébraud, and M. E. Cates. Rheology of soft glassy materials. *Physical Review Letters*, 78(10):2020–2023, 1997.

[104] E. Lazarides and K. Burridge. Alpha-actinin: Immunofluorescent localization of a muscle structural protein in nonmuscle cells. *Cell*, 6(3):289–98, 1975.

[105] M. C. Beckerle. Identification of a new protein localized at sites of cell-substrate adhesion. *The Journal of Cell Biology*, 103(5):1679–1687, 1986.

[106] A. W. Crawford, J. W. Michelsen, and M. C. Beckerle. An interaction between zyxin and alpha-actinin. *The Journal of Cell Biology*, 116(6):1381–1393, 1992.

[107] L. Sachs. *Angewandte Statistik: Anwendung statistischer Methoden.* Springer Verlag, New York, 2004.

[108] J. Colombelli, C. Taengemo, C. Haselmann-Weiss U., Anthony, E. H. K. Stelzer, R. Pepperkok, and E. G. Reynaud. A correlative light and electron microscopy method based on laser micropatterning and etching. *Methods in Molecular Biology*, 2008.

[109] J. M. Ervasti. Costameres: The achilles' heel of herculean muscle. *Journal of Biological Chemistry*, 278(16):13591–13594, 2003.

[110] M. Yoshigi, L. M. Hoffman, C. C. Jensen, H. J. Yost, and M. C. Beckerle. Mechanical force mobilizes zyxin from focal adhesions to actin filaments and regulates cytoskeletal reinforcement. *The Journal of Cell Biology*, 171(2):209–215, 2005.

[111] W. H. Guo and Y. L. Wang. Retrograde fluxes of focal adhesion proteins in response to cell migration and mechanical signals. *Molecular Biology of the Cell*, 18(11):4519–27, 2007.

[112] M. Reinhard, J. Zumbrunn, D. Jaquemar, M. Kuhn, U. Walter, and B. Trueb. An α-actinin binding site of zyxin is essential for subcellular zyxin localization and α-actinin recruitment. *Journal of Biological Chemistry*, 274(19):13410–13418, 1999.

[113] B. Li and B. Trueb. Analysis of the α-actinin/zyxin interaction. *Journal of Biological Chemistry*, 276(36):33328–33335, 2001.

[114] K. Djinovic-Carugo, M. Gautel, J. Ylänne, and P. Young. The spectrin repeat: A structural platform for cytoskeletal protein assemblies. *FEBS Letters*, 513(1):119–123, 2002.

[115] D. T. Mirijanian and G. A. Voth. Unique elastic properties of the spectrin tetramer as revealed by multiscale coarse-grained modeling. *Proceedings of the National Academy of Sciences*, 105(4):1204–1208, 2008.

[116] N. Wang, I. M. Tolic-Norrelykke, J. Chen, S. M. Mijailovich, J. P. Butler, J. J. Fredberg, and D. Stamenovic. Cell prestress. I. Stiffness and prestress are closely associated in adherent contractile cells. *American Journal of Physiology- Cell Physiology*, 282(3):606–616, 2002.

[117] B. Sabass, M. L. Gardel, C. M. Waterman, and U. S. Schwarz. High resolution traction force microscopy based on experimental and computational advances. *Biophysical Journal*, 94(1):207–20, 2008.

[118] Y. Sawada, M. Tamada, B. J. Dubin-Thaler, O. Cherniavskaya, R. Sakai, S. Tanaka, and M. P. Sheetz. Force sensing by mechanical extension of the Src family kinase substrate p130Cas. *Cell*, 127(5):1015–1026, 2006.

[119] M. Abercrombie, J. E. Heaysman, and S. M. Pegrum. The locomotion of fibroblasts in culture. IV. Electron microscopy of the leading lamella. *Experimental Cell Research*, 67(2):359–367, 1971.

[120] M. Abercrombie and G. A. Dunn. Adhesions of fibroblasts to substratum during contact inhibition observed by interference reflection microscopy. *Experimental Cell Research*, 92(1):57–62, 1975.

[121] C. S. Izzard and L. R. Lochner. Cell-to-substrate contacts in living fibroblasts: An interference reflexion study with an evaluation of the technique. *Journal of Cell Science*, 21(1):129–159, 1976.

[122] C. S. Izzard and L. R. Lochner. Formation of cell-to-substrate contacts during fibroblast motility: An interference-reflexion study. *Journal of Cell Science*, 42(1):81–116, 1980.

[123] R. O. Hynes. Integrins: A family of cell surface receptors. *Cell*, 48(4):549–554, 1987.

[124] B. Geiger. A 130K protein from chicken gizzard: Its localization at the termini of microfilament bundles in cultured chicken cells. *Cell*, 18:193–205, 1979.

[125] K. Burridge and J. R. Feramisco. Microinjection and localization of a 130K protein in living fibroblasts: A relationship to actin and fibronectin. *Cell*, 19(3):587–595, 1980.

[126] B. Geiger, K. T. Tokuyasu, A. H. Dutton, and S. J. Singer. Vinculin, an intracellular protein localized at specialized sites where microfilament bundles terminate at cell membranes. *Proceedings of the National Academy of Sciences*, 77(7):4127–4131, 1980.

[127] K. Burridge and L. Connell. A new protein of adhesion plaques and ruffling membranes. *The Journal of Cell Biology*, 97(2):359–367, 1983.

[128] K. Burridge and L. Connell. Talin: A cytoskeletal component concentrated in adhesion plaques and other sites of actin-membrane interaction. *Cell Motility*, 3(5-6):405–17, 1983.

[129] E. Zamir and B. Geiger. Molecular complexity and dynamics of cell-matrix adhesions. *Journal of Cell Science*, 114(20):3583–3590, 2001.

[130] G. D. Bader, D. Betel, and C. W. V. Hogue. BIND: The biomolecular interaction network database. *Nucleic Acids Research*, 31(1):248–250, 2003.

[131] G. R. Mishra, M. Suresh, K. Kumaran, N. Kannabiran, S. Suresh, P. Bala, K. Shivakumar, N. Anuradha, R. Reddy, T. M. Raghavan, et al. Human protein reference database-2006 update. *Nucleic Acids Research*, 34(1):D411–D414, 2006.

[132] M. Kanehisa, S. Goto, S. Kawashima, and A. Nakaya. The KEGG databases at GenomeNet. *Nucleic Acids Research*, 30(1):42–46, 2002.

[133] E. E. Sander, J. P. ten Klooster, S. van Delft, R. A. van der Kammen, and J. G. Collard. Rac downregulates Rho activity: Reciprocal balance between both GTPases determines cellular morphology and migratory behavior. *The Journal of Cell Biology*, 147(5):1009–1022, 1999.

[134] A. Hall. Rho GTPases and the actin cytoskeleton. *Science*, 279:509–514, 1998.

[135] S. Etienne-Manneville and A. Hall. Rho GTPases in cell biology. *Nature*, 420:629–35, 2002.

[136] M. C. Seabra. Membrane association and targeting of prenylated Ras-like GTPases. *Cellular Signalling*, 10(3):167–172, 1998.

[137] A. P. Somlyo and A. V. Somlyo. Signal transduction by G-proteins, Rho-kinase and protein phosphatase to smooth muscle and non-muscle myosin II. *The Journal of Physiology*, 522(2):177–185, 2000.

[138] J. Feng, M. Ito, Y. Kureishi, K. Ichikawa, M. Amano, N. Isaka, K. Okawa, A. Iwamatsu, K. Kaibuchi, D. J. Hartshorne, and T. Nakano. Rho-associated kinase of chicken gizzard smooth muscle. *Journal of Biological Chemistry*, 274(6):3744–3752, 1999.

[139] K. E. Kamm and J. T. Stull. The function of myosin and myosin light chain kinase phosphorylation in smooth muscle. *Annual Reviews in Pharmacology and Toxicology*, 25(1):593–620, 1985.

[140] J. D. Murray. *Mathematical Biology*. Springer, New York, 2002.

[141] D. J. Hartshorne, M. Ito, and F. Erdoedi. Myosin light chain phosphatase: Subunit composition, interactions and regulation. *Journal of Muscle Research and Cell Motility*, 19(4):325–341, 1998.

[142] H. Nagamoto and K. Yagi. Properties of myosin light chain kinase prepared from rabbit skeletal muscle by an improved method. *Journal of Biochemistry*, 95(4):1119–1130, 1984.

[143] T. M. Butler, S. R. Narayan, S. U. Mooers, and M. J. Siegman. Rapid turnover of myosin light chain phosphate during cross-bridge cycling in smooth muscle. *American Journal of Physiology- Cell Physiology*, 267(4):C1160–1166, 1994.

[144] M. Amano, M. Ito, K. Kimura, Y. Fukata, K. Chihara, T. Nakano, Y. Matsuura, and K. Kaibuchi. Phosphorylation and activation of myosin by Rho-associated kinase (Rho-kinase). *Journal of Biological Chemistry*, 271(34):20246–20249, 1996.

[145] D. R. Hathaway and R. S. Adelstein. Human platelet myosin light chain kinase requires the calcium-binding protein calmodulin for activity. *Proceedings of the National Academy of Sciences*, 76(4):1653–1657, 1979.

[146] M. H. Nunnally, S. B. Rybicki, and J. T. Stull. Characterization of chicken skeletal muscle myosin light chain kinase. Evidence for muscle-specific isozymes. *Journal of Biological Chemistry*, 260(2):1020–1026, 1985.

[147] D. C. Bartelt, S. Moroney, and D. J. Wolff. Purification, characterization and substrate specificity of calmodulin-dependent myosin light-chain kinase from bovine brain. *Biochemical Journal*, 247(3):747–756, 1987.

[148] M. D. Pato and R. S. Adelstein. Purification and characterization of a multisubunit phosphatase from turkey gizzard smooth muscle. The effect of calmodulin binding to myosin light chain kinase on dephosphorylation. *Journal of Biological Chemistry*, 258(11):7047–7054, 1983.

[149] J. Lippincott-Schwartz, E. Snapp, and A. Kenworthy. Studying protein dynamics in living cells. *Nature Reviews. Molecular Cell Biology*, 2(6):444–456, June 2001.

[150] S. Umemoto and J. R. Sellers. Characterization of in vitro motility assays using smooth muscle and cytoplasmic myosins. *Journal of Biological Chemistry*, 265(25):14864–14869, 1990.

[151] E. Klipp, R. Herwig, A. Kowald, C. Wierling, and H. Lehrach. *Systems biology in practice. concepts, implementation and application.* Wiley-VCH, Berlin, 2005.

[152] S. Hoops, S. Sahle, R. Gauges, C. Lee, J. Pahle, N. Simus, M. Singhal, L. Xu, P. Mendes, and U. Kummer. COPASI: A COmplex PAthway SImulator. *Bioinformatics*, 22(24):3067–3074, 2006.

[153] X. D. Ren, W. B. Kiosses, and M. A. Schwartz. Regulation of the small GTP-binding protein Rho by cell adhesion and the cytoskeleton. *The EMBO Journal*, 18:578–585, 1999.

[154] M. A. del Pozo, L. S. Price, N. B. Alderson, X. D. Ren, and M. A. Schwartz. Adhesion to the extracellular matrix regulates the coupling of the small GTPase Rac to its effector PAK. *The EMBO Journal*, 19:2008–2014, 2000.

[155] U. S. Schwarz, T. Erdmann, and I. B. Bischofs. Focal adhesions as mechanosensors: The two-spring model. *BioSystems*, 83:225–232, 2006.

[156] S. H. Strogatz. *Nonlinear Dynamics and Chaos.* Addison-Wesley Reading, MA, 1994.

[157] X. Z. Shu, Y. Liu, Y. Luo, M. C. Roberts, and G. D. Prestwich. Disulfide cross-linked hyaluronan hydrogels. *Biomacromolecules*, 3(6):1304–1311, 2002.

[158] S. Cai, Y. Liu, X. Zheng Shu, and G. D. Prestwich. Injectable glycosamino-glycan hydrogels for controlled release of human basic fibroblast growth factor. *Biomaterials*, 26(30):6054–6067, 2005.

[159] X. Z. Shu, S. Ahmad, Y. Liu, and G. D. Prestwich. Synthesis and evaluation of injectable, in situ crosslinkable synthetic extracellular matrices for tissue engineering. *Journal of Biomedical Materials Research Part A*, 79(4):902–912, 2006.

[160] A. J. Engler, F. Rehfeldt, S. Sen, and D. E. Discher. Microtissue elasticity: Measurements by atomic force microscopy and its influence on cell differentiation. *Methods in Cell Biology*, 83:521–45, 2007.

[161] K. C. Neuman and S. M. Block. Optical trapping. *Review of Scientific Instruments*, 75(9):2787–2809, 2004.

[162] R. A. Brown, R. Prajapati, D. A. Mc Grouther, I. V. Yannas, and M. Eastwood. Tensional homeostasis in dermal fibroblasts: Mechanical responses to mechanical loading in three-dimensional substrates. *Journal of Cellular Physiology*, 175:323–332, 1998.

[163] J. J. Tomasek, G. Gabbiani, B. Hinz, C. Chaponnier, R. A. Brown, et al. Myofibroblasts and mechano-regulation of connective tissue remodelling. *Nature Reviews Molecular Cell Biology*, 3:349–363, 2002.

[164] A. C. Pipkin. *Lectures on viscoelasticity theory*. Springer, New York, 1972.

Acknowledgements

Hiermit erkläre ich, dass ich die vorgelegte Dissertation selbst verfasst und mich dabei keiner anderen als der von mir ausdrücklich bezeichneten Quellen und Hilfen bedient habe.

Heidelberg, den ....

                                                                   Achim Besser